SAND2020-10344R

Blind Modeling Validation Exercises Using the Horizontal Dry Cask Simulator

Spent Fuel and Waste Disposition

Prepared for
US Department of Energy
Spent Fuel and Waste Science and Technology

R.J.M. Pulido, R.E. Fasano, E.R. Lindgren, G.J. Koenig, S.G. Durbin
Sandia National Laboratories, Albuquerque, NM

A. Zigh, J. Solis, K. Hall
Nuclear Regulatory Commission, Washington, DC

S.R. Suffield, D.J. Richmond, J.A. Fort
Pacific Northwest National Laboratory, Richland, WA

M. LLoret, M. Galbán, A. Sabater
Empresa Nacional del Uranio, S.A., S.M.E. (ENUSA), Madrid (Spain)

September 25, 2020
Milestone No. M2SF-20SN010203034
SAND2020-10344 R

Prepared by
Sandia National Laboratories
Albuquerque, New Mexico 87185 and Livermore, California 94550

Sandia National Laboratories is a multimission laboratory managed and operated by National Technology and Engineering Solutions of Sandia, LLC, a wholly owned subsidiary of Honeywell International, Inc., for the U.S. Department of Energy's National Nuclear Security Administration under contract DE-NA0003525.

ABSTRACT

The U.S. Department of Energy (DOE) established a need to understand the thermal-hydraulic properties of dry storage systems for commercial spent nuclear fuel (SNF) in response to a shift towards the storage of high-burnup (HBU) fuel (> 45 gigawatt days per metric ton of uranium, or GWd/MTU). This shift raises concerns regarding cladding integrity, which faces increased risk at the higher temperatures within spent fuel assemblies present within HBU fuel compared to low-burnup fuel (≤ 45 GWd/MTU). A dry cask simulator (DCS) was built at Sandia National Laboratories (SNL) in Albuquerque, New Mexico to produce validation-quality data that can be used to test the accuracy of the modeling used to predict cladding temperatures. These temperatures are critical to evaluating cladding integrity throughout the storage cycle of commercial spent nuclear fuel.

A model validation exercise was previously carried out for the DCS in a vertical configuration. Lessons learned during the previous validation exercise have been applied to a new, blind study using a horizontal dry cask simulator (HDCS). Three modeling institutions – the Nuclear Regulatory Commission (NRC), Pacific Northwest National Laboratory (PNNL), and Empresa Nacional del Uranio, S.A., S.M.E. (ENUSA) – were granted access to the input parameters from the DCS Handbook, SAND2017-13058R, and results from a limited data set from the horizontal BWR dry cask simulator tests reported in the HDCS update report, SAND2019-11688R. With this information, each institution was tasked to calculate peak cladding temperatures and air mass flow rates for ten HDCS test cases. Axial as well as vertical and horizontal transverse temperature profiles were also calculated. These calculations were done using modeling codes (ANSYS/Fluent, STAR-CCM+, or COBRA-SFS), each with their own unique combination of modeling assumptions and boundary conditions. For this validation study, the ten test cases of the horizontal dry cask simulator were defined by three independent variables – fuel assembly decay heat (0.5 kW, 1 kW, 2.5 W, and 5 kW), internal backfill pressure (100 kPa and 800 kPa), and backfill gas (helium and air).

The plots provided in Chapter 3 of this report show the axial, vertical, and horizontal temperature profiles obtained from the dry cask simulator experiments in the horizontal configuration and the corresponding models used to describe the thermal-hydraulic behavior of this system. The tables provided in Chapter 3 illustrate the closeness of fit of the model data to the experiment data through root mean square (RMS) calculations of the error in peak cladding temperatures (PCTs), PCT axial locations, axial temperature profiles, vertical and horizontal temperature profiles at two different axial locations, and air mass flow rates for the ten test cases, normalized by the experimental results. The model results are assigned arbitrary model numbers to retain anonymity.

Due to the relatively flat axial temperature profiles, small temperature gradients resulted in large deviations of all models' PCT axial location from the experimental PCT axial location. When the PCT axial location error is excluded in the calculation of the combined RMS of the normalized errors that considers PCT, the temperature profiles, and the air mass flow rates, the model data fits the experimental data to within 5%. When the vault information is excluded, the model data fits the experimental data to within 2.5%.

An error analysis was developed further for one model, using the model and experimental uncertainties in each validation parameter to calculate validation uncertainties. The uncertainties for each parameter were used to define quantifiable validation criteria. For this analysis, the model was considered validated for a given comparison metric if the normalized error in that metric divided by the validation uncertainty was less than or equal to 1. When considering the combined RMS of the normalized errors of all metrics divided by their validation uncertainties, the model was found to have satisfied the criterion for model validation.

This page is intentionally left blank.

ACKNOWLEDGEMENTS

The authors would like to gratefully acknowledge the hard work and commitment to excellence of Adrian Peralez, Ronald Williams, Beau Baigas, and Thad Vice, which made the success of this project possible.

This work was conducted under the Department of Energy Spent Fuel and Waste Science and Technology campaign. Sylvia Saltzstein (8845) and Geoff Freeze (8843) are to be commended for exceptional project leadership.

This page is intentionally left blank.

CONTENTS

This page is intentionally left blank.

LIST OF FIGURES

This page is intentionally left blank.

LIST OF TABLES

This page is intentionally left blank.

ACRONYMS

BWR	boiling water reactor
CFD	computational fluid dynamics
CNWRA	Center for Nuclear Waste Regulatory Analyses
COBRA-SFS	Coolant Boiling in Rod Arrays – Spent Fuel Storage
CYBL	Cylindrical Boiling
DAQ	data acquisition
DCS	Dry Cask Simulator
DCSS	dry cask storage system
DOE	U.S. Department of Energy
ENUSA	Empresa Nacional del Uranio, S.A., S.M.E.
GCI	grid convergence index
GWd	gigawatt day
HBU	high burnup
HDCS	Horizontal Dry Cask Simulator
HSM	horizontal storage module
INL	Idaho National Laboratory
ISFSI	independent spent fuel storage installation
MAWP	maximum allowable working pressure
MgO	magnesium oxide
MTU	metric ton of uranium
NE	Office of Nuclear Energy
NIST	National Institute of Standards and Technology
NRC	Nuclear Regulatory Commission
NUHOMS	NUTECH Horizontal Modular Storage
PCT	peak cladding temperature
PNNL	Pacific Northwest National Laboratory
PTB	power test board
PWR	pressurized water reactor
RMS	root mean square
SCR	silicon-controlled rectifier
SFWD	Spent Fuel and Waste Disposition
SNF	spent nuclear fuel
SNL	Sandia National Laboratories

TAN	Test Area North
TC	thermocouple

BLIND MODELING VALIDATION EXERCISES USING THE HORIZONTAL DRY CASK SIMULATOR

This report fulfills milestone M2SF-20SN010203034 in the Spent Fuel and Waste Science and Technology work package (SF-20SN01020303). This work was sponsored under the Department of Energy's (DOE) Office of Nuclear Energy (NE) Spent Fuel and Waste Disposition (SFWD) campaign.

1 INTRODUCTION

Dry cask storage systems (DCSSs) for spent nuclear fuel (SNF) are designed to provide a confinement barrier that prevents the release of radioactive material, maintains SNF in an inert environment, provides radiation shielding, and maintains subcriticality conditions. SNF is initially stored in pools of water for cooling where the water also provides radiation shielding. As these pools approach capacity, dry cask storage systems are becoming the primary alternative for interim storage. After sufficient cooling in pools, SNF is loaded into a canister and placed inside a cask, where the canister is sealed. The dry cask storage system is then decontaminated and dried, and the system is ultimately placed either vertically or horizontally in aboveground or belowground storage.

The effectiveness of these dry cask storage systems in fulfilling their confinement barrier purpose is evaluated through detailed analytical modeling of their thermal performance. The modeling is carried out by the vendor to demonstrate the performance and regulatory compliance of each DCSS. The Nuclear Regulatory Commission (NRC) then independently verifies these licensing factors. Thermal-hydraulic testing of either full-sized casks or scaled cask analogs is recognized as vital for the validation of design and performance models. Previous studies on single assemblies [Bates, 1986; Irino *et al.*, 1987] and full-scale, multi-assembly casks [Dziadosz *et al*., 1986; McKinnon *et al.*,1986; McKinnon *et al*., 1987; Creer *et al*., 1987; McKinnon *et al*.,1989; McKinnon *et al*., 1992] have contributed to the knowledge base of heat transfer and gas flow in dry storage casks. These contributions help with the evaluation of cladding integrity and the definition of regulatory limits for key parameters in these systems, such as peak cladding temperatures (PCTs).

To add to the dry storage cask thermal-hydraulic response knowledge base, the boiling water reactor (BWR) dry cask simulator (DCS) was built and tested [Durbin and Lindgren, 2018] in a simulated vertical aboveground configuration with a helium backfill. This was done by obtaining characteristic data under various heat loads, internal canister pressures, and external configurations. The motivation was to determine the influences of elevated helium pressures that have become more prevalent in modern cask designs and the external convection of aboveground dry cask storage systems not accounted for in previous studies. This vertical DCS test simulated a single, full-length prototypic BWR fuel assembly – a large temperature data set was collected from the 97 thermocouples (TCs) arranged at 0.152 m (6 in.), 0.305 m (12 in.), and 0.610 m (24 in.) intervals.

Data sets from the vertically-oriented DCS were used in a previous model validation activity [Pulido *et al.*, 2020]. In this previous study, a model validation exercise was carried out using the data obtained from DCS testing in the vertical, aboveground configuration. Five modeling institutions – Nuclear Regulatory Commission (NRC), Pacific Northwest National Laboratory (PNNL), Centro de Investigaciones Energéticas, MedioAmbientales y Tecnológicas (CIEMAT), and Empresa Nacional del Uranio, S.A., S.M.E. (ENUSA) in collaboration with Universidad Politécnica de Madrid (UPM) – were granted access to the input parameters from the DCS Handbook, SAND2017-13058R [Lindgren and Durbin, 2017], and results from the vertical aboveground BWR dry cask simulator tests reported in NUREG/CR-7250 [Durbin and Lindgren, 2018]. With this information, each institution was tasked to calculate minimum, average, and maximum fuel axial temperature profiles for the fuel region as well as the axial temperature profiles of the DCS structures. Transverse temperature profiles (in both vertical and horizontal directions) and air mass flow rates within the dry cask simulator were also calculated. These calculations were done

using modeling codes (ANSYS/Fluent, STAR-CCM+, or COBRA-SFS), each with their own unique combination of modeling assumptions and boundary conditions. For this validation study, four test cases of the vertical, aboveground DCS were considered, defined by two independent variables – either 0.5 kW or 5 kW fuel assembly decay heat, and either 100 kPa or 800 kPa internal helium pressure. However, this model validation activity was not fully blind in that all the modeling participants had access to complete data sets.

Lessons learned during the previous vertically-oriented DCS validation exercise have been applied to a new, blind study using a horizontally dry cask simulator (HDCS). Figure 1.1 shows a diagram for a horizontally-oriented, aboveground dry cask storage system, which provides the basis for the HDCS.

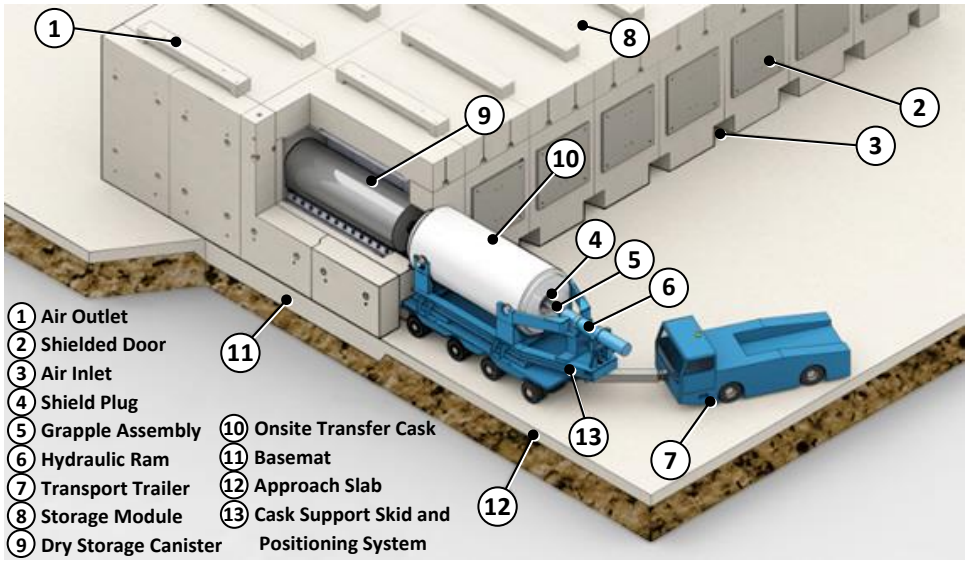

Source: http://us.areva.com/EN/home-3138/areva-nuclear-materials-tn-americas--nuhoms-used-fuel-storage-system.html#tab=tab6

Figure 1.1 Horizontal dry storage cask system.

1.1 Objective

The purpose of this study was to conduct a blind model validation exercise using the HDCS. The approach used in the model validation exercise for the vertically-oriented dry cask simulator [Pulido *et al.*, 2020] was expanded for this exercise using the horizontal dry cask simulator, which considers ten test cases as shown in Table 1.1. In this study, two limited data sets from the 2.5 kW power and 100 kPa backfill pressure HDCS tests for both helium and air backfills reported in SAND2019-11688R [Lindgren et al. 2019] were provided for model calibration. Input parameters from the DCS handbook [Lindgren and Durbin, 2017] were also given, but only three additional input parameters – assembly power, interior vessel pressure, and ambient temperature – were supplied for the other eight test cases. The results from those eight test cases were purposely withheld, making those cases blind to the modeling institutions. Three institutions – Nuclear Regulatory Commission (NRC), Pacific Northwest National Laboratory (PNNL), and Empresa Nacional del Uranio, S.A., S.M.E. (ENUSA) –were tasked to calculate peak cladding temperatures (PCTs), axial PCT locations, temperature profiles across six axial locations, vertical and horizontal temperature profiles across two different axial levels, and air mass flow rates within the horizontal dry cask simulator using modeling codes, each with their own unique combination of modeling assumptions and boundary conditions.

1.2 Previous Studies

NUREG-2152 [Zigh and Solis, 2013] states that model validation exercises examine whether the physical models used in computational fluid dynamics (CFD) calculations correlate with real-world observations, and that a basic validation strategy involves identifying and quantifying any errors and uncertainties that arise through the comparison of modeling results to experimental data. These types of validation exercises can be used for any type of modeling code. Numerous studies have contributed to the comparisons between computer modeling simulation outputs and experimental data from dry cask investigations, with some initial studies done on single assemblies and later studies done on full-scale, multi-assembly systems, as discussed in the following sections.

1.2.1 Small Scale, Single Assembly Model Validation

The COBRA-SFS (Coolant Boiling in Rod Arrays – Spent Fuel Storage) computer code is "a steady-state, lumped-parameter, finite-difference code which predicts flow and temperature distributions in spent fuel storage systems…by providing solutions to the equations governing mass, momentum, and energy conservation for single-phase incompressible flows". It was used to make predictions on the temperature profiles of both an actual spent fuel single assembly and an electrically heated assembly [Lombardo *et al.*, 1986]. The study marked the first instance of the COBRA-SFS code being used to study spent fuel. The spent fuel assembly was a discharged 15×15 pressurized water reactor (PWR) assembly from the Florida Power and Light Turkey Point Unit Number 3 reactor with a burnup of 28 GWd/MTU. The decay heat levels were 1.17 kW for air and vacuum fill media and 1.16 kW for helium fill media. The electrically-heated assembly was built to simulate a 15×15 light water reactor PWR fuel assembly, and 18 tests were performed which modified the fill media (air at atmospheric pressure, helium at 6.9 ± 3.5 kPa, vacuum at -610 mm mercury), the test assembly power level (0.5 kW, 1 kW), and the test cask orientation (vertical, horizontal, inclined or 25° from horizontal). Each assembly was instrumented with thermocouples to obtain experimental temperature data during each test run – 20 thermocouples were placed at 5 axial locations on the outer wall, while 15 instrument tubes (each with 7 thermocouples at different axial locations) were placed in the emptied control rod guide tubes to collect axial temperature information within the assembly. To simulate a multi-assembly cask, the outer surfaces of both of the test casks containing the single assemblies were heated to maintain a fixed, elevated wall temperature that simulates the presence of adjacent fuel assemblies. For both cases, the canister was surrounded by a carbon steel liner and was heated to a temperature that would be expected in a multi-assembly system. Once this elevated temperature reached steady state, temperature data within the assembly was collected.

Blind, or "pre-look", runs of the COBRA-SFS code were first conducted before the tests to judge how accurately the code could predict internal cask temperatures. Once the internal cask temperatures were measured, the predicted peak cladding temperatures for the spent fuel and electrically heated PWR fuel assemblies were compared to the measured results and were found to be within ±10°C and ±27°C, respectively. The discrepancy between the predicted temperatures and the experimental data was primarily attributed to inadequate modeling of the convection in the test casks and an over-prediction of the temperature drop from the fuel tubes to the cask wall. Following the collection of experimental data, post-test optimization simulations were run. For the electrically heated cask model, when the emissivity was changed from 0.2 to 0.25, better agreement in the fuel tube-to-cask wall temperature difference for both the 0.5 kW and 1 kW cases was found. Although there were still slight discrepancies between the COBRA-SFS predictions and the experimental data (due to the increased friction factor applied to the downcomer assembly, which aided in computational stability), the post-test predicted peak rod temperatures lay within ± 3°C and ± 15°C for the spent fuel and electrically-heated assemblies, respectively. Therefore, the optimized code was claimed to have improved capability of predicting temperatures in the two test assemblies.

1.2.2 Full Scale, Multi Assembly Model Validation

PNNL conducted visual inspections and temperature measurements of two NUHOMS (NUTECH Horizontal Modular Storage) horizontal storage modules (HSMs) located at the Calvert Cliffs Nuclear Power Station Independent Spent Fuel Storage Installation (ISFSI) and developed detailed models of the HSMs using STAR-CCM+ [Suffield *et al*., 2012]. The horizontal storage modules each contained twenty-four 4×14 PWR fuel assemblies. The immediate goal of this work was to obtain temperature predictions of the two HSMs in actual storage conditions using STAR-CCM+, while the long-term goal was to obtain realistic thermal evaluations of actual spent nuclear fuel systems, which would include the development of a COBRA-SFS model. Temperature measurements were made on the exposed face of the canister base on each storage module using a hand-held thermocouple probe. The STAR-CCM+ models were developed before the temperatures were measured and the models predicted temperatures that were in reasonable agreement with the measured temperatures. Three additional pieces of modeling information (additional protective screening on the inlet and outlet vents, the actual ambient temperature, new information on the fuel axial positioning) were added post-measurement, and the inclusion of each piece improved the model accuracy. When all three pieces were included, the storage module temperatures were predicted to within 2°C.

The Center for Nuclear Waste Regulatory Analyses (CNWRA), in coordination with NRC, also conducted a thermal analysis of the NUHOMS HSMs located at the Calvert Cliffs ISFSI using an ANSYS/Fluent porous media model to determine the fuel assembly region thermal conductivity [Das *et al*., 2014]. The analysis involved a model validation and verification study. Model validation was carried out by comparing modeling results of peak temperatures and temperature distributions at the dry storage canister shell surfaces of HSM-15 and HSM-1 to thermocouple probe measurements [Suffield *et al.*, 2012], while model verification was carried out using the grid convergence index (GCI) method, which converts discretization errors from Richardson extrapolation grid refinement into uncertainties. The study also extrapolated its modeling results to make predictions of the HSM-15 and HSM-1 temperature distributions over a 300-year period and found that maximum temperatures would drop rapidly over the first 100-year period and decline more gradually over the next 200 years. Baseline model predictions were consistently higher than measured temperatures, and this was attributed to measurement uncertainties such as the need to open the storage module doors to obtain temperature measurements, which exposed the normally closed modules to ambient air, as well as difficulty in accessing measurement positions and a lack of repeated temperature measurements along the storage canisters. Sensitivity studies were carried out as well, which determined the effects of using various turbulence models, changing the porous media thermal resistance, omitting insulation, and extending the calculation domain to include the atmosphere surrounding the storage modules on the temperature distributions.

The capability of COBRA-SFS to predict temperature profiles in dry storage casks containing spent nuclear fuel was tested via a validation study [Michener *et al*., 2017]. This study compared model results to experimental thermocouple data from the multi-assembly CASTOR-V/21 and TN-24P casks that were tested at the Idaho National Laboratory (INL) Test Area North (TAN) facility. Temperature data from thermocouple lances inserted into four 15×15 PWR spent fuel casks were compared to results from COBRA-SFS modeling predictions. For the CASTOR-V/21 tests, cask temperatures were obtained for helium and nitrogen backfills in both horizontal and vertical configurations, and for vacuum in the vertical configuration. For the TN-24P tests, helium, nitrogen, and vacuum backfills were investigated for both horizontal and vertical cask configurations. The temperatures calculated by COBRA-SFS were found to be within experimental uncertainty for the majority of the steady state cases, and temperature differences were mainly attributed to differences in design basis versus as-built geometry configurations, which could change the contact thermal conductance values. The casks contained actual spent nuclear fuel, but the instrumented thermocouple lances were placed in locations four to six rods away from the hottest rods. Therefore, peak cladding temperatures were underestimated. The study also did not take external ventilation structures into account.

1.3 Uniqueness of Current Study

This study contains unique features that differ from previous studies on modeling predictions of dry cask experimental data. First and foremost, the horizontal dry cask simulator in this study is set up to incorporate the integral effects of external ventilation within a vault enclosure and internal natural convection within the system. The mock assembly itself is geometrically prototypic and accommodates both helium and air backfill gas with elevated pressures up to 800 kPa.

For the modeling, three institutions (NRC, PNNL, and ENUSA) were enlisted to provide their own unique approaches to capturing the temperature profiles and air mass flow rates within the BWR dry cask simulator in the horizontal configuration. For these comparisons, ten test cases of the vertical, aboveground dry cask simulator were considered, defined by three independent variables –fuel assembly decay heat (0.5 kW, 1.0 kW, 2.5 kW, and 5.0 kW), internal backfill pressure (100 kPa and 800 kPa), and backfill gas (helium and air). The test matrix for experiment and model data comparison is shown in Table 1.1. Low and high decay heats and pressures were chosen to cover the range of temperatures and natural convection conditions that would be observed in a dry storage cask. Temperature and air mass flow rate data for two of the test cases (highlighted in gray in Table 1.1) were provided to the modelers for model calibration; data for the other eight test cases were purposely withheld for the purposes of conducting a blind study. For all cases, the modelers obtained steady state comparison metrics as shown in Table 1.2, where the steady state start time for each test is defined as when the change in temperature with respect to time on the heater rod with the highest temperature is less than or equal to 0.3 K per hour. The modeling codes used by each institution encompassed a variety of computational approaches to determining these target variables, which were characterized by the software used (ANSYS/Fluent, STAR-CCM+, or COBRA-SFS) and the use of either porous media, explicit fuel, or subchannel models to describe the HDCS fuel assembly.

Table 1.1 HDCS test matrix. Calibration tests are highlighted in gray.

Fill Gas	Pressure (kPa)	Power (kW)
Helium	100	0.5
	100	1.0
	100	2.5
	100	5.0
	800	0.5
	800	5.0
Air	100	0.5
	100	1.0
	100	2.5
	100	5.0

Table 1.2 Steady state comparison metrics for the blind model validation study.

Metric	Notes
Peak Cladding Temperature	PCT
Axial PCT Location	z
Air mass flow rate	$\dot{m}_{Air}$
Axial temperature profile	T(z) at WEU (5 locations)
Transverse x-axis temp. profile	T(x) at z = 48 in. (11 locations)
Transverse y-axis temp. profile	T(y) at z = 72 in. (7 locations)

This page is intentionally left blank.

2 APPARATUS AND PROCEDURES

The core of the vertical dry cask simulator used in previous studies [Durbin and Lindgren, 2018] was modified for configuration to a horizontal orientation, as shown in Figure 2.1. The general design details with the required support modifications are shown in Figure 2.2. As was the case for the vertical DCS, an existing electrically heated and Incoloy-clad but otherwise prototypic 9×9 BWR test assembly was deployed inside of a representative storage basket and cylindrical pressure vessel that represents the canister. Transverse and axial temperature profiles (using TCs detailed in Section 2.3.1) as well as induced cooling air flow rates (using hotwire anemometers detailed in Section 2.3.4) have been measured for a wide range of decay power and canister pressures as detailed in Section 1.3.

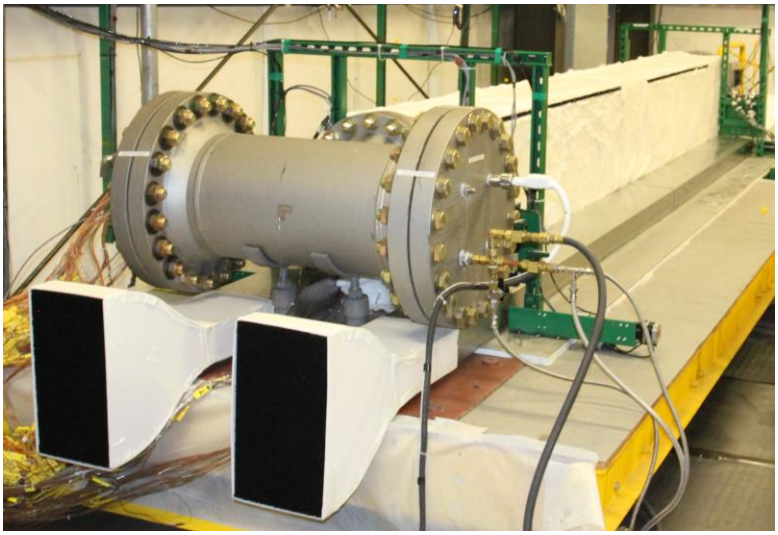

Figure 2.1 Photo of the HDCS system.

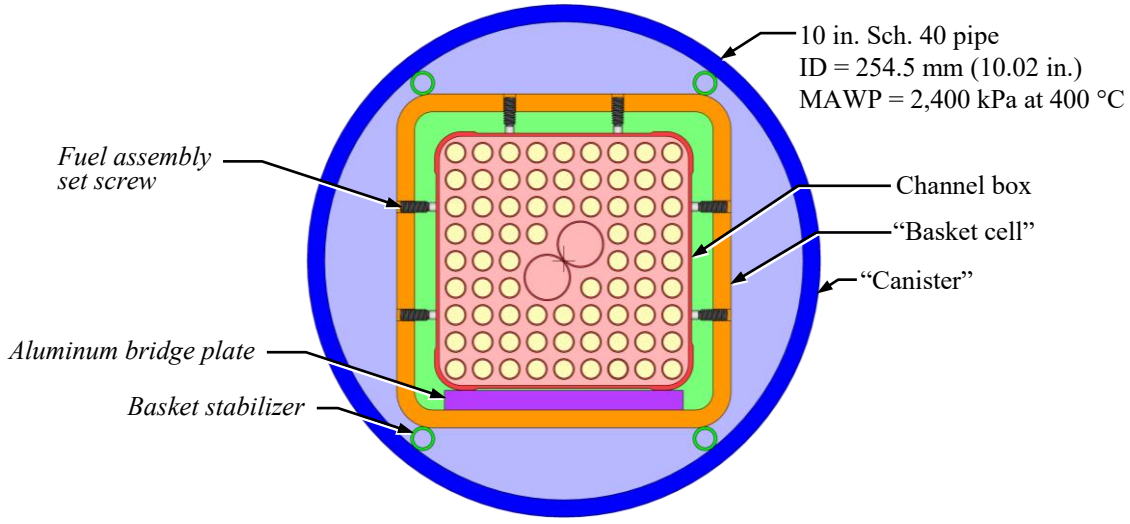

Figure 2.2 General design details of the dry cask simulator with *modifications*.

In prototypic horizontal systems, the assemblies are free to make direct contact with the bottom face of the basket. Due to existing mechanical fixturing and instrumentation at the fuel assembly base, the HDCS assembly used in this study is not free to make direct contact with the basket and must maintain

concentricity to avoid damage during reorientation to a horizontal configuration. Therefore, a full-length aluminum (alloy 6061) bridge plate (127 mm (5 in.) wide and 9.6 mm (0.378 in.) thick) was installed between the assembly channel box and the inside face of the basket to establish a conductive pathway and maintain concentric spacing of the assembly. Set screws were also installed through the basket on the other three sides to center and stabilize the channel box. Geometric details of the contact between the aluminum plate and the channel box are shown in the HDCS update report [Lindgren *et al.*, 2019]. There is limited contact between the corners of the channel box and the aluminum bridge plate. Of the 127 mm width of the bridge plate, only a total of 13.4 mm (0.528 in.) makes contact with the channel box shoulders and the center 97 mm (3.82 in.) is separated by a 0.9 mm (0.0354 in.) gas gap.

Full-length stabilizing tubes along the corners of the basket provided limited conductive paths between the basket and the pressure vessel while keeping the basket centered in the pressure vessel and limiting convective cells as shown in Figure 2.3. The stainless steel 304 tubes had an outer diameter of 12.7 mm (0.500 in.) and wall thickness of 1.59 mm (0.0625 in.). The tubes were stitch welded to the basket at 0.61 m (24 in.) intervals from the basket bottom to the top. These stitch welds had a nominal length of 25.4 mm (1.00 in.). Once the pressure vessel was installed, these stabilizer tubes formed line contacts on both the basket and the pressure vessel.

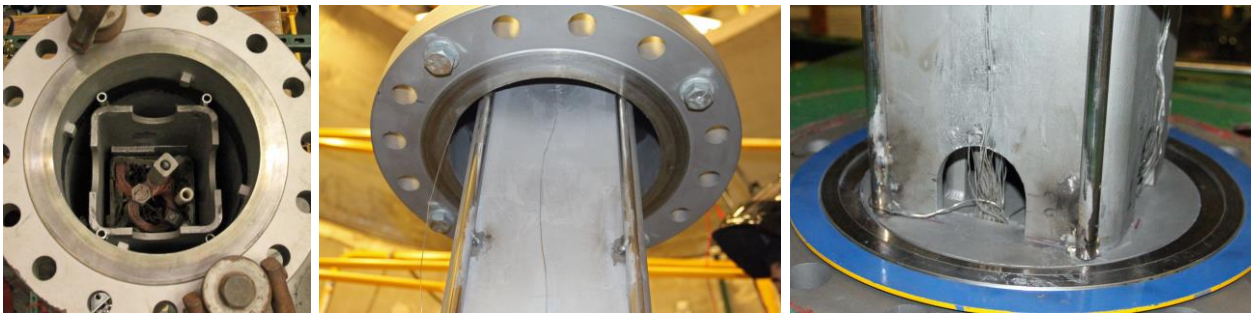

Top View **Middle View** **Bottom View**

Figure 2.3 Photographs of the test assembly showing the basket stabilizer rods.

The horizontal test apparatus is enclosed in an insulated stainless-steel sheet metal enclosure that simulates the concrete vault as shown as a partially exploded view in Figure 2.4 and described in detail in Section 2.1. The vault is comprised of 11-gauge stainless steel sheet metal components. Three side ribs on each side support two side panels and two top panels. Panels on each end enclose the pressure vessel pipe. Inlet and outlet vents to the vault enclosure are located on the top and bottom of each of the four side panels. The vault inlets are supplied by rectangular ducts in which the induced flow is measured using hot wire anemometers. Because the induced flow for the HDCS is expected to be similar to that measured in the aboveground DCS study, the inlet ducts are designed to be the same size. The flow area of the vault inlet and outlet vents also match the flow area of the inlet ducts. The exterior of the sheet metal is covered with a thin layer of insulation (not shown) to mimic the thermal resistance of the walls in a commercial concrete vault (see Section 2.1 for details).

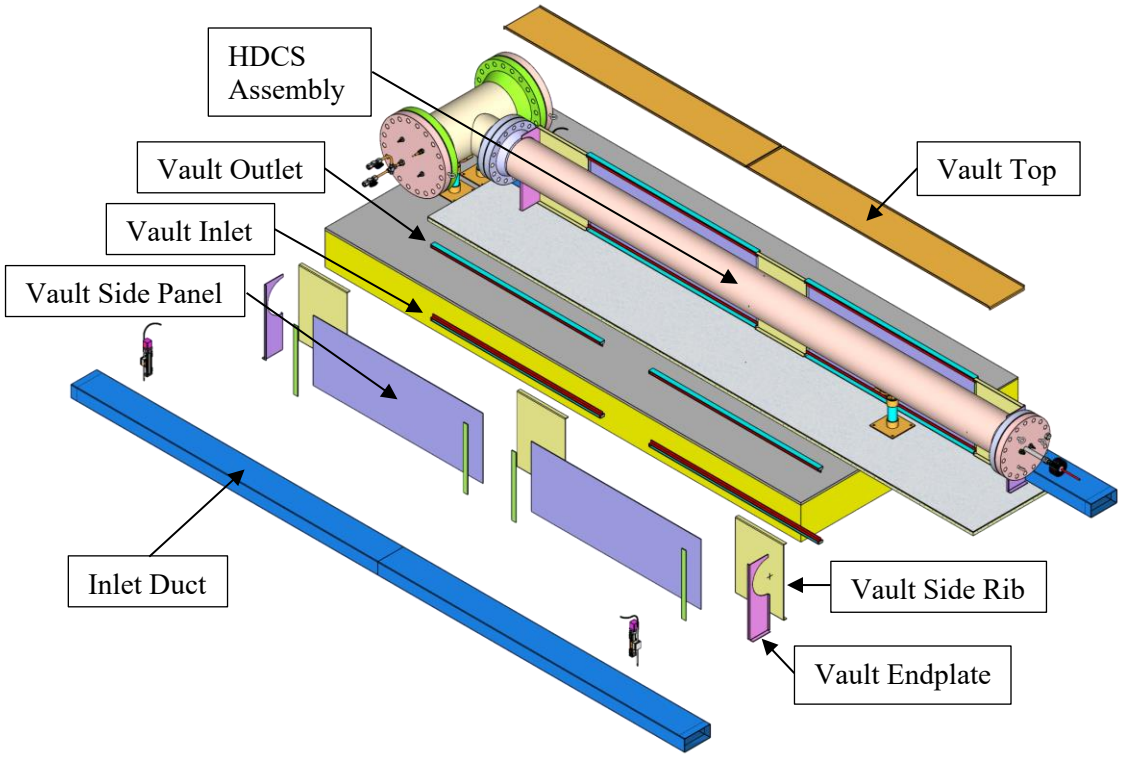

Figure 2.4 HDCS and partially exploded sheet metal vault components.

The new test configuration was assembled and operated inside of the Cylindrical Boiling (CYBL) test facility, which is the same facility used for earlier fuel assembly studies [Lindgren and Durbin, 2013; Durbin and Lindgren, 2018]. The apparatus was lifted out of the CYBL vessel and rotated to a horizontal orientation on a platform on the third (top) floor of the CYBL building. Figure 2.5 shows a scaled diagram of CYBL facility with the DCS inside. The stainless-steel vault enclosure was assembled around the pressure vessel after it was laid in the horizontal position.

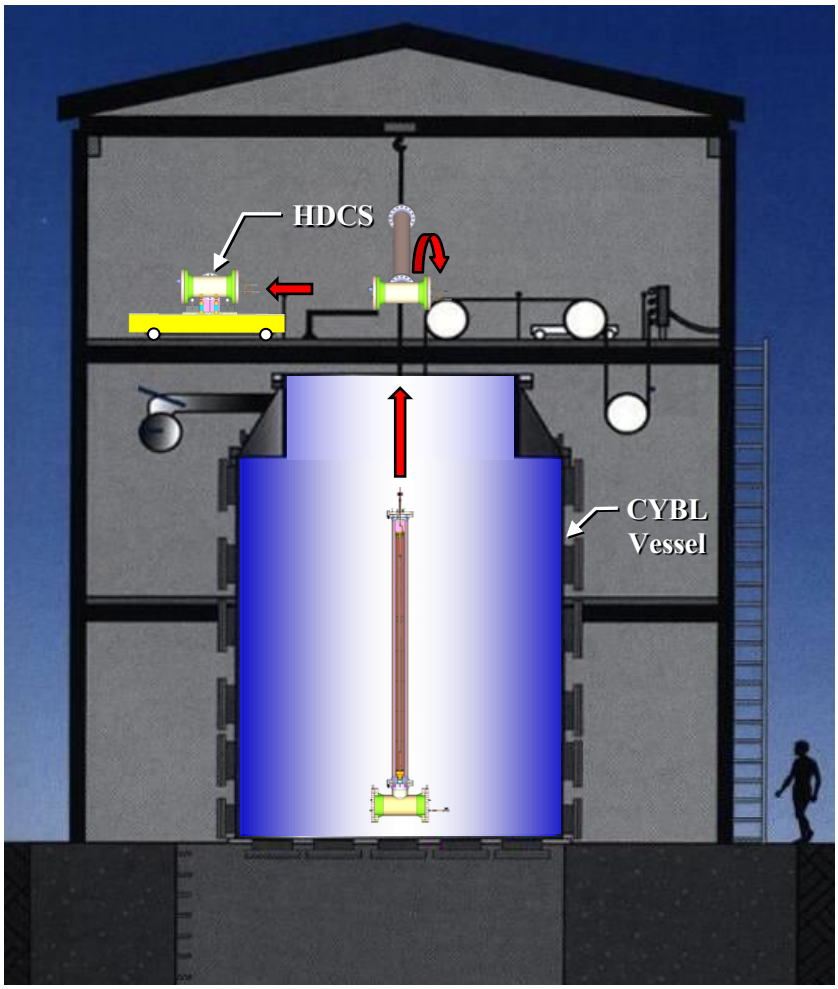

Figure 2.5 CYBL facility housing dry cask simulator testing.

2.1 Design of Vault

The HDCS enclosure was scaled to a NUHOMS HSM Model 80 and Model 102 vault containing a NUHOMS 61BT canister by the blockage ratio (BR). This ratio is defined as the ratio of the diameter of the canister to the inside width of the vault as shown in Figure 2.6. For design purposes, the air mass flow rate for the HDCS was assumed from values measured during similar, vertical test conditions [Durbin and Lindgren, 2018]. This assumption was justified by observing the comparability in the air mass flow calculated by the modeling two prototypic systems NUHOMS HSM (0.25 kg/s) and the Holtec HI-STORM 100 (0.32 kg/s) with computational fluid dynamics [Solis and Zigh, 2015]. Thus, the inlet and outlets to the vault enclosure were designed to have a flow area that matched the aboveground, vertical DCS apparatus. As with the aboveground vertical case, the HDCS had four inlet ducts each with inside dimensions of 0.102 m (4.02 in.) by 0.229 m (9.02 in.) and air velocity anemometers were used to measure the inlet air flow rate. Computer-controlled stages were used to automatically traverse across the inlet opening to measure the flow field.

A simple analysis using one-dimensional thermal resistances for combined heat transfer was performed for the vault side walls and top of an HSM and the HDCS. This analysis showed that the combined thermal resistance of the HSM vault from the heat shield to the outside of the concrete wall was equivalent to the stainless steel HDCS vault wall backed with 6.4 mm (0.25 in.) of high-temperature, alumina-silica insulation. Thus, the analysis includes the effects of the heat shield from radiation and

convection. The equivalency of a relatively thin layer of insulation to 0.51 m (20 in.) of reinforced concrete with a heat shield may be realized in large part because the thermal conductivity of the insulation is roughly 30 times less than that of the concrete. Therefore, the two systems will lose thermal energy through the vault walls at the same rate for the same temperature on the HSM heat shield as on the HDCS vault interior wall.

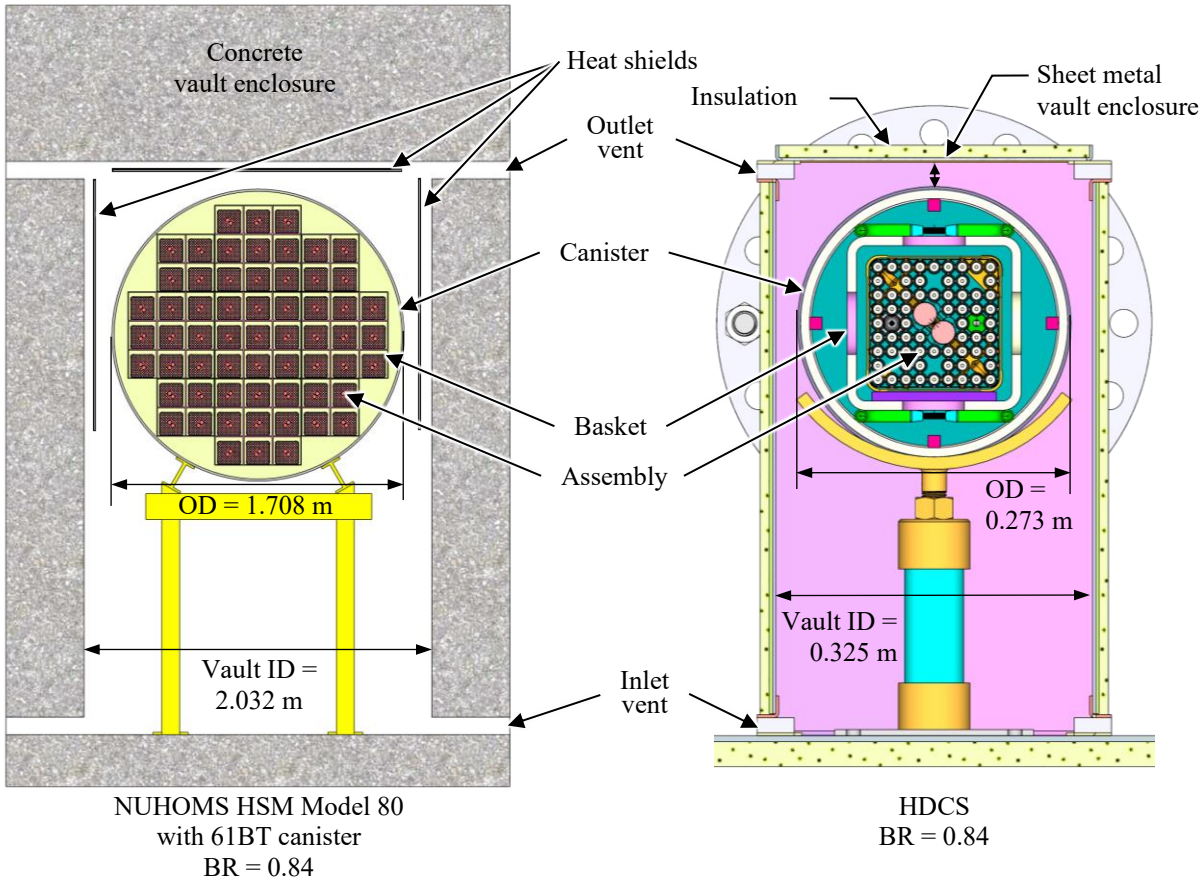

Figure 2.6 Cross sections of a NUHOMS HSM Model 80 and the Horizontal Dry Cask Simulator.

Table 2.1 gives the key parameters for the HDCS at two simulated decay heats and a commercial horizontal storage system. As in previous studies [Durbin and Lindgren, 2018], a known scaling distortion in simulated assembly power is necessary to more closely match the thermal-hydraulic response of a full-sized spent fuel storage cask. This need for additional decay heat is reasonable given the higher external surface-area-to-volume ratio of a single-assembly arrangement as in the HDCS compared to a modern canister with up to eighty-nine assemblies. The air mass flow rate shown for the HDCS is assumed from values measured during similar, vertical test conditions [Durbin and Lindgren, 2018]. The air mass flow rate and other parameters for the commercial horizontal system were taken from a CFD study of various dry storage systems [Solis and Zigh, 2015]. The average velocity, U_{avg}, is calculated by assuming uniform air flow in the vault below the canister. The characteristic length for convection was defined as the canister height for previous vertical testing with the DCS assembly and matched well with vertical, commercial systems. For the current testing in a horizontal configuration, the characteristic length is defined by the outer canister diameter, $D_{canister}$. The significant difference between the HDCS and the commercial canister diameters introduces additional scaling distortions as described next by dimensional analyses.

Table 2.1 Comparison of key dimensional quantities for the HDCS and commercial systems.

Parameter	HDCS		Cask
Power (W)	500	5,000	24,000
$\dot{m}_{Air}$ (kg/s)	0.026	0.069	0.251
$D_{canister}$ (m)	0.273	0.273	1.708
U_{avg} (m/s)	0.019	0.049	0.021

Table 2.2 gives the critical dimensionless groups of the HDCS and a commercial system, namely Reynolds, modified Rayleigh, and Nusselt numbers. As previously noted, the disparity in the canister diameters causes scaling distortions. However, closer examination of the Reynolds numbers indicates that the HDCS and commercial canisters do share the same flow regime. This irregular regime is generally defined for cylinders with $270 < Re_D < 5{,}000$ and is characterized by irregular shedding of von Kármán vortex streets in the cylinder wake. For $Re_D < 1{,}000$ in the irregular regime, the vortices in the near-wake exhibit laminar behavior whereas turbulent dissipation is observed in these vortices for $Re_D > 1{,}000$ [Noack, 1999]. The impact of this difference is expected to be mitigated by the proximity of the vault walls and ceiling.

The modified Rayleigh number is preferred for these analyses because the canister boundary condition is more closely approximated by a uniform heat flux than an isothermal wall temperature. Three-dimensional separation of the cylinder wake defines the onset of the transition to turbulence. Visualization experiments have shown that this important transition occurs when the modified Rayleigh number exceeds 3.5×10^9 [Misumi *et al.*, 2003]. Therefore, the highest power planned for HDCS tests will be transitional if not turbulent as in a commercial system. Power-law fits of Nusselt number to the Rayleigh number are a common treatment for cylinders. Sparrow and Pfeil [Sparrow and Pfeil, 1984] offer a series of correlations for symmetrically confined cylinders between vertical walls. These Nusselt numbers for confined cylinders are within an order of magnitude of each other.

Table 2.2 Comparison of dimensionless groups for the HDCS and commercial systems.

Dimensionless Group	HDCS		Cask
Power (W)	500	5,000	24,000
Re_D	280	730	2,000
Ra_D^*	1.3×10^9	1.3×10^{10}	1.4×10^{13}
$Nu_{D,\ Confined}$	30	50	170

2.2 Details of the Heated Fuel Bundle

The highly prototypic fuel assembly was modeled after a 9×9 BWR. Commercial components were purchased to create the assembly including the top and bottom tie plates, spacers, water rods, channel box, and all related assembly hardware (see Figure 2.7). Incoloy heater rods were substituted for the fuel rods for heated testing. Due to fabrication constraints, the diameter of the Incoloy heaters was slightly smaller than prototypic rods, 10.9 mm (0.430 in.) versus 11.2 mm (0.440 in.). The slightly simplified Incoloy mock fuel rods were fabricated based on drawings and physical examples from the nuclear component supplier. The dimensions of the assembly components are listed in Table 2.3. The assembly was hydraulically characterized in a previous study [Lindgren and Durbin, 2013].

Table 2.3 Dimensions of assembly components in the mock 9×9 BWR.

Description	Lower (Full) Section	Upper (Partial) Section
Number of rods	74	66
Full heater rod length (m)	3.96	
Partial heater rod length (m)	2.61	
Heater OD (mm)	10.9	
Rod pitch (mm)*	14.4	
Rod separation (mm)	3.5	
Water rod OD (main section) (mm)*	24.9	
Water rod ID (mm)*	23.4	
Channel box length (m)	4.13	
Channel box ID (mm)*	134	
Channel box OD (mm)*	139	
Corner channel box wall (mm)*	2.5	

*[Yamamoto *et al.,* 2002]

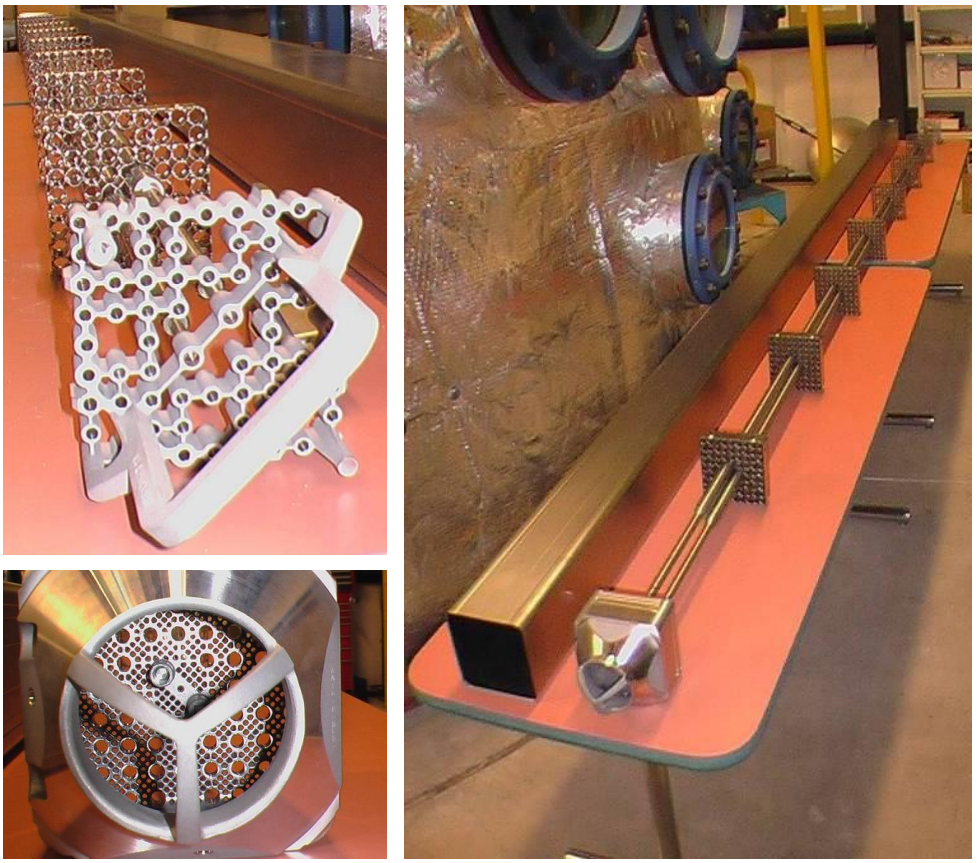

Figure 2.7 Typical 9×9 BWR components used to construct the test assembly including top tie plate (upper left), bottom tie plate (bottom left) and channel box and spacers assembled onto the water rods (right).

2.3 Instrumentation

The test apparatus was instrumented with thermocouples for temperature measurements, pressure transducers for internal gas pressure monitoring, and hot wire anemometers for flow velocity measurements in the exterior ducting. Voltage, amperage, and electrical power transducers were used to monitor electrical energy input to the test assembly.

Ninety-two TCs were previously installed on the BWR test assembly. The TCs used are ungrounded junction type-K with an Incoloy sheath diameter of 0.762 mm (0.030 in.) held in intimate contact with the cladding by thin Nichrome shims. These shims are spot welded to the cladding as shown in Figure 2.8. The TC attachment method allows the direct measurement of the cladding temperature. Details of the BWR test assembly and TC locations are described below and elsewhere [Lindgren and Durbin, 2013]. Additional TCs were installed on the other major components of the test apparatus such as the channel box, storage basket, canister wall, and exterior air ducting. TC placement on these components was designed to correspond with the existing TC placement in the BWR assembly.

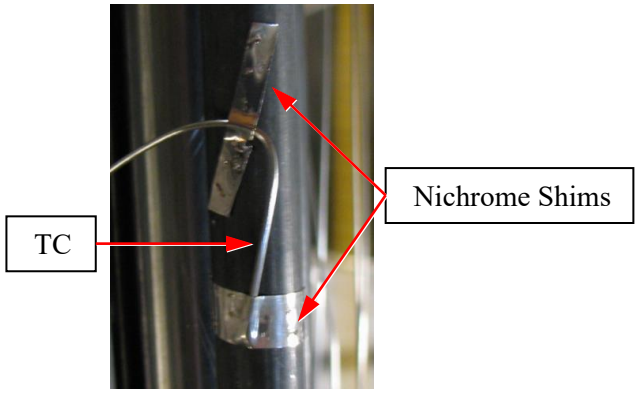

Figure 2.8 Typical TC attachment to heater rod.

Hot wire anemometers were chosen to measure the inlet flow rate because this type of instrument is sensitive and robust while introducing almost no unrecoverable flow losses. Due to the nature of the hot wire measurements, best results are achieved when the probe is placed in an isothermal, unheated gas flow. Hot wires were used to map the two-dimensional flow field across the inlet ducts. As implemented in the previous study [Durbin and Lindgren, 2018], these hot wires were traversed with computer-controlled stages.

2.3.1 Thermocouples

2.3.1.1 BWR Assembly TC Locations

The existing electrically heated and Incoloy-clad but otherwise prototypic BWR test assembly was previously instrumented with thermocouples in a layout shown in Figure 2.9. The TC naming convention is based on the alpha-alpha grid shown along the top and right-hand sides of the plan views shown in Figure 2.9b. As examples, the locations are shown for the TC on heater rod CS and the TC on the water rod at EU (WEU). Also shown with the plan views are the relative location of the four Quadrants and the elevations applicable for each of the three plan views.

The assembly TCs are arranged in axial and transverse arrays. The axial cross-section is depicted in Figure 2.9a and transverse cross-sections are shown in Figure 2.9b. The axial array A1 has TCs nominally spaced every 0.152 m (6 in.) starting from the top of the bottom tie plate (z_o = 0 reference plane). Axial array A2 has TCs nominally spaced every 0.305 m (12 in.) and the transverse arrays are nominally spaced every 0.610 m (24 in.). The spacings are referred to as nominal due to a deviation at the 3.023 m (119 in.)

elevation because of interference by a spacer. Note that the TCs in the axial array intersect with the transverse arrays.

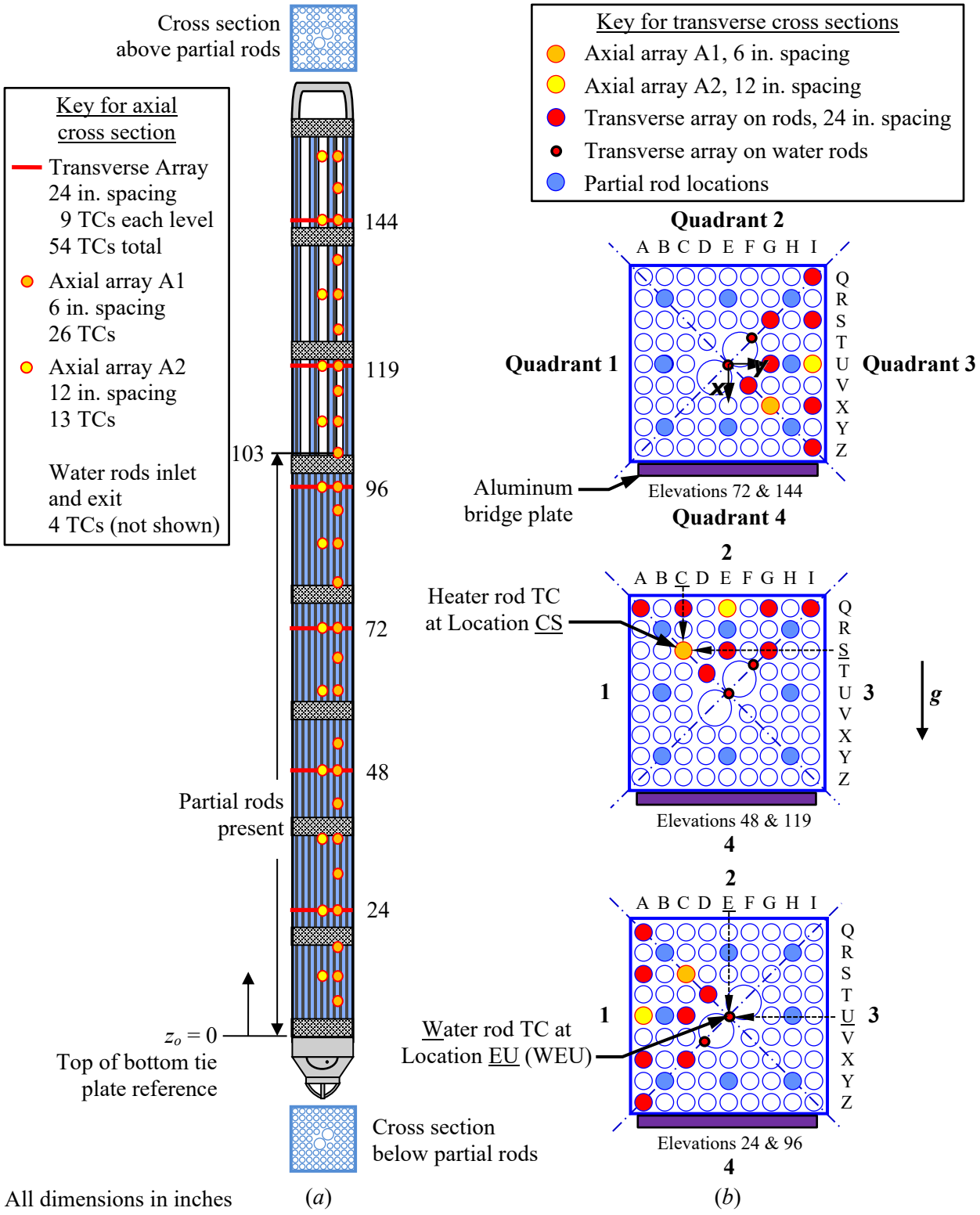

Figure 2.9 Experimental BWR assembly showing as-built *a*) axial and *b*) transverse thermocouple locations.

Based on the need to optimally balance the TC routing through the assembly, the axial and transverse arrays of TCs were distributed among three separate quadrants relying on the assumption of axial symmetry that was valid for the initial, vertical orientation studied previously. However, the assumption of axial symmetry is not valid in the horizontal orientation. Based on the previous vertical orientation of the test apparatus inside of the CYBL vessel, the assembly was laid on the aluminum bridge plate on Quadrant 4, which lacks any TCs in the tube bundle. In the horizontal orientation, there is symmetry between Quadrants 1 and 3, and the peak cladding temperature was expected to be in Quadrant 2.

Figure 2.10 shows the definition of the reference coordinate system. The reference origin is defined as the center of the top surface of the bottom tie plate. The *x*-axis is positive in the direction of Quadrant 4, which points in the same direction as gravity, and negative in the direction of Quadrant 2. The *y*-axis is positive in the direction of Quadrant 3 and negative in the direction of Quadrant 1. The *z*-axis is along the axial direction.

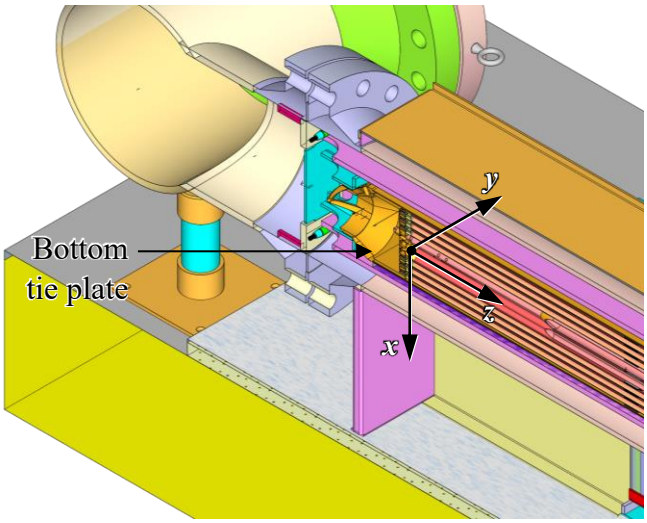

Figure 2.10 Definition of coordinate references in test apparatus.

2.3.1.2 BWR Channel Box TC Locations

The BWR channel box was instrumented with 25 TCs as depicted in Figure 2.11. Twenty-one of the TCs are on the channel faces, three are on the corners and one is on the pedestal. The TCs on the faces of the channel box are nominally located at $|x|, |y| = 0.069, 0$ m (2.704, 0 in.) or $|x|, |y| = 0, 0.069$ m (0, 2.704 in.) depending on the quadrant in which they are placed. TCs on the corners are nominally located at $|x|, |y| =$ 0.065, 0.065 m (2.564, 2.564 in.). The reference plane, z_o, is measured from the top of the bottom tie plate, the same as the BWR assembly. In the horizontal orientation, Quadrant 4 is down.

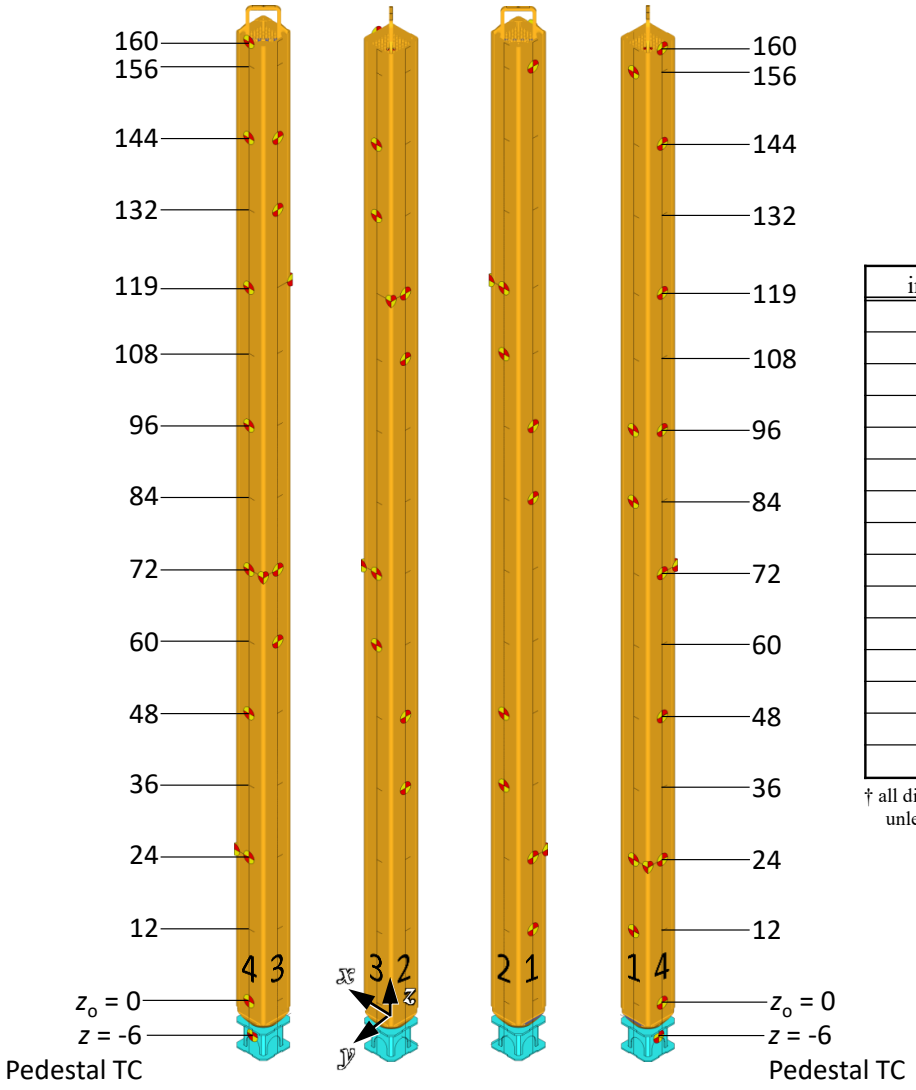

in.†	m
160	4.064
156	3.962
144	3.658
132	3.353
119	3.023
108	2.743
96	2.438
84	2.134
72	1.829
60	1.524
48	1.219
36	0.914
24	0.610
12	0.305
-6	-0.152

† all dimensions are in inches unless otherwise noted

Figure 2.11 BWR channel box showing thermocouple locations.

2.3.1.3 Storage Basket TC Locations

The storage basket is instrumented with 26 TCs as depicted in Figure 2.12. Twenty-one of the TCs are on the basket faces at the same positions as on the channel box, four are on the corners (the corner TC at the 4.191 m (165 in.) level does not correspond to a channel box TC) and one is on the basket face at the elevation of the pedestal. TCs located on the basket faces are nominally located at $|x|$, $|y|$ = 0, 0.089 m (0, 3.5 in.) and $|x|$, $|y|$ = 0.089, 0 m (3.5, 0 in.). TCs on the corners are nominally located at $|x|$, $|y|$ = 0.083, 0.083 m (3.281, 3.281 in.) The reference plane, z_o, is measured from the top of the bottom tie plate. The coordinates given are with respect to the test apparatus reference origin, as shown in Figure 2.10.

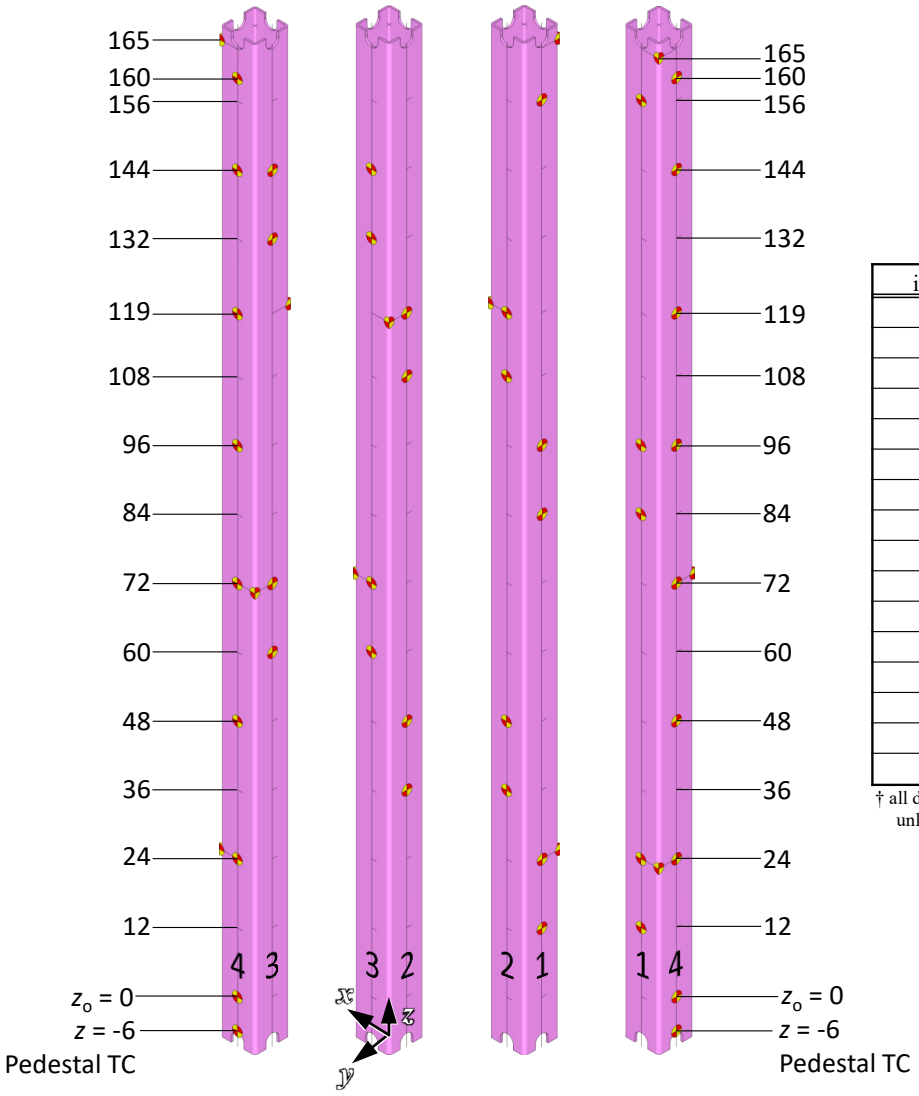

in.†	m
165	4.191
160	4.064
156	3.962
144	3.658
132	3.353
119	3.023
108	2.743
96	2.438
84	2.134
72	1.829
60	1.524
48	1.219
36	0.914
24	0.610
12	0.305
-6	-0.152

† all dimensions are in inches unless otherwise noted

Figure 2.12 Storage basket showing thermocouple locations.

2.3.1.4 Pressure Vessel TC Locations

The pressure vessel was instrumented with 27 TCs as depicted in Figure 2.13. Twenty-four of the TCs are aligned with the TCs on the storage basket faces and three are aligned with the TCs on the storage basket corners. TCs aligned with the storage basket faces are nominally located at $|x|$, $|y|$ = 0, 0.137 m (0, 5.375 in.) and $|x|$, $|y|$ = 0.137, 0 m (5.375, 0 in.). TCs aligned with the storage basket corners are nominally located at $|x|$, $|y|$ = 0.097, 0.097 m (3.801, 3.801 in.). The reference plane, z_o, is measured from the top of the bottom tie plate. The coordinates given are with respect to the test apparatus reference origin, as shown in Figure 2.10.

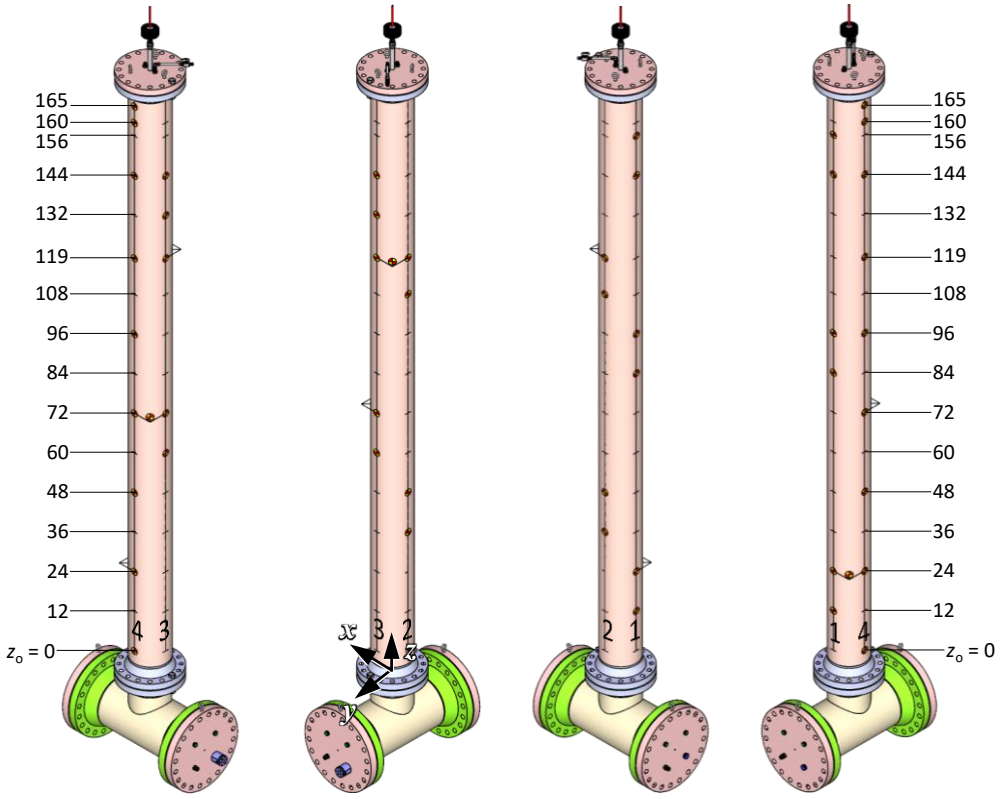

in.†	m
165	4.191
160	4.064
156	3.962
144	3.658
132	3.353
119	3.023
108	2.743
96	2.438
84	2.134
72	1.829
60	1.524
48	1.219
36	0.914
24	0.610
12	0.305

† all dimensions are in inches unless otherwise noted

Figure 2.13 Pressure vessel showing thermocouple locations.

2.3.1.5 Vault Enclosure and External TC Locations

The vault enclosure and the external ambient temperature regions are instrumented with 106 TCs, with some TCs shown in Figure 2.14 and Figure 2.15 and a comprehensive list included in the HDCS update report [Lindgren *et al.*, 2019]. Fourteen of the TCs are aligned along the centerline of the top lid at 0.305 m (12.0 in.) spacing. Twelve TCs are arranged in eight vertical arrays on the external side of the vault at nominally 0.610 m (24.0 in.) spacing. Twelve more TCs are placed on the opposite external side at nominally 0.610 m (24.0 in.) as well. Three TCs are placed internal to the vault at z = 2.13 m (84.0 in.) – two of these TCs are placed on the internal side of the side ribs at this axial location, and the remaining TC is placed on the internal side of the top lid. The alternating, one-two TC layout pattern on the vertical side in Figure 2.14 is reversed (two-one) on the vertical side not shown. The TC locations for both sides of the vault are shown in the HDCS update report [Lindgren *et al.*, 2019]. Nine TCs are placed along the baseplate that forms the bottom of the vault. One TC is placed on each of the four endplates of the vault (which adds up to 4 TCs total on all endplates). Ten gas TCs are placed around the pressure vessel, baseplate, and vault. Twenty gas TCs are placed internally within the vault inlets and outlets. Four TCs are placed around the HDCS instrumentation, and eighteen TCs are placed external to the vault to measure ambient temperatures. The reference plane, z_o, is measured from the top of the bottom tie plate.

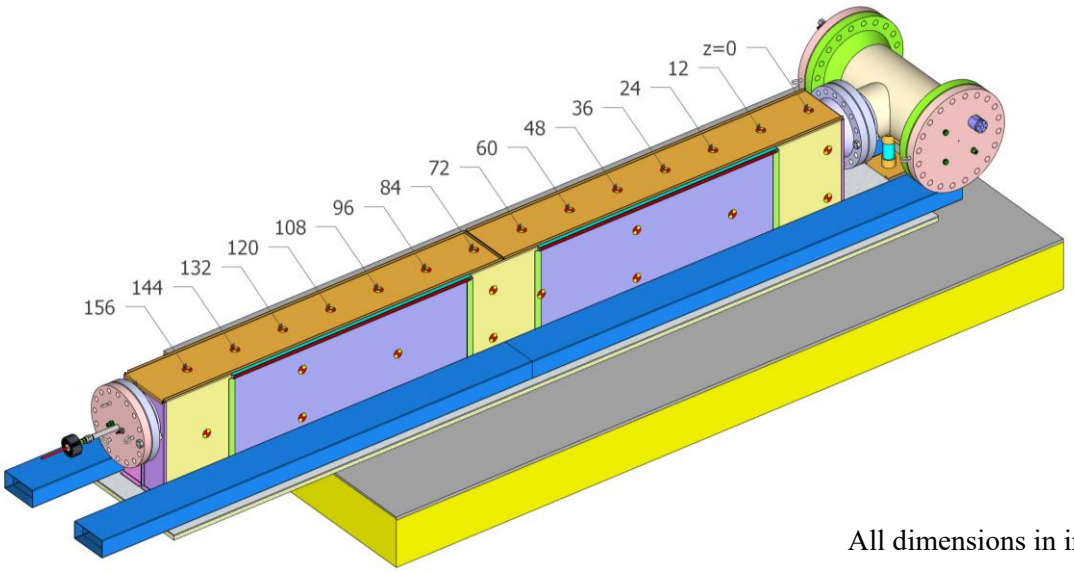

All dimensions in inches

Figure 2.14 Vault without insulation showing thermocouple locations on the top and north sides.

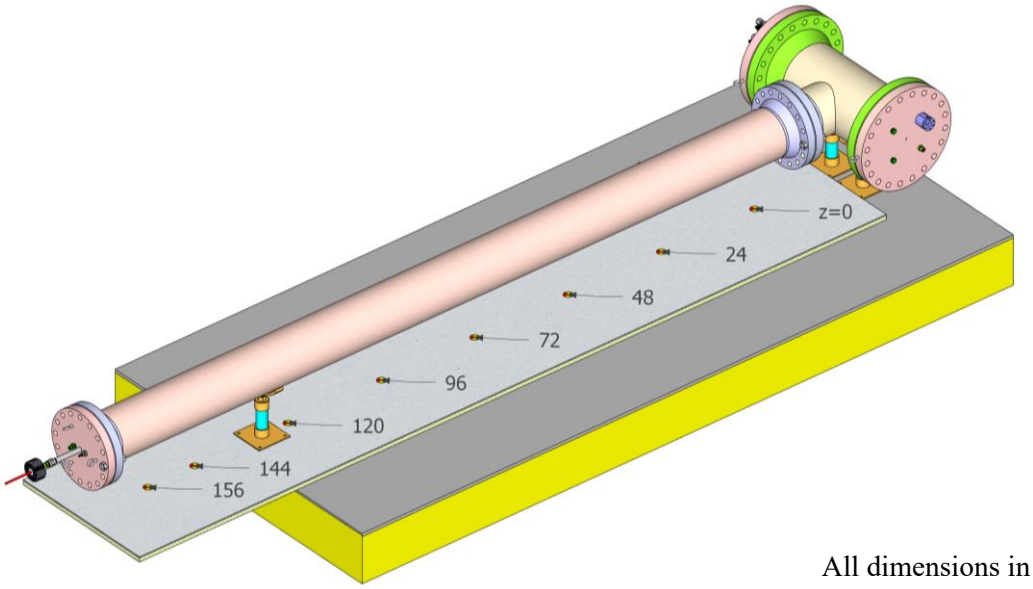

All dimensions in inches

Figure 2.15 Base plate thermocouple locations.

2.3.2 Pressure and Pressure Vessel Leak Rates

Two high-accuracy 0 to 1,034 kPa (0 to 150 psia) absolute pressure transducers (Setra Systems ASM1-150P-A-1M-2C-03-A-01) are installed in the instrument well. The pressure measurements are made in duplicate due of the importance of the measurement. The experimental uncertainty associated with these gauges is ±0.05% of full scale, or ±0.52 kPa (±0.075 psi).

All penetrations and fittings were selected for the apparatus to have helium leak rates of 1×10^{-6} std. cm^3/s or better at 100 kPa. In addition, spiral-wound gaskets capable of leak rates of better than 1×10^{-7} std. cm^3/s were used to form the seals at each flange. The ANSI N14.5 leak rate of 1×10^{-4} std. cm^3/s [ANSI, 2014] would result in an observable pressure drop of 0.03 kPa (4×10^{-3} psi) after a one-week period, which is far below the experimental uncertainty of 0.52 kPa (0.075 psi). During previous testing, leaks in the as-

built apparatus were identified and repaired as best as possible [Durbin and Lindgren, 2018]. Ultimately, a small leak path of undetermined origin remains, and a positive pressure control system was implemented to maintain pressure as described next.

2.3.2.1 Pressure Control

A pressure control system has been implemented using the high-accuracy, absolute-pressure transducers, three low-flow needle valves, and three positive-shutoff actuator valves under control of the LabView data acquisition (DAQ) system (Figure 2.16). Two actuator valves (vent) control flow out of the vessel, and the third valve (fill) controls the fill gas flow into the vessel. As the vessel heats up, the expanding backfill gas vents out of the first actuator and needle valve to maintain a constant pressure. A second vent valve (overflow) activates if the vessel continues to pressurize. As steady state is reached, the small leak will slowly reduce the backfill pressure, at which point the control system opens the third actuator valve (fill) to allow a small flow through the third needle valve. Overall, a similar pressure control system used in past testing was able to maintain the vessel pressure constant to within ±0.3 kPa (0.044 psi).

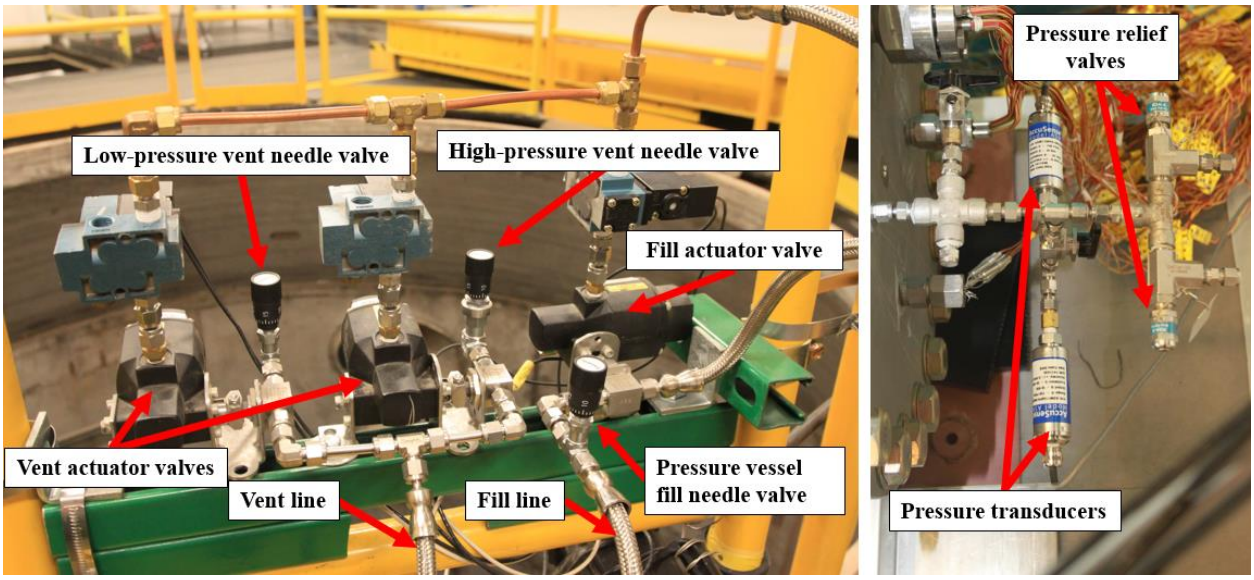

Figure 2.16 HDCS pressure control system.

2.3.2.2 Pressure Vessel Internal Volume Measurement

The pressure vessel internal volume was measured during previous testing [Durbin and Lindgren, 2018]. The total internal volume was determined to be 252.0 liters, with an uncertainty of ±2.6 liters. This measurement includes the volume of the instrument well that is insulated from the heated test section.

2.3.3 Power Control

A diagram of the test assembly power control system is shown in Figure 2.17 and the details inside the instrument panel are shown in Figure 2.18. The electrical voltage and current delivered to the test assembly heaters is controlled to maintain a constant power by a digital silicon-controlled rectifier (SCR). The DAQ system provides a power setpoint to the SCR that is constantly compared to the measured output power. The power, voltage, and current measurements are collected by the DAQ. The details of the instrumentation used to control and measure the electrical power are provided in Table 2.4. A special calibration schedule of thirty-two points was ordered for the power diagnostic (Ohio Semitronics PTB-112D1PCY48). The observed 95% uncertainty bounds based off the Student's t-value and the standard error of the regression for this instrument give an uncertainty of $U_{\text{Watt}} = \pm 13$ W. Additional details may be found in Appendix A.

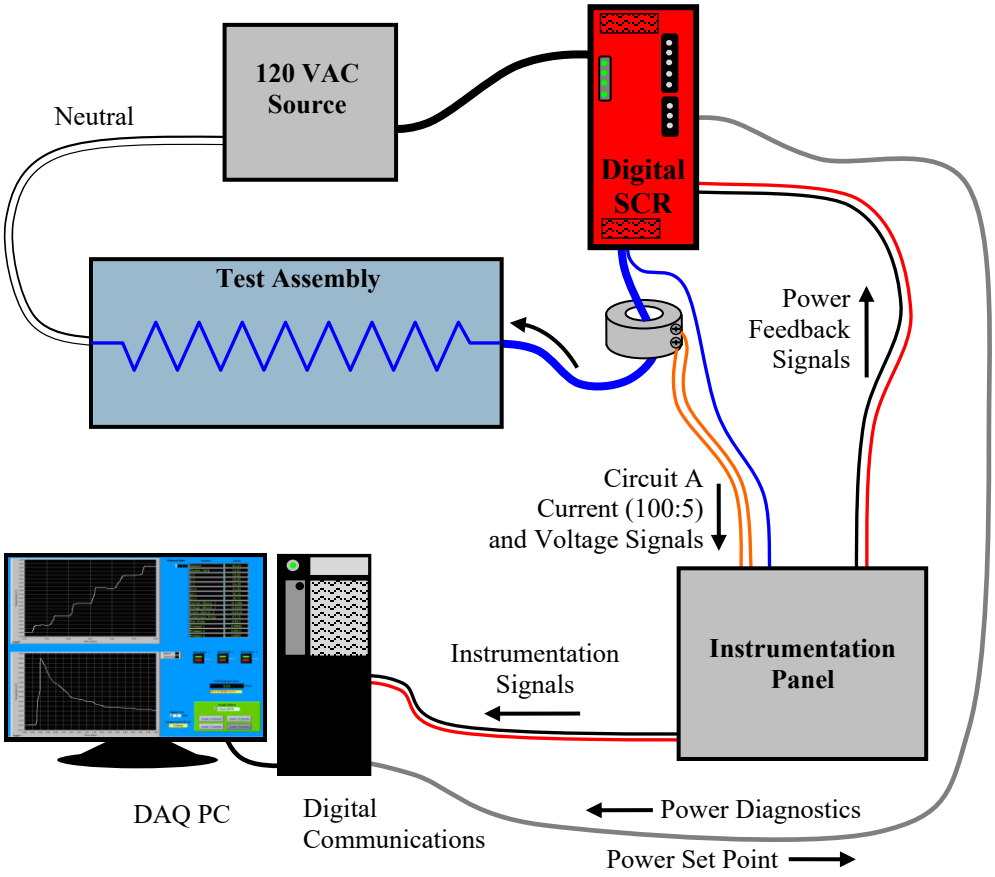

Figure 2.17 Power control system and test circuits.

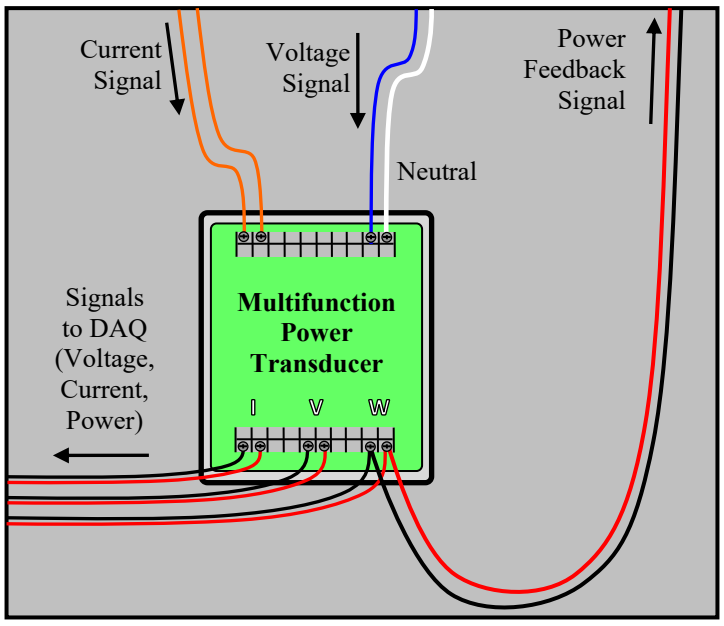

Figure 2.18 Schematic of the instrumentation panel for voltage, current, and power measurements.

Table 2.4 List of power control equipment.

Description	Manufacturer	Model
Power Test Board (PTB) – Measures Volts, Amps, Watts	Ohio Semitronics	PTB-112D1PCY48
Digital SCR Power Controller	Control Concepts	uF1HXLGI-130-P1RSZ

2.3.4 Hotwires

The hotwire anemometers used are TSI model 8455 where the tip detail is shown in Figure 2.19. For scale, the largest shaft diameter shown is 6 mm (0.25 in.). The sensing element of the model 8455 is protected inside of an open cage and is sensitive to flows down to 0.13 m/s (25 ft/min) with a response time of 0.2 seconds. The instrument uncertainty in the air mass flow rate per duct was calculated to be $U_{\dot{m},\,\text{per duct}} = \pm 1.5 \times 10^{-4}$ kg/s. The combined error in the total air mass flow rate across all four ducts is $U_{\dot{m},\,\text{Total}} = \pm 3.0 \times 10^{-4}$ kg/s. Additional details may be found in Appendix A.

Figure 2.19 Photograph of the hot wire anemometer tip.

2.4 Air Mass Flow Rate

Figure 2.20 shows the air flow pattern through the HDCS vault. Cold air is drawn into the air inlet ducts and flows into the vault inlets on the sides of the enclosure. The air heats as it passes between the vault and the simulated canister. The hot air exhausts at the top of the enclosure sides via the vault outlets. The hotwires are mounted on motorized stages (Velmex Stage XN10-0040-M02-71, Motor PK245-01AA). The data acquisition computer communicates with the stage controller (Velmex Controller VXM-4) to identify and verify hot wire positioning.

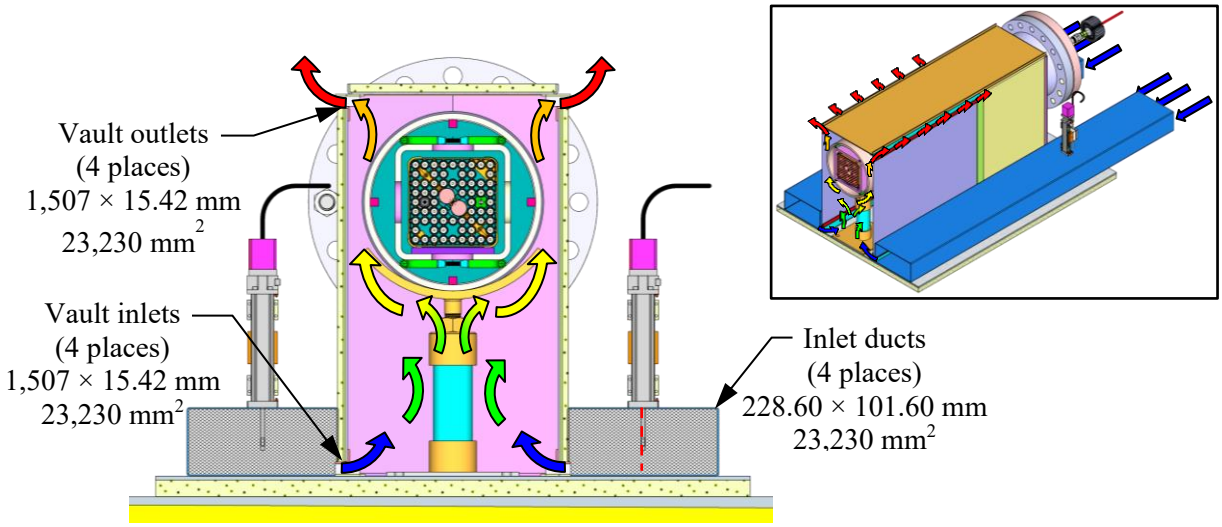

Figure 2.20 Air flow pattern in the HDCS from natural convection.

The methods for determining the induced air flow in the HDCS are based on the successful methods developed in the previous aboveground and belowground, vertical DCS studies [Durbin and Lindgren, 2018]. The methods used hot wire anemometers to measure inlet air velocity and subsequently calculate an overall air mass flow rate.

2.4.1 Flow Straightening

To obtain the most stable and repeatable measurements possible, a honeycomb element is inserted into all four assembly inlets to align the flow in the desired direction and reduce any flow disturbances on the hot wire anemometers. As shown in Figure 2.21, a plastic honeycomb element was chosen with a cell diameter, wall thickness, and flow length of 3.8, 0.1, and 25.8 mm (0.150, 0.004, and 1.015 in.), respectively. This type of flow straightening element has been found to provide the greatest reduction in hot wire fluctuations while introducing the smallest pressure drop to the system. The effective frictional coefficient for this honeycomb material was found to be $D = 2.7 \times 10^6$ m^{-2} for porous media in CFD simulations.

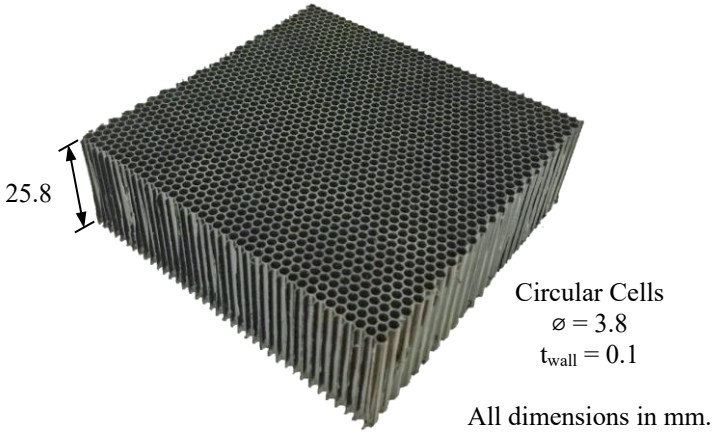

Figure 2.21 Photograph of the honeycomb element used for flow straightening.

As depicted in Figure 2.22, the flow straightener section featured a convergent nozzle made of corrugated fiberboard and scrim-backed, pressure-sensitive tape. This nozzle minimized the flow losses associated with the honeycomb element by increasing the flow area by a factor of four. The honeycomb dimensions used in each of the four inlets was 0.425 m (16.7 in.) tall by 0.233 m (9.2 in.) wide and 0.0258 m (1.02 in.) thick for a flow area of 0.099 m^2. The nozzle design included two straight sections to accommodate the honeycomb and the assembly inlet. Long-sweep arcs with matching tangents at the inflection point were chosen to provide a smooth transition from the honeycomb section to the assembly inlet.

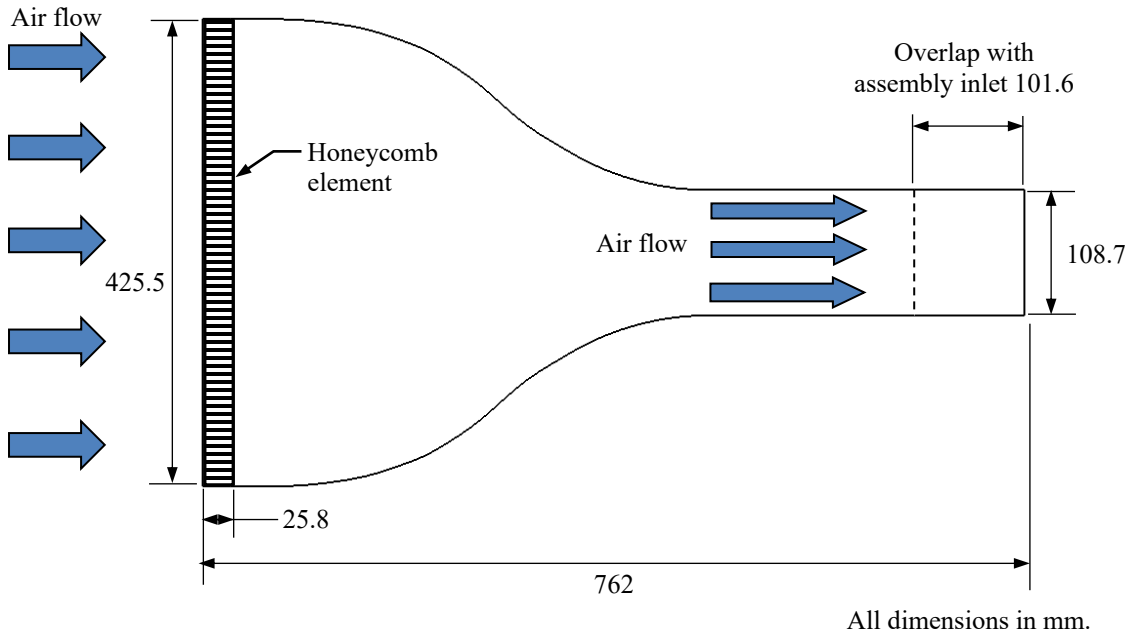

Figure 2.22 Cutaway schematic of the flow straightener.

2.4.2 Air Flow Measurement

The inlet flow straightening nozzles and hot wire anemometer locations for the HDCS are depicted in Figure 2.23. After the four convergent nozzles, rectangular ducts with nominal cross-sectional dimensions of 0.229 m (9.00 in.) by 0.102 m (4.00 in.) convey the inlet flow into the simulated vault. Multiple hot wire anemometers are located nominally 0.5400 m (21.25 in.) downstream from the inlet of each duct to map the inlet air flow. Shown is a single representative motorized stage and hot wire anemometers on each duct.

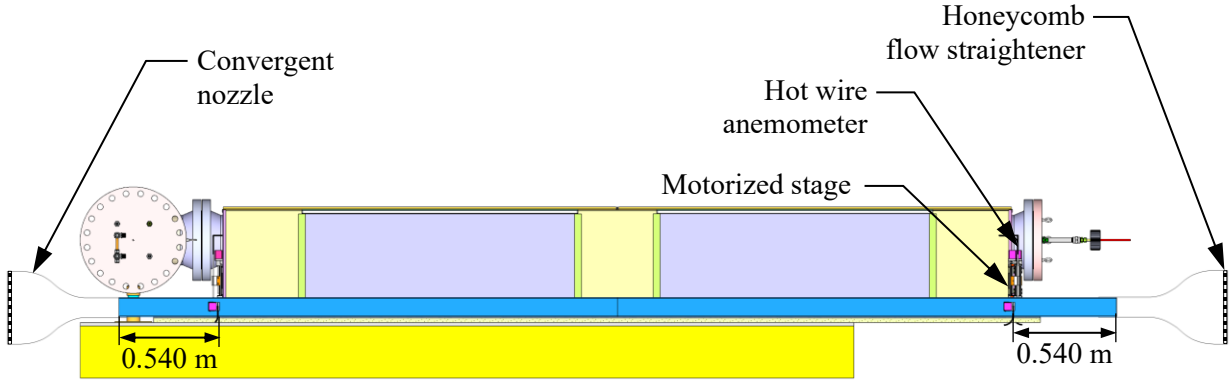

Figure 2.23 Flow straightening nozzles and hot wire anemometer locations in the inlet ducts.

As illustrated in Figure 2.24, in each duct there are at least three (and in one duct four) hot wire anemometers on motorized stages. Each duct has a vertical hot wire anemometer that traverses across the center of the duct in the *x*-direction and a horizontal hot wire anemometer that traverses across the center of the duct in the *y*-direction 25.4 mm (1.00 in.) farther downstream. Additionally, the NE duct and the

SW duct have a vertical hot wire anemometer that traverses in the *x*-direction 9.5 mm (0.38 in.) from the outer duct wall, the NW duct has a vertical hot wire anemometer that traverses in the *x*-direction 9.5 mm (0.38 in.) from the inner duct wall, and the SE duct has two additional vertical hot wire anemometers that traverses in the *x*-direction 9.5 mm (0.38 in.) from both the inner and outer duct walls.

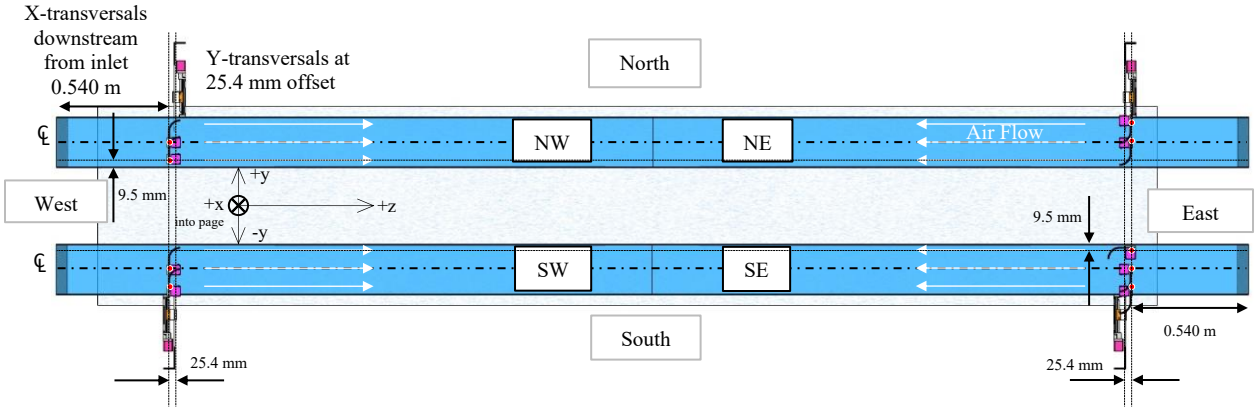

Figure 2.24 Plan view location details of hotwire anemometers in the inlet ducts.

The measured steady state velocities in all four ducts were averaged and used to determine a 2-dimensional distribution of average duct velocity across the duct flow area. The duct flow area is discretized into rectangular elements with a flow velocity determination associated with the center of each element as illustrated in Figure 2.25. The values shown in green are derived from the vertical traverses. The values shown in blue are derived from the horizontal traverse. The values shown in yellow are derived by similarity with the horizontal and vertical velocity profile measurements. The region shown in red on the periphery is the no-slip region with no flow along the outer walls.

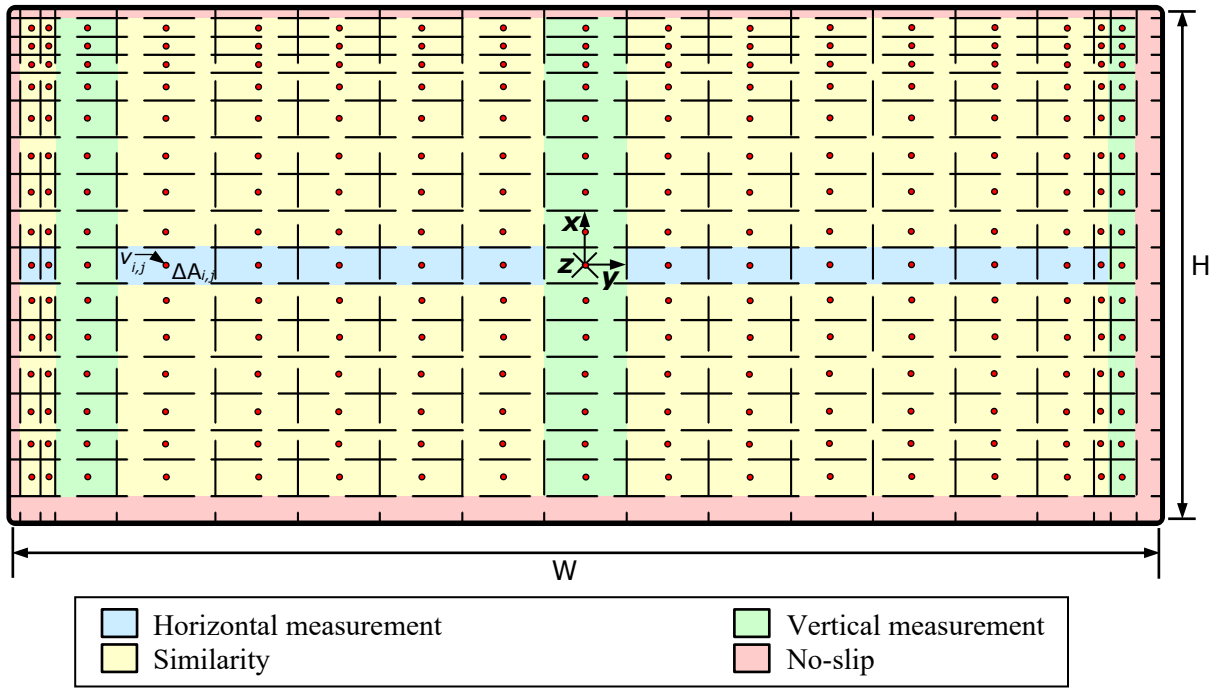

Figure 2.25 Diagram showing the integration scheme for the calculation of air mass flow rate at the inlet.

Each velocity was assumed to be constant across the differential area, $\Delta A_{i,j}$, defined by the coordinates of $\left(\frac{x_i+x_{i-1}}{2}, \frac{y_j+y_{j-1}}{2}\right)$ and $\left(\frac{x_i+x_{i+1}}{2}, \frac{y_j+y_{j+1}}{2}\right)$ where i is the x-coordinate index and j is the y-coordinate index. The integrated, natural air mass flow rate is given in Equation 2-1.

$$\dot{m}_{\text{Tot}} = \sum_{j=1}^{17} \sum_{i=1}^{19} \rho_{\text{ref}} \cdot \Delta A_{i,j} \cdot v_{i,j} \qquad 2\text{-}1$$

The reference density is defined by the standard conditions for the TSI hot wires, or ρ_{ref} = 1.2 kg/m^3 at 21.1 °C and 101.4 kPa. Using this midpoint approximation scheme, the no-slip condition is assumed to apply to the area half-way between the wall and the nearest available velocity values. Applying the no-slip condition in this manner equates to assuming the velocity varies linearly between zero at the wall to the nearest measured value, which is expected to underestimate the flow rate based on comparisons with boundary layer theory.

Table 2.5 gives differential area, $\Delta A_{i,j}$, by location in the inlet. These differential areas are used for all calculations of air mass flow rate as defined in Equation 2-1. The measured locations of the hot wire anemometers were used to determine each differential area.

Table 2.5 Differential areas for the calculation of air mass flow rate.

All values in mm^2.

y (mm) / *x* (mm)	-113.2	-110.2	-106.1	-104.6	-81.6	-65.3	-49.0	-32.6	-16.3	0.0	16.3	32.6	49.0	65.3	81.6	97.9	104.1	104.6	111.8
50.4	4	7	5	22	36	30	30	30	30	30	30	30	30	30	30	21	6	9	9
47.7	7	15	10	45	72	60	60	60	60	60	60	60	60	60	60	41	12	19	18
44.0	7	15	10	45	72	60	60	60	60	60	60	60	60	60	60	41	12	19	18
40.3	7	15	10	45	72	60	60	60	60	60	60	60	60	60	60	41	12	19	18
36.7	11	22	15	67	108	90	90	90	90	90	90	90	90	90	90	62	18	28	27
29.3	15	30	21	90	144	120	120	120	120	120	120	120	120	120	120	82	24	37	35
22.0	15	30	21	90	144	120	120	120	120	120	120	120	120	120	120	82	24	37	35
14.7	15	30	21	90	144	120	120	120	120	120	120	120	120	120	120	82	24	37	35
7.3	15	30	21	90	144	120	120	120	120	120	120	120	120	120	120	82	24	37	35
0.0	15	30	21	90	144	120	120	120	120	120	120	120	120	120	120	82	24	37	36
-7.3	15	30	21	90	144	120	120	120	120	120	120	120	120	120	120	82	24	37	36
-14.7	15	30	21	90	144	120	120	120	120	120	120	120	120	120	120	82	24	37	35
-22.0	15	30	21	90	144	120	120	120	120	120	120	120	120	120	120	82	24	37	35
-29.3	15	30	21	90	144	120	120	120	120	120	120	120	120	120	120	82	24	37	35
-36.7	12	24	17	72	116	96	96	96	96	96	96	96	96	96	96	66	20	30	29
-41.1	15	30	21	90	144	120	120	120	120	120	120	120	120	120	120	82	24	37	35
-48.8	10	21	14	62	100	83	83	83	83	83	83	83	83	83	83	57	17	26	25

This page is intentionally left blank.

3 RESULTS

3.1 Model Summary

A brief summary of the models used for the validation exercises is shown in Table 3.1. This table outlines the code used for each model. It also shows how the HDCS fuel assembly is represented with each code, using either an explicit model that represents the fuel rods and spacers in detail, a porous media model where the fuel is homogenized into a simplified volume with corresponding inertial and frictional loss coefficients, or an explicit subchannel model where the fuel is divided into a number of flow paths or channels. The modeling codes can be grouped into one of three categories – CFD detailed modeling, CFD porous media modeling, and subchannel modeling – which are defined by their approaches. Figure 3.1 illustrates these three categories.

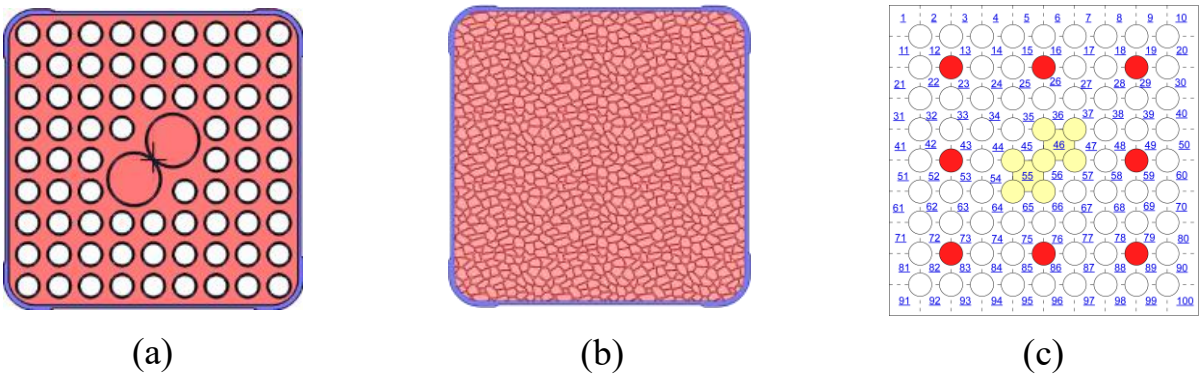

(a) (b) (c)

Figure 3.1 Visual representations of (a) CFD explicit modeling, (b) CFD porous media modeling, and (c) explicit subchannel modeling of the DCS fuel assembly.

Table 3.1 also details the flow treatments the codes utilize in both the fuel assembly and HDCS outer structure regions – both the internal helium flow and the external air flow were modeled as either laminar or turbulent. Radiation and convection are treated independently for the explicit models, but for the porous media models, radiation and convection are both accounted for by using an effective thermal conductivity (k_{eff}). The input parameters for the materials and flow gases in each code were taken from the DCS Handbook [Lindgren and Durbin, 2017]. The treatment of the helium depends on the code and is either temperature-dependent only or temperature- and pressure-dependent in the ideal gas assumption. The table briefly outlines the initial and boundary conditions for the experiment simulations, such as how the flow straightening element is treated. The table also describes the type of symmetry used in each model for computational efficiency purposes. More details on each code can be found in the Appendices.

An initial review by SNL staff of the blind modeling results identified issues with one of the model submissions, most likely in the prescribed boundary condition inputs. Given the anomalous nature of these modeling results and the short amount of time before publication, these modeling efforts are detailed in an appendix but are not shown in the reported results.

Table 3.1 Summary of modeling parameters.

Modeling Contributor	Code, Code Type	Fuel Representation	Internal Flow Treatments	Cooling Air Flow Treatment	Input Parameters	Initial/Boundary Conditions	Cross-Sectional Symmetry
NRC	ANSYS/Fluent version 19.0, CFD	Porous media	Gas inside pressure vessel assumed to be laminar; 0.9 mm gap between channel box and aluminum bridge plate meshed as a fluid volume.	Air outside the pressure vessel assumed to behave according to the Low Reynolds K- ε turbulence model with full buoyancy effect on both the k and epsilon equations.	Material properties taken from DCS Handbook; helium and air modeled using the ideal gas law.	Model outflow boundary simulated as constant pressure boundary (same ambient pressure as the inflow boundary); Honeycomb inlet flow straighteners modeled using porous media.	1/2
PNNL	STAR-CCM+ version 2019.1, CFD	Explicit	Laminar flow model applied to internal helium/air region within the canister; Boussinesq model applied to the fluid inside the canister.	Standard K-ε Low-Re flow model applied to external air flow region; internal radiation included in air gas regions; emissivity values applied along the inner surfaces.	Material properties taken from DCS Handbook; effective properties for heater rods calculated based on volume weighted averaging of Incoloy cladding and magnesium oxide (MgO).	Porous flow loss coefficients calculated based on detailed CFD models of the flow straightener.	Full
PNNL	STAR-CCM+ version 2019.1, CFD	Porous media	Internal fuel assembly region treated as porous media with effective thermal conductivity; no flow through assembly assumed.	Standard K-ε Low-Re flow model applied to external air flow region; internal radiation included in air gas regions; emissivity values applied along the inner surfaces.	Material properties taken from DCS Handbook; effective properties for heater rods calculated based on volume weighted averaging of Incoloy cladding and MgO.	Porous flow loss coefficients calculated based on detailed CFD models of the flow straightener.	1/2
PNNL	COBRA-SFS version 5.0.0, Subchannel	Quasi-3D rods	Flow within the assembly is modeled as laminar or turbulent based on the Reynolds number of the channels.	External HDCS structure omitted due to the nature of the program.	Solid material properties taken directly from DCS Handbook; fluid properties taken from a NIST reference as isobaric helium and air properties.	Canister surface temperatures from the STAR-CCM+ detailed model used as a boundary condition.	Full

3.2 Experiment Versus Model Data Comparison

Comprehensive data sets from two test cases (2.5 kW, 100 kPa helium backfill and 2.5 kW, 100 kPa air backfill) were presented in the HDCS update report, SAND2019-11688R [Lindgren *et al.*, 2019], and provided to the modelers for model calibration. Data from the other eight test cases in Table 1.1 were withheld from the modelers to properly conduct a blind study. The thermal test data were collected from thermocouples during experimental runs for ten different test cases defined by heater rod powers (representative of spent fuel decay powers), backfill pressures (representing both ambient and elevated pressures), and backfill gases (helium or air) – the ten cases are shown in Table 1.1. The thermocouples were placed axially at 0.152 m (6 in.) intervals and radially at select axial levels that are spaced nominally 0.610 m (24 in.) apart, with the thermocouple locations specified in Section 2.3.1. Hot wire anemometers were used to measure air flow velocities in the four inlet ducts – air mass flow rates were derived from the voltage readings of these devices.

For the results in this report, each model was assigned a model number. Two of the models used porous media model representations of the fuel, one used explicit fuel representations, and one used an explicit subchannel representation of the fuel. These model numbers are reflected in the plots and tables in this report. The model numbers do not necessarily correspond to the ordering of the models in Table 3.1 – arbitrary model numbers were assigned at random to retain anonymity. The simulation uncertainties provided by the modeling institution that generated the results for model 1 are shown in the plots; the numerical values of these uncertainties can be found in Appendix B. The data corresponding to the plots in this section and the measurement uncertainties can be found in Appendix F.

When comparing the results, it should be noted that the COBRA-SFS models for horizontal storage systems require canister surface temperature boundary conditions calculated by external models. The steady state COBRA-SFS results for horizontal systems are therefore strongly dependent on external modeling codes.

3.2.1 0.5 kW, 100 kPa Helium Test Case

The model comparison data for the 0.5 kW, 100 kPa helium test is shown in this section. The temperature profiles are shown in Figure 3.2 (axial), Figure 3.3 (vertical), and Figure 3.4 (horizontal). As discussed in further detail in Appendix A, while uncertainties of up to 2 to 5% are justified for surface-mounted thermocouples in high heat flux and/or highly transient environments, the relatively small spatial and temporal gradients experienced during the HDCS testing warrant an expanded uncertainty for this type of TC of U_T = 1% of the reading in Kelvin [Nakos, 2004]. Here, the experimental measurement uncertainty bars in the temperature profile plots (red) correspond to 1% of the PCT plus a small contribution from the observed fluctuation – in this case, the measurement uncertainty is ±3.7 K. Simulation uncertainties, indicated by the blue uncertainty bars, are provided for model 1's temperature profiles by the institution that generated those results. The simulation uncertainties included iterative uncertainty and spatial discretization uncertainty, and the experimental uncertainty considered in the numerical calculations was 1% of the simulation result. The numerical values for the simulation uncertainties can be found in Appendix B.

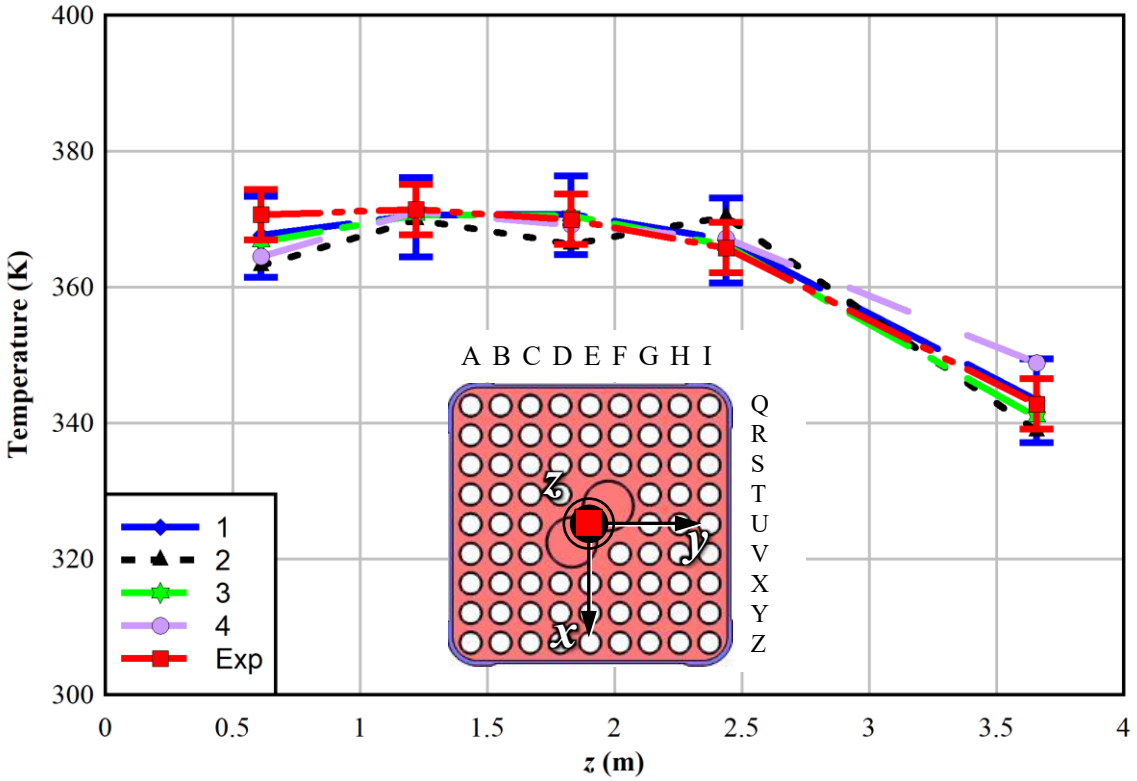

Figure 3.2 **Axial temperature profile data comparison for the 0.5 kW, 100 kPa helium test.**

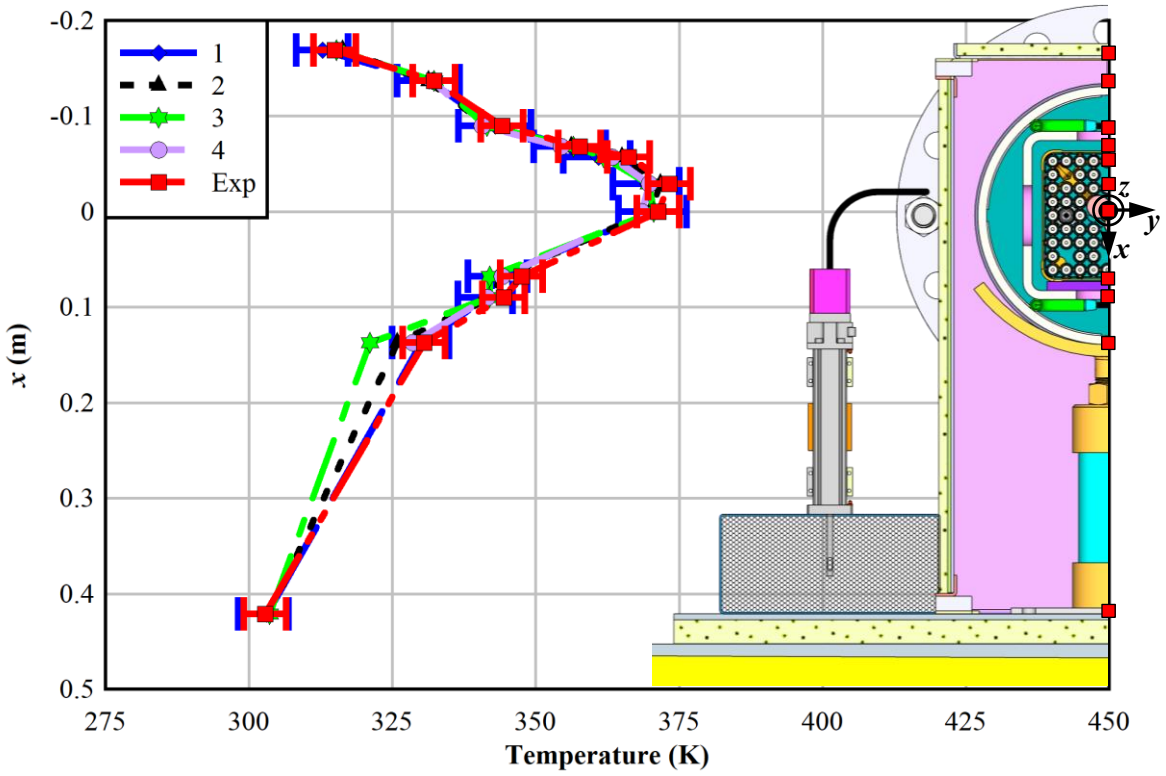

Figure 3.3 **Vertical temperature profile data comparison from the 0.5 kW, 100 kPa helium test.**

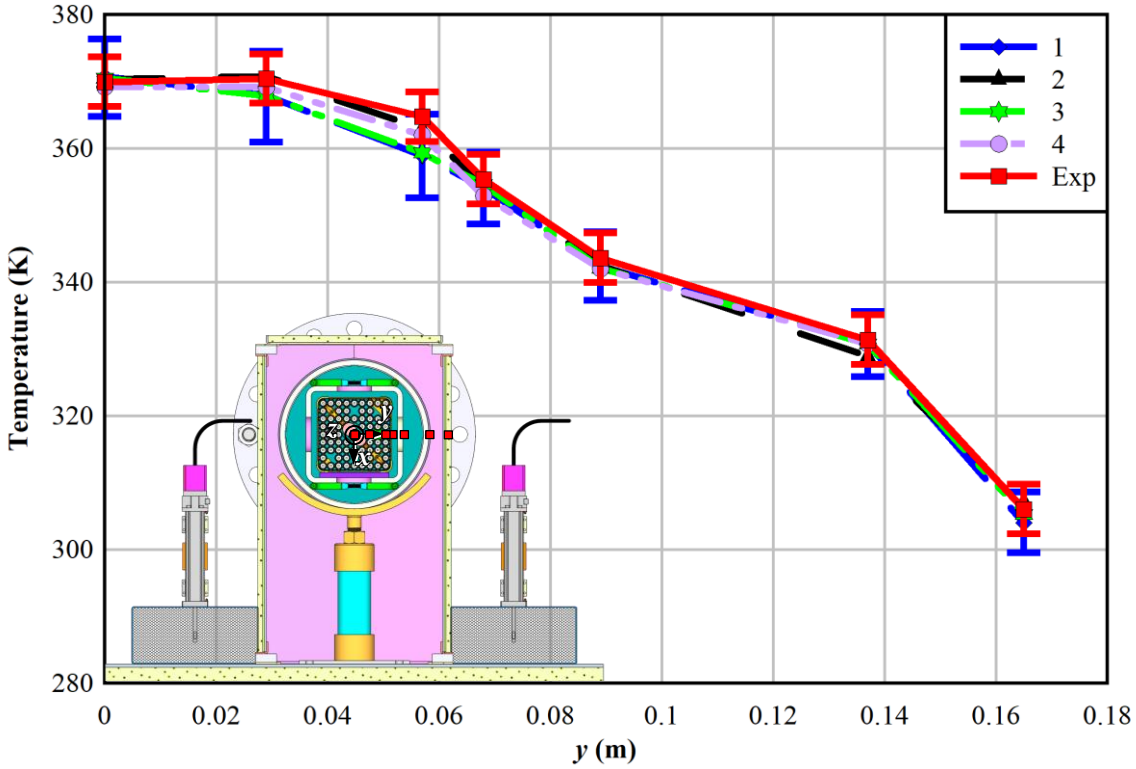

Figure 3.4 Horizontal temperature profile data comparison for the 0.5 kW, 100 kPa helium test.

3.2.2 1.0 kW, 100 kPa Helium Test Case

The model comparison data for the 1.0 kW, 100 kPa helium test is shown in this section. The temperature profiles are shown in Figure 3.5 (axial), Figure 3.6 (vertical), and Figure 3.7(horizontal). The experimental measurement uncertainty bars in the temperature profile plots (red) correspond to 1% of the PCT plus a small contribution from the observed fluctuation – in this case, the measurement uncertainty is ±4.3 K. Simulation uncertainties, indicated by the blue uncertainty bars, are provided for model 1's temperature profiles.

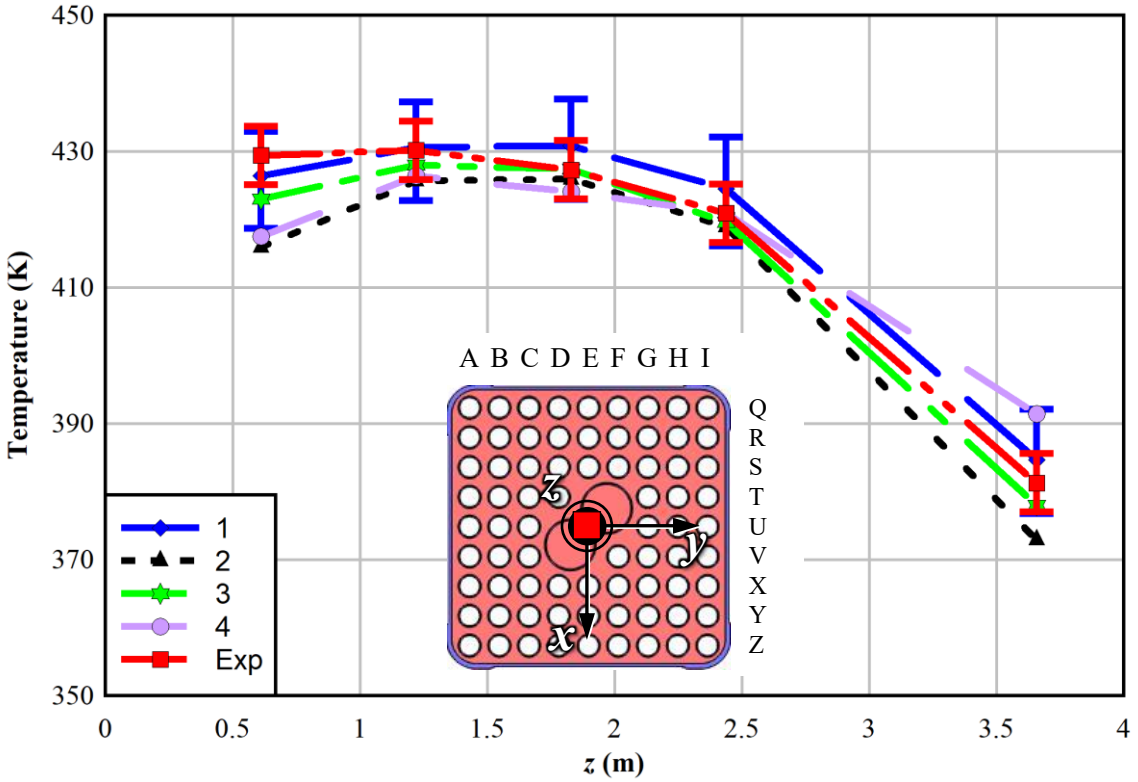

Figure 3.5 **Axial temperature profile data comparison for the 1.0 kW, 100 kPa helium test.**

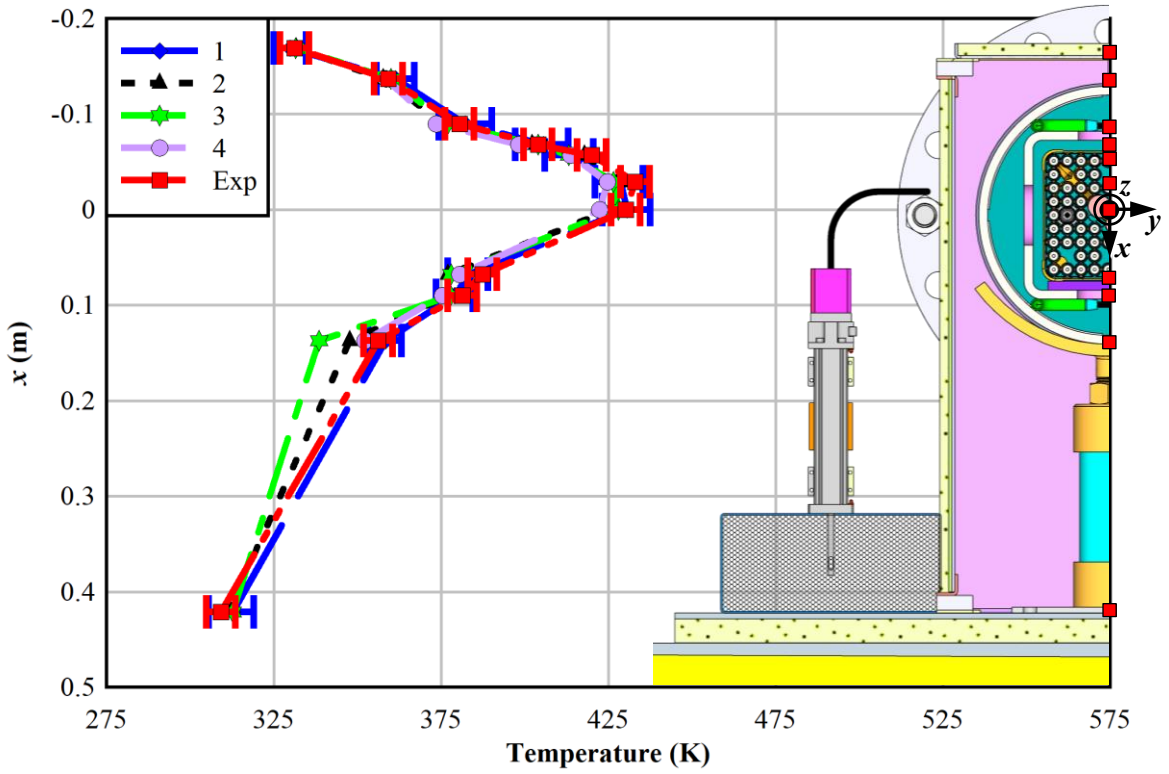

Figure 3.6 **Vertical temperature profile data comparison for the 1.0 kW, 100 kPa helium test.**

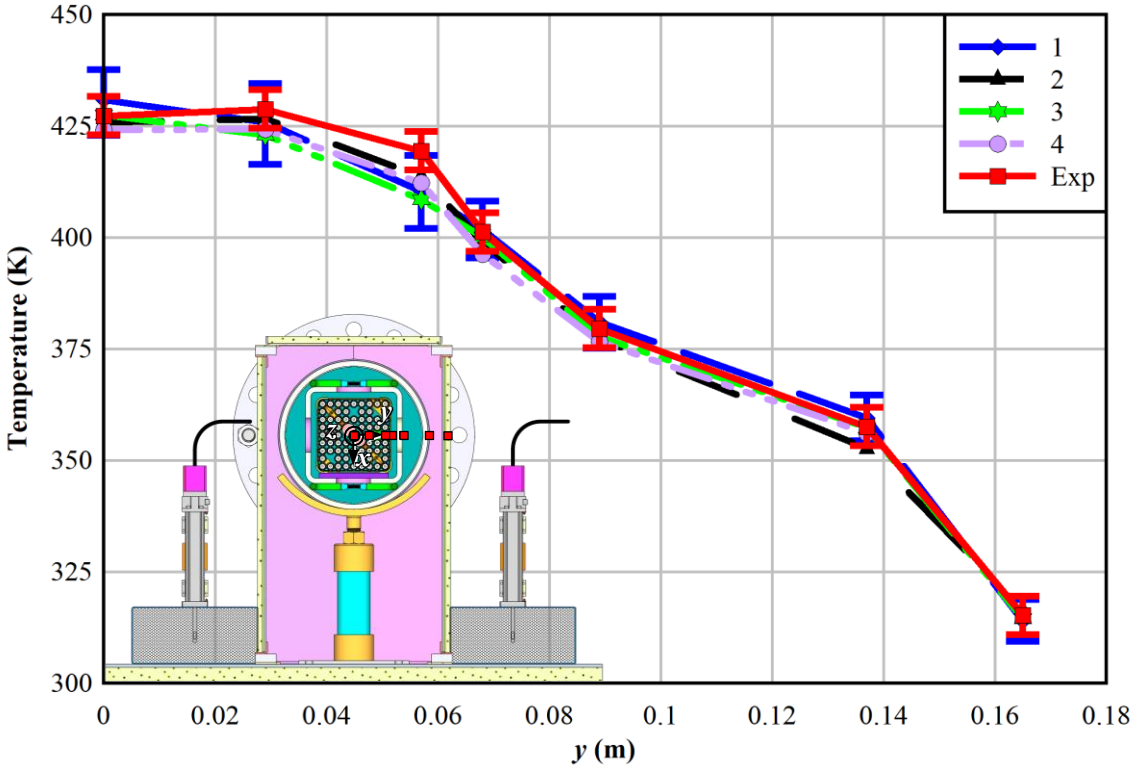

Figure 3.7 Horizontal temperature profile data comparison for the 1.0 kW, 100 kPa helium test.

3.2.3 2.5 kW, 100 kPa Helium Test Case

The model comparison data for the 2.5 kW, 100 kPa helium test is shown in this section. The experimental results for this test were provided to the modelers for model calibration purposes, so the model calculations for this test were not performed blindly. The temperature profiles are shown in Figure 3.8 (axial), Figure 3.9 (vertical), and Figure 3.10 (horizontal). The experimental measurement uncertainty bars in the temperature profile plots (red) correspond to 1% of the PCT plus a small contribution from the observed fluctuation – in this case, the measurement uncertainty is ±5.6 K. Simulation uncertainties, indicated by the blue uncertainty bars, are provided for model 1's temperature profiles.

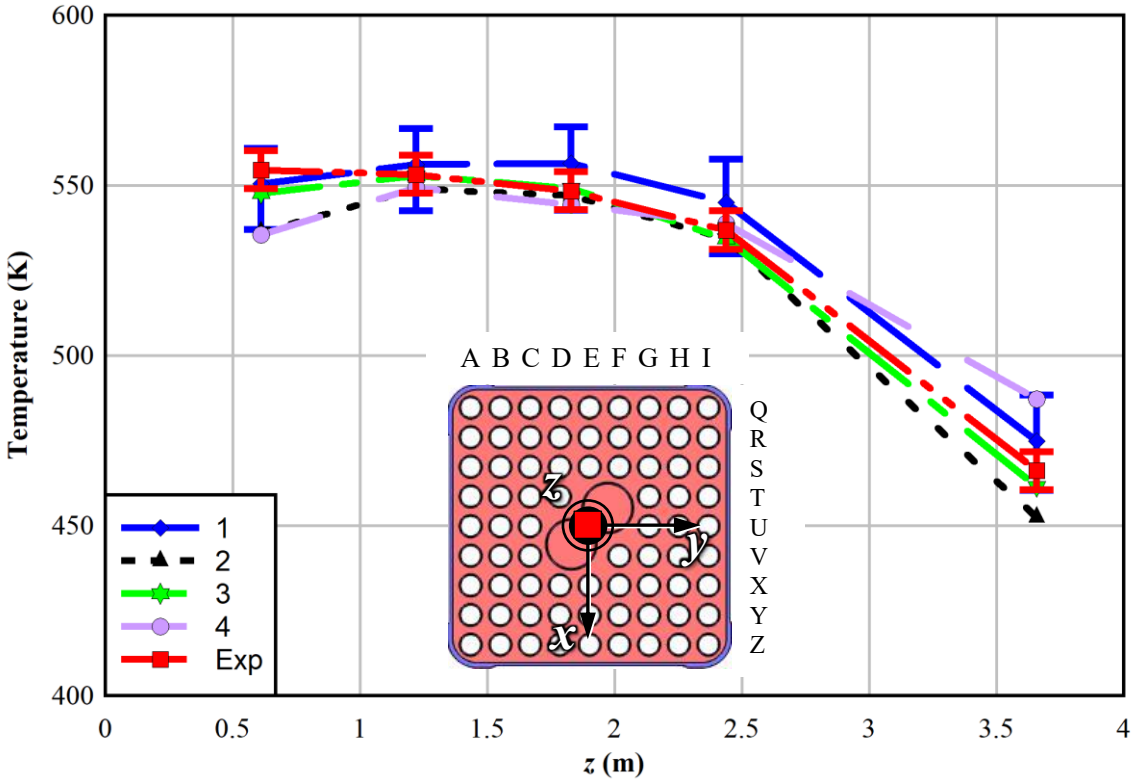

Figure 3.8 **Axial temperature profile data comparison for the 2.5 kW, 100 kPa helium test.**

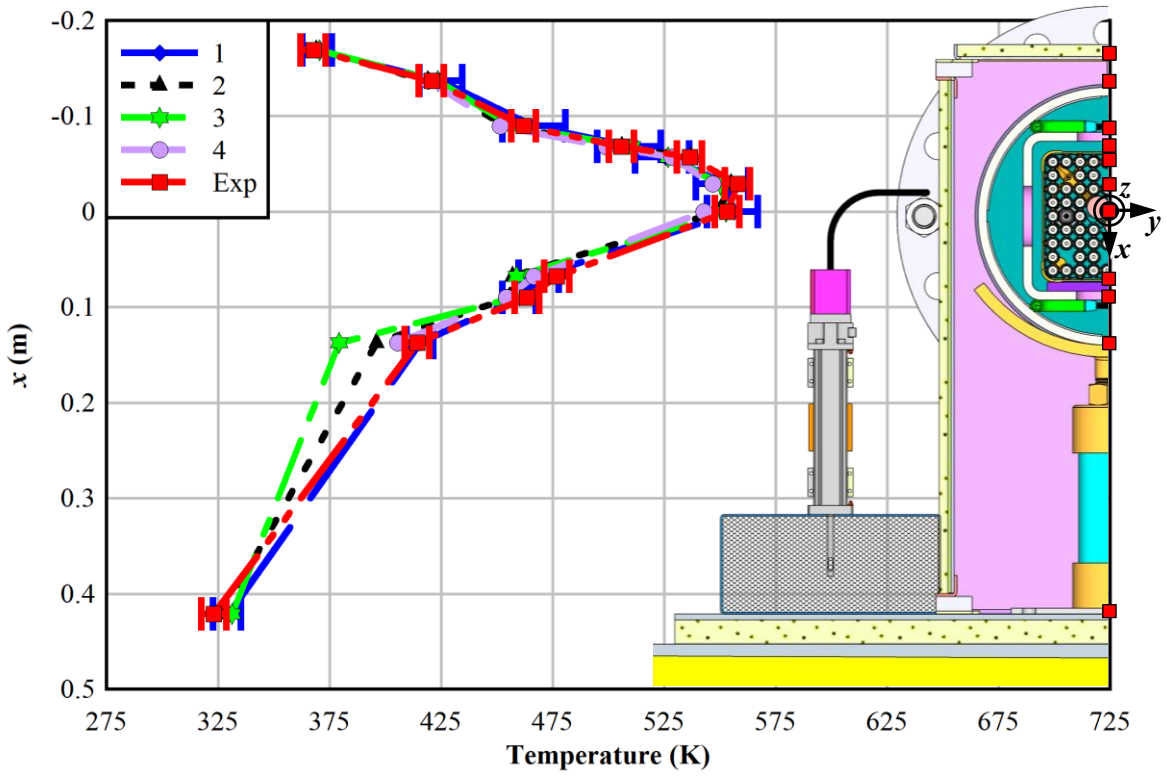

Figure 3.9 **Vertical temperature profile data comparison for the 2.5 kW, 100 kPa helium test.**

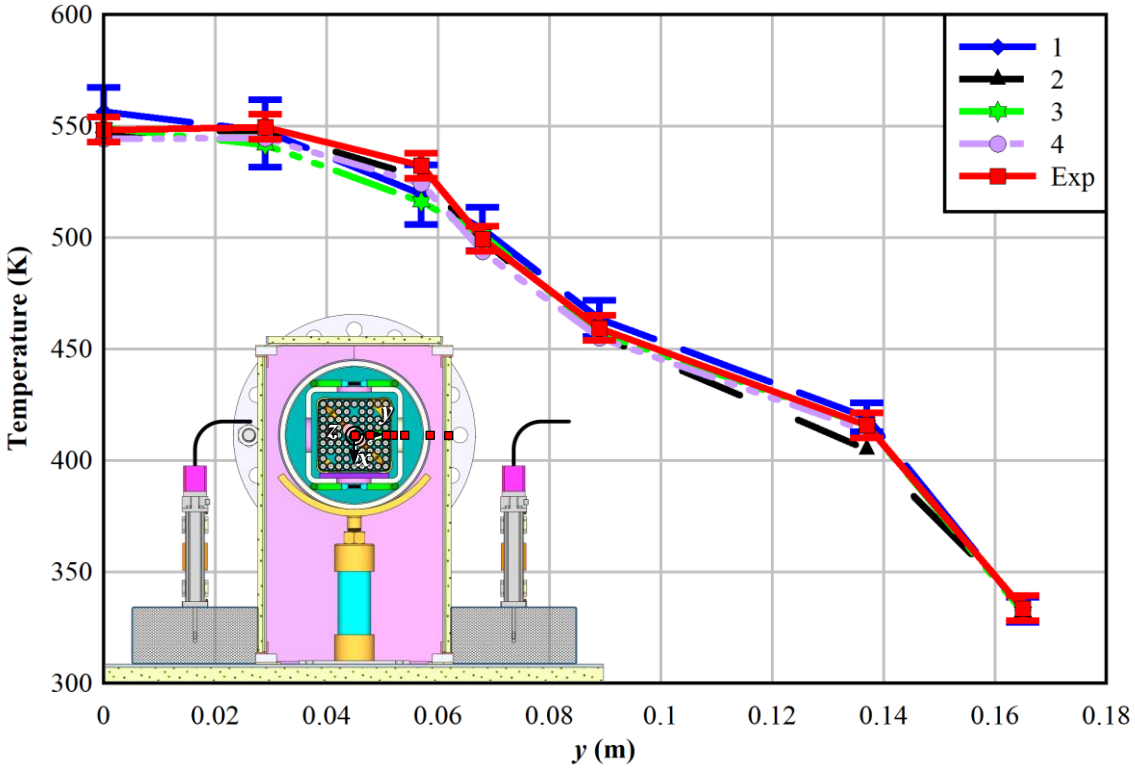

Figure 3.10 Horizontal temperature profile data comparison for the 2.5 kW, 100 kPa helium test.

3.2.4 5.0 kW, 100 kPa Helium Test Case

The model comparison data for the 5.0 kW, 100 kPa helium test is shown in this section. The temperature profiles are shown in Figure 3.11 (axial), Figure 3.12 (vertical), and Figure 3.13 (horizontal). The experimental measurement uncertainty bars in the temperature profile plots (red) correspond to 1% of the PCT plus a small contribution from the observed fluctuation – in this case, the measurement uncertainty is ±6.9 K. Simulation uncertainties, indicated by the blue uncertainty bars, are provided for model 1's temperature profiles.

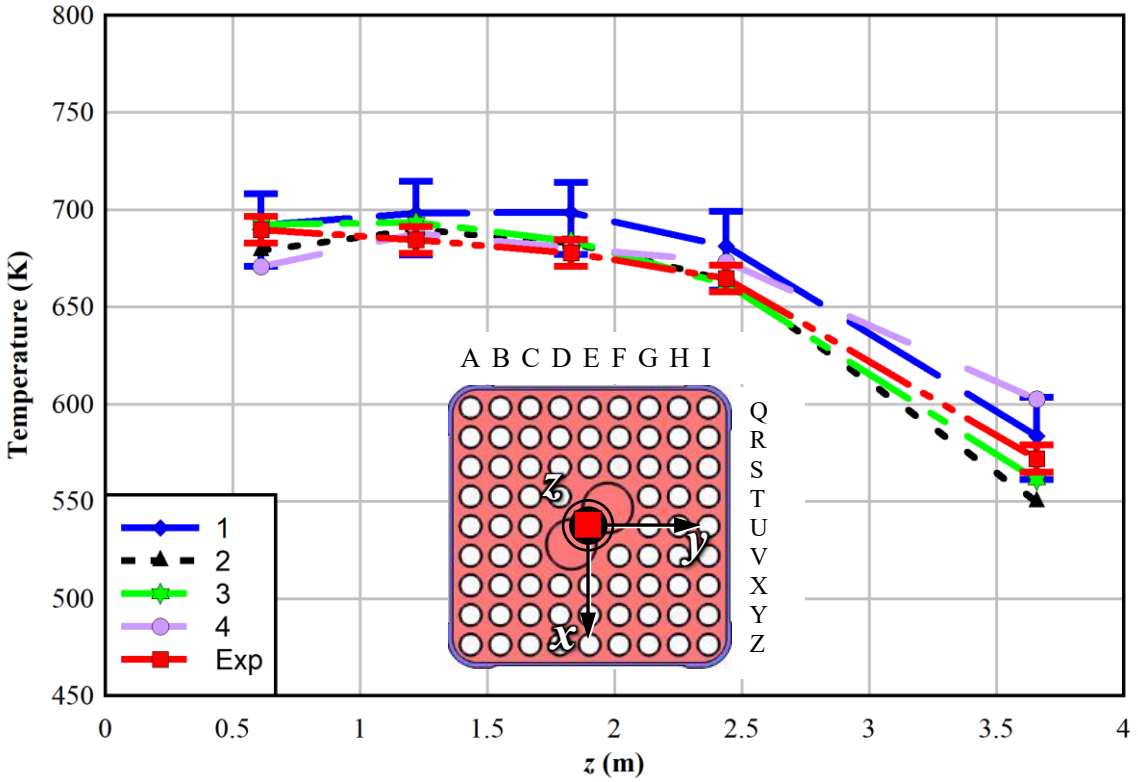

Figure 3.11 Axial temperature profile data comparison for the 5.0 kW, 100 kPa helium test.

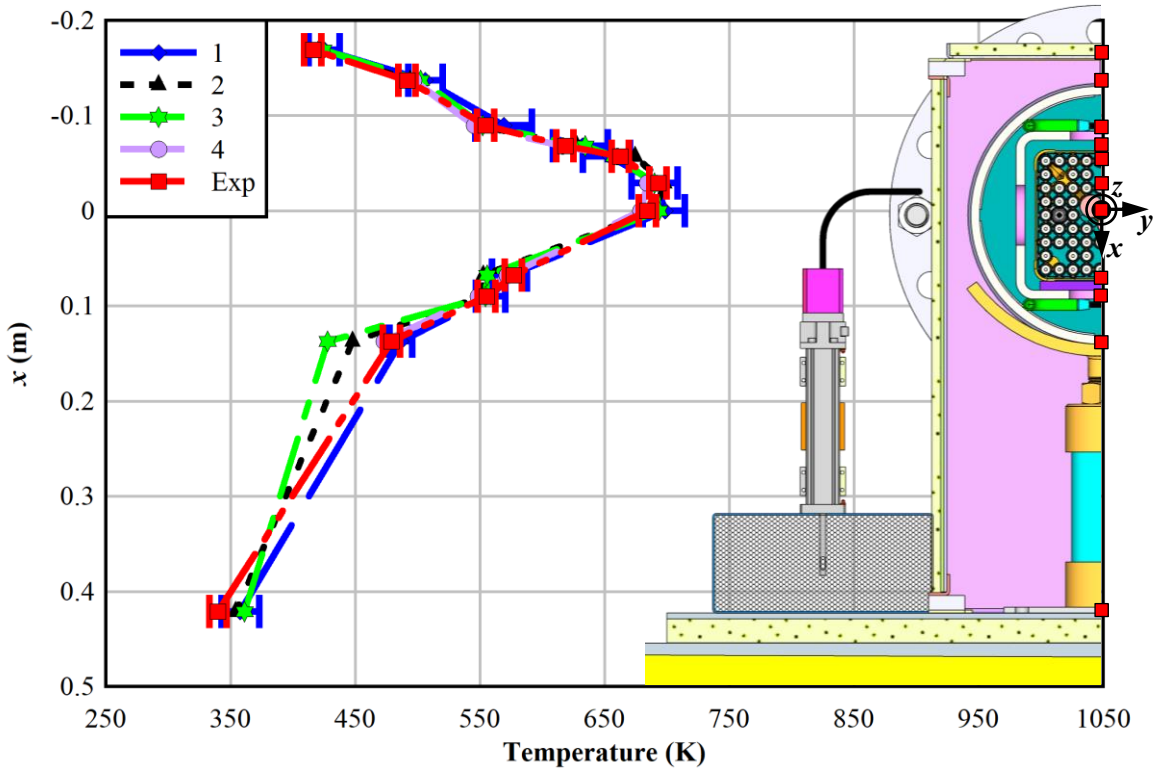

Figure 3.12 Vertical temperature profile data comparison for the 5.0 kW, 100 kPa helium test.

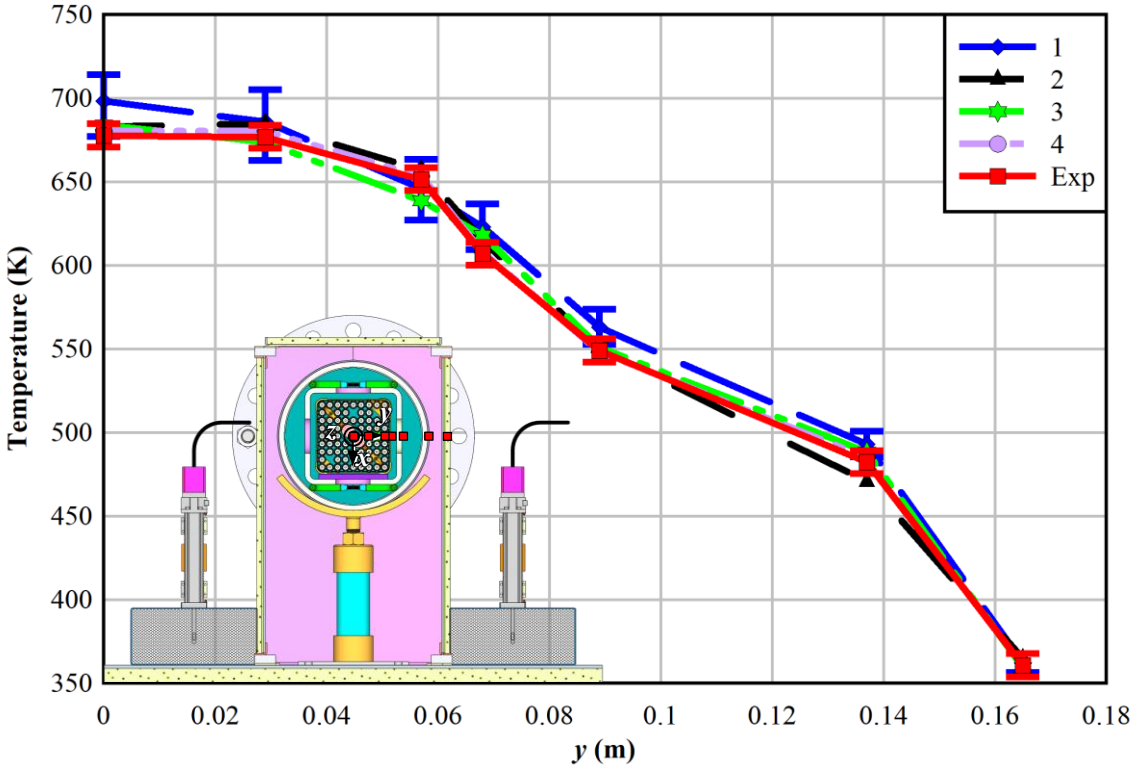

Figure 3.13 Horizontal temperature profile data comparison for the 5.0 kW, 100 kPa helium test.

3.2.5 0.5 kW, 800 kPa Helium Test Case

The model comparison data for the 0.5 kW, 800 kPa helium test is shown in this section. The temperature profiles are shown in Figure 3.14 (axial), Figure 3.15 (vertical), and Figure 3.16 (horizontal). The experimental measurement uncertainty bars in the temperature profile plots (red) correspond to 1% of the PCT plus a small contribution from the observed fluctuation – in this case, the measurement uncertainty is ±3.7 K. Simulation uncertainties, indicated by the blue uncertainty bars, are provided for model 1's temperature profiles.

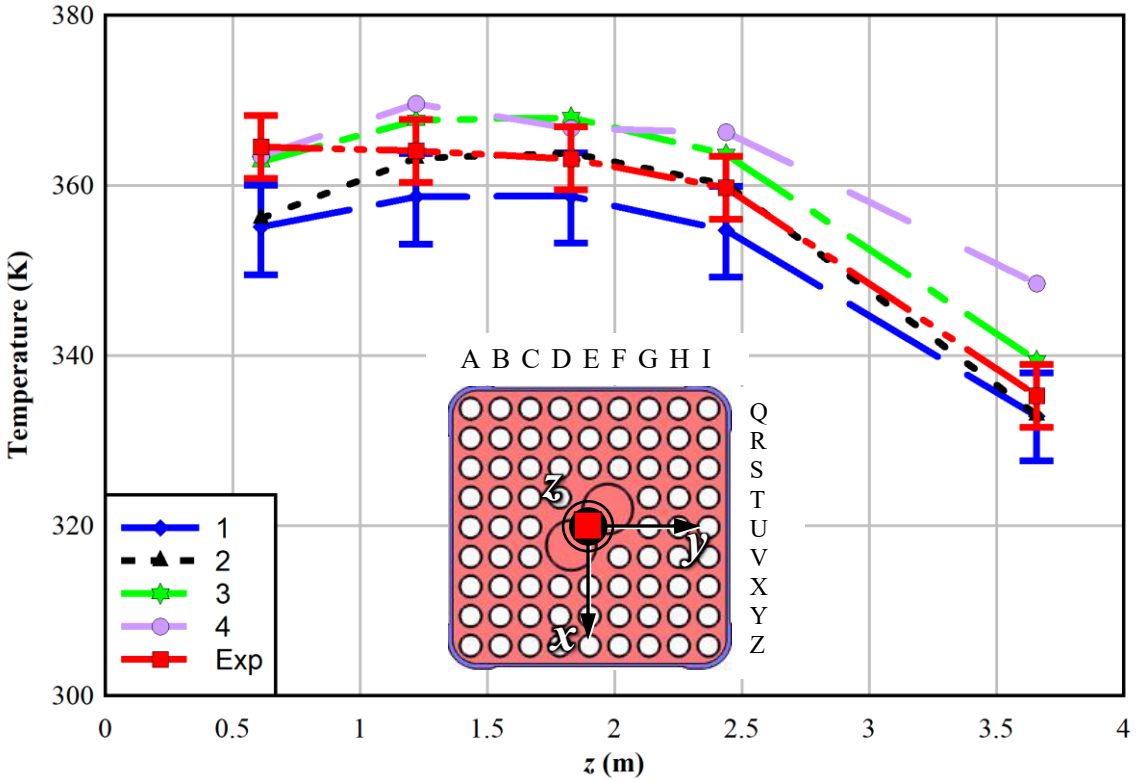

Figure 3.14 Axial temperature profile data comparison for the 0.5 kW, 800 kPa helium test.

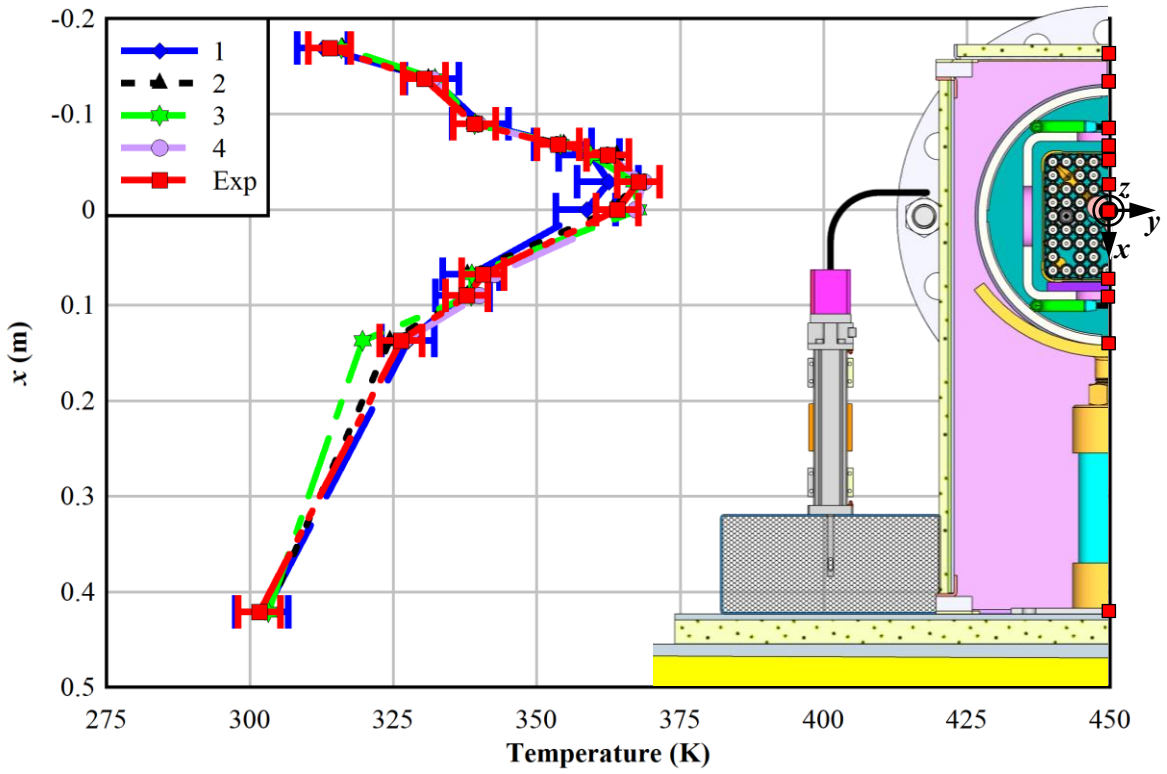

Figure 3.15 Axial temperature profile data comparison for the 0.5 kW, 800 kPa helium test.

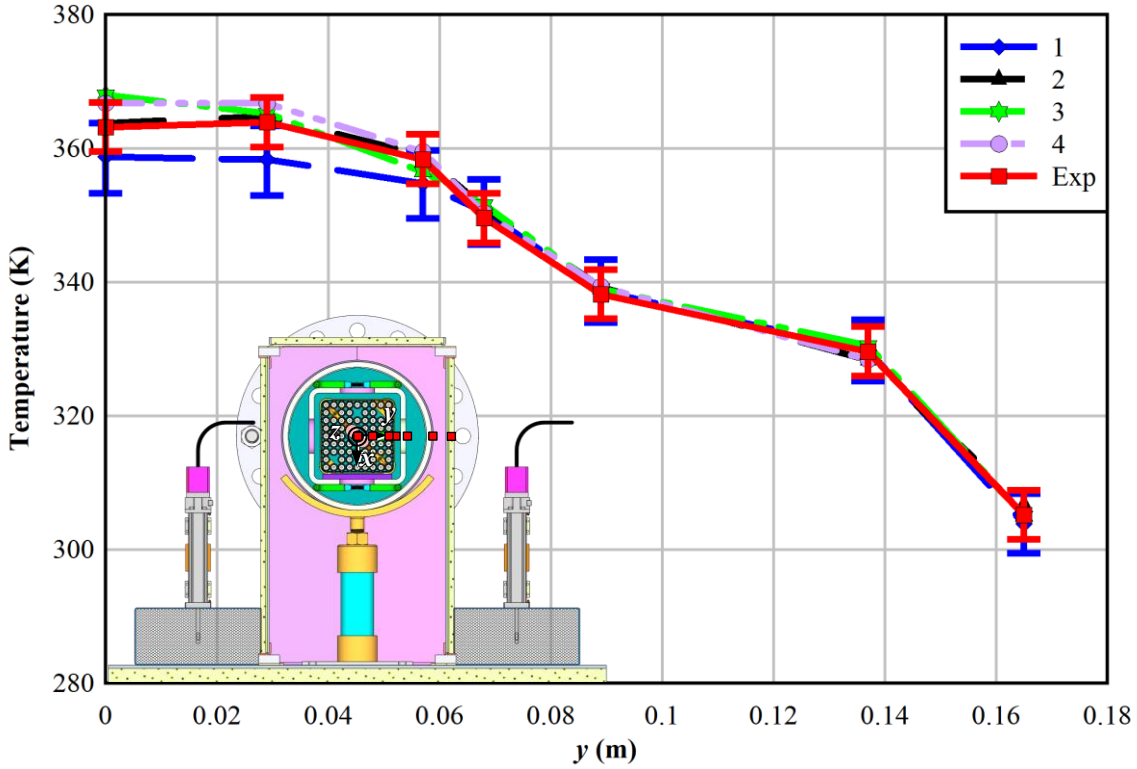

Figure 3.16 Horizontal temperature profile data comparison for the 0.5 kW, 800 kPa helium test.

3.2.6 5.0 kW, 800 kPa Helium Test Case

The model comparison data for the 5.0 kW, 800 kPa helium test is shown in this section. The temperature profiles are shown in Figure 3.17 (axial), Figure 3.18 (vertical), and Figure 3.19 (horizontal). The experimental measurement uncertainty bars in the temperature profile plots (red) correspond to 1% of the PCT plus a small contribution from the observed fluctuation – in this case, the measurement uncertainty is ±6.8 K. Simulation uncertainties, indicated by the blue uncertainty bars, are provided for model 1's temperature profiles.

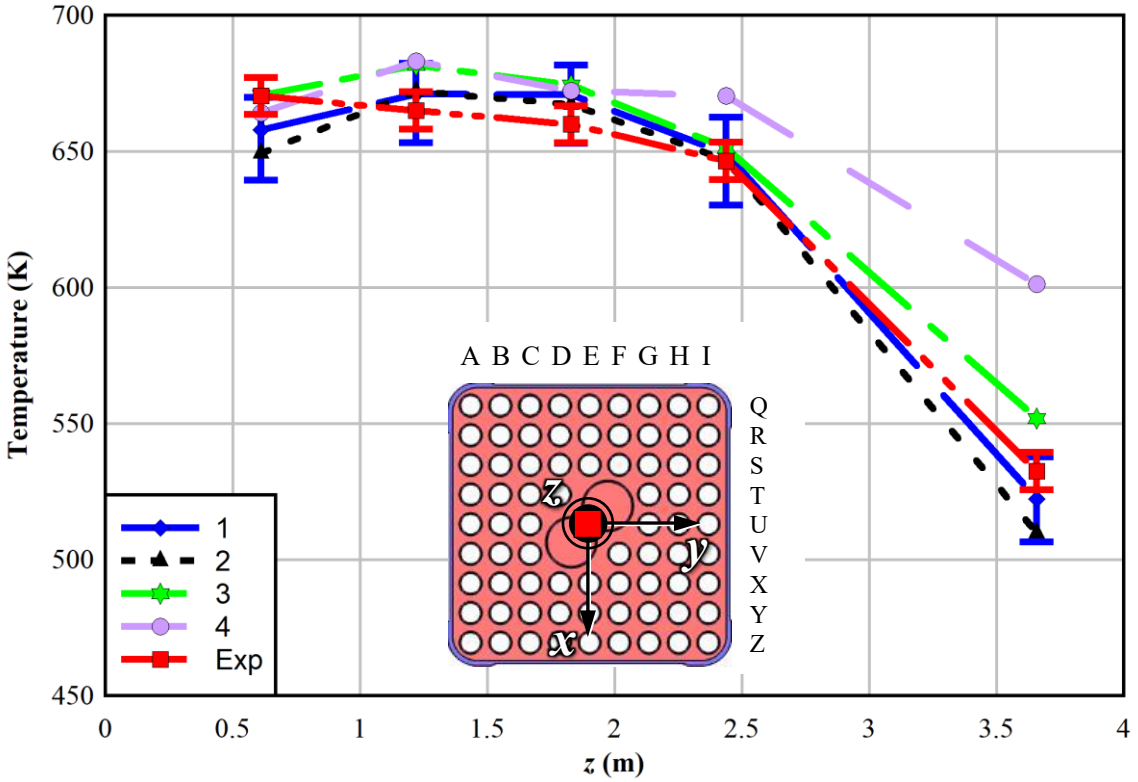

Figure 3.17 Axial temperature profile data comparison for the 5.0 kW, 800 kPa helium test.

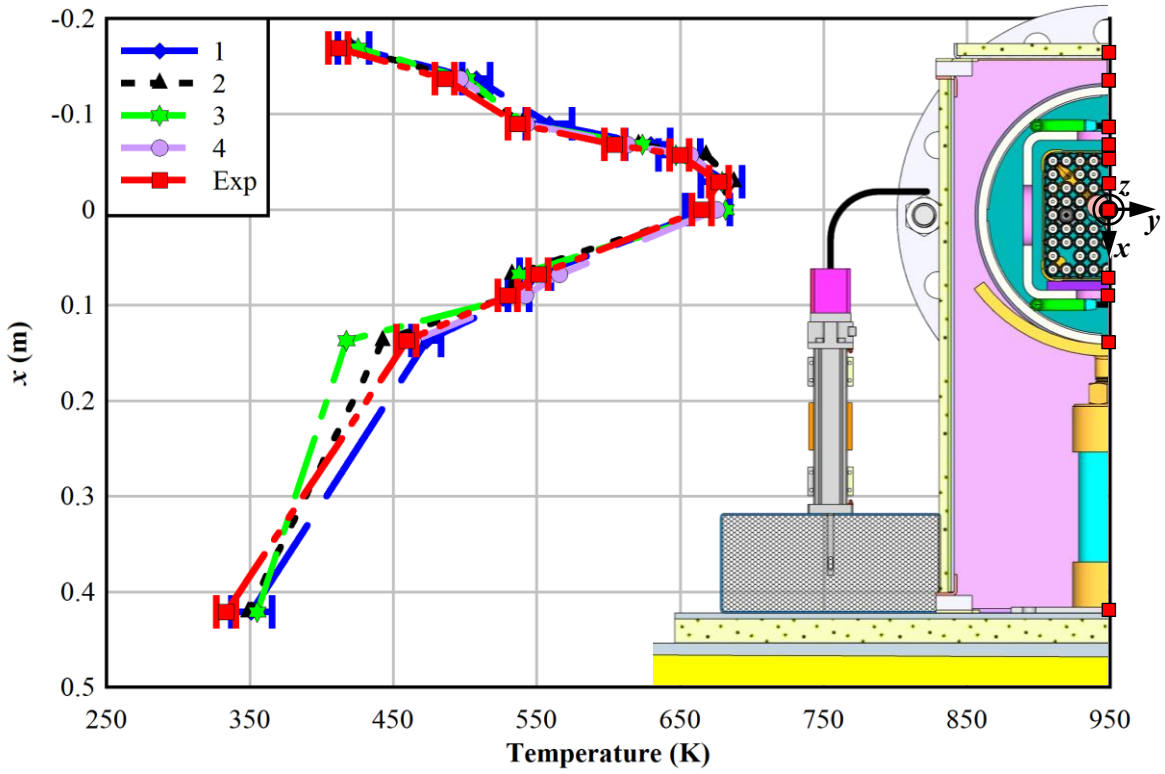

Figure 3.18 Vertical temperature profile data comparison for the 5.0 kW, 800 kPa helium test.

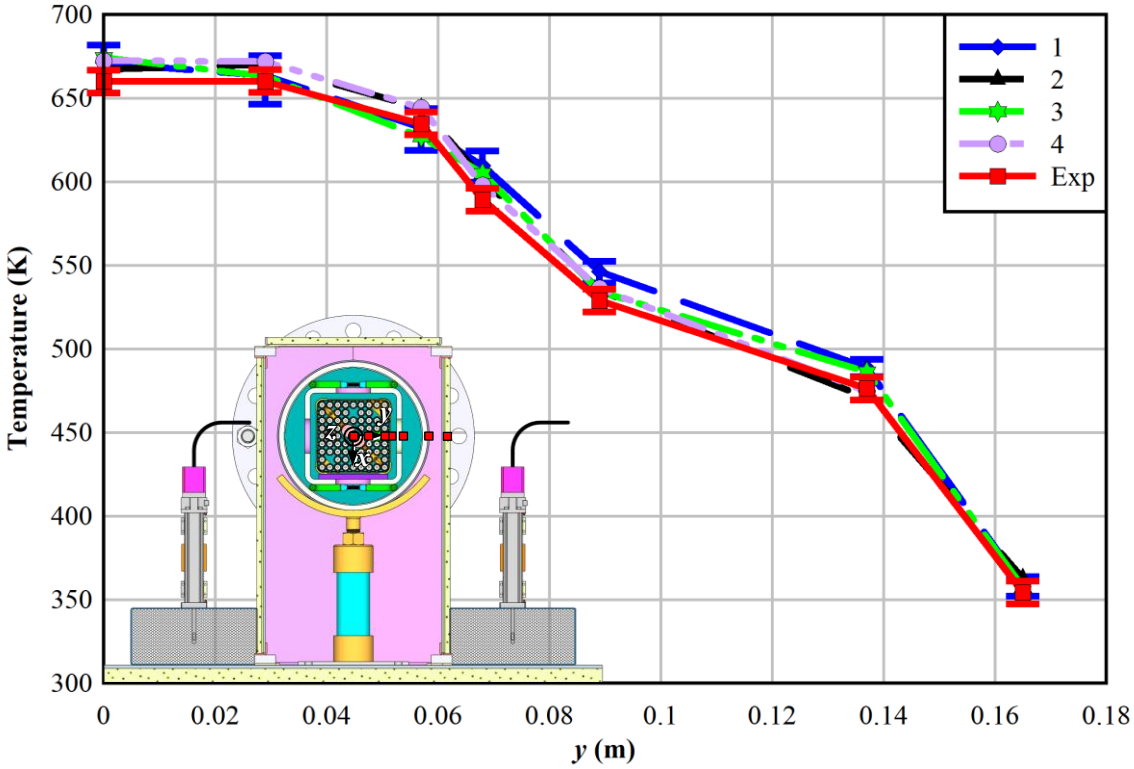

Figure 3.19 Horizontal temperature profile data comparison for the 5.0 kW, 800 kPa helium test.

3.2.7 0.5 kW, 100 kPa Air Test Case

The model comparison data for the 0.5 kW, 100 kPa air test is shown in this section. The temperature profiles are shown in Figure 3.20 (axial), Figure 3.21 (vertical), and Figure 3.22 (horizontal). The experimental measurement uncertainty bars in the temperature profile plots (red) correspond to 1% of the PCT plus a small contribution from the observed fluctuation – in this case, the measurement uncertainty is ±4.3 K. Simulation uncertainties, indicated by the blue uncertainty bars, are provided for model 1's temperature profiles.

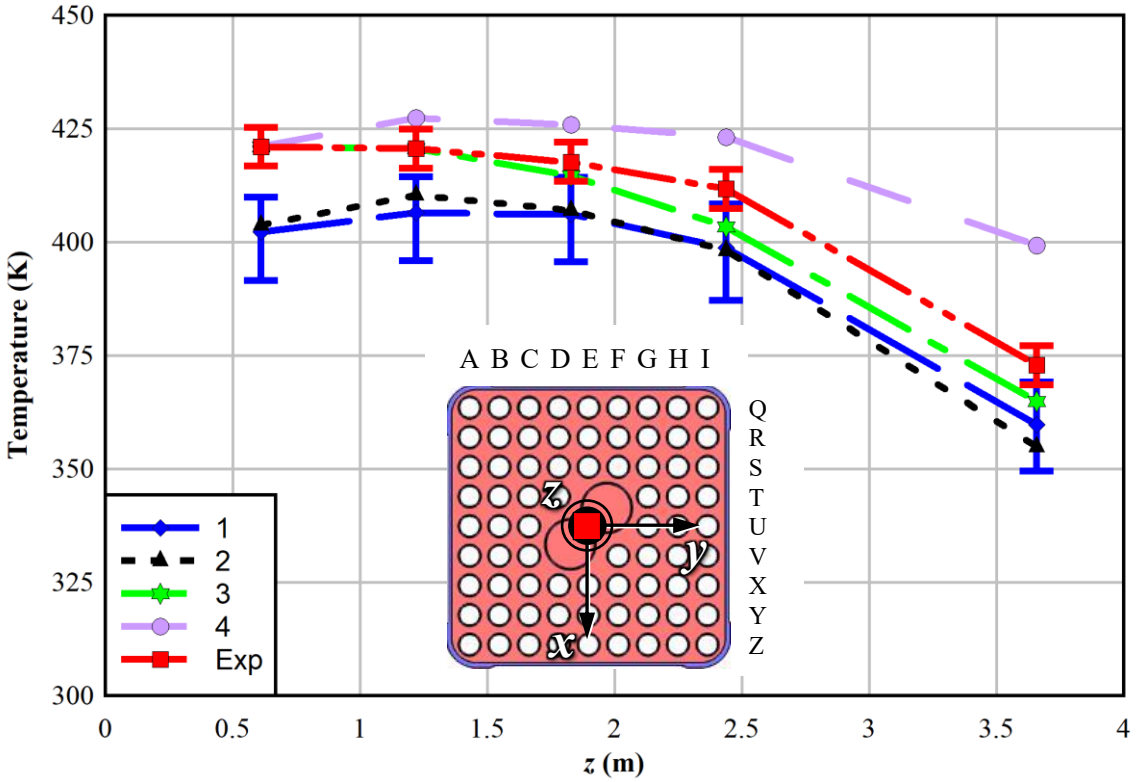

Figure 3.20 Axial temperature profile data comparison for the 0.5 kW, 100 kPa air test.

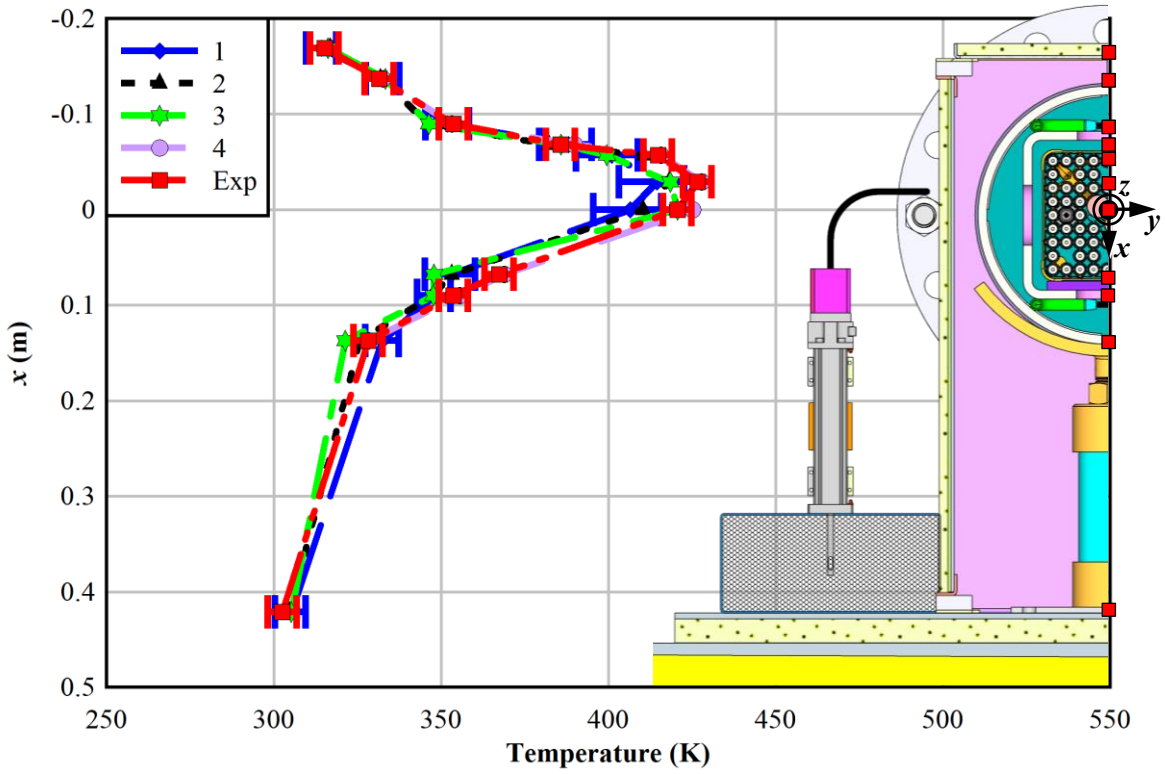

Figure 3.21 Vertical temperature profile data comparison for the 0.5 kW, 100 kPa air test.

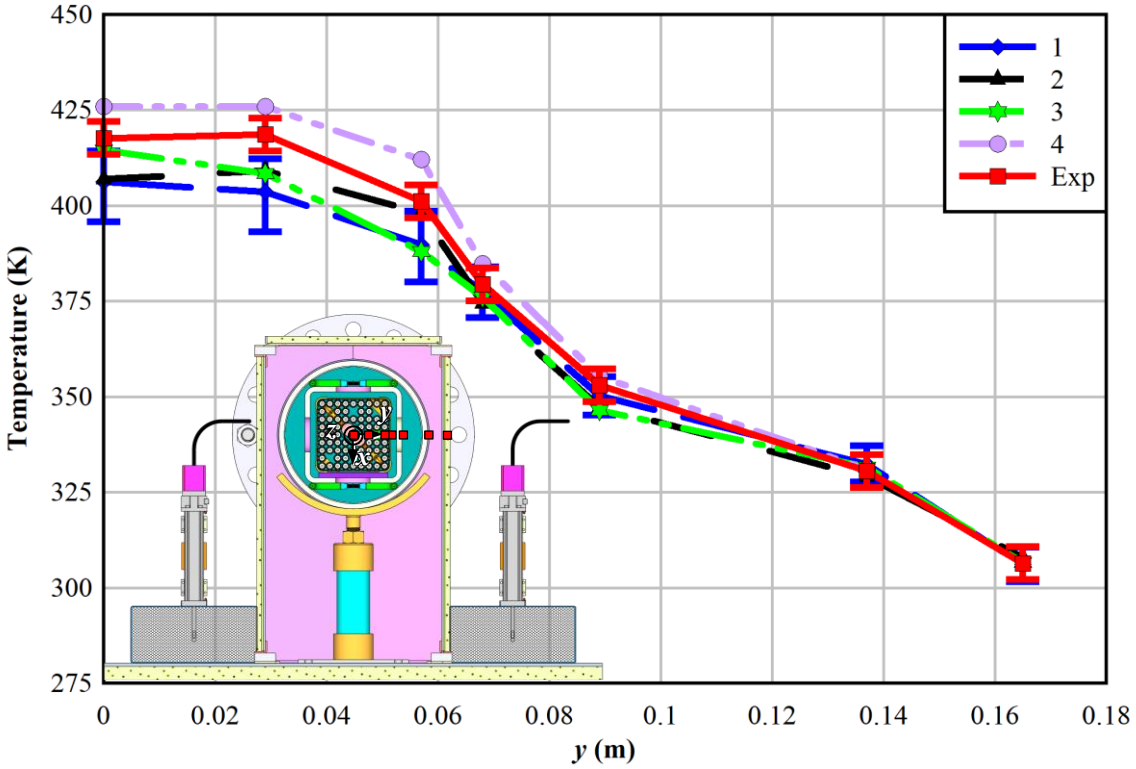

Figure 3.22 Horizontal temperature profile data comparison for the 0.5 kW, 100 kPa air test.

3.2.8 1.0 kW, 100 kPa Air Test Case

The model comparison data for the 1.0 kW, 100 kPa air test is shown in this section. The temperature profiles are shown in Figure 3.23 (axial), Figure 3.24 (vertical), and Figure 3.25 (horizontal). The experimental measurement uncertainty bars in the temperature profile plots (red) correspond to 1% of the PCT plus a small contribution from the observed fluctuation – in this case, the measurement uncertainty is ±5.2 K. Simulation uncertainties, indicated by the blue uncertainty bars, are provided for model 1's temperature profiles.

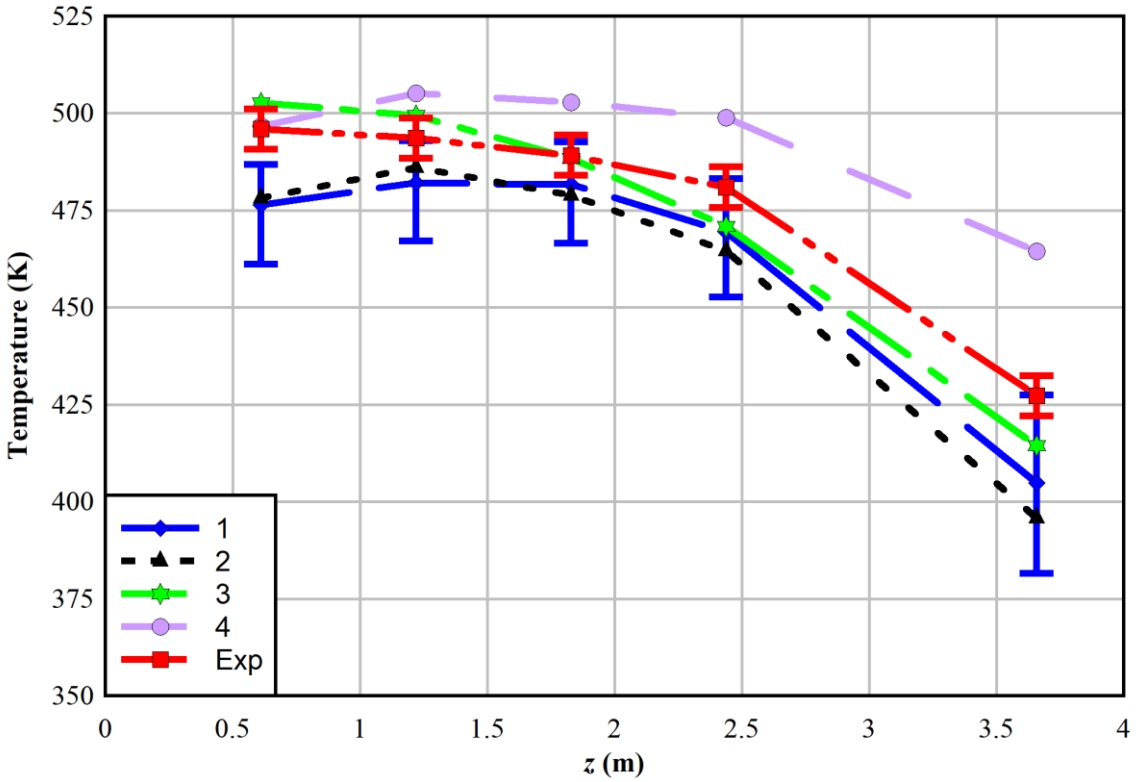

Figure 3.23 Axial temperature profile data comparison for the 1.0 kW, 100 kPa air test.

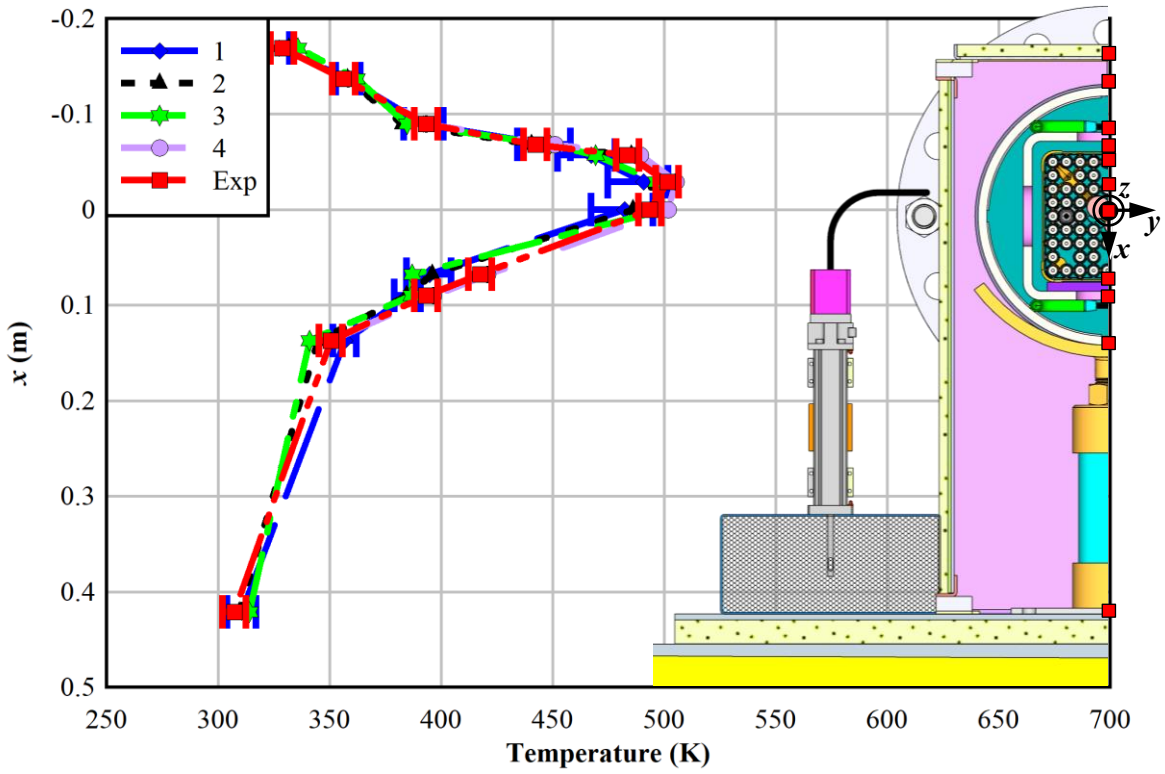

Figure 3.24 Vertical temperature profile data comparison for the 1.0 kW, 100 kPa air test.

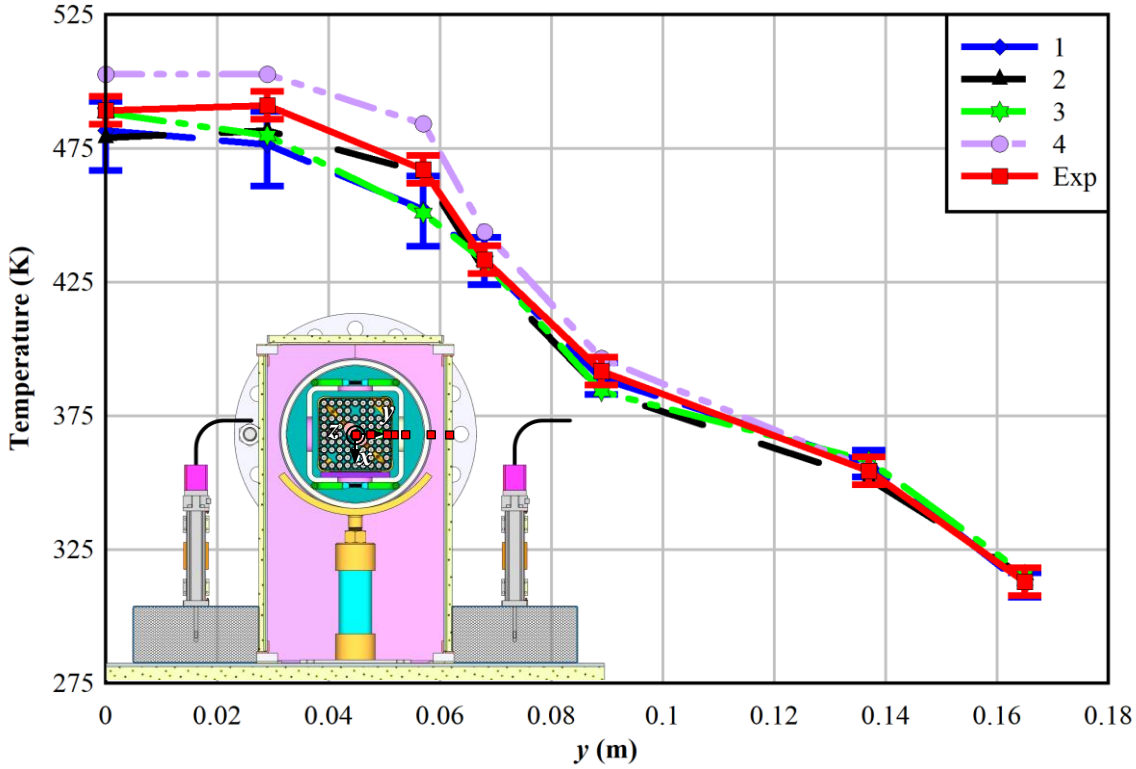

Figure 3.25 Horizontal temperature profile data comparison for the 1.0 kW, 100 kPa air test.

3.2.9 2.5 kW, 100 kPa Air Test Case

The model comparison data for the 2.5 kW, 100 kPa air test is shown in this section. The experimental results for this test were provided to the modelers for model calibration purposes, so the model calculations for this test were not performed blindly. The temperature profiles are shown in Figure 3.26 (axial), Figure 3.27 (vertical), and Figure 3.28 (horizontal). The experimental measurement uncertainty bars in the temperature profile plots (red) correspond to 1% of the PCT plus a small contribution from the observed fluctuation – in this case, the measurement uncertainty is ±6.5 K. Simulation uncertainties, indicated by the blue uncertainty bars, are provided for model 1's temperature profiles.

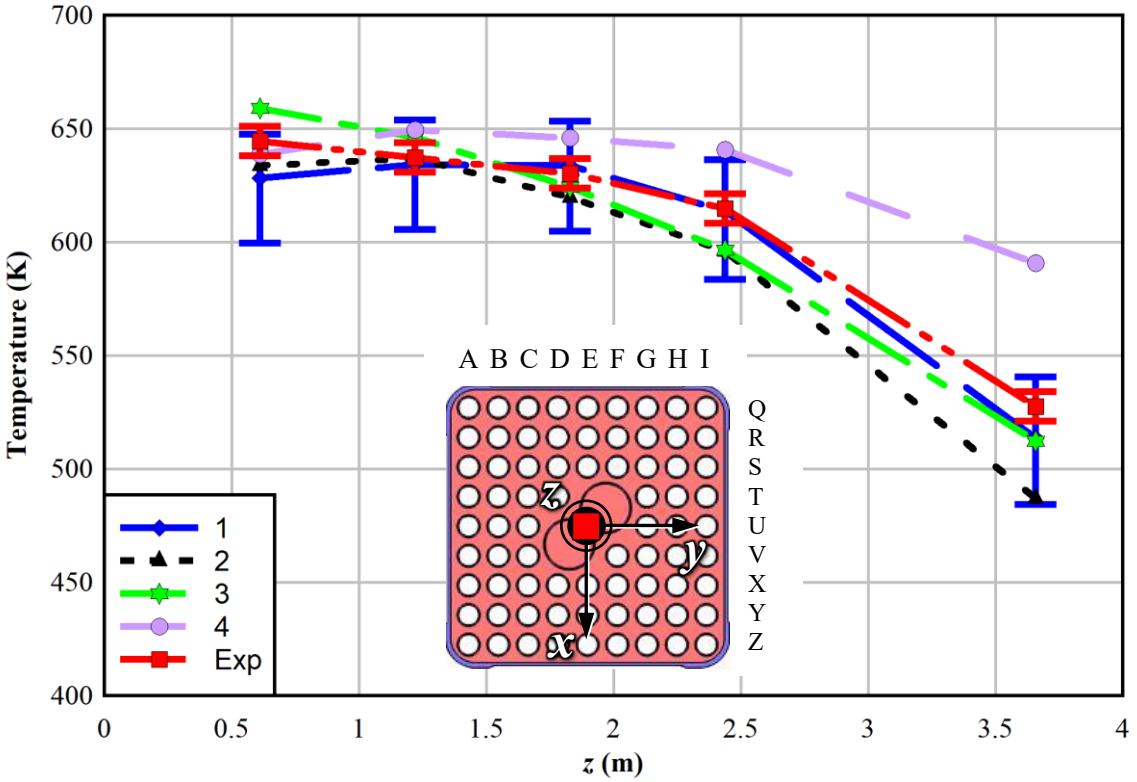

Figure 3.26 Axial temperature profile data comparison for the 2.5 kW, 100 kPa air test.

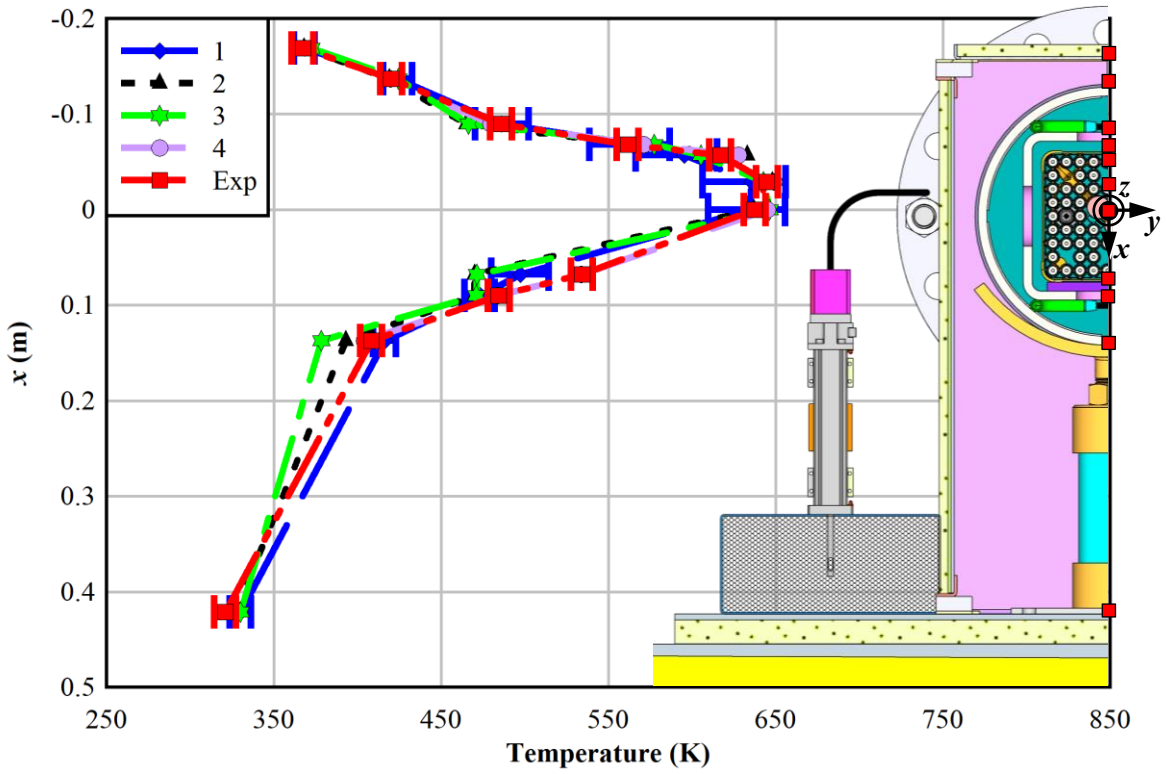

Figure 3.27 Vertical temperature profile data comparison for the 2.5 kW, 100 kPa air test.

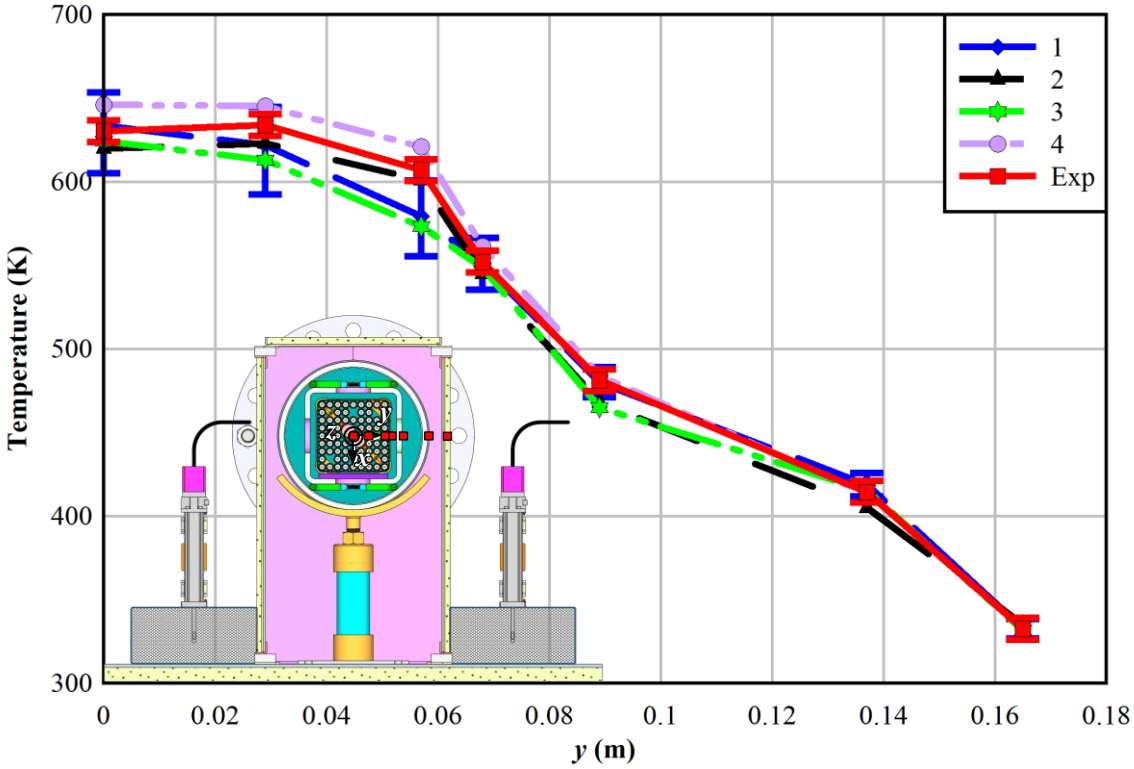

Figure 3.28 Horizontal temperature profile data comparison for the 2.5 kW, 100 kPa air test.

3.2.10 5.0 kW, 100 kPa Air Test Case

The model comparison data for the 5.0 kW, 100 kPa air test is shown in this section. The temperature profiles are shown in Figure 3.29 (axial), Figure 3.30 (vertical), and Figure 3.31 (horizontal). The experimental measurement uncertainty bars in the temperature profile plots (red) correspond to 1% of the PCT plus a small contribution from the observed fluctuation – in this case, the measurement uncertainty is ±7.8 K. Simulation uncertainties, indicated by the blue uncertainty bars, are provided for model 1's temperature profiles.

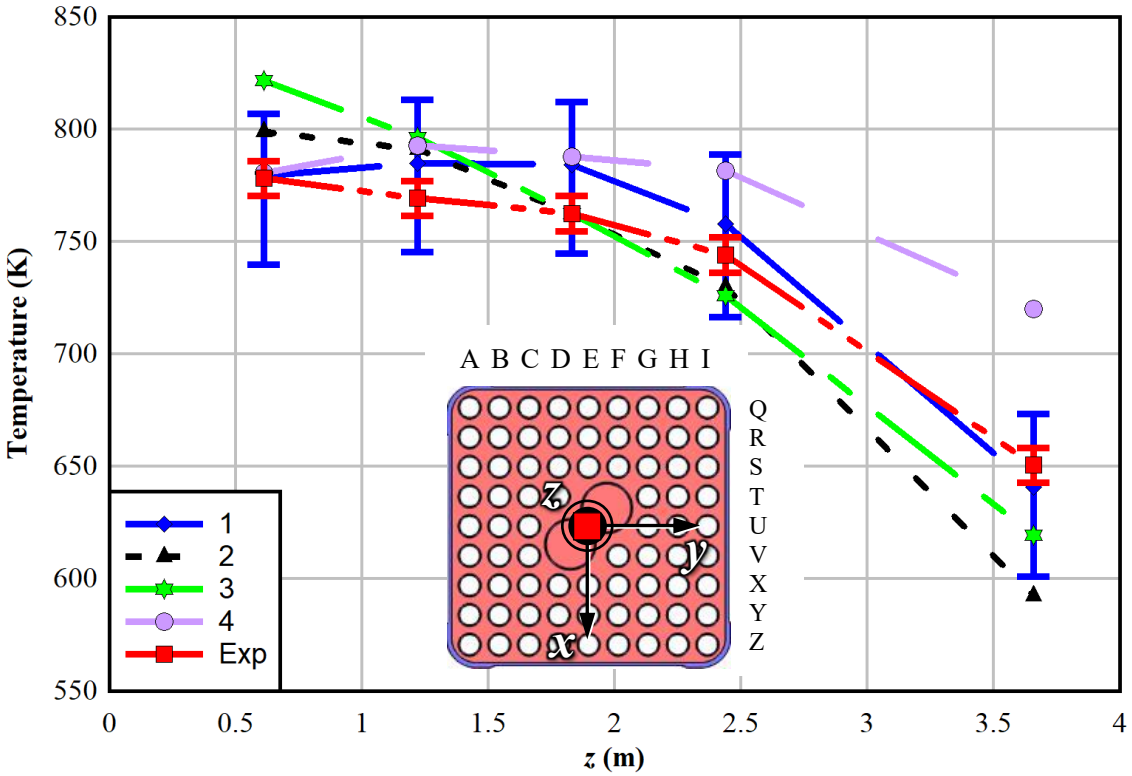

Figure 3.29 Axial temperature profile data comparison for the 5.0 kW, 100 kPa air test.

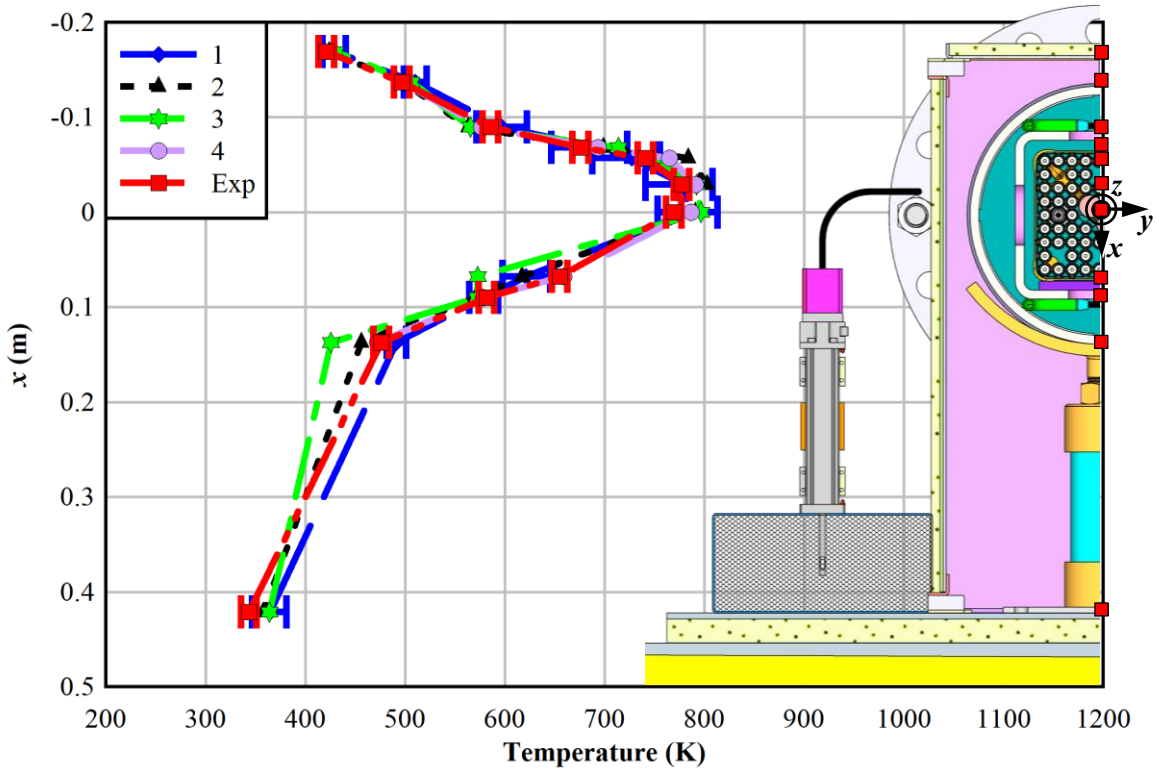

Figure 3.30 Vertical temperature profile data comparison for the 5.0 kW, 100 kPa air test.

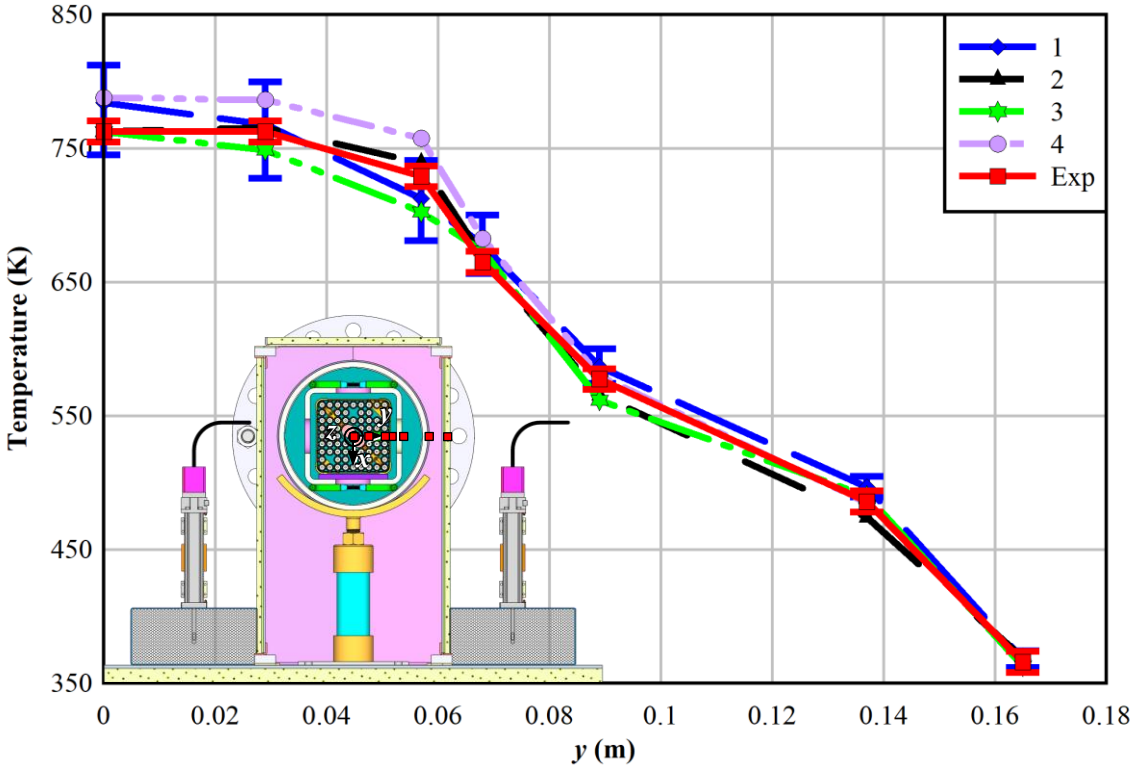

Figure 3.31 Horizontal temperature profile data comparison for the 5.0 kW, 100 kPa air test.

3.3 Root Mean Square of Normalized Error Comparisons

The error found in the comparison of modeling results to experimental results for the comparison metrics (PCT, PCT axial location, temperature profiles in the *x*, *y*, and *z* directions, and air mass flow rate), normalized by the experimental result, is calculated as the difference in modeling and experimental results divided by the experimental result. Equation 3-1 expresses this, where ε_x is the normalized error in the comparison metric "x" (not to be confused with the *x*-coordinate) and x_E and x_M refer to the experimental and model results, respectively.

$$\varepsilon_x = \frac{x_M - x_E}{x_E} \tag{3-1}$$

Calculation of the root mean square (RMS) of the normalized errors for the comparison metrics across the ten test cases quantifies the closeness of fit of each model's results to the experimental data, as shown in Equation 3-2.

$$\mathrm{RMS}(\varepsilon_x) = \sqrt{\sum_{n=1}^{N} \frac{\varepsilon_{x,n}^{\,2}}{N}} \tag{3-2}$$

Here, "*n*" refers to a test case with a defined power and pressure (see Table 1.1 for the test cases) and "*N*" is the total number of test cases, which is 10 in this report. A root mean square of the normalized error that gives a value close to 0 indicates that the model results closely match the experimental data.

One of the models in these comparisons has a boundary condition set at the pressure vessel. Therefore, no information from the vault, including temperatures and air mass flow rates, is available from this model. This section presents a comparison of the root mean squares of the normalized errors of the temperature

data with the exclusion of the data from the vault. The root mean squares of the normalized errors for the peak cladding temperature, the PCT axial location, the axial temperature profile along the centerline, the vertical temperature profile, and the horizontal temperature profile are shown in Table 3.2 through Table 3.8. In these tables, the model calibration test cases are highlighted in gray. The raw data these error values are calculated from can be found in Appendix F.

3.3.1 Peak Cladding Temperature Measurement Normalized Errors

The peak cladding temperature measurement normalized errors across all tests are presented here. The PCT normalized error is shown in Table 3.2, and the PCT axial location normalized error is shown in Table 3.3. The bottom row of each table is the RMS of the normalized errors across all tests for each model, which serves as a summary metric that can be used to compare the goodness of fit of the models. It is acknowledged that the PCT location metric initially proposed in the HDCS update report [Lindgren *et al*., 2019] was to include the transverse location of the PCT in x and y coordinates. However, the thermal gradient across the x and y coordinates is relatively small and comparable to the uncertainty in temperature measurements across the entirety of the fuel assembly cross-section. Therefore, only the axial (z) location of the PCT is considered in this analysis.

Table 3.2 Peak cladding temperature normalized error.

Conditions / Model			1	2	3	4
Power (kW)	**Pressure (kPa)**	**Fill Gas**	$\varepsilon_{PCT} = \frac{PCT_{Model} - PCT_{Exp}}{PCT_{Exp}}$			
0.5	100	Helium	-0.0055	-0.0035	-0.0058	-0.0064
1.0	100	Helium	-0.0032	-0.0092	-0.0100	-0.0135
2.5	100	Helium	-0.0017	-0.0064	-0.0082	-0.0161
5.0	100	Helium	0.0084	0.0101	0.0056	-0.0095
0.5	800	Helium	-0.0118	0.0034	0.0023	0.0046
5.0	800	Helium	0.0093	0.0146	0.0100	0.0093
0.5	100	Air	-0.0275	-0.0178	-0.0087	0.0049
1.0	100	Air	-0.0204	0.0012	0.0059	0.0107
2.5	100	Air	-0.0118	0.0155	0.0227	-0.0022
5.0	100	Air	0.0071	0.0487	0.0554	0.0164
RMS(ε_{PCT})			**0.013**	**0.018**	**0.020**	**0.010**

Table 3.3 Peak cladding temperature axial location normalized error.

Conditions / Model			1	2	3	4
Power (kW)	**Pressure (kPa)**	**Fill Gas**	$\varepsilon_{z_{PCT}} = \frac{z_{PCT,Model} - z_{PCT,Exp}}{z_{PCT,Exp}}$			
0.5	100	Helium	0.3676	0.0000	0.2459	0.5511
1.0	100	Helium	0.3676	0.0000	0.0000	0.5511
2.5	100	Helium	0.3742	0.0000	0.0000	0.5511
5.0	100	Helium	0.3742	-0.2541	-0.2541	0.5511
0.5	800	Helium	0.2694	0.5000	0.2459	0.5511
5.0	800	Helium	0.2825	0.0000	0.0000	0.5511
0.5	100	Air	0.2432	-0.2541	-0.2505	0.5511
1.0	100	Air	0.2432	-0.2508	-0.5003	0.5511
2.5	100	Air	1.5519	0.4984	-0.0007	2.1021
5.0	100	Air	1.6043	0.4984	-0.0007	2.1021
RMS($\varepsilon_{z_{PCT}}$)			**0.762**	**0.306**	**0.223**	**1.061**

3.3.2 Temperature Profile Normalized Errors

The axial and transverse (vertical and horizontal) normalized errors across all tests are presented here. The axial temperature profile normalized error along the centerline (water rod WEU, see Figure 2.9) is shown in Table 3.4. The vertical temperature profile includes vault information, so the normalized errors are split into two tables. Table 3.5 includes the vault data (for a total of 11 data points), and Table 3.6 excludes the vault data (for a total of 9 data points). Similarly, the horizontal temperature profile normalized errors are split into normalized error tables including and excluding the vault data (Table 3.7 and Table 3.8, respectively), which accounts for one data point in the horizontal profile.

Table 3.4 Axial temperature profile normalized error.

Conditions / Model			1	2	3	4
Power (kW)	**Pressure (kPa)**	**Fill Gas**	$\varepsilon_{T(z)} = \sqrt{\sum_{i=1}^{5} \frac{\left[(T_{z,\mathrm{Model},i} - T_{z,\mathrm{Exp},i})/T_{z,\mathrm{Exp},i}\right]^2}{5}}$, where i denotes axial locations			
0.5	100	Helium	0.0042	0.0127	0.0055	0.0110
1.0	100	Helium	0.0074	0.0179	0.0082	0.0179
2.5	100	Helium	0.0134	0.0201	0.0075	0.0259
5.0	100	Helium	0.0220	0.0193	0.0114	0.0276
0.5	800	Helium	0.0159	0.0108	0.0107	0.0211
5.0	800	Helium	0.0147	0.0246	0.0223	0.0620
0.5	100	Air	0.0349	0.0356	0.0136	0.0358
1.0	100	Air	0.0336	0.0412	0.0182	0.0454
2.5	100	Air	0.0167	0.0384	0.0224	0.0588
5.0	100	Air	0.0190	0.0443	0.0381	0.0566
RMS($\varepsilon_{T(z)}$)			**0.020**	**0.029**	**0.018**	**0.040**

Table 3.5 Vertical temperature profile normalized error including vault data.

Conditions / Model			1	2	3
Power (kW)	**Pressure (kPa)**	**Fill Gas**	$\varepsilon_{T(x)} = \sqrt{\sum_{i=1}^{11} \frac{\left[(T_{x,\mathrm{Model},i} - T_{x,\mathrm{Exp},i})/T_{x,\mathrm{Exp},i}\right]^2}{11}}$, where i denotes vertical locations		
0.5	100	Helium	0.0068	0.0063	0.0107
1.0	100	Helium	0.0076	0.0106	0.0175
2.5	100	Helium	0.0116	0.0165	0.0285
5.0	100	Helium	0.0249	0.0257	0.0401
0.5	800	Helium	0.0057	0.0036	0.0074
5.0	800	Helium	0.0350	0.0256	0.0396
0.5	100	Air	0.0153	0.0134	0.0175
1.0	100	Air	0.0162	0.0153	0.0204
2.5	100	Air	0.0178	0.0257	0.0336
5.0	100	Air	0.0276	0.0352	0.0478
RMS($\varepsilon_{T(x)}$)			**0.019**	**0.020**	**0.029**

Table 3.6 Vertical temperature profile normalized error excluding vault data.

Conditions / Model			1	2	3	4
Power (kW)	**Pressure (kPa)**	**Fill Gas**	$\varepsilon_{T(x)} = \sqrt{\sum_{i=1}^{9} \frac{\left[(T_{x,\text{Model},i} - T_{x,\text{Exp},i})/T_{x,\text{Exp},i}\right]^2}{9}}$, where *i* denotes vertical locations			
0.5	100	Helium	-0.0027	-0.0029	-0.0001	-0.0008
1.0	100	Helium	-0.0033	-0.0071	-0.0077	-0.0101
2.5	100	Helium	-0.0041	-0.0041	-0.0031	-0.0090
5.0	100	Helium	-0.0144	-0.0033	-0.0119	-0.0081
0.5	800	Helium	-0.0102	-0.0041	-0.0098	-0.0094
5.0	800	Helium	-0.0033	-0.0071	-0.0077	-0.0101
0.5	100	Air	-0.0041	-0.0041	-0.0031	-0.0090
1.0	100	Air	-0.0090	-0.0067	-0.0072	-0.0085
2.5	100	Air	-0.0015	-0.0140	-0.0285	-0.0057
5.0	100	Air	-0.0027	-0.0029	-0.0001	-0.0008
RMS($\varepsilon_{T(x)}$)			**0.007**	**0.007**	**0.012**	**0.008**

Table 3.7 Horizontal temperature profile normalized error including vault data.

Conditions / Model			1	2	3
Power (kW)	**Pressure (kPa)**	**Fill Gas**	$\varepsilon_{T(y)} = \sqrt{\sum_{i=1}^{7} \frac{\left[(T_{y,\text{Model},i} - T_{y,\text{Exp},i})/T_{y,\text{Exp},i}\right]^2}{7}}$, where *i* denotes horizontal locations		
0.5	100	Helium	0.0073	0.0040	0.0065
1.0	100	Helium	0.0096	0.0083	0.0113
2.5	100	Helium	0.0122	0.0109	0.0131
5.0	100	Helium	0.0210	0.0127	0.0120
0.5	800	Helium	0.0086	0.0034	0.0034
5.0	800	Helium	0.0220	0.0165	0.0170
0.5	100	Air	0.0206	0.0155	0.0175
1.0	100	Air	0.0180	0.0140	0.0181
2.5	100	Air	0.0192	0.0175	0.0279
5.0	100	Air	0.0192	0.0137	0.0195
RMS($\varepsilon_{T(y)}$)			**0.017**	**0.013**	**0.016**

Table 3.8 Horizontal temperature profile normalized error excluding vault data.

Conditions / Model			1	2	3	4
Power (kW)	**Pressure (kPa)**	**Fill Gas**	$\varepsilon_{T(y)} = \sqrt{\sum_{i=1}^{6} \frac{\left[(T_{y,\text{Model},i} - T_{y,\text{Exp},i})/T_{y,\text{Exp},i}\right]^2}{6}}$, where i denotes horizontal locations			
0.5	100	Helium	0.0074	0.0040	0.0070	0.0049
1.0	100	Helium	0.0102	0.0089	0.0122	0.0107
2.5	100	Helium	0.0132	0.0117	0.0140	0.0101
5.0	100	Helium	0.0226	0.0130	0.0129	0.0039
0.5	800	Helium	0.0091	0.0031	0.0031	0.0057
5.0	800	Helium	0.0234	0.0148	0.0180	0.0150
0.5	100	Air	0.0222	0.0166	0.0189	0.0168
1.0	100	Air	0.0194	0.0149	0.0193	0.0238
2.5	100	Air	0.0207	0.0187	0.0301	0.0173
5.0	100	Air	0.0206	0.0145	0.0208	0.0268
RMS($\varepsilon_{T(y)}$)			**0.018**	**0.013**	**0.017**	**0.015**

3.3.3 Air Mass Flow Rate Normalized Errors

The air mass flow rate normalized error from the models that include vault data is presented in Table 3.9.

Table 3.9 Air mass flow rate normalized error.

Conditions / Model			1	2	3
Power (kW)	**Pressure (kPa)**	**Fill Gas**	$\varepsilon_{\dot{m}} = \frac{\dot{m}_{\text{Model}} - \dot{m}_{\text{Exp}}}{\dot{m}_{\text{Exp}}}$		
0.5	100	Helium	-0.1657	-0.1784	-0.2091
1.0	100	Helium	-0.0729	0.0241	0.0038
2.5	100	Helium	-0.0731	-0.0315	-0.0591
5.0	100	Helium	-0.0237	-0.0413	-0.0715
0.5	800	Helium	-0.1384	-0.1602	-0.1845
5.0	800	Helium	-0.0047	-0.0312	-0.0637
0.5	100	Air	-0.0318	0.0414	0.0271
1.0	100	Air	-0.0570	-0.0309	0.0731
2.5	100	Air	-0.0508	-0.0151	-0.0444
5.0	100	Air	-0.0550	-0.0135	-0.0416
RMS($\varepsilon_{\dot{m}}$)			**0.082**	**0.081**	**0.100**

3.3.4 Combined Root Mean Square of the Normalized Errors

This section presents the combined root mean square of the normalized errors across all parameters listed in Section 3.3.3 to provide an overall quantitative measure of the goodness of fit of model results to experimental data. As a reminder, the raw data the errors are calculated from can be found in Appendix F.

The inclusion of vault data can be used to generate a comprehensive comparison between the models that incorporate the vault through a combined RMS table of the normalized errors, as calculated in Equation 3-3.

$$\text{Combined RMS of Normalized Errors} = \sqrt{\sum_{x=1}^{X} \frac{[\text{RMS}(\varepsilon_x)]^2}{X}} \tag{3-3}$$

Here, "x" refers to a comparison metric (again, not to be confused with the *x*-coordinate) and "X" refers to the total number of comparison metrics, which varies per table.

The combined RMS of the normalized errors, which includes vault data, is shown in Table 3.10. These tables are based on the RMS of the normalized errors calculated in Table 3.2 through Table 3.4, Table 3.5, Table 3.7, and Table 3.9.

Table 3.10 Combined root mean square of the normalized errors including vault data.

Model / RMS	1	2	3
$\text{RMS}(\varepsilon_{PCT})$	0.013	0.018	0.020
$\text{RMS}(\varepsilon_{z_{PCT}})$	0.762	0.306	0.223
$\text{RMS}(\varepsilon_{T(z)})$	0.020	0.029	0.018
$\text{RMS}(\varepsilon_{T(x)})$	0.018	0.020	0.029
$\text{RMS}(\varepsilon_{T(y)})$	0.018	0.013	0.017
$\text{RMS}(\varepsilon_{\dot{m}})$	0.082	0.081	0.100
Combined RMS of Normalized Errors	**0.313**	**0.130**	**0.101**

A separate combined RMS table was generated that excludes the vault data and air mass flow rate. The combined RMS table includes the RMS of the normalized errors calculated in Table 3.2 through Table 3.4, Table 3.6, and Table 3.8.

Table 3.11 Combined root mean square of the normalized errors excluding vault data and air mass flow rate.

Model / RMS	1	2	3	4
$\text{RMS}(\varepsilon_{PCT})$	0.013	0.018	0.020	0.010
$\text{RMS}(\varepsilon_{z_{PCT}})$	0.762	0.306	0.223	1.061
$\text{RMS}(\varepsilon_{T(z)})$	0.020	0.029	0.018	0.040
$\text{RMS}(\varepsilon_{T(x)})$	0.018	0.020	0.029	0.017
$\text{RMS}(\varepsilon_{T(y)})$	0.018	0.013	0.017	0.015
Combined RMS of Normalized Errors	**0.341**	**0.138**	**0.102**	**0.475**

Considering the relatively flat axial temperature profiles, small temperature gradients resulted in large deviations of the model PCT location from the experimentally determined location, which introduces a large uncertainty in the PCT location. Furthermore, the discrete nature of the experimental axial temperature data, based on thermocouples spaced at least 6 inches apart, may not resolve the PCT location as accurately as a continuous temperature band across the axial length. The RMS of the normalized error of PCT location thus dominates the combined RMS of the normalized errors for each model. The following two tables show the result of excluding the PCT location as a metric – Table 3.12 shows the combined RMS of the normalized errors including the vault data, while Table 3.13 shows the combined RMS of the normalized errors excluding the vault data and air mass flow rate.

Table 3.12 Combined root mean square of the normalized errors including vault data and excluding PCT location.

RMS \ Model	1	2	3
RMS(ε_{PCT})	0.013	0.018	0.020
RMS($\varepsilon_{T(z)}$)	0.020	0.029	0.018
RMS($\varepsilon_{T(x)}$)	0.018	0.020	0.029
RMS($\varepsilon_{T(y)}$)	0.018	0.013	0.017
RMS($\varepsilon_{\dot{m}}$)	0.082	0.081	0.100
Combined RMS of the Normalized Errors	**0.040**	**0.041**	**0.049**

Table 3.13 Combined root mean square of the normalized errors excluding vault data, air mass flow rate, and PCT location.

RMS \ Model	1	2	3	4
RMS(ε_{PCT})	0.013	0.018	0.020	0.010
RMS($\varepsilon_{T(z)}$)	0.020	0.029	0.018	0.040
RMS($\varepsilon_{T(x)}$)	0.018	0.020	0.029	0.017
RMS($\varepsilon_{T(y)}$)	0.018	0.013	0.017	0.015
Combined RMS of the Normalized Errors	**0.017**	**0.021**	**0.022**	**0.023**

3.4 Validation Uncertainty

The institution that generated the results for model 1 provided upper and lower validation uncertainty bounds for all comparison metrics, including the peak cladding temperature, the peak cladding temperature axial location, the temperature profile data points (*x*, *y*, and *z*), and the air mass flow rate, so a separate analysis was conducted to explore the effects of the inclusion of modeling validation uncertainties in the normalized error analysis. This analysis, which was derived from ASME V&V 20-2009 [ASME, 2009], involves the application of experimental and modeling uncertainties in the normalized error of the comparison metrics of interest. The validation uncertainty in the normalized error for each metric is calculated using Equation 3-4 [Taylor, 1996; Ifan and Hughes, 2010]:

$$U_{\varepsilon_x} = \sqrt{\left(\frac{\partial \varepsilon_x}{\partial x_E}\right)^2 \cdot U_{x_E}^2 + \left(\frac{\partial \varepsilon_x}{\partial x_M}\right)^2 \cdot U_{x_M}^2} \tag{3-4}$$

Here, the validation (95%) uncertainty in the normalized error U_{ε_x} is found by taking the square root of the sum of the squares of two terms – the partial derivative of the normalized error ε_x with respect to the experimental result multiplied by the experimental expanded uncertainty U_{x_E}, and the partial derivative of the normalized error with respect to the modeling result multiplied by the simulation (model) expanded uncertainty U_{x_M}. For each data point, the model expanded uncertainty was chosen to be either the upper or the lower simulation uncertainty bound (values provided in Appendix B). The upper simulation uncertainty bound and the lower experimental uncertainty bound was chosen to calculate Equation 3-4 if the model value for a given parameter x_M was less than the experimental value x_E of that parameter. If x_M was greater than x_E, the lower simulation uncertainty bound and the upper experimental uncertainty bound were chosen to calculate Equation 3-4. Because model 1 includes vault data, the validation uncertainty analysis also includes vault data.

The validation uncertainties in the normalized error were used to generate the validation criterion. For the normalized error tables in the following section, each value is divided by the test-specific validation uncertainty (as calculated by Equation 3-4). The model can thus be considered validated if the combined RMS of the normalized errors that are each divided by their own test-specific validation uncertainties is less than or equal to 1.

3.4.1 Validation Uncertainty in Peak Cladding Temperature Measurement Normalized Errors

The validation uncertainties for model 1 applied to the peak cladding temperature measurement normalized errors across all tests are presented here. The validation uncertainties in PCT normalized error and PCT axial location normalized error are shown in Table 3.14 and Table 3.16, respectively. The PCT and PCT axial location normalized errors (Table 3.2 and Table 3.3), divided by the validation uncertainties, are shown in Table 3.15 and Table 3.17, respectively.

The bottom row of the validation uncertainty tables shows the RMS of the validation uncertainties across all tests for each model, as shown in Equation 3-5.

$$\mathrm{RMS}(U_{\varepsilon_x}) = \sqrt{\sum_{n=1}^{N} \frac{U_{\varepsilon_{x,n}}{}^2}{N}} \tag{3-5}$$

The bottom row of the tables that present the normalized errors divided by the validation uncertainty shows the RMS of these normalized errors across all tests for each model, as shown in Equation 3-6.

$$\mathrm{RMS}(\varepsilon_x / U_{\varepsilon_x}) = \sqrt{\sum_{n=1}^{N} \frac{(\varepsilon_{x,n} / U_{\varepsilon_x,n})^2}{N}} \tag{3-6}$$

As a reminder, "x" in Equation 3-5 and Equation 3-6 refers to a comparison metric (PCT, PCT axial location, etc.) and is not to be confused with the *x*-coordinate. The summation in both equations is over "*n*", which refers to a test case, and "*N*" is the total number of test cases considered in this report, which is 10.

The tables that show the normalized errors normalized by the validation uncertainty are heat mapped. Green represents a normalized error divided by the validation uncertainty that is less than or equal to 1 (which serves as the pass criterion for model validation). Red represents a normalized error divided by the validation uncertainty greater than 1 (which serves as the fail criterion for model validation).

Table 3.14 Validation uncertainty in peak cladding temperature normalized error.

Conditions			
Power (kW)	**Pressure (kPa)**	**Fill Gas**	**Model 1**
0.5	100	Helium	0.0179
1.0	100	Helium	0.0185
2.5	100	Helium	0.0213
5.0	100	Helium	0.0328
0.5	800	Helium	0.0170
5.0	800	Helium	0.0279
0.5	100	Air	0.0214
1.0	100	Air	0.0243
2.5	100	Air	0.0325
5.0	100	Air	0.0520
RMS($U_{\varepsilon_{PCT}}$)			**0.028**

Table 3.15 Peak cladding temperature normalized error divided by validation uncertainty.

Conditions			
Power (kW)	**Pressure (kPa)**	**Fill Gas**	**Model 1**
0.5	100	Helium	0.31
1.0	100	Helium	0.17
2.5	100	Helium	0.08
5.0	100	Helium	0.26
0.5	800	Helium	0.70
5.0	800	Helium	0.33
0.5	100	Air	1.28
1.0	100	Air	0.84
2.5	100	Air	0.36
5.0	100	Air	0.14
RMS(ε_{PCT} / $U_{\varepsilon_{PCT}}$)			**0.57**

Table 3.16 Validation uncertainty in peak cladding temperature axial location normalized error.

Conditions			
Power (kW)	**Pressure (kPa)**	**Fill Gas**	**Model 1**
0.5	100	Helium	1.518
1.0	100	Helium	1.138
2.5	100	Helium	0.852
5.0	100	Helium	0.973
0.5	800	Helium	1.419
5.0	800	Helium	0.787
0.5	100	Air	0.990
1.0	100	Air	0.830
2.5	100	Air	4.085
5.0	100	Air	4.347
RMS($U_{\varepsilon_{z_{PCT}}}$)			**2.13**

Table 3.17 Peak cladding temperature axial location normalized error divided by validation uncertainty.

Conditions			
Power (kW)	**Pressure (kPa)**	**Fill Gas**	**Model 1**
0.5	100	Helium	0.24
1.0	100	Helium	0.32
2.5	100	Helium	0.44
5.0	100	Helium	0.38
0.5	800	Helium	0.19
5.0	800	Helium	0.36
0.5	100	Air	0.25
1.0	100	Air	0.29
2.5	100	Air	0.38
5.0	100	Air	0.37
RMS($\varepsilon_{z_{PCT}} / U_{\varepsilon_{z_{PCT}}}$)			**0.36**

3.4.2 Validation Uncertainty in Temperature Profile Normalized Errors

The validation uncertainties for model 1 applied to the temperature profile normalized errors across all tests are presented here. The validation uncertainties in the axial, vertical, and horizontal temperature profile normalized errors are shown in Table 3.18, Table 3.20, and Table 3.22, respectively. The axial (Table 3.4), vertical (Table 3.5), and horizontal (Table 3.7) temperature profile normalized errors divided by the validation uncertainties are shown in Table 3.19, Table 3.21, and Table 3.23, respectively.

Table 3.18 Validation uncertainty in axial temperature profile normalized error.

Conditions			
Power (kW)	**Pressure (kPa)**	**Fill Gas**	**Model 1**
0.5	100	Helium	0.0195
1.0	100	Helium	0.0214
2.5	100	Helium	0.0281
5.0	100	Helium	0.0355
0.5	800	Helium	0.0174
5.0	800	Helium	0.0284
0.5	100	Air	0.0234
1.0	100	Air	0.0334
2.5	100	Air	0.0411
5.0	100	Air	0.0531
RMS($U_{\varepsilon_{T(z)}}$)			**0.032**

Table 3.19 Axial temperature profile normalized error divided by validation uncertainty.

Conditions			
Power (kW)	**Pressure (kPa)**	**Fill Gas**	**Model 1**
0.5	100	Helium	0.22
1.0	100	Helium	0.34
2.5	100	Helium	0.48
5.0	100	Helium	0.62
0.5	800	Helium	0.92
5.0	800	Helium	0.52
0.5	100	Air	1.49
1.0	100	Air	1.01
2.5	100	Air	0.41
5.0	100	Air	0.36
RMS($\varepsilon_{T(z)}$ / $U_{\varepsilon_{T(z)}}$)			**0.74**

Table 3.20 Validation uncertainty in vertical temperature profile normalized error.

Conditions			
Power (kW)	**Pressure (kPa)**	**Fill Gas**	**Model 1**
0.5	100	Helium	0.0195
1.0	100	Helium	0.0207
2.5	100	Helium	0.0257
5.0	100	Helium	0.0333
0.5	800	Helium	0.0180
5.0	800	Helium	0.0300
0.5	100	Air	0.0216
1.0	100	Air	0.0252
2.5	100	Air	0.0347
5.0	100	Air	0.0447
RMS($U_{\varepsilon_{T(x)}}$)			**0.028**

Table 3.21 Vertical temperature profile normalized error divided by the validation uncertainty.

Conditions			
Power (kW)	**Pressure (kPa)**	**Fill Gas**	**Model 1**
0.5	100	Helium	0.35
1.0	100	Helium	0.37
2.5	100	Helium	0.45
5.0	100	Helium	0.75
0.5	800	Helium	0.32
5.0	800	Helium	1.17
0.5	100	Air	0.71
1.0	100	Air	0.64
2.5	100	Air	0.51
5.0	100	Air	0.62
RMS($\varepsilon_{T(x)}$ / $U_{\varepsilon_{T(x)}}$)			**0.64**

Table 3.22 Validation uncertainty in horizontal temperature profile normalized error.

Conditions			
Power (kW)	**Pressure (kPa)**	**Fill Gas**	**Model 1**
0.5	100	Helium	0.0193
1.0	100	Helium	0.0205
2.5	100	Helium	0.0245
5.0	100	Helium	0.0281
0.5	800	Helium	0.0177
5.0	800	Helium	0.0234
0.5	100	Air	0.0211
1.0	100	Air	0.0240
2.5	100	Air	0.0329
5.0	100	Air	0.0387
RMS($U_{\varepsilon_{T(y)}}$)			**0.026**

Table 3.23 Horizontal temperature profile normalized error divided by the validation uncertainty.

Conditions			
Power (kW)	**Pressure (kPa)**	**Fill Gas**	**Model 1**
0.5	100	Helium	0.38
1.0	100	Helium	0.47
2.5	100	Helium	0.50
5.0	100	Helium	0.75
0.5	800	Helium	0.49
5.0	800	Helium	0.94
0.5	100	Air	0.97
1.0	100	Air	0.75
2.5	100	Air	0.58
5.0	100	Air	0.50
RMS($\varepsilon_{T(y)}$ / $U_{\varepsilon_{T(y)}}$)			**0.66**

3.4.3 Validation Uncertainty in Air Mass Flow Rate Normalized Errors

The validation uncertainties for model 1 applied to the air mass flow rate normalized errors across all tests are presented here. The validation uncertainties in the air mass flow rate normalized errors are shown in Table 3.24 and the air mass flow rate normalized errors divided by the validation uncertainties are shown in Table 3.25.

Table 3.24 Validation uncertainty in air mass flow rate normalized error.

Conditions			
Power (kW)	**Pressure (kPa)**	**Fill Gas**	**Model 1**
0.5	100	Helium	0.0810
1.0	100	Helium	0.0658
2.5	100	Helium	0.0447
5.0	100	Helium	0.0543
0.5	800	Helium	0.0747
5.0	800	Helium	0.0680
0.5	100	Air	0.0900
1.0	100	Air	0.0682
2.5	100	Air	0.0433
5.0	100	Air	0.0431
RMS($U_{\varepsilon_{\dot{m}}}$)			**0.065**

Table 3.25 Air mass flow rate normalized error divided by the validation uncertainty.

Conditions			
Power (kW)	**Pressure (kPa)**	**Fill Gas**	**Model 1**
0.5	100	Helium	2.05
1.0	100	Helium	1.11
2.5	100	Helium	1.64
5.0	100	Helium	0.44
0.5	800	Helium	1.85
5.0	800	Helium	0.07
0.5	100	Air	0.35
1.0	100	Air	0.84
2.5	100	Air	1.17
5.0	100	Air	1.28
RMS($\varepsilon_{\dot{m}}$ / $U_{\varepsilon_{\dot{m}}}$)			**1.25**

3.4.4 Combined Root Mean Square of the Normalized Errors Divided by Validation Uncertainty

This section presents the combined root mean square of the normalized errors divided by their validation (95%) uncertainties of all comparison metrics for model 1's results. This analysis provides an alternative measure of the goodness of fit of model results to experimental data and is derived from ASME V&V 20-2009 [ASME, 2009]. As stated previously, the model can be considered validated if the combined RMS of the normalized errors divided by their validation uncertainties is less than or equal to 1, which is indicated by the pass/fail heat mapping (green if less than or equal to 1, red if greater than 1). Based on the combined RMS metric, model 1 is considered validated as shown in Table 3.26. While it may be argued that the model failed to produce validated metrics across all test conditions, recall that the model-predicted PCT, which is the prime metric for these types of analyses, was validated for nine out of ten cases.

Table 3.26 Combined root mean square of the normalized errors divided by their validation uncertainties.

Metric	RMS of Normalized Errors/ U_{ε_x}
PCT (K)	0.57
PCT Axial Location (m)	0.36
T(*z*) (K)	0.74
T(*x*) (K)	0.64
T(*y*) (K)	0.66
$\dot{m}$ (kg/s)	1.25
Combined RMS of Normalized Errors / U_{ε_x}	**0.75**

4 SUMMARY

In this blind model validation exercise, three institutions (NRC, PNNL, and ENUSA) provided their own unique approaches to capturing the temperature profiles and air mass flow rates within the BWR dry cask simulator in the horizontal configuration. For these comparisons, ten test cases of the horizontal dry cask simulator were considered, defined by three independent variables – fuel assembly decay heat (0.5 kW, 1 kW, 2.5 kW, and 5 kW), internal backfill pressure (100 kPa and 800 kPa), and backfill gas (helium and air). For all cases, the modelers obtained the peak cladding temperatures, the axial temperature profiles, the vertical and horizontal temperature profiles across two different axial locations, and the air mass flow rates external to the assembly. The different modeling codes used by each institution encompassed a variety of computational approaches to determining these target variables – these approaches were characterized mainly by the software used (ANSYS/Fluent, STAR-CCM+, or COBRA-SFS) and the use of either porous media or explicit fuel models to describe the horizontal dry cask simulator. A total of 4 different models from the 3 institutions were compared.

The plots provided in Chapter 3 show the axial and transverse temperature profiles obtained from the dry cask simulator experiments in the horizontal configuration and the corresponding models used to describe the thermal-hydraulic behavior of this system. The tables provided in Chapter 3 illustrate the closeness of fit of the model data to the experiment data through root mean square calculations of the error in peak cladding temperatures, peak cladding temperature locations, axial temperature profiles, vertical transverse temperature profiles across the z = 1.219 m (48 in.) axial location, horizontal transverse temperature profiles across the z = 1.829 m (72 in.) axial location, and air mass flow rates for the ten test cases, normalized by the experimental results.

The root mean square of the normalized errors presented in Chapter 3 served as a quantitative comparison of the goodness of fit of the model results to the experimental data. Due to the relatively flat axial temperature profiles, small temperature gradients resulted in large deviations of all models' PCT axial location from the experimental PCT axial location. When the PCT axial location normalized error is excluded in the combined RMS of the normalized errors that considers PCT, the temperature profiles, and the air mass flow rates, the data from all models fits the experimental data to within 5%. When the vault information is excluded, the data from all models fits the experimental data to within 2.5%.

Based on the combined RMS of the normalized errors, model 1 offered the best overall fit to the experimental data. This was the case with both including and excluding the vault information. When including the vault information and excluding the PCT axial location normalized error (Table 4.1), model 1's combined RMS of the normalized errors was 0.040, while model 2 and model 3 produced very similar values for the combined RMS of the normalized errors (0.041 and 0.049, respectively). When excluding the vault information (Table 4.2), model 1's combined RMS of the normalized errors was 0.017. The combined RMS of the normalized errors for models 2, 3, and 4 were slightly greater at 0.021, 0.022, and 0.023, respectively.

Table 4.1 Summary table of combined root mean square of the normalized errors including vault data.

RMS \ Model	1	2	3
RMS(ε_{PCT})	0.013	0.018	0.020
RMS($\varepsilon_{T(z)}$)	0.020	0.029	0.018
RMS($\varepsilon_{T(x)}$)	0.018	0.020	0.029
RMS($\varepsilon_{T(y)}$)	0.018	0.013	0.017
RMS($\varepsilon_{\dot{m}}$)	0.082	0.081	0.100
Combined RMS of Normalized Errors	**0.040**	**0.041**	**0.049**

Table 4.2 Summary table of combined root mean square of the normalized errors excluding vault data and air mass flow rate.

RMS \ Model	1	2	3	4
RMS(ε_{PCT})	0.013	0.018	0.020	0.010
RMS($\varepsilon_{T(z)}$)	0.020	0.029	0.018	0.040
RMS($\varepsilon_{T(x)}$)	0.018	0.020	0.029	0.017
RMS($\varepsilon_{T(y)}$)	0.018	0.013	0.017	0.015
Combined RMS of Normalized Errors	**0.017**	**0.021**	**0.022**	**0.023**

The previous DCS study [Pulido *et al.*, 2020] demonstrated the capability of COBRA-SFS in modeling vertically oriented dry storage systems. However, the COBRA-SFS models for ventilated horizontal storage systems require canister surface temperature boundary conditions calculated by external models. The steady state COBRA-SFS results for ventilated horizontal systems are therefore strongly dependent on external modeling codes. The coupling between the codes is critical for ventilated horizontal storage systems, as COBRA-SFS was developed for vertical systems.

The plots in Chapter 3 include simulation uncertainties provided by the institution who generated the results for model 1. This was an extensive effort that captured the effect of introducing experimental and simulation uncertainty bounds in the comparison of model results to experimental data. The method, which was derived from ASME V&V 20-2009 [ASME, 2009], is explored in the validation uncertainty section in Chapter 3, which shows how the uncertainty quantification can be used to provide a better measure of model prediction accuracies. Overall, this model validation method takes both experimental and simulation uncertainties into account and serves as an example of how the model validation uncertainty quantification can be further explored. By definition, model 1 is considered validated if the combined RMS of the normalized errors divided by their validation uncertainties is less than or equal to 1, and this was shown to be the case (Table 4.3).

Table 4.3 Summary table of combined root mean square of the normalized errors divided by the validation uncertainty.

Metric	RMS of Normalized Errors /U_ε
PCT (K)	0.57
PCT Axial Location (m)	0.36
T(z) (K)	0.74
T(x) (K)	0.64
T(y) (K)	0.66
$\dot{m}$ (kg/s)	1.25
Combined RMS of Normalized Errors / U_ε	**0.75**

REFERENCES

American National Standards Institute, "American National Standard for Radioactive Materials – Leakage Tests on Packages for Shipment," ANSI N14.5-2014, New York, NY, June 2014.

American Society of Mechanical Engineers, "ASME V&V 20-2009 – Standard for Verification and Validation in Computational Fluid Dynamics and Heat Transfer," New York, NY, November 2009.

ASTM International, "Standard Specification for Temperature-Electromotive Force (emf) Tables for Standardized Thermocouples," E230/E230M-17, West Conshohocken, PA, November 2017.

Bates, J.M., "Single PWR Spent Fuel Assembly Heat Transfer Data for Computer Code Evaluations," PNL-5571, Pacific Northwest Laboratory, Richland, Washington, January 1986.

Creer, J.M., T.E. Michener M.A. McKinnon, J.E. Tanner, E.R. Gilbert, R.L. Goodman, "The TN-24P PWR Spent Fuel Storage Cask: Testing and Analyses," EPRI NP-5128 Proj. 2406-4, PNL-6054, Pacific Northwest Laboratory, Richland, Washington, April 1987.

Das, K., D. Basu, and G. Walter, "Thermal Analysis of Horizontal Storage Casks for Extended Storage Applications," NUREG/CR-7191, Center for Nuclear Waste Regulatory Analyses Southwest Research Institute, San Antonio, Texas, December 2014.

Durbin, S.G. and E.R. Lindgren, "Thermal-Hydraulic Experiments Using a Dry Cask Simulator," NUREG/CR-7250, Sandia National Laboratories, Albuquerque, New Mexico, October 2018.

Dziadosz, D., E.V. Moore, J.M. Creer, R.A. McCann, M.A. McKinnon, J.E. Tanner, E.R. Gilbert, R.L. Goodman, D.H. Schoonen, M. Jensen, and C. Mullen, "The Castor-V/21 PWR Spent-Fuel Storage Cask: Testing and Analyses," Electrical Power Research Institute, EPRI NP-4887, Project 2406-4, PNL-5917, Pacific Northwest Laboratory, Richland, Washington, November 1986.

Ifan, H. and T. Hughes, Measurements And Their Uncertainties: A Practical Guide To Modern Error Analysis, Oxford University Press, 1st Ed., October 2010.

Irino, M., M. Oohashi, T. Irie, and T. Nishikawa, "Study on Surface Temperatures of Fuel Pins in Spent Fuel Dry Shipping/Storage Casks," IAEA-SM-286/139P, in Proceedings of Packaging and Transportation of Radioactive Materials (PATRAM '86), Volume 2, p. 585, International Atomic Energy Agency Vienna, 1987.

Lindgren, E.R. and S.G. Durbin, "Characterization of Thermal-Hydraulic and Ignition Phenomena in Prototypic, Full-Length Boiling Water Reactor Spent Fuel Pool Assemblies after a Complete Loss-of-Coolant Accident," NUREG/CR-7143, SAND2007-2270, Sandia National Laboratories, Albuquerque, New Mexico, March 2013.

Lindgren, E.R. and S.G. Durbin, "Materials and Dimensional Reference Handbook for the Boiling Water Reactor Dry Cask Simulator," SAND2017-13058R, Sandia National Laboratories, Albuquerque, New Mexico, November 2017.

Lindgren, E.R., S.G. Durbin, R.J.M. Pulido, and A. Salazar, "Update on the Thermal-Hydraulic Investigations of a Horizontal Dry Cask Simulator," SAND2019-11688R, Sandia National Laboratories, Albuquerque, New Mexico, September 2019.

Lombardo, N.J., T.E. Michener, C.L. Wheeler, and D.R. Rector, "Cobra-SFS Predictions of Single Assembly Spent Fuel Heat Transfer Data," PNL-5781, Pacific Northwest Laboratory, Richland, Washington, April 1986.

McKinnon, M.A., J.W. Doman, J.E. Tanner, R.J. Guenther, J.M. Creer and C.E. King, "BWR Spent Fuel Storage Cask Performance Test, Volume 1, Cask Handling Experience and Decay Heat, Heat Transfer, and Shielding Data," PNL-5777 Vol. 1, Pacific Northwest Laboratory, Richland, Washington, February 1986.

McKinnon, M.A., J.M. Creer, C. L. Wheeler, J.E. Tanner, E.R. Gilbert, R.L. Goodman, D.P. Batala, D.A. Dziadosz, E.V. Moore, D.H. Schoonen, M.F. Jensen, and J.H. Browder, "The MC-10 PWR Spent Fuel Storage Cask: Testing and Analysis," EPRI NP-5268, PNL-6139, Pacific Northwest Laboratory, Richland, Washington, July 1987.

McKinnon, M.A., T.E. Michener, M.F. Jensen, G.R. Rodman, "Testing and Analyses of the TN-24P Spent Fuel Dry Storage Cask Loaded with Consolidated Fuel," EPRI NP-6191 Project 2813-16, PNL-6631, Pacific Northwest Laboratory, Richland, Washington, February 1989.

McKinnon, M.A., R.E. Dodge, R.C. Schmitt, L.E. Eslinger, & G. Dineen, "Performance Testing and Analyses of the VSC-17 Ventilated Concrete Cask," EPRI-TR-100305, Electric Power Research Institute, Palo Alto, California, May 1992.

Michener, T.E., D.R. Rector, and J.M. Cuta, "Validation of COBRA-SFS with Measured Temperature Data from Spent-Fuel Storage Casks," Nuclear Technology, Volume 199, p. 350-368, May 2017.

Misumi, T., Suzuki, K., and Kitamura, K., "Fluid Flow and Heat Transfer of Natural Convection Around Large Horizontal Cylinders: Experiments with Air," Heat Trans. – Asian Res., 32 (4), 293-305, 2003.

Nakos, J.T., "Uncertainty Analysis of Thermocouple Measurements Used in Normal and Abnormal Thermal Environment Experiments at Sandia's Radiant Heat Facility and Lurance Canyon Burn Site," SAND2004-1023, Sandia National Laboratories, Albuquerque, New Mexico, April 2004.

Noack, B.R., "On the Flow Around a Circular Cylinder. Part II: Turbulent Regime,", ZAMM-Z. Angew. Math. Me., 79, S227-S230, 1999.

Pulido, R.J.M., E.R. Lindgren, S.G. Durbin, A. Zigh, J. Solis, S.R. Suffield, D.J. Richmond, J.A. Fort, L.E. Herranz, F. Feria, J. Penalva, M. LLoret, M. Galbán, J. Benavides, and G. Jiménez, "Modeling Validation Exercises Using the Dry Cask Simulator," SAND2019-6079R, Sandia National Laboratories, Albuquerque, New Mexico, January 2020.

Solis, J. and Zigh, A., "Impact of Variation in Environmental Conditions on the Thermal Performance of Dry Storage Casks," NUREG-2174, Nuclear Regulatory Commission, Washington, D.C., February 2015.

Sparrow, E.M. and Pfeil, D.R., "Enhancement of Natural Convection Heat Transfer from a Horizontal Cylinder Due to Vertical Shrouding Surfaces," J. Heat Trans., 106, 124-130, February 1984.

Suffield, S.R., J.M. Cuta, J.A. Fort, B.A. Collins, H.E. Adkins, and E.R. Siciliano, "Thermal Modeling of NUHOMS HSM-15 and HSM-1 Storage Modules at Calvert Cliffs Nuclear Power Station ISFSI," PNNL-21788, Pacific Northwest National Laboratory, Richland, Washington, October 2012.

Taylor, J.R., An Introduction to Error Analysis: The Study of Uncertainties in Physical Measurements, University Science Books, 2nd Ed., August 1996.

Yamamoto, A., Ikehara, T., and Ito, T. "Benchmark Problem Suite for Reactor Physics Study of LWR Next Generation Fuels," J. Nucl. Sci. Tech., 39 (8), 900-912, 2002.

Zigh, A., and J. Solis. "Computational Fluid Dynamics Best Practice Guidelines for Dry Cask Applications," U.S. Nuclear Regulatory Commission, NUREG-2152, Washington, DC, March 2013.

APPENDIX A ERROR PROPAGATION ANALYSIS

The error and uncertainty inherent to an experimental result are critical to the accurate interpretation of the data. Therefore, the uncertainties in the experimental measurements are estimated in this section. Results of this analysis are given, followed by a general description of the method used and a brief explanation of the source of each reported measurement uncertainty.

The overall standard uncertainty of an indirect measurement y, dependent on N indirect measurements x_i, is defined in Equation A-1. The standard uncertainty associated with an indirect measurement is analogous to the standard deviation of a statistical population.

$$u^2 = \sum_{i=1}^{N} \left(\frac{\partial y}{\partial x_i} u_i \right)^2 \quad \text{A-1}$$

Here, u is used to define the standard uncertainty of a measurement [Taylor, 1996; Ifan and Hughes, 2010].

The expanded uncertainty, U, is reported in this appendix and defines the bounds that include 95% of the possible data. The expanded uncertainty is assumed to be defined as the product of the standard uncertainty and the Student's t-value. Unless otherwise stated, all uncertainty measurements are assumed to be based on a Student's t-distribution with no fewer than 30 measurements. Considering that the HDCS DAQ collects data at least every 5 seconds over the steady state period, which lasts at least 6 hours for any given test, the steady state period contains at least 4320 data points for all comparison metrics, so this assumption is valid. The associated t-value for 95% confidence intervals is 2.0 for 29 degrees of freedom. Therefore, Equation A-2 shows the definition of the expanded uncertainty as used in the following sections for a 95% confidence interval.

$$U = t_{\text{value}} \cdot u \quad \text{A-2}$$

A.1 Temperature Measurements

A.1.1 Uncertainty in Cladding Temperature Measurement

Cladding temperature was measured with a standard k-type TC using the standard ASTM calibration specifications [ASTM, 2017]. No additional calibrations were performed. While uncertainties of up to 2 to 5% are justified for surface-mounted thermocouples in high heat flux and/or highly transient environments, the relatively small spatial and temporal gradients experienced during the HDCS testing warrant an expanded uncertainty for this type of TC of U_T = 1% of the reading in Kelvin [Nakos, 2004]. In this case, the expanded uncertainty was 1% of the maximum temperature reading from each test (the peak cladding temperature). Table A.1 shows the experimental uncertainties in the cladding temperatures from the ten test cases. These experimental uncertainties applied to the peak cladding temperature as well as the axial, vertical, and horizontal temperature profiles. Note the symmetry in the upper and lower uncertainty bounds since the calculation of 1% of the PCT contains no uncertainty bias in either direction.

Table A.1 Temperature experimental uncertainties.

Conditions			Upper Uncertainty Bound (K)	Lower Uncertainty Bound (K)
Power (kW)	Pressure (kPa)	Fill Gas		
0.5	100	Helium	3.7	3.7
1.0	100	Helium	4.3	4.3
2.5	100	Helium	5.6	5.6
5.0	100	Helium	6.9	6.9
0.5	800	Helium	3.7	3.7
5.0	800	Helium	6.8	6.8
0.5	100	Air	4.3	4.3
1.0	100	Air	5.2	5.2
2.5	100	Air	6.5	6.5
5.0	100	Air	7.8	7.8

A.1.2 Uncertainty in Peak Cladding Temperature Location

The uncertainty in peak cladding temperature location was calculated by determining the locations along the rod where a value of 0.99·PCT occurred, representing the application of 1% PCT uncertainty to the PCT as a lower uncertainty bound. Figure A.1 illustrates this method, using data from the 2.5 kW, 100 kPa helium test. $U_{z_{PCT}^{+},exp}$ and $U_{z_{PCT}^{-},exp}$ are the PCT axial location upper and lower experimental uncertainty bounds, respectively.

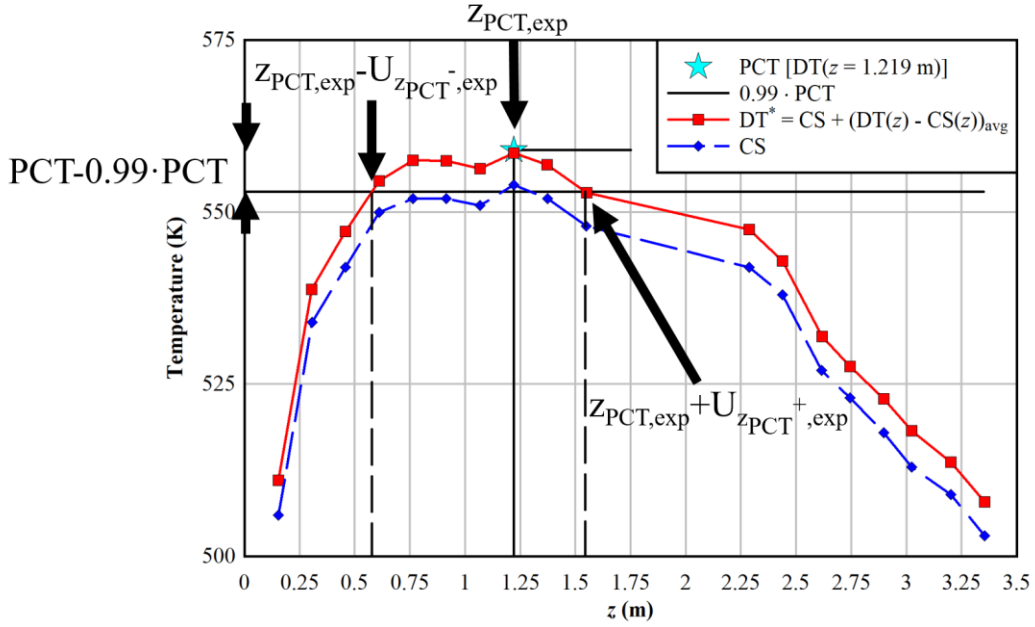

Figure A.1 Visualization of the method used for the determination of the peak cladding temperature location uncertainty. The data presented here are from the 2.5 kW, 100 kPa helium test.

The peak cladding temperatures from the ten tests considered in this report were all found either on rod DT, which has 4 thermocouples, or rod ES, which has 2 thermocouples. For optimal spatial resolution, a

fixed numerical temperature offset was calculated from the average of the temperature differences between rod CS, which contained thermocouples at six-inch spacings along the length of the assembly, and the rod containing the PCT for all matching axial locations. Table A.2 demonstrates this offset calculation, using the 2.5 kW, 100 kPa helium test as an example.

Table A.2 Temperature offset table example using rod CS for optimal spatial resolution. The data presented here are from the 2.5 kW, 100 kPa helium test.

DT, ES Offset				
z (m)	DT(z) (K)	DT(z) - CS(z) (K)	ES (K)	ES(z) - CS(z) (K)
0.6096	555.4	5.8	--	--
1.2192	558.6	5.1	557.9	4.4
2.4384	541.5	3.6	--	--
3.0226	518.9	5.7	517.6	4.4
Average	--	5.1	--	4.4

Using this offset, a numerical temperature profile along the PCT rod was calculated, and the intercepts between this temperature profile and the line generated by the PCT minus 1% of the PCT were used to define the upper and lower experimental uncertainty bounds ($U_{z^+_{PCT},exp}$ and $U_{z^-_{PCT},exp}$, respectively). Table A.3 shows the calculated upper and lower PCT location experimental uncertainty bounds for the ten test cases.

Table A.3 PCT location experimental uncertainties.

Conditions			Upper Uncertainty Bound (m)	Lower Uncertainty Bound (m)
Power (kW)	Pressure (kPa)	Fill Gas		
0.5	100	Helium	0.656	1.078
1.0	100	Helium	0.624	0.657
2.5	100	Helium	0.642	0.324
5.0	100	Helium	0.681	0.330
0.5	800	Helium	0.642	1.145
5.0	800	Helium	0.628	0.389
0.5	100	Air	0.668	0.634
1.0	100	Air	0.699	0.374
2.5	100	Air	0.245	0.897
5.0	100	Air	0.239	0.932

A.1.3 Uncertainty in Ambient Air Temperature

The air temperature was measured with a standard k-type TC. The expanded uncertainty for this type of TC is U_T = 1% of the reading in Kelvin [Nakos, 2004]. The maximum ambient temperature reading was 302 K for the 2.50 kW 100 kPa helium test. The maximum expanded uncertainty for the ambient temperature is $U_{T\text{-amb}} = \pm 3.0$ K.

A.2 Pressure Measurements

A.2.1 Uncertainty in Ambient Air Pressure

The air pressure was measured with an Omega pressure sensor (Model PX2760-600A5V, S/N 6857389). The uncertainty of the ambient air pressure was taken from the manufacturer's calibration sheet, which indicated an expanded uncertainty in the instrument of ±0.25% of full scale (110 kPa). Therefore, the expanded uncertainty in the pressure reading is $U_{\text{P-atm}} = \pm 0.275$ kPa.

A.2.2 Uncertainty in Vessel Pressure

The interior vessel pressure was measured as the average output of two high-accuracy 0 to 1,034 kPa (0 to 150 psia) absolute pressure transducers (Setra Systems ASM1-150P-A-1M-2C-03-A-01) installed in the instrument well. The experimental uncertainty associated with a single gage is ±0.05% of full scale, or $U_{\text{PV,1}} = \pm 0.52$ kPa (±0.075 psi). The combined uncertainty of the average of the two transducers is $U_{\text{PV, AVG}} = \pm 0.37$ kPa (±0.053 psia). Note that the pressure was controlled to within ±0.35 kPa (±0.051 psia) as measured by taking half of the difference between the overall maximum and minimum internal average pressure observed during testing.

A.3 Uncertainty in Electrical Measurements

The voltage, current, and power supplied to the internal spent fuel assembly heater rods were measured by an Ohio Semitronics, Inc. Multifunction Power Test Board (Model PTB-112D1PCY48, SN 18100713). The stated manufacturer's uncertainty was given as ±0.25% of full scale for each measurement. The full scales for each measurement are Voltage = 150 V, Amps = 100 A, Power Factor = 1.00, and Power = 12.00 kW. However, a special calibration schedule of thirty-two points was ordered for this instrument. The expanded uncertainty based on the *t*-statistic ($t_{31} = 2.0$) and the standard error of the regression for each measurement variable was $U_{\text{Volt}} = \pm 0.11$ V, $U_{\text{Amp}} = \pm 0.07$ A, $U_{\text{PF}} = \pm 0.036$, $U_{\text{Watt}} = \pm 13$ W. These instrument-specific uncertainties represent considerably better accuracy than the generic manufacturer's certification.

A.4 Flow Measurements

The methodology for determining the induced air flow is described in detail in Section 2.4.2. Air velocity profiles were recorded across the inlet ducts. These velocities were then used to derive the two-dimensional flow field in the ducts. This flow field was then integrated to determine the air mass flow rate.

The instrument uncertainty in the air mass flow rate per duct was calculated to be $U_{\dot{m},\text{ per duct}} = \pm 1.5 \times 10^{-4}$ kg/s. The combined error in the total air mass flow rate across all four ducts is $U_{\dot{m},\text{ Total}} = \pm 3.0 \times 10^{-4}$ kg/s. Note that 90% of this error is associated with uncertainties in the differential areas and integration scheme. The remaining error is due to uncertainty in the hot wire anemometers. Finally, the observed fluctuations in the air mass flow rate per duct, given by $(\dot{m}_{max} - \dot{m}_{min})/2 = 1.7 \times 10^{-4}$ kg/s, was roughly in agreement with the estimated uncertainty.

The instrument uncertainty, together with the observed fluctuations in the steady state flow (calculated as the 95% confidence interval of the flow measurements during the test steady state period), were used to calculate a combined measurement uncertainty for the air mass flow rate. Table A.4 shows the results of these calculations for the ten test cases. Note the symmetry in the upper and lower uncertainty bounds since the calculation of the combined measurement uncertainty contains no uncertainty bias in either direction.

Table A.4 Air mass flow rate experimental uncertainties.

Conditions			Upper Uncertainty Bound (kg/s)	Lower Uncertainty Bound (kg/s)
Power (kW)	Pressure (kPa)	Fill Gas		
0.5	100	Helium	0.0004	0.0004
1.0	100	Helium	0.0006	0.0006
2.5	100	Helium	0.0004	0.0004
5.0	100	Helium	0.0006	0.0006
0.5	800	Helium	0.0006	0.0006
5.0	800	Helium	0.0008	0.0008
0.5	100	Air	0.0006	0.0006
1.0	100	Air	0.0007	0.0007
2.5	100	Air	0.0004	0.0004
5.0	100	Air	0.0005	0.0005

A.4.1 Uncertainty in Hot Wire Anemometer Measurements

The TSI Model 8455 hot wire anemometer has a manufacturer's expanded uncertainty of ±2% of reading +0.5% of full scale. The chosen full scale for all tests was 1 m/s. Therefore, the maximum expanded uncertainty was defined as $U_v = \pm 0.025$ m/s for the ambient temperatures encountered. Standard conditions for the TSI hotwire are 21.1 °C and 101.4 kPa.

For velocities near the wall, an alternative approach was adopted to estimate uncertainty. The difference in the velocity central to the differential area and the average of the estimated velocities along the periphery of the differential area was taken to estimate the maximum uncertainty. The average of this alternative uncertainties along the perimeter of the inlet gives an expanded uncertainty of $U_{v,\nabla v} = \pm 0.033$ m/s for these edge velocities.

A.4.2 Uncertainty in Differential Areas

The positional accuracy of each motorized stage (Velmex Xslide) based on straight line accuracy is given by the manufacturer as $U_{stage} = \pm 0.08$ mm. However, this estimate does not include other sources of uncertainty such as slight errors in stage alignment and deviations in the duct itself. An uncertainty for each dimension of the differential area of $U_{\Delta x} = U_{\Delta y} = \pm 1.6$ mm was chosen to incorporate all known and unknown uncertainties in the differential area.

Table A.5 gives the uncertainty of the average differential area $U_{\Delta A,AVG} = \pm 2.3 \times 10^{-5}$ m^2.

Table A.5 Representative calculation to estimate the expanded error of flow area determination.

Measurement, x_i	Units	Value	Expanded uncertainty, U_i	Influence coefficient ($U_i \cdot [(\partial \Delta A/\partial x_i)/\Delta A]$)	Contribution
Δx_{AVG}	m	6.4E-03	1.6E-03	2.5E-01	0.81
Δy_{AVG}	m	1.3E-02	1.6E-03	1.2E-01	0.19
ΔA_{AVG}	m^2	8.3E-05	2.3E-05	2.8E-01	1.00

This page is intentionally left blank.

APPENDIX B MODEL 1 SIMULATION UNCERTAINTIES

The tables in this Appendix were provided by the institution that generated the results for model 1 in the results section (Chapter 3). The tables give the upper and lower simulation uncertainty bounds for the peak cladding temperatures, the air mass flow rates, the axial internal centerline temperature profiles, the vertical temperature profiles, and the horizontal temperature profiles. As mentioned in Section 3.2.1, the simulation uncertainties included iterative uncertainty and spatial discretization uncertainty, and the experimental uncertainty considered in the numerical calculations was 1% of the simulation result.

B.1 Peak Cladding Temperature Simulation Uncertainties

Table B.1 Model 1 simulation uncertainties for the peak cladding temperatures for all tests.

Conditions			Upper Uncertainty Bound (kg/s)	Lower Uncertainty Bound (kg/s)
Power (kW)	Pressure (kPa)	Fill Gas		
0.5	100	Helium	5.5	6.0
1.0	100	Helium	6.7	7.8
2.5	100	Helium	10.5	13.7
5.0	100	Helium	16.0	21.7
0.5	800	Helium	5.1	5.6
5.0	800	Helium	10.9	17.6
0.5	100	Air	8.2	11.2
1.0	100	Air	11.1	15.8
2.5	100	Air	20.0	29.5
5.0	100	Air	28.3	39.9

B.2 Temperature Profile Simulation Uncertainties

B.2.1 0.5 kW 100 kPa Helium Test

Table B.2 Model 1 simulation uncertainties for the axial internal centerline temperature profile coordinates as a function of the z-coordinate from the 0.5 kW 100 kPa helium test.

z (m)	Upper Uncertainty Bound (K)	Lower Uncertainty Bound (K)
0.61	5.6	6.3
1.219	5.6	6.1
1.829	5.6	6.0
2.438	6.1	6.4
3.658	6.1	6.3

Table B.3 Model 1 simulation uncertainties for vertical temperature profile coordinates at z = 1.219 m (48.0 in.) from the 0.5 kW 100 kPa helium test.

Location	x (m)	Upper Uncertainty Bound (K)	Lower Uncertainty Bound (K)
Vault Top	-0.169	3.9	5.0
Pressure Vessel Top	-0.137	4.9	5.0
Basket Top	-0.090	4.7	4.9
Channel Top	-0.068	5.0	5.2
EQ	-0.057	5.8	6.1
ES	-0.029	5.5	6.0
WEU	0	5.6	6.1
Channel Bottom	0.068	6.1	6.5
Basket Bottom	0.090	6.2	6.4
Pressure Vessel Bottom	0.137	5.4	5.5
Vault Bottom	0.421	4.5	4.5

Table B.4 Model 1 simulation uncertainties for the horizontal temperature profile coordinates at z = 1.829 m (72.0 in.) from the 0.5 kW 100 kPa helium test.

Location	y (m)	Upper Uncertainty Bound (K)	Lower Uncertainty Bound (K)
WEU	0	5.6	6.0
GU	0.029	6.6	6.9
IU	0.057	6.2	6.4
Channel	0.068	5.3	5.4
Basket	0.089	5.1	5.2
Pressure Vessel	0.137	4.8	4.8
Vault	0.165	4.6	4.5

B.2.2 1.0 kW 100 kPa Helium Test

Table B.5 Model 1 simulation uncertainties for the internal centerline temperature profile coordinates as a function of the *z*-coordinate from the 1.0 kW 100 kPa helium test.

z (m)	Upper Uncertainty Bound (K)	Lower Uncertainty Bound (K)
0.61	6.5	7.8
1.219	6.7	7.8
1.829	6.9	7.9
2.438	7.5	8.4
3.658	7.5	8.0

Table B.6 Model 1 simulation uncertainties for vertical temperature profile coordinates at *z* = 1.219 m (48.0 in.) from the 1.0 kW 100 kPa helium test.

Location	*x* (m)	Upper Uncertainty Bound (K)	Lower Uncertainty Bound (K)
Vault Top	-0.169	6.3	7.2
Pressure Vessel Top	-0.137	4.9	5.1
Basket Top	-0.09	5.4	5.5
Channel Top	-0.068	5.9	6.1
EQ	-0.057	6.9	7.4
ES	-0.029	6.6	7.6
WEU	0	6.7	7.8
Channel Bottom	0.068	7.5	8.4
Basket Bottom	0.090	7.9	8.0
Pressure Vessel Bottom	0.137	5.7	5.7
Vault Bottom	0.421	4.8	4.8

Table B.7 Model 1 simulation uncertainties for the horizontal temperature profile coordinates at *z* = 1.829 m (72.0 in.) from the 1.0 kW 100 kPa helium test.

Location	*y* (m)	Upper Uncertainty Bound (K)	Lower Uncertainty Bound (K)
WEU	0	6.9	7.9
GU	0.029	8.7	9.4
IU	0.057	8.0	8.3
Channel	0.068	6.3	6.5
Basket	0.089	5.8	5.9
Pressure Vessel	0.137	5.1	5.1
Vault	0.165	4.7	4.6

B.2.3 2.5 kW 100 kPa Helium Test

Table B.8 Model 1 simulation uncertainties for the internal centerline temperature profile coordinates as a function of the *z*-coordinate from the 2.5 kW 100 kPa helium test.

z (m)	Upper Uncertainty Bound (K)	Lower Uncertainty Bound (K)
0.61	10.5	13.5
1.219	10.5	13.6
1.829	10.6	13.8
2.438	12.6	15.2
3.658	13.4	14.6

Table B.9 Model 1 simulation uncertainties for vertical temperature profile coordinates at *z* = 1.219 m (48.0 in.) from the 2.5 kW 100 kPa helium test.

Location	*x* (m)	Upper Uncertainty Bound (K)	Lower Uncertainty Bound (K)
Vault Top	-0.169	5.5	7.2
Pressure Vessel Top	-0.137	6.0	6.2
Basket Top	-0.090	7.5	7.5
Channel Top	-0.068	8.9	9.1
EQ	-0.057	10.9	11.8
ES	-0.029	10.4	13.1
WEU	0	10.5	13.6
Channel Bottom	0.068	13.0	15.3
Basket Bottom	0.090	14.2	14.1
Pressure Vessel Bottom	0.137	9.7	9.5
Vault Bottom	0.421	6.6	6.6

Table B.10 Model 1 simulation uncertainties for the horizontal temperature profile coordinates at *z* = 1.829 m (72.0 in.) from the 2.5 kW 100 kPa helium test.

Location	*y* (m)	Upper Uncertainty Bound (K)	Lower Uncertainty Bound (K)
WEU	0	10.6	13.8
GU	0.029	14.2	16.2
IU	0.057	13.0	13.8
Channel	0.068	9.6	9.7
Basket	0.089	8.2	8.1
Pressure Vessel	0.137	6.5	6.5
Vault	0.165	5.6	5.6

B.2.4 5.0 kW 100 kPa Helium Test

Table B.11 Model 1 simulation uncertainties for the internal centerline temperature profile coordinates as a function of the *z*-coordinate from the 5.0 kW 100 kPa helium test.

z (m)	Upper Uncertainty Bound (K)	Lower Uncertainty Bound (K)
0.61	15.9	21.4
1.219	16.3	21.7
1.829	15.5	21.5
2.438	17.7	22.9
3.658	19.8	22.4

Table B.12 Model 1 simulation uncertainties for vertical temperature profile coordinates at *z* = 1.219 m (48.0 in.) from the 5.0 kW 100 kPa helium test.

Location	*x* (m)	Upper Uncertainty Bound (K)	Lower Uncertainty Bound (K)
Vault Top	-0.169	15.6	14.8
Pressure Vessel Top	-0.137	9.4	8.8
Basket Top	-0.090	12.1	11.5
Channel Top	-0.068	14.2	13.8
EQ	-0.057	16.4	17.6
ES	-0.029	16.2	20.7
WEU	0	16.3	21.7
Channel Bottom	0.068	20.5	23.9
Basket Bottom	0.090	22.8	22.3
Pressure Vessel Bottom	0.137	13.8	13.4
Vault Bottom	0.421	12.4	12.4

Table B.13 Model 1 simulation uncertainties for the horizontal temperature profile coordinates at *z* = 1.829 m (72.0 in.) from the 5.0 kW 100 kPa helium test.

Location	*y* (m)	Upper Uncertainty Bound (K)	Lower Uncertainty Bound (K)
WEU	0	15.5	21.5
GU	0.029	19.1	23.3
IU	0.057	17.3	18.8
Channel	0.068	13.6	13.7
Basket	0.089	10.5	10.4
Pressure Vessel	0.137	7.5	7.7
Vault	0.165	5.5	6.0

B.2.5 0.5 kW 800 kPa Helium Test

Table B.14 Model 1 simulation uncertainties for the internal centerline temperature profile coordinates as a function of the *z*-coordinate from the 0.5 kW 800 kPa helium test.

z (m)	Upper Uncertainty Bound (K)	Lower Uncertainty Bound (K)
0.61	4.9	5.6
1.219	5.0	5.6
1.829	5.0	5.5
2.438	5.1	5.5
3.658	5.0	5.3

Table B.15 Model 1 simulation uncertainties for vertical temperature profile coordinates at *z* = 1.219 m (48.0 in.) from the 0.5 kW 800 kPa helium test.

Location	*x* (m)	Upper Uncertainty Bound (K)	Lower Uncertainty Bound (K)
Vault Top	-0.169	4.1	5.2
Pressure Vessel Top	-0.137	4.5	4.7
Basket Top	-0.090	4.6	4.8
Channel Top	-0.068	4.8	5.1
EQ	-0.057	5.0	5.3
ES	-0.029	5.1	5.6
WEU	0	5.0	5.6
Channel Bottom	0.068	4.7	5.3
Basket Bottom	0.090	4.8	5.0
Pressure Vessel Bottom	0.137	4.7	4.8
Vault Bottom	0.421	4.4	4.4

Table B.16 Model 1 simulation uncertainties for the horizontal temperature profile coordinates at *z* = 1.829 m (72.0 in.) from the 0.5 kW 800 kPa helium test.

Location	*y* (m)	Upper Uncertainty Bound (K)	Lower Uncertainty Bound (K)
WEU	0	5.0	5.5
GU	0.029	5.0	5.4
IU	0.057	5.0	5.2
Channel	0.068	4.8	5.0
Basket	0.089	4.6	4.7
Pressure Vessel	0.137	4.6	4.6
Vault	0.165	4.5	4.4

B.2.6 0.5 kW 800 kPa Helium Test

Table B.17 Model 1 simulation uncertainties for the internal centerline temperature profile coordinates as a function of the *z*-coordinate from the 5.0 kW 800 kPa helium test.

z (m)	Upper Uncertainty Bound (K)	Lower Uncertainty Bound (K)
0.61	11.7	18.6
1.219	11.3	18.0
1.829	10.9	17.9
2.438	13.4	18.9
3.658	15.4	15.8

Table B.18 Model 1 simulation uncertainties for vertical temperature profile coordinates at *z* = 1.219 m (48.0 in.) from the 5.0 kW 800 kPa helium test.

Location	*x* (m)	Upper Uncertainty Bound (K)	Lower Uncertainty Bound (K)
Vault Top	-0.169	14.5	13.6
Pressure Vessel Top	-0.137	10.3	10.3
Basket Top	-0.090	6.8	7.8
Channel Top	-0.068	9.7	12.0
EQ	-0.057	13.8	17.2
ES	-0.029	11.0	17.8
WEU	0	11.3	18.0
Channel Bottom	0.068	14.0	17.7
Basket Bottom	0.090	16.1	16.2
Pressure Vessel Bottom	0.137	9.8	9.9
Vault Bottom	0.421	10.9	10.9

Table B.19 Model 1 simulation uncertainties for the horizontal temperature profile coordinates at *z* = 1.829 m (72.0 in.) from the 5.0 kW 800 kPa helium test.

Location	*y* (m)	Upper Uncertainty Bound (K)	Lower Uncertainty Bound (K)
WEU	0	10.9	17.9
GU	0.029	11.9	17.2
IU	0.057	11.2	13.8
Channel	0.068	8.4	9.9
Basket	0.089	6.2	7.0
Pressure Vessel	0.137	5.0	5.2
Vault	0.165	5.6	6.1

B.2.7 0.5 kW 100 kPa Air Test

Table B.20 Model 1 simulation uncertainties for the internal centerline temperature profile coordinates as a function of the *z*-coordinate from the 0.5 kW 100 kPa air test.

z (m)	Upper Uncertainty Bound (K)	Lower Uncertainty Bound (K)
0.61	7.6	10.8
1.219	7.9	10.5
1.829	8.0	10.5
2.438	9.7	11.5
3.658	9.4	10.2

Table B.21 Model 1 simulation uncertainties for vertical temperature profile coordinates at *z* = 1.219 m (48.0 in.) from the 0.5 kW 100 kPa air test.

Location	*x* (m)	Upper Uncertainty Bound (K)	Lower Uncertainty Bound (K)
Vault Top	-0.169	4.2	4.9
Pressure Vessel Top	-0.137	4.9	5.0
Basket Top	-0.090	4.9	5.1
Channel Top	-0.068	7.1	7.7
EQ	-0.057	9.4	11.0
ES	-0.029	8.1	11.4
WEU	0	7.9	10.5
Channel Bottom	0.068	7.1	8.6
Basket Bottom	0.090	6.4	6.5
Pressure Vessel Bottom	0.137	4.9	5.1
Vault Bottom	0.421	4.5	4.5

Table B.22 Model 1 simulation uncertainties for the horizontal temperature profile coordinates at *z* = 1.829 m (72.0 in.) from the 0.5 kW 100 kPa air test.

Location	*y* (m)	Upper Uncertainty Bound (K)	Lower Uncertainty Bound (K)
WEU	0	8.0	10.5
GU	0.029	8.5	10.5
IU	0.057	8.9	9.7
Channel	0.068	6.5	6.7
Basket	0.089	5.0	5.1
Pressure Vessel	0.137	4.7	4.7
Vault	0.165	4.5	4.5

B.2.8 1.0 kW 100 kPa Air Test

Table B.23 Model 1 simulation uncertainties for the internal centerline temperature profile coordinates as a function of the *z*-coordinate from the 1.0 kW 100 kPa air test.

z (m)	Upper Uncertainty Bound (K)	Lower Uncertainty Bound (K)
0.61	10.5	15.2
1.219	10.8	15.1
1.829	10.9	15.1
2.438	13.7	16.8
3.658	22.6	23.4

Table B.24 Model 1 simulation uncertainties for vertical temperature profile coordinates at *z* = 1.219 m (48.0 in.) from the 1.0 kW 100 kPa air test.

Location	*x* (m)	Upper Uncertainty Bound (K)	Lower Uncertainty Bound (K)
Vault Top	-0.169	6.3	6.7
Pressure Vessel Top	-0.137	5.2	5.3
Basket Top	-0.090	5.8	6.1
Channel Top	-0.068	9.6	10.2
EQ	-0.057	12.8	14.9
ES	-0.029	11.1	15.9
WEU	0	10.8	15.1
Channel Bottom	0.068	10.0	13.8
Basket Bottom	0.090	8.8	8.8
Pressure Vessel Bottom	0.137	5.4	5.4
Vault Bottom	0.421	4.7	4.8

Table B.25 Model 1 simulation uncertainties for the horizontal temperature profile coordinates at *z* = 1.829 m (72.0 in.) from the 1.0 kW 100 kPa air test.

Location	*y* (m)	Upper Uncertainty Bound (K)	Lower Uncertainty Bound (K)
WEU	0	10.9	15.1
GU	0.029	12.3	15.5
IU	0.057	12.5	13.8
Channel	0.068	8.8	8.9
Basket	0.089	5.9	6.0
Pressure Vessel	0.137	5.0	5.0
Vault	0.165	4.6	4.7

B.2.9 2.5 kW 100 kPa Air Test

Table B.26 Model 1 simulation uncertainties for the internal centerline temperature profile coordinates as a function of the *z*-coordinate from the 2.5 kW 100 kPa air test.

z (m)	Upper Uncertainty Bound (K)	Lower Uncertainty Bound (K)
0.61	19.3	28.8
1.219	19.5	29.0
1.829	19.4	28.9
2.438	22.6	30.2
3.658	26.9	29.2

Table B.27 Model 1 simulation uncertainties for vertical temperature profile coordinates at *z* = 1.219 m (48.0 in.) from the 2.5 kW 100 kPa air test.

Location	*x* (m)	Upper Uncertainty Bound (K)	Lower Uncertainty Bound (K)
Vault Top	-0.169	6.3	6.3
Pressure Vessel Top	-0.137	6.7	6.9
Basket Top	-0.090	8.9	9.2
Channel Top	-0.068	17.1	17.3
EQ	-0.057	21.2	24.8
ES	-0.029	20.2	29.3
WEU	0	19.5	29.0
Channel Bottom	0.068	18.6	29.4
Basket Bottom	0.090	16.2	15.9
Pressure Vessel Bottom	0.137	8.8	8.4
Vault Bottom	0.421	6.1	6.4

Table B.28 Model 1 simulation uncertainties for the horizontal temperature profile coordinates at *z* = 1.829 m (72.0 in.) from the 2.5 kW 100 kPa air test.

Location	*y* (m)	Upper Uncertainty Bound (K)	Lower Uncertainty Bound (K)
WEU	0	19.4	28.9
GU	0.029	22.8	29.8
IU	0.057	21.2	24.0
Channel	0.068	15.6	15.5
Basket	0.089	9.0	8.9
Pressure Vessel	0.137	6.8	6.9
Vault	0.165	5.7	5.8

B.2.10 5.0 kW 100 kPa Air Test

Table B.29 Model 1 simulation uncertainties for the internal centerline temperature profile coordinates as a function of the *z*-coordinate from the 5.0 kW 100 kPa air test.

z (m)	Upper Uncertainty Bound (K)	Lower Uncertainty Bound (K)
0.61	27.7	28.8
1.219	28.1	39.7
1.829	27.7	39.5
2.438	31.0	41.2
3.658	32.8	39.5

Table B.30 Model 1 simulation uncertainties for vertical temperature profile coordinates at *z* = 1.219 m (48.0 in.) from the 5.0 kW 100 kPa air test.

Location	*x* (m)	Upper Uncertainty Bound (K)	Lower Uncertainty Bound (K)
Vault Top	-0.169	17.2	17.5
Pressure Vessel Top	-0.137	9.9	9.4
Basket Top	-0.090	14.6	14.0
Channel Top	-0.068	24.2	23.1
EQ	-0.057	28.4	31.6
ES	-0.029	28.5	38.8
WEU	0	28.1	39.7
Channel Bottom	0.068	28.0	48.1
Basket Bottom	0.090	25.8	24.9
Pressure Vessel Bottom	0.137	11.8	11.2
Vault Bottom	0.421	11.4	11.5

Table B.31 Model 1 simulation uncertainties for the horizontal temperature profile coordinates at *z* = 1.829 m (72.0 in.) from the 5.0 kW 100 kPa air test.

Location	*y* (m)	Upper Uncertainty Bound (K)	Lower Uncertainty Bound (K)
WEU	0	27.7	39.5
GU	0.029	31.6	40.5
IU	0.057	28.5	31.5
Channel	0.068	22.4	21.4
Basket	0.089	13.3	12.6
Pressure Vessel	0.137	7.7	7.4
Vault	0.165	6.5	6.4

B.3 Air Mass Flow Rate Simulation Uncertainties

Table B.32 Model 1 simulation uncertainties for the air mass flow rates for all tests.

Conditions			Upper Uncertainty Bound (kg/s)	Lower Uncertainty Bound (kg/s)
Power (kW)	Pressure (kPa)	Fill Gas		
0.5	100	Helium	0.0013	0.0012
1.0	100	Helium	0.0012	0.0011
2.5	100	Helium	0.0012	0.0011
5.0	100	Helium	0.0018	0.0019
0.5	800	Helium	0.0011	0.0010
5.0	800	Helium	0.0022	0.0021
0.5	100	Air	0.0011	0.0010
1.0	100	Air	0.0011	0.0011
2.5	100	Air	0.0011	0.0011
5.0	100	Air	0.0015	0.0014

APPENDIX C NRC MODEL

The thermal model used to simulate the horizontal dry cask simulator (HDCS) is similar to earlier simulations for prototypic cask systems [Zigh and Solis, 2015; Hall, Zigh, and Solis, 2019; Zigh and Gonzalez, 2020]. The commercially available, finite-volume, computational fluid dynamics (CFD) code ANSYS/Fluent version 19.0 was used to create a 3D model of the HDCS. The model domain took advantage of symmetry about the vertical longitudinal plane of the fuel assembly and vault, so that ½ of the full domain was simulated as shown in Figure C.1 through Figure C.4. The model geometry was built and created using Gambit version 2.4, and the same software was also used to create the mesh.

The entire domain, including features both inside and outside the pressure vessel, was simulated in one model. In order to simplify the details of the fuel bundle assembly, a porous media approach was used to simulate the heat generation, hydraulic resistance, and thermal conductivity of the actual assembly.

The HDCS model was calibrated to two open cases – one with helium fill gas, and the other with air. Both cases had a total heat input of 2.5 kW and a fill gas pressure of 100 kPa. The same modeling approach was used on the 8 blind cases, which consisted of cases with either fill gas, a range of heat input values, and a higher fill gas pressure (helium only).

The uncertainty for all cases was rigorously calculated according to ASME V&V 20-2009 [ASME, 2009], and for the two open cases, the simulation results matched the experimentally measured values within the validation uncertainty for nearly all measured values. For the blind cases, the simulation uncertainty is also provided so that the evaluation of whether or not the simulation values match the experimental values within the specified uncertainty band can be investigated.

C.1 Model Description

C.1.1 Representation of Fuel Assembly

To model the fuel region, porous media was used as all dry cask applicants favor the use of the porous media method because it simplifies the configuration and saves on processing time. The use of porous media involves representing the components inside the assembly with an equivalent hydraulic resistance and thermal conductivity. In NUREG-2208, "Validation of Computational Fluid Dynamics Methods Using Prototypic Light Water Reactor Spent Fuel Assembly Thermal-Hydraulic Data" [Zigh and Gonzalez, 2017], the use of the porous media was validated and shown to give comparable results as in the detailed model where fuel rods and grid spacers were represented.

C.1.2 Representation of HDCS Structures

The 1-inch thick honeycomb inlet flow straighteners at the inlet duct were modeled using porous media. The viscous loss through the inlet straightener in the axial direction was 2.7e+06 m^{-2} as instructed in the test description [Lindgren *et al*., 2019], with two orders of magnitude higher resistance in the transverse directions. The outer surfaces bounding the control volume as shown in Figure C.1 was allowed to interact with the surroundings using both convection and radiation. The convection coefficient was implemented by using a Nusselt number correlation for natural convection at the average wall temperature and orientation for different wall sections in the model domain.

C.1.3 Approximations and Treatments

C.1.3.1 Internal Fuel Assembly and External HDCS Structure Treatment

Heat generation was uniformly distributed within each of two different sections of the fuel bundle assembly according to the number of heating rods present in each section. The lower (full) section had 74 heating rods and a correspondingly higher heat generation rate, and the upper (partial) section had 66 rods, and a correspondingly lower heating rate.

The gas inside the pressure vessel (helium or air) was assumed to be laminar, while the air outside the pressure vessel was assumed to behave according to the Low Reynolds k-epsilon turbulence model with full buoyancy effect on both the k and epsilon equations. No wall function model was used to integrate the turbulence equations at the wall. Second order upwind discretization was used for all the conservation equations. Radiation heat transfer was modeled using the Discrete Ordinates (DO) model using second order upwind discretization. A pressure solver was used using Semi-Implicit Method for Pressure-Linked Equations (SIMPLE) to link the conservation of momentum equation to the continuity equation. The least square cell-based method was used for gradient discretization. Body force weighted pressure interpolation was used.

All solid structures within the model domain were meshed and were included as volumes in the simulation. The 0.9 mm gap between the channel box and aluminum bridge plate was meshed as a fluid volume. This allowed the capability to turn this volume into solid zircaloy to remove the gap and increase the rate of conductive heat transfer between the channel box and bridge plate as a sensitivity study regarding the importance of this gap.

The line contact between the basket stabilizer tubes and the pressure vessel was expanded into a narrow surface to facilitate meshing. The welded contact between the basket and the stabilizer tubes was similarly expanded. The top basket stabilizer tube was assumed to not be in contact with the pressure vessel, and a small gap was included in this area.

Items that were omitted from the domain include: fuel assembly set screws, pressure vessel support posts, vault inlet and outlet vent vertical dividers, and the Tee-shaped pressure vessel structure below the pressure vessel lower flange.

C.1.3.2 Input Parameters

Both helium and air were modeled using the ideal gas law, which uses the local temperature, pressure, and gas molecular weight to compute the local gas density. The pressure inside the pressure vessel was initialized to the correct value for each case analyzed (100 kPa or 800 kPa), and being a closed volume, the solution was always found to maintain the correct pressure while solving.

The emissivity values used for each surface in the simulation were provided in the HDCS update report [Lindgren *et al*., 2019] and did not vary with temperature. Instead, an uncertainty was prescribed for each emissivity value used, and the uncertainty in emissivity values was found to be the greatest source of uncertainty in the simulation. This is particularly true for the cases that used air as the fill-gas since the primary mode of heat transfer was radiation, owing to the low thermal conductivity of air relative to helium.

The effective thermal conductivity (k_{eff}) represents radiation and conduction through the gas inside the assembly, as well as conduction through the fuel rods. The k_{eff} value is a strong function of temperature and has different magnitudes in the axial and transverse directions. This approach also allows for convection of heat by transport of gas within the fuel bundle due to natural convection. The TRW Environmental Safety Systems, Inc. (TRW) report, “Spent Nuclear Fuel Effective Thermal Conductivity,” dated July 11, 1996 [TRW Environmental Safety Systems Inc., 1996], describes the k_{eff} approach in

detail. In NUREG-2208, calculations in the TRW report were confirmed using the developed model using CFD ANSYS, which was then used to obtain the k_{eff} for the BWR 9×9 assembly.

To calculate the radial components of k_{eff}, a two-dimensional (2D) CFD model representing the detailed cross section of an assembly was used, which included the water rods, heating elements and fuel rod cladding. The k_{eff} was calculated for different boundary conditions including heating rate, channel box temperature, and emissivity values of Inconel and zircaloy. The k_{eff} values were calculated as a function of temperature, and different values were computed for the partial (upper) and full (lower) sections of the fuel bundle due to the different internal geometry.

Axial components of k_{eff} were calculated using an area-weighted average of thermal conductivity of all the components in the fuel bundle, including the gas. Radiation is omitted from the calculation of the axial k_{eff} values. Further details about how to obtain the proper porous media input are explained in NUREG-2208 [Zigh and Gonzalez, 2017].

The lower (full) portion of the fuel bundle was split at an axial coordinate of z=2.000m, to demark the boundary on the zircaloy channel box where the emissivity goes from approximately 0.56±0.11 below z=2 m, to approximately 0.70±0.09 above 2 m. Corresponding k_{eff} values were calculated accordingly.

C.1.3.3 Initial/Boundary Conditions and Symmetry

A ½ symmetry model of the horizontal DCS apparatus was created in 3D, with the symmetry plane on the vertical, longitudinal axis of the fuel bundle assembly. The boundary conditions and models input used in the CFD model were representative of those present during the experiment, as documented in the horizontal DCS test description [Lindgren *et al*., 2019]. The model inflow boundary was located at the inlet to the flow straighteners, with a constant pressure inflow boundary. Background turbulence was assumed to be negligible, and the inlet temperature was set to the ambient temperature measured for each test condition. Ambient pressure was assumed to be 83 kPa for all tests. Ambient density was calculated using the ideal gas law using the ambient pressure, ambient temperature, and molecular weight of air.

The model outflow boundary was simulated as a constant pressure boundary at the same ambient pressure as the inflow boundary (83 kPa). By specifying the ambient operating density external to the model domain, the simulation calculated the appropriate mass flow of air through the vault to balance the chimney effect of hotter gas within the vault than outside and maintain the constant ambient pressure values at the CFD model domain inlets and outlets.

Temperature dependent material properties for solids and fluids were implemented in the model including density (ideal gas law), thermal conductivity, and specific heat. These properties were obtained from "Materials and Dimensional Reference Handbook for the Boiling Water Reactor Dry Cask Simulator" [Durbin and Lindgren, 2017].

An investigation into the effect of differential heating along the length of the channel box was conducted to see if there would be any bowing due to the top of the channel box being approximately 30°C hotter than the bottom according to the experimental data in the open cases. However, it was determined that the weight of the channel box and heater rods was enough to overcome any deformation due to differential heating and maintain contact between the channel box and the bridge plate.

The mesh was created using the best practice guideline, NUREG-2152 [Zigh and Solis, 2013]. The fine mesh, which was used for all the simulations besides the Grid Convergence Index (GCI) evaluation, had 12.8 million cells, with the vast majority being hexahedral cells. Tetrahedral cells were used in a very limited area around the nozzle and pedestal at the lower end of the fuel bundle assembly. Triangular prisms were also used in a few select locations. In the air flow region, a y+ close to unity was used to appropriately use the Low Reynolds k-epsilon turbulence model. CFD best practice guidelines [Zigh and Solis, 2013] were used for expansion ratio for successive volume meshing and mesh skewness.

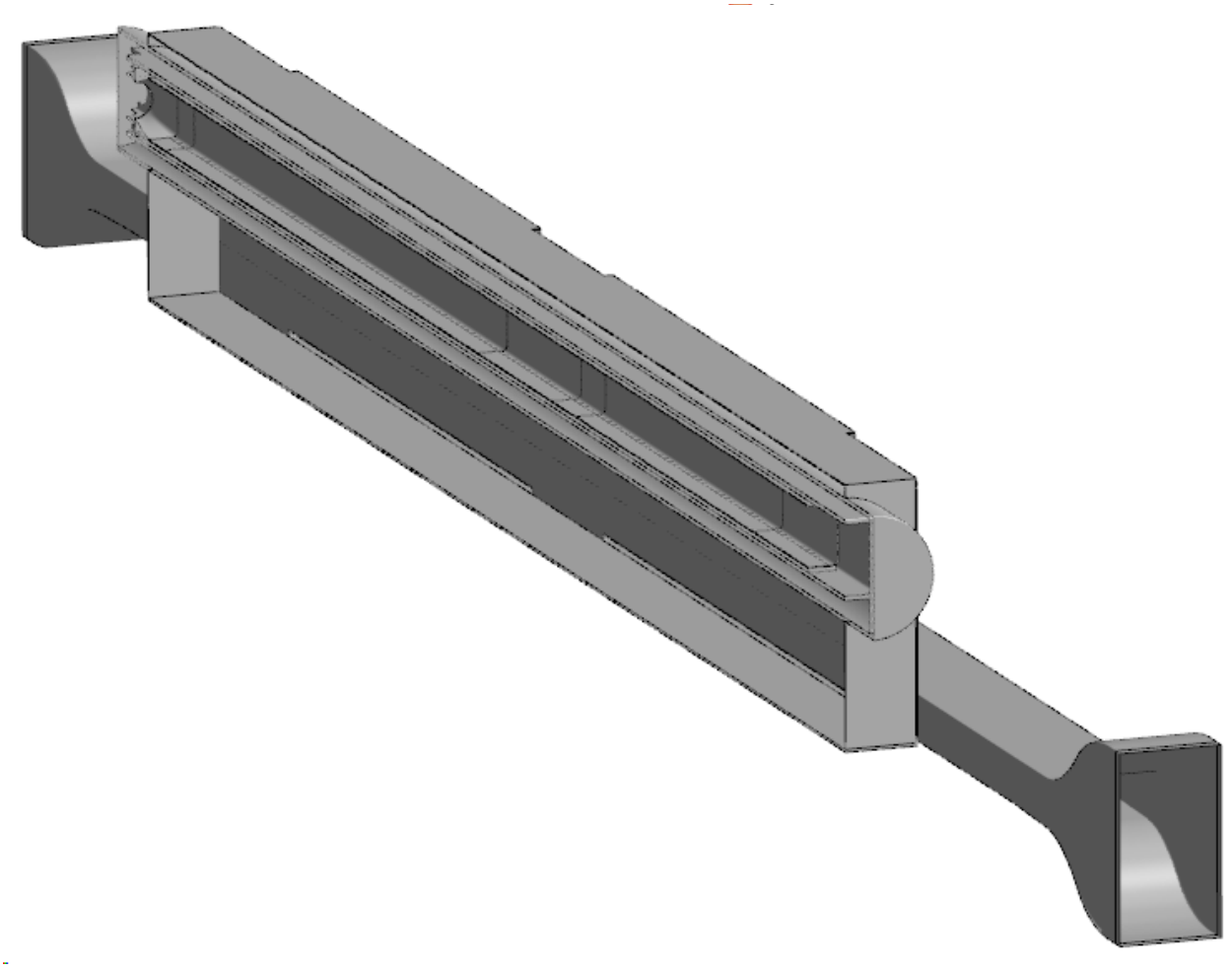

Figure C.1 HDCS model domain.

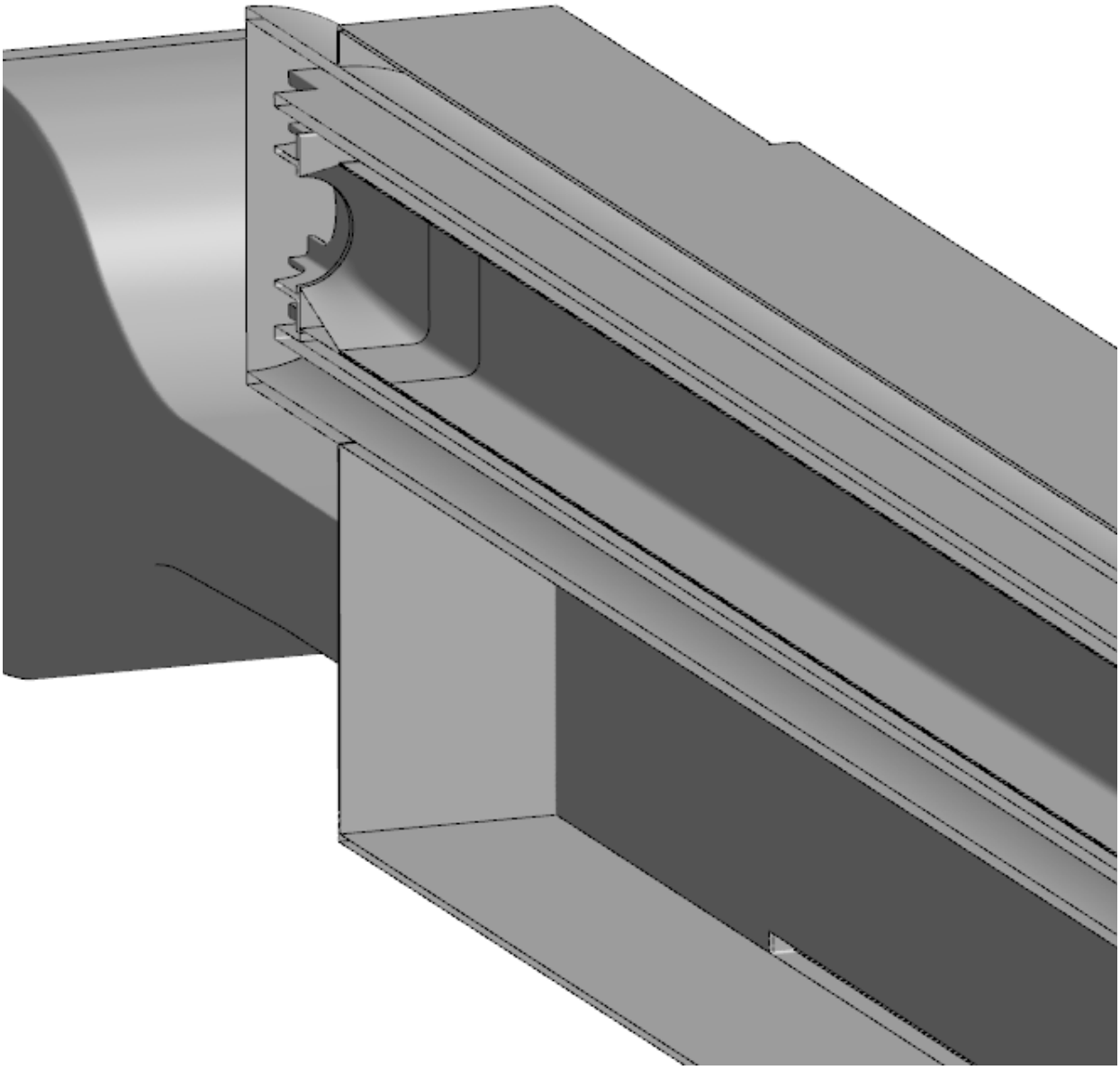

Figure C.2 HDCS model domain - view of nozzle and inlet vent.

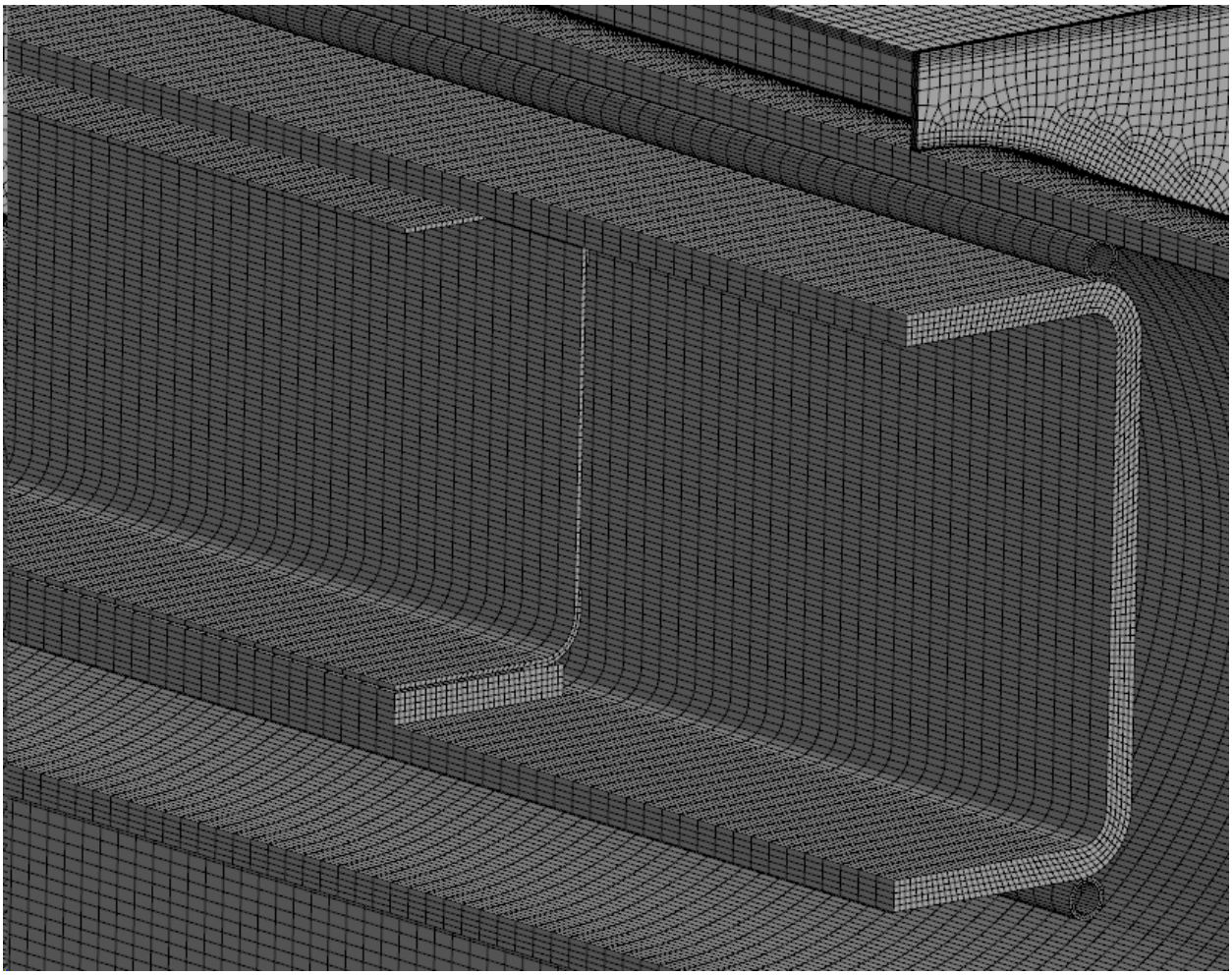

Figure C.3 Surface mesh of channel box, bridge plate, basket, basket stabilizers, vessel, and vault at the upper end of the HDCS apparatus.

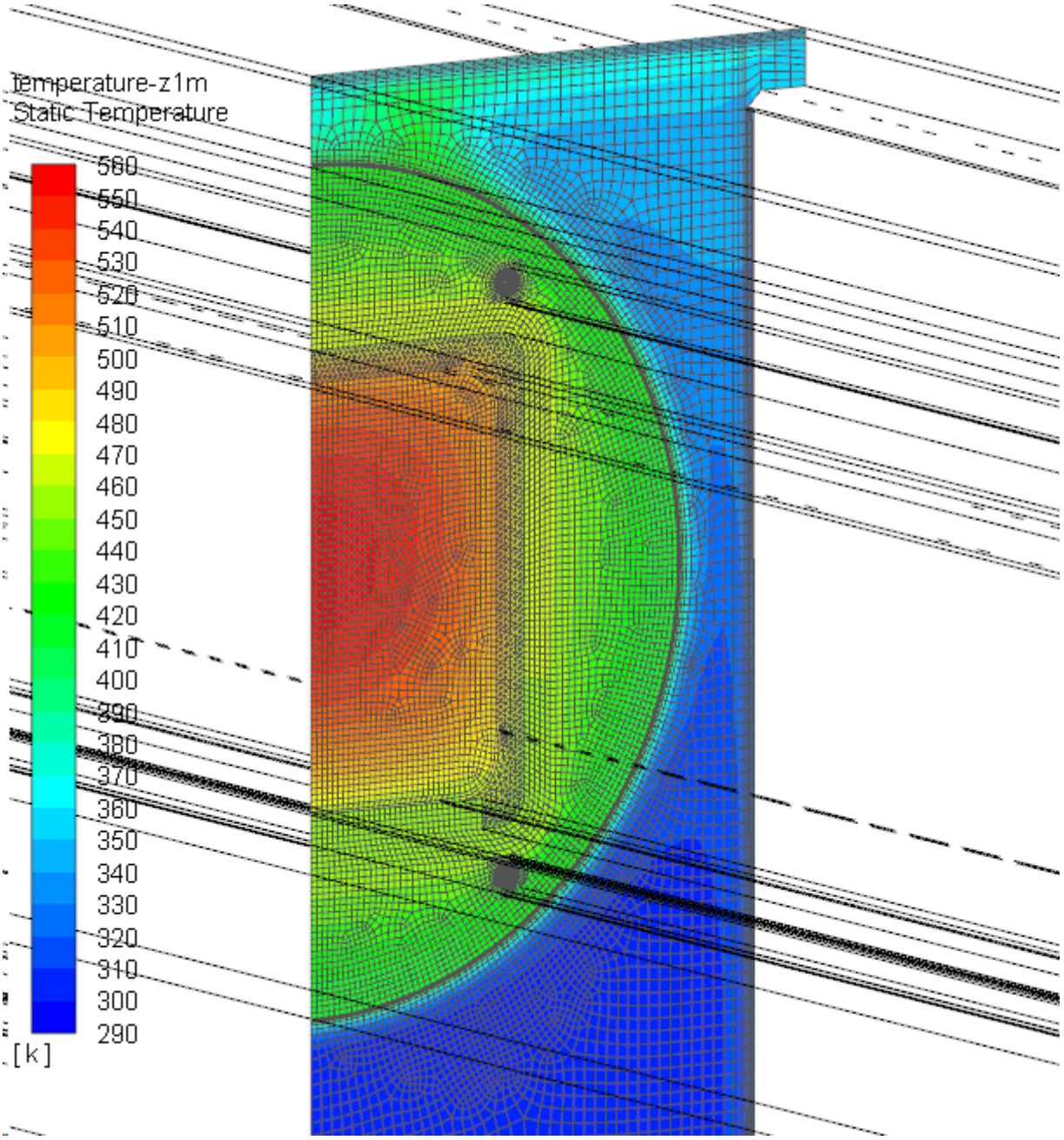

Figure C.4 Contours of temperature (K) and view of mesh at z = 1.000m for the 2.5 kW, 100 kPa, He case.

C.2 Model Validation and Uncertainty Quantification

Uncertainty quantification was performed for the 10 cases analyzed using the techniques outlined in ASME V&V 20-2009 [ASME, 2009]. Sources of uncertainty that were considered include numerical, experimental, and simulation input uncertainty.

Sources of numerical uncertainty considered include iterative uncertainty, and spatial discretization uncertainty. For iterative uncertainty, the baseline simulation for each case was run until convergence, and then run for an additional 1000 iterations. The variation in each simulation output parameter – taken

as 2 standard deviations, or the 95% confidence interval - was taken over those 1000 iterations to provide the iterative uncertainty for each simulation output parameter.

The spatial discretization uncertainty was calculated using a GCI on three meshes: a coarse, medium and fine mesh. The fine mesh was used for the baseline case. It was found that the three meshes did not obey asymptotic convergence, which is not atypical of complex simulations that involve important boundary layer physics. Since the asymptotic convergence with the three meshes was not achieved, only the fine and medium meshes were used to calculate the GCI. Since using only two mesh sizes introduces more uncertainty into the GCI calculation, a factor of safety of 3.0 was used per ASME V&V 20-2009. The total numerical uncertainty was calculated by summing the iterative uncertainty and GCI values, since the two are not independent [ASME, 2009].

Experimental uncertainty was provided for the air mass flow rate and temperature measurements for the open cases and for these cases the provided values were used. For the blind cases, a temperature uncertainty of 1% was applied to the simulation result (as opposed to the measured value) and used as the experimental uncertainty. For the air mass flow uncertainty, an uncertainty of 1.5% of the simulation result of air mass flow was used, which is consistent with the uncertainty that was provided in the open cases.

The input uncertainty – or the uncertainty in the simulation result due to uncertainty in the simulation inputs – was calculated for 8 different simulation inputs that were deemed to be the largest contributors to the total simulation uncertainty:

- Heat input
- External heat transfer coefficient
- Inlet straightener hydraulic resistance
- Fuel hydraulic resistance
- Orientation angle relative to vertical
- Filled 0.9 mm gap between the channel box and aluminum bridge plate
- Ambient temperature
- Emissivity values

For the filled 0.9 mm gap in the channel box that provides extra thermal resistance in heat travelling into the aluminum bridge plate, this was a binary sensitivity study as to whether the gap was present, as in the baseline simulation, or if there was no gap. For all other cases, the inputs were perturbed both higher and lower by the amount of the uncertainty in the input.

For the heat input and the ambient temperature, the uncertainties in the input values were provided with the boundary conditions for each case. For many of the other inputs, uncertainty in the input values were not provided, and in some cases the input values themselves were not provided either, which increases the uncertainty in these inputs. In these cases, a reasonable estimate of the uncertainty in these input values was assumed as described below.

When ambient temperatures were perturbed higher and lower, the ambient density was also modified accordingly. This ensures that an artificially high or low mass flow rate would not be induced through the vault via the constant pressure inlet and outlet boundaries, which are at different elevations relative to each other. Changes in barometric pressure would also have this effect, but sensitivity testing demonstrated that the range of natural variation in barometric pressure at the test location had a negligible effect on the air mass flow rate and temperatures within the HDCS compared to the other inputs that were evaluated.

The external heat transfer correlations that were calculated based on Nusselt number correlations using the wall temperature and geometric configuration of the vault were assumed to be accurate to within ±33%. The straightener hydraulic resistance, provided as a simulation input [Lindgren *et al*., 2019], was assumed to have an uncertainty of ±30%. The hydraulic resistance of the fuel bundle, an input to the porous media properties in the simulation, was assumed to have an uncertainty of ±50%.

The orientation angle of the HDCS installation relative to vertical was assumed to be ±1° with respect to the z-axis. In the open tests, the results were found to be quite insensitive to changes in orientation of 1°, so these sensitivity tests were not included in the 8 blind cases.

The uncertainty in many of the emissivity values were provided with the problem setup description [Lindgren *et al*., 2019] and were all measured with the same type of instrument. Since the same instrument was used to measure the emissivity values, the uncertainty in the separate emissivity measurements were considered to be correlated with each other. When evaluating the uncertainty due to emissivity values, all emissivity values were perturbed higher and lower together, resulting in a colder and hotter condition within the HDCS, respectively. A notable exception to the emissivity values used is the upper uncertainty in Inconel emissivity. The measured value of Inconel emissivity provided for the experiment was 0.61±0.07 [Lindgren *et al*., 2019]. The same baseline value and lower value were used in the simulation; however, an upper value of 0.9 was used to represent fully oxidized Inconel after exposure to heating within the test apparatus.

The uncertainties due to each of these 8 inputs were presumed to be independent of each other, so the total input uncertainty was calculated using root mean square summation. The dominant input uncertainty for temperature measurements in all cases was found to be the uncertainty in emissivity.

Quantifying the uncertainty for each of the 10 test conditions required 18 separate simulation runs for each of the open cases, and 16 separate runs for each of the blind cases (because the orientation angle was omitted from these cases). This included 3 cases for grid sensitivity (including the baseline case on the fine mesh), as well as 15 or 13 input sensitivity cases. This is a large number of simulations to run.

Input sensitivity runs were not completed for 3 cases: 1.0 kW air at 100 kPa, 1.0 kW He at 100 kPa, and 0.5 kW He at 800 kPa. Instead, the overall input uncertainty values were interpolated from neighboring conditions for the two 1.0 kW conditions. For the 0.5 W He at 800 kPa, the input uncertainty was assumed to be the same as the 0.5 kW He at 100 kPa condition on the basis that the 5.0 kW He, 800 kPa condition had a lower input uncertainty than the 5.0 kW He, 100 kPa condition.

C.3 Lessons Learned

The numerical uncertainty due to iterative uncertainty was low for all cases. In areas where the temperature gradients were low, such as at the location of the PCT, the spatial discretization uncertainty was also quite low. However, in areas with high temperature gradients such as the top of the fuel assembly, the spatial discretization error became one of the largest sources of error.

The main source of uncertainty in the simulation was the uncertainty in emissivity values. This makes sense, as radiation is the primary mode of heat transfer within the fuel bundle – particularly using air as the fill gas. There are many different facets to the radiation heat transfer within the HDCS apparatus, and with all of them evaluated together it does not provide any insight as to which facet is responsible for the greatest component of uncertainty. As follow-on work, a sensitivity study will be conducted for the two open cases to determine the contribution of the uncertainty in emissivity for each material separately, to determine the largest contributing factor. This will include modifying the k_{eff} value for each assessment.

During the open validation period, it became clear that the simulation results are sensitive to many of the inputs and geometric assumptions. Many times, during validation, the simulation result would appear to be close to the experimentally measured value, only to find upon further refinement that there were offsetting errors. It was very helpful to have an abundance of data for use in validation to identify where the simulation was matching experimental results, and where it was not. This greatly helped to isolate areas of the model that were in need of scrutiny.

C.4 References

American Society of Mechanical Engineers, "ASME V&V 20-2009 – Standard for Verification and Validation in Computational Fluid Dynamics and Heat Transfer," New York, NY, November 2009.

Durbin, S.G. and E.R. Lindgren "Materials and Dimensional Reference Handbook for the Boiling Water Reactor Dry Cask Simulator," Sandia National Laboratories, Albuquerque, New Mexico, 2017.

Hall, K., A. Zigh, and J. Solis, "CFD Validation of Vertical Dry Cask Storage System", NUREG/CR-7260, U.S. Nuclear Regulatory Commission, Washington, DC, 2019.

Lindgren, E.R., S.G. Durbin, R.J.M. Pulido, and A. Salazar, "Update on the Thermal Hydraulic Investigations of a Horizontal Dry Cask Simulator", Sandia National Laboratories, Albuquerque, New Mexico, 2019.

TRW Environmental Safety Systems, Inc., "Spent Nuclear Fuel Effective Thermal Conductivity Report," TRW Environmental Safety Systems, Inc. 1996.

Zigh, A. and S. Gonzalez, "Validation of Computational Fluid Dynamics Methods Using Prototypic Light Water Reactor Spent Fuel Assembly Thermal-Hydraulic Data," NUREG-2208, U.S. Nuclear Regulatory Commission, Washington, DC, 2017.

Zigh, A. and S. Gonzalez, "Validation of Computational Fluid Dynamics Method Using Vertical Dry Cask Simulator Data," NUREG-2238, U.S. Nuclear Regulatory Commission, Washington, DC, 2020.

Zigh A. and J. Solis, "Computational Fluid Dynamics Best Practice Guidelines for Dry Cask Applications," NUREG-2152, U.S. Nuclear Regulatory Commission, Washington, DC, 2013.

Zigh, A. and J. Solis, "Impact of Variation in Environmental Conditions on the Thermal Performance of Dry Storage Casks," NUREG-2174, U.S. Nuclear Regulatory Commission, Washington, DC, 2015.

APPENDIX D PNNL MODELS

D.1 Model Information Summary

Three different thermal analysis models were developed to simulate the horizontal dry cask simulator (HDCS). The HDCS is an experimental setup to simulate a single boiling water reactor fuel assembly under a variety of different heat loads and internal pressures. Also, cases were run with both air and helium as the canister fluid. The models include a detailed STAR-CCM+ model, half symmetry porous STAR-CCM+ model, and a COBRA-SFS model. The detailed STAR-CCM+ model explicitly modeled the fuel assembly where the porous STAR-CCM+ model replaced the fuel region with a solid region and effective thermal conductivity. Also, half of the HDCS was modeled in the porous model using a symmetry condition.

D.1.1 Brief introduction of CFD code

D.1.1.1 Software description (Name, version)

For this modeling effort Siemens PLM Software, STAR-CCM+ version 2019.1 was used for the full detailed and half porous models. STAR-CCM+ is a full featured computational fluid dynamics software.

In addition to STAR-CCM+, COBRA-SFS version 5.0.0 was utilized for an additional model. COBRA-SFS is a computational fluid dynamics software built specifically for thermal modeling of spent fuel casks.

D.2 Model description

D.2.1 Representation of fuel assembly

D.2.1.1 Detailed

All parts of the fuel assembly, except for the heater rods, were explicitly modeled. The parts in the detailed fuel assembly included the full and partial length heater rods, the tie plates, water rods, and spacers. The heater rod is made up of Incoloy cladding, magnesium oxide (MgO) and Nichrome elements, and carbon steel pins. Each heater rod is modeled as a single volume in the CAD geometry and effective material properties were calculated and applied to the heater rods. The flow straighteners located near each inlet entrance were not modeled explicitly but were instead modeled as a porous flow region.

The CAD geometry is shown in Figure D.1. Due to asymmetries in the fuel assembly, the detailed model is a full 360-degree model.

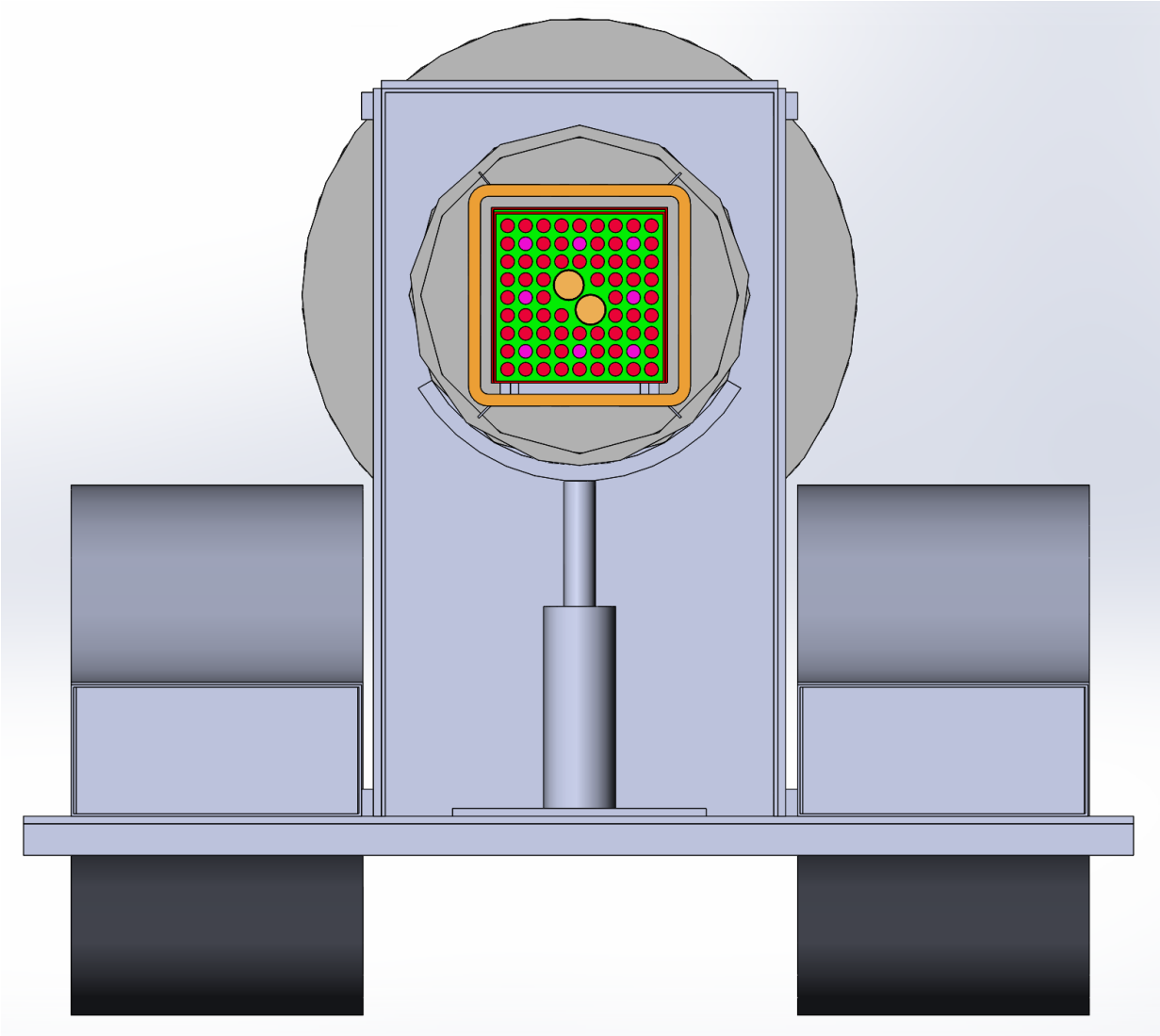

Figure D.1 CAD geometry of HDCS – radial cross-sectional view at 75 inches from the top of the bottom plate.

D.2.1.2 Half Porous

For the STAR-CCM+ porous media model, the detailed fuel assembly in the previous detailed model was replaced by a porous media region with an effective thermal conductivity to represent the fuel assembly and the surrounding fluid. In the porous model, the asymmetric details that were in the detailed model have now been simplified allowing for use of a half symmetry boundary condition. Figure D.2 shows the HDCS geometry for the STAR-CCM+ half porous model.

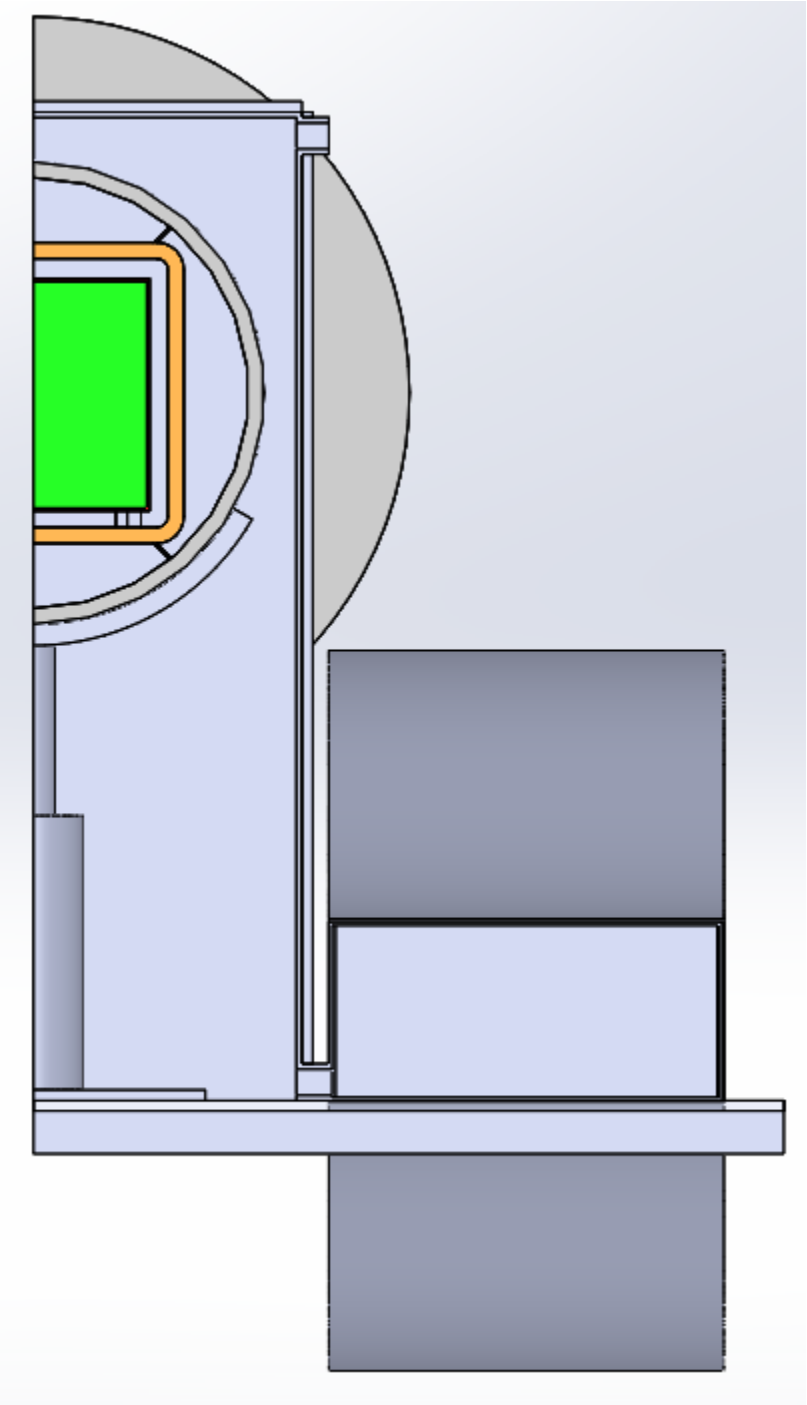

Figure D.2 STAR-CCM+ half porous model geometry

D.2.1.3 COBRA-SFS

Figure D.3 shows a representation of the 9×9 BWR fuel assembly used in the HDCS. The yellow highlighting shows rods and subchannels that represent the water rods. For the COBRA-SFS model, these are modeled by blocking the channels occupied by the water rods and turning off heat generation in the affected rods. This approach sufficiently represents both the true hydraulic resistance of the assembly and the heat generation distribution. There are also eight part-length rods shown in red in Figure D.3.

Hydraulically these rods are represented as full-length rods. This simplification is generally applicable to a horizontal spent fuel system because the flow and heat transfer due to convection will be minimal in this scenario. The heat generation changes from the part length rods are accounted for as described below.

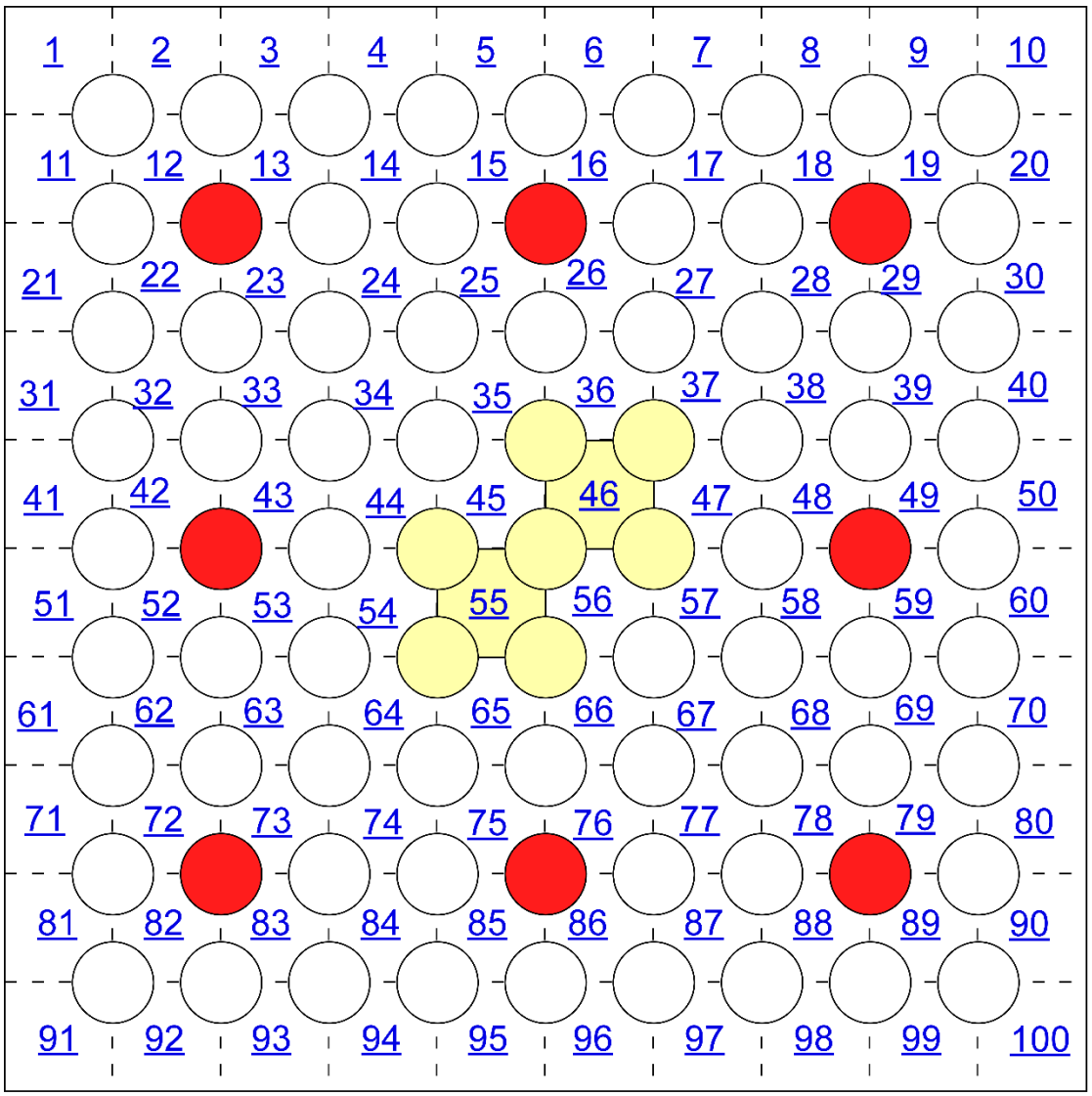

Figure D.3 Rod and subchannel array diagram for COBRA-SFS model of the 9×9 BWR fuel assembly. (Not to scale; yellow represents water rods, red represents part-length rods; channels numbered, rod numbers not shown.)

Heat generation of each rod was modeled individually and used a flat profile along the designated active length. Although this profile is not typical of spent fuel the overall behavior of the model is not greatly affected in this case. Partial length rods in the HDCS were accounted for with two adjustments to the standard power profile. First, the partial length rod power generation was decreased according to their relative worth. Second the axial power profile was changed to reflect the overall power profile of the assembly (Figure D.4). This simplification still results in too much power input to the top part of the assembly, but it does help COBRA-SFS model the overall system behavior more accurately. In the future, a code change to adjust axial power on an individual rod basis is planned that will allow a more direct

simulation of BWR assembly power. In this case, there is not a significant loss in predictive capability of the model because the assembly does not include an excessive amount of partial length rods.

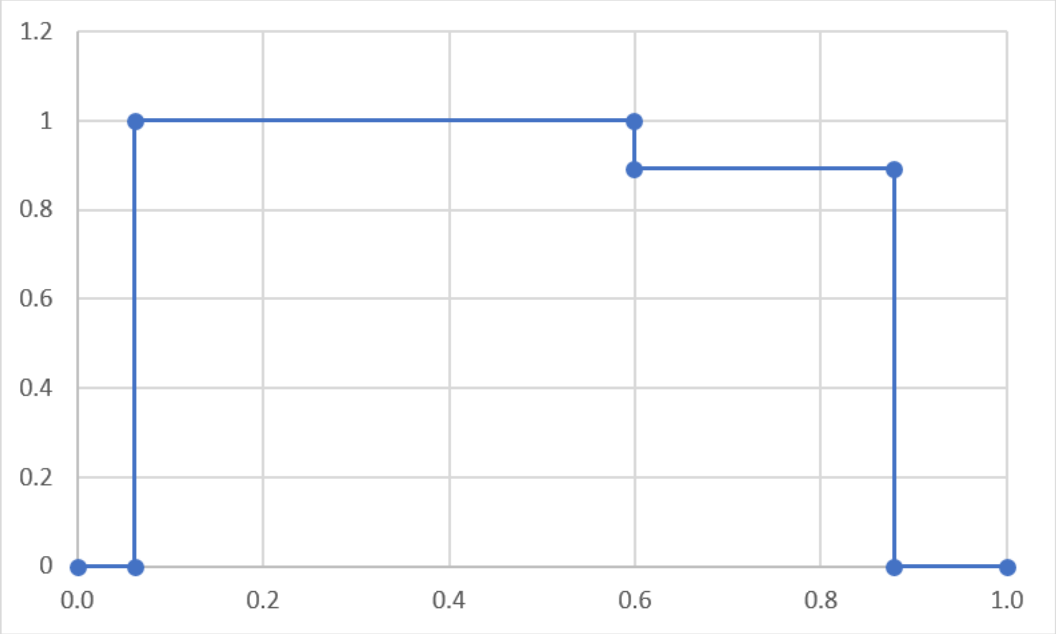

Figure D.4 Normalized axial power profile.

D.2.2 Representation of DCS structures

D.2.2.1 STAR-CCM+ geometry

The geometry for the detailed CFD model was generated using the commercial computer aided design (CAD) software SolidWorks (Dassault Systems SolidWorks Corp., 2019). The CAD geometry was constructed from drawings and details listed in the Sandia National Laboratories (SNL) report on the HDCS [Lindgren *et al.*, 2019] and the DCS handbook [Lindgren and Durbin, 2017]. The flow straighteners were modeled as porous regions with flow resistances calculated from a detailed sub-model of the flow straightener. This was done to increase computational efficiency. The rest of the components of the cask were modeled explicitly. Figure D.5 and Figure D.6 show the exterior geometry of the STAR-CCM+ models. These images represent the porous model from the channel box outward, except that a half-symmetry boundary condition is applied.

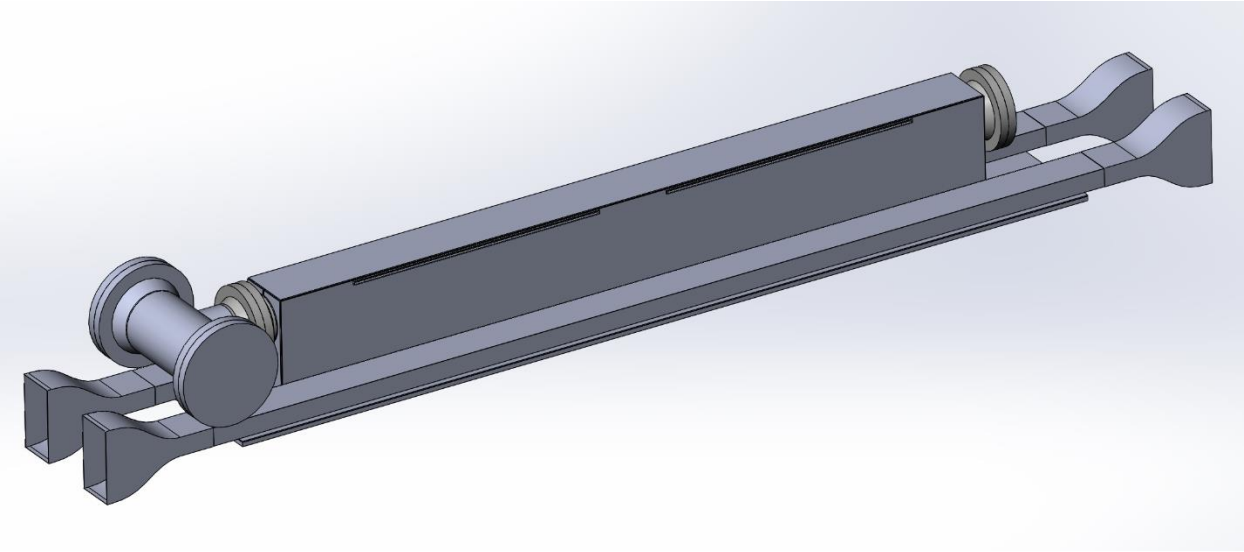

Figure D.5 CAD geometry of STAR-CCM+ detailed HDCS model – exterior view.

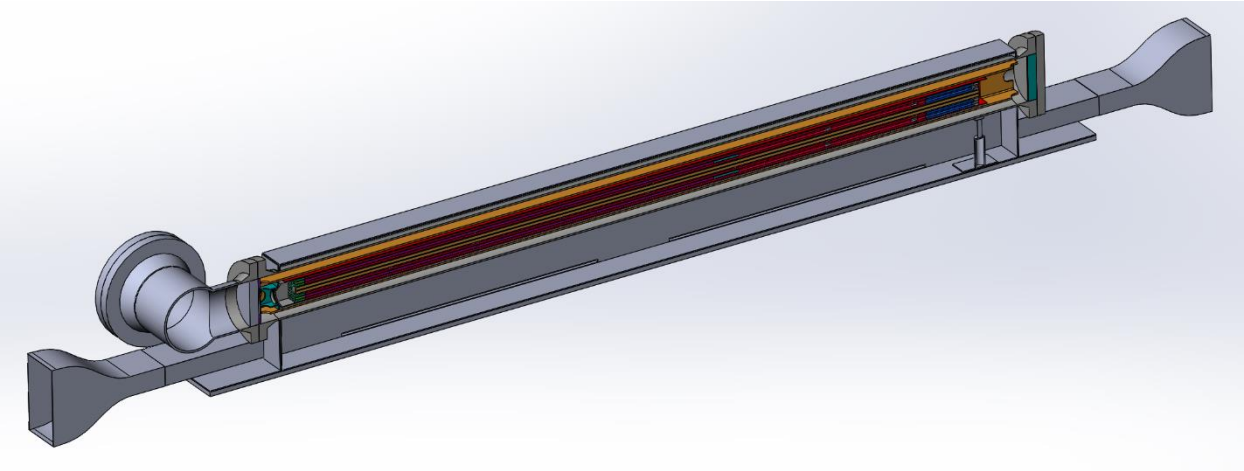

Figure D.6 CAD geometry of STAR-CCM+ detailed HDCS model – axial cross-sectional view.

D.2.2.2 STAR-CCM+ Meshing - Detailed

The SolidWorks geometry was imported into STAR-CCM+. The geometry was then meshed into regions connected by interface boundaries, resulting in a single conformal polyhedral volume mesh across all regions. The mesh contained a total of 21,707,813 cells, 110,963,765 faces, and 89,673,183 vertices. Along each wall/fluid interface, the mesh contains a prism cell layer to improve the accuracy of the flow solution near the walls. The prism cell layer consists of orthogonal prismatic cells adjacent to the wall boundaries. The prism cell layer was two cells thick. Figure D.7 and Figure D.8 show the resulting mesh for the detailed model.

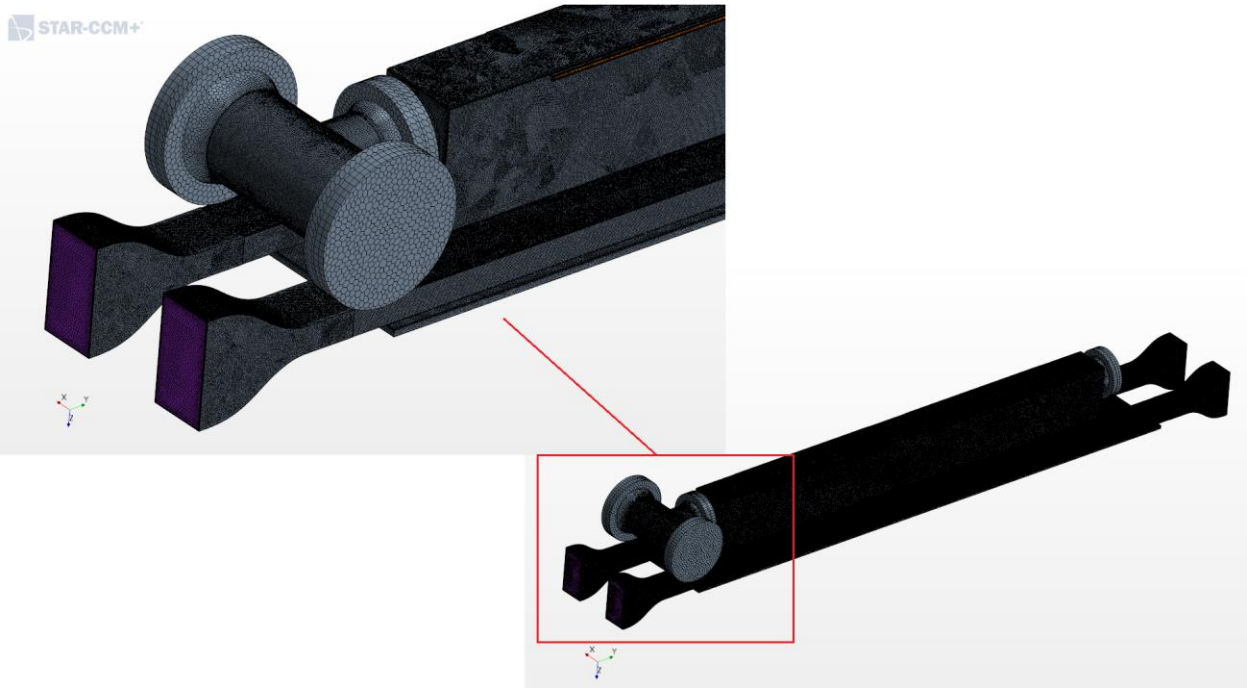

Figure D.7 Mesh for detailed model – external view.

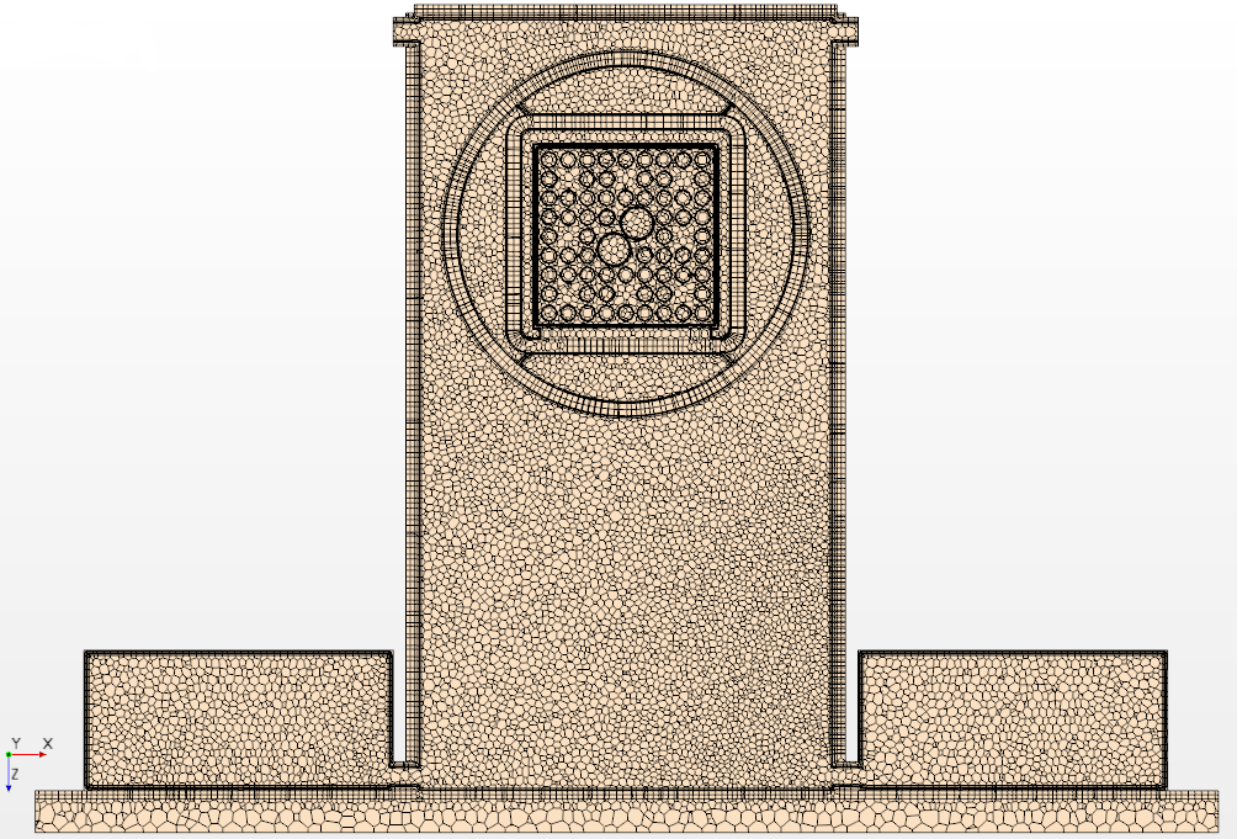

Figure D.8 Mesh for detailed model – radial cross-sectional view at 75 inches from the top of the bottom plate.

D.2.2.3 STAR-CCM+ Meshing - Half Symmetry Porous

The mesh for the half porous model requires significantly fewer cells than the detailed STAR-CCM+ model. The half porous model mesh consists of 3,034,188 cells, 17,103,960 faces, and 14,332,983 vertices. A cross section of the mesh used in this model is shown in Figure D.9. This coarser mesh increases the computational efficiency and makes sensitivity analysis more practical.

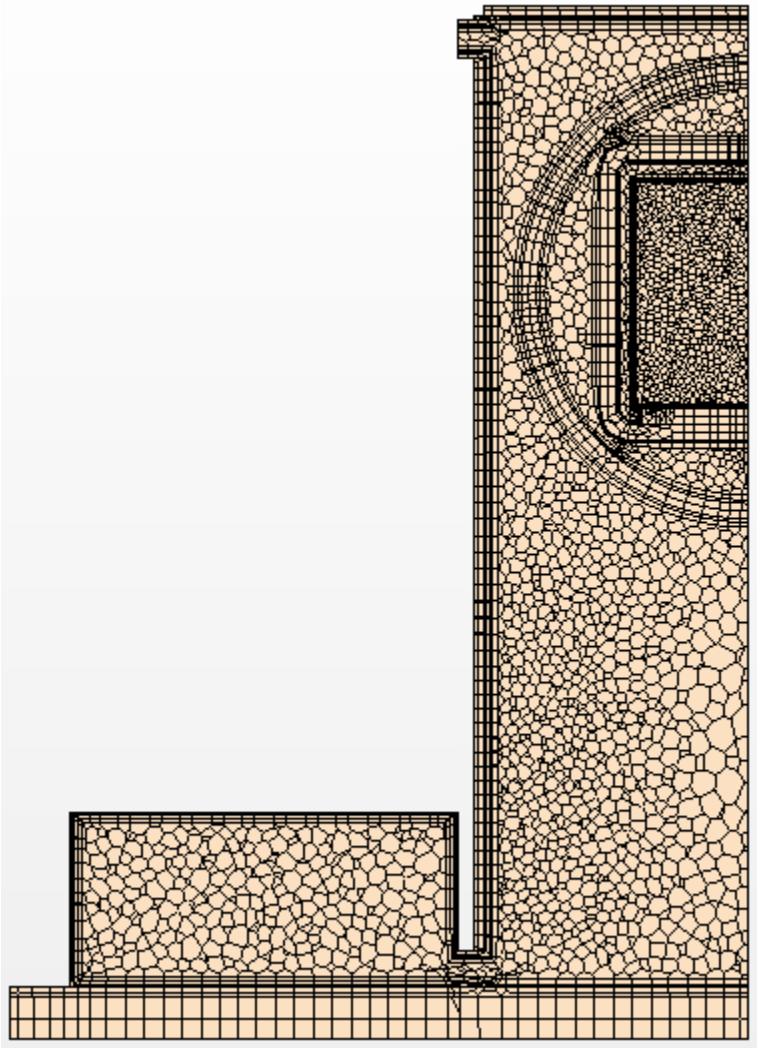

Figure D.9 Half porous mesh.

D.2.2.4 COBRA-SFS Geometry and Noding

COBRA-SFS has an input structure and solution method that takes into account the features of a spent fuel storage system and makes engineering simplifications to reduce complexity while still providing highly resolved model results where needed. The code uses what is often termed a 2.5-dimensional representation of the main region of the cask. This approach is chosen because heat transfer is primarily in the radial direction for spent fuel casks and they have an axially consistent geometry that is readily divisible into control volumes defined by axial length. In a typical full-size system, a sufficiently detailed model will result in approximately 1000 user defined solid nodes per axial level. Additional refinement is not generally useful and becomes impractical due to the large amount of manual input for defining thermal connections.

In the case of the HDCS, the small size would make it possible to refine the model with an extreme amount of detail and stay within practical limits for the user and the code. However, for the purposes of this modeling exercise, the model employed here uses only 32 solid nodes at a given level. 50 axial levels were used for this model which proved sufficient to capture the axial temperature profile of the HDCS. The node map for the simulator is shown in Figure D.10. Nodes 17-24 encompass the canister boundary. Stabilizer tubes (nodes 29-32) are modeled as an effective thermal conductivity with the appropriate fill gas and the metal that they are made of. Note that nodes 11, 12, 15, and 16 are connected to the canister wall even though it is not obvious from the diagram. No axial variations in the materials were explicitly modeled. However, intermittent contact was factored into decision about gap resistance values that are used.

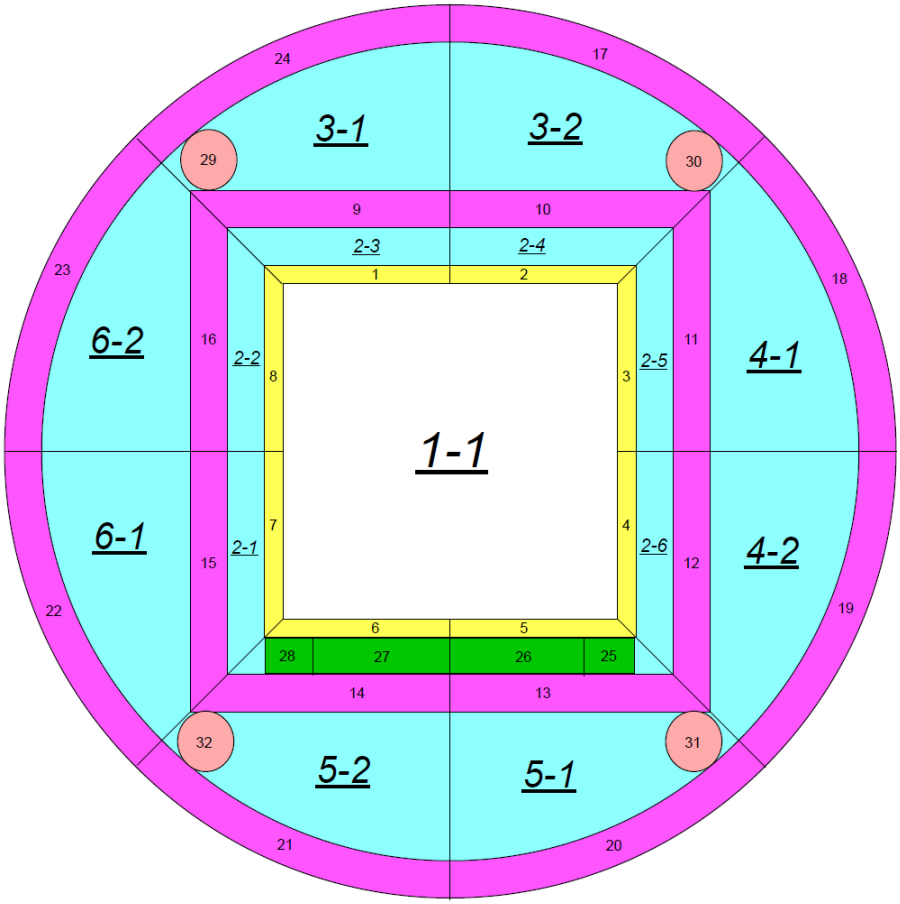

Figure D.10 Cross-section of the COBRA-SFS model representation of the HDCS. (Not to scale.)

D.2.3 Approximations and treatments

D.2.3.1 Internal fuel assembly treatment – Detailed STAR-CCM+ model

A laminar flow model was applied to the internal helium and air region within the canister, which included flow within the fuel assembly. The Boussinesq model, which provides a buoyancy source term when there are small variations of density due to temperature variations, was applied to the fluid inside the canister. Internal radiation was included in the helium gas and air regions, and the emissivity values applied along the inner surfaces were taken from the DCS handbook [Lindgren and Durbin, 2017]. The heat load was assumed to be uniform across the full and partial length heater rods.

D.2.3.2 Internal fuel assembly treatment – STAR-CCM+ half symmetry porous model

For the STAR-CCM+ half symmetry model, the internal fuel assembly region was treated as a solid with an effective thermal conductivity. It was assumed that there is no flow through the assembly.

D.2.3.3 Internal fuel assembly treatment – COBRA-SFS model

Flow within the assembly is modeled as laminar or turbulent based on the Reynolds number of the channels. However, in practice this flow is primarily laminar. All heat transfer pathways are based off the given geometry. Radiation heat transfer is modeled with 2-D view factors that are then resolved axially. This approach is applicable as long as the enclosures are relatively slender compared to their width. All flow losses are either derived from past modeling experience or accepted book values.

D.2.4 Basis for Additional Heat Transfer Treatments

D.2.4.1 Detailed STAR-CCM+ and COBRA-SFS fuel assemblies

The detailed STAR-CCM+ and COBRA-SFS models explicitly modeled the fuel assemblies.

D.2.4.2 Porous STAR-CCM+ effective thermal conductivity

Effective thermal conductivities (k_{eff}) were calculated separately for radial and axial heat transfer in the homogeneous region representing the fuel assembly. The radial effective thermal conductivity includes both conduction and thermal radiation. The axial effective thermal conductivity includes conduction only, neglecting any contribution from thermal radiation. These effective thermal conductivities are used for the overall effective thermal conductivity of the fuel region. Convective heat transfer within the rod array is neglected in the HDCS porous model.

D.2.4.3 Axial k_{eff} model

The axial k_{eff} value for the fuel region was calculated assuming a volume averaging scheme. The heater rods, water rods, top tie plate, spacers and gas volumes were considered when calculating effective axial thermal conductivity. A separate axial k_{eff} was calculated for helium and air-filled gas volume within the fuel region. Table D.1 and Table D.2 lists the resulting axial k_{eff} for the fuel assembly.

Table D.1 Axial k_{eff} for fuel assembly with helium.

Temperature (K)	Thermal Conductivity (W/m-K)
300	2.2179
450	2.6127
650	3.0554
850	3.4931
1050	3.9443

Table D.2 Axial k_{eff} for fuel assembly with air.

Temperature (K)	Thermal Conductivity (W/m-K)
300	2.1394
450	2.5086
650	2.9215
850	3.3324
1050	3.7649

D.2.4.4 Radial k_{eff} model

For a uniform boundary temperature at the wall and a uniform heat generation rate, the radial effective thermal conductivity can be expressed as [TRW, 1996]:

$$k_{eff} = \frac{0.2947Q}{4L_a(T_c - T_{wall})} \quad \text{D-1}$$

Where

Q = total decay heat in the assembly

L_a = active fuel length for the assembly

T_c = peak (center) temperature of the homogeneous cross-section

T_{wall} = uniform wall temperature

The equation gives the radial effective thermal conductivity of an assembly as a function of assembly decay heat, assembly peak temperature, and the enclosing wall temperature. The assembly decay heat is a known quantity, but the assembly wall and peak temperatures are not. To develop an appropriate radial effective thermal conductivity for the HDCS fuel assembly, a detailed model of the fuel assembly was created, and the peak assembly temperature was solved for various heat loads and wall temperature

boundaries. Two different models were run: one with helium as the gas within the fuel assembly and one with air as the gas within the fuel assembly.

A 2-D model of the fuel assembly was set up in STAR-CCM+ to determine the radial effective fuel thermal conductivity. Two different STAR-CCM+ 2-D models were set up, one that included the full array of rods (full length and partial length rods) and one that did not include the partial length rods (partial array). The emissivity of the zircaloy channel box, which is the outer temperature boundary for the fuel assembly model, was measured and found to vary with axial position [Durbin and Lindgren, 2017]. This axial distribution in emissivity of the channel box is not typical of BWR spent fuel assemblies; rather, it is a result of previous test history. For the 2-D models an average emissivity value must be used since it is a cross-section of the fuel assembly and has no axial geometry. The emissivity was averaged over multiple axial sections of the full array and partial array lengths for the respective STAR-CCM+ models (air and helium). This resulted in multiple k_{eff} correlations based on the average emissivity. The radial k_{eff} values located from 0 to 2.438 m (0 to 96 in.) along the axial length represent the full array region, and the values located from 2.438 to 3.658 m (96 to 144 in.) represent the partial array region. The resulting k_{eff} values for helium and air-filled fuel assemblies are shown in Table D.3 and Table D.4.

Table D.3 Radial k_{eff} for HDCS helium filled fuel assembly.

Axial Location (inches)	**Average Emissivity -**	**Radial K_{eff} (W/m-K)**
0-36	0.17	2.008E-6*T^2+1.569E-4*T+0.2209
36-60	0.262	2.623E-6*T^2-2.710E-4*T+0.303
60-84	0.43	3.638E-6*T^2-9.815E-4*T+0.4404
84-96	0.54	4.007E-6*T^2-1.180E-3*T+0.4726
96-120	0.615	5.182E-6*T^2-1.668E-3*T+0.5538
120-144	0.651	5.346E-6*T^2-1.772E-3*T+0.5728
144-156	0.531	4.778E-6*T^2-1.417E-3*T+0.5086

*T = temperature

Table D.4 Radial k_{eff} for HDCS air-filled fuel assembly.

Axial Location (inches)	Average Emissivity -	Radial K_{eff} (W/m-K)
0-36	0.17	2.014E-6*T^2-7.688E-4*T+0.1911
36-60	0.262	2.805E-6*T^2-1.262E-3*T+0.2787
60-84	0.43	3.881E-6*T^2-1.899E-3*T+0.3886
84-96	0.54	4.422E-6*T^2-2.204E-3*T+0.4397
96-120	0.615	5.564E-6*T^2-2.725E-3*T+0.5201
120-144	0.651	5.739E-6*T^2-2.820E-3*T+0.5358
144-156	0.531	5.112E-6*T^2-2.475E-3*T+0.4786

*T = temperature

D.2.5 Basis for fuel assembly flow losses

Flow losses for the fuel assembly in the porous STAR-CCM+ model were calculated using an isothermal model of the assembly and flow channel. The geometry for the fuel assembly in the detailed STAR-CCM+ model was used for the isothermal sub-model.

D.2.6 External HDCS structure treatment

D.2.6.1 STAR-CCM+ models

A "Standard K-ε Low-Re" flow model was applied to the air region within the HDCS. Internal radiation was included in the air gas regions and the emissivity values were applied along the inner surfaces.

D.2.6.2 COBRA-SFS models

The external DCS structure was omitted from the COBRA-SFS model due to the nature of the program. In lieu of the external DCS structure, canister surface temperatures from the STAR-CCM+ detailed model were used as a boundary condition.

D.2.7 Input parameters

D.2.7.1 STAR-CCM+ models

The properties used for helium and air are listed in Table D.5 through Table D.7. The material properties for the solid parts in the model were taken from the DCS handbook [Lindgren and Durbin, 2017]. These are shown in Table D.8 through Table D.11. The effective properties for the heater rods were calculated based on volume weighted averaging of the Incoloy cladding and MgO. The Nichrome and carbon steel pins only represent a small percentage of the overall volume of the heater rod and were therefore neglected in the overall effective property calculation. The effective material properties for the heater rods is listed in Table D.12.

Table D.5 Air thermal conductivity.

T (K)	k (W/m-K)
294	0.0251
311	0.0264
422	0.0339
533.15	0.0405
644	0.0469
755	0.0531

Table D.6 Air kinematic viscosity.

T (K)	V (m^2/s)
100	7.11E-06
200	1.33E-05
300	1.85E-05
400	2.30E-05
500	2.70E-05
600	3.06E-05
700	3.39E-05
800	3.70E-05
900	3.98E-05
1000	4.24E-05

Table D.7 Helium properties.

T (K)	Thermal Conductivity (W/m-K)	Kinematic Viscosity (m^2/s)
100	0.073	9.63E-06
120	0.0819	1.07E-05
140	0.0907	1.18E-05
160	0.0992	1.29E-05
180	0.1072	1.39E-05
200	0.1151	0.000015
220	0.1231	0.000016
240	0.13	0.000017
260	0.137	0.000018
280	0.145	0.000019
300	0.152	1.99E-05
350	0.17	2.21E-05
400	0.187	2.43E-05
450	0.204	2.63E-05
500	0.22	2.83E-05
600	0.252	0.000032
650	0.264	3.32E-05
700	0.278	0.000035
750	0.291	3.64E-05
800	0.304	3.82E-05
900	0.33	4.14E-05
1000	0.354	4.46E-05

Table D.8 Carbon steel thermal conductivity.

T (K)	k (W/m-K)
273.15	45.4
373.15	44.2
473.15	43.7
573.15	40.8
673.15	38.6
773.15	36.0
873.15	33.1
973.15	29.9
1076.8	26.1

Table D.9 Kaowool thermal conductivity.

T (K)	k (W/m-K)
273.15	0.0208
373.15	0.0345
473.15	0.0502
573.15	0.0681
673.15	0.088
773.15	0.11
873.15	0.134
973.15	0.16
1073.15	0.188
1173.15	0.219

Table D.10 Stainless steel thermal conductivity.

T (K)	k (W/m-K)
300	13
400	14.6
500	16.2
600	17.8
700	19.4
800	21.1
900	22.7
1000	24.3
1100	25.9

Table D.11 Zircaloy thermal conductivity.

T (K)	k (W/m-K)
273.15	12.1
293.2	12.6
473.2	14.5
673.2	17
873.2	19.9
1073.2	23.1

Table D.12 Heater rod properties.

Temperature (K)	Density (kg/m^3)	Specific Heat (J/kg-K)	Thermal Conductivity (W/m-K)
300	3926.15	754.99	4.149
450	3926.15	878.32	4.922
650	3926.15	942.37	5.771
850	3926.15	978.8	6.605
1050	3926.15	1006.14	7.402

D.2.7.2 COBRA-SFS

Solid material properties were taken directly from the materials and dimensions handbook provided by Sandia. The fluid properties were taken from a National Institute of Standards and Technology (NIST) reference as isobaric helium properties and air properties [NIST, 2019].

The fuel channel has a wide range of axial variation in emissivity with a minimum of 0.172 and a maximum of 0.655. This variation is atypical of BWR channels that have been in operation and are being placed in dry storage. In that case we would expect the profile to be much flatter and the magnitude to be close to the fuel's profile. This parameter becomes important at high temperatures because there is a strong radiation heat transfer path between the rods and the fuel channel. For best estimate modeling the average emissivity of 0.405 was used in the COBRA-SFS model. COBRA-SFS does not have a ready ability to vary the emissivity axially for this parameter, meaning there is no way to fully capture the effects of this simplification.

D.2.8 Initial and boundary conditions

D.2.8.1 Inlet treatment of honeycomb flow straightening – STAR-CCM+ Models

Porous flow loss coefficients are required for the porous flow straightener regions. The loss coefficients were calculated based on detailed CFD models of the flow straightener. Pressure drops have been measured for this assembly in previous experiments [Lindgren and Durbin, 2007]. Typically, measured pressure drop data is not available and calculated loss coefficients are used in the construction of a cask model. Therefore, the measured pressure drop data was not included in the HDCS model and instead the pressure drop was calculated for the porous regions.

A sub-model for the fluid region of the flow straightener was constructed. This sub-model was used to determine the pressure drop across each porous region. Figure D.11 shows the geometry for the respective flow model.

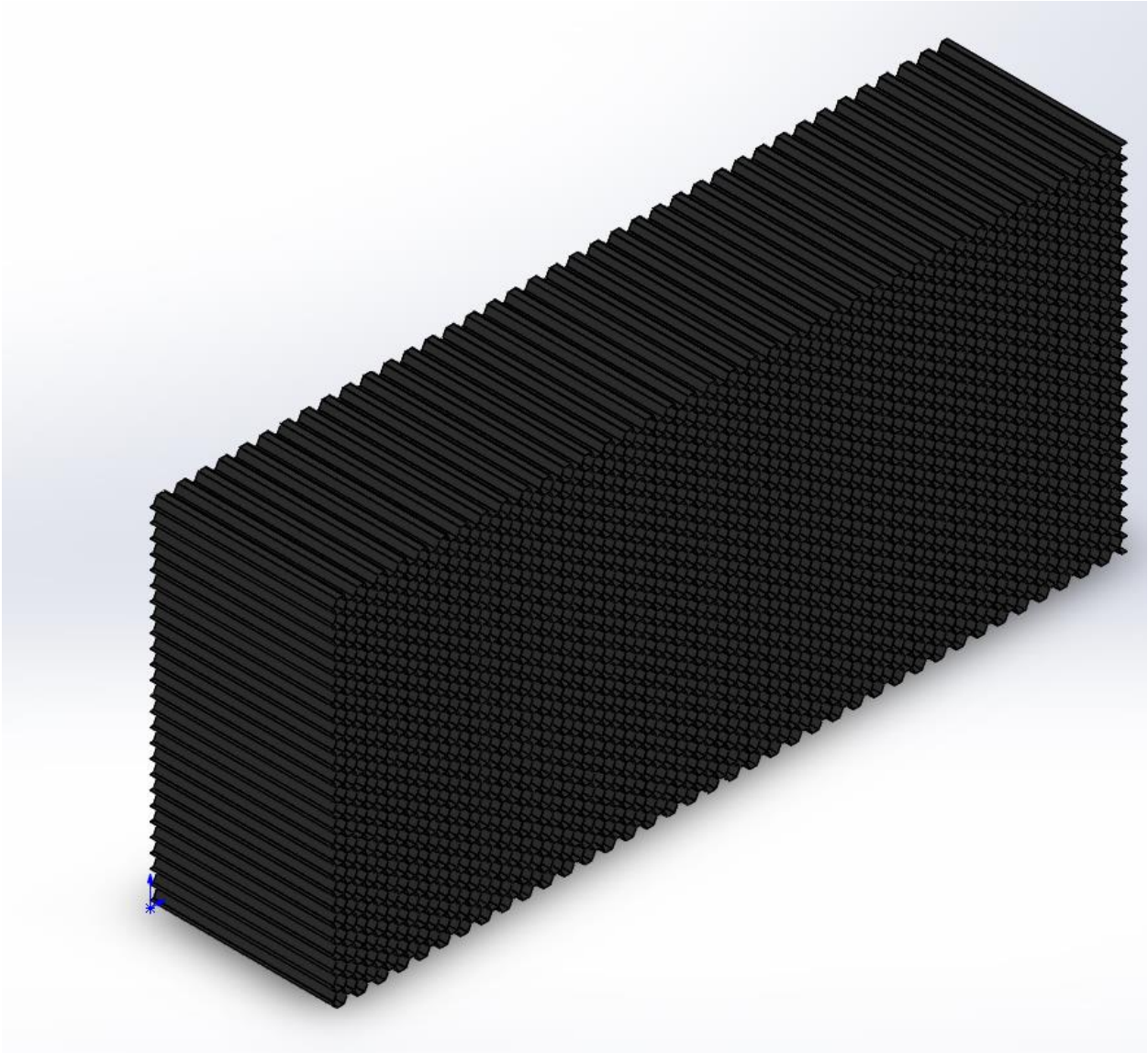

Figure D.11 Flow straightener geometry for porous flow loss model.

The STAR-CCM+ user guide (Siemens PLM Software 2018) defines the inertial and viscous coefficients in the following equation:

$$\frac{\Delta P}{L} = -(\alpha v + \beta)v \qquad \text{D-2}$$

Where

ΔP = pressure drop (Pa)

L = critical length (m)

α = inertial coefficient (kg/m^4)

v = superficial velocity (m/s)

β = viscous coefficient (kg/m^3-s)

The model was run with various inlet velocities and the resulting pressure drop per length was plotted. Figure D.12 shows the resulting plot and gives an equation for the pressure drop per length with respect to superficial velocity. The coefficients for the equation on the plots correspond to the inertial and viscous coefficients. These coefficients are listed in Table D.13.

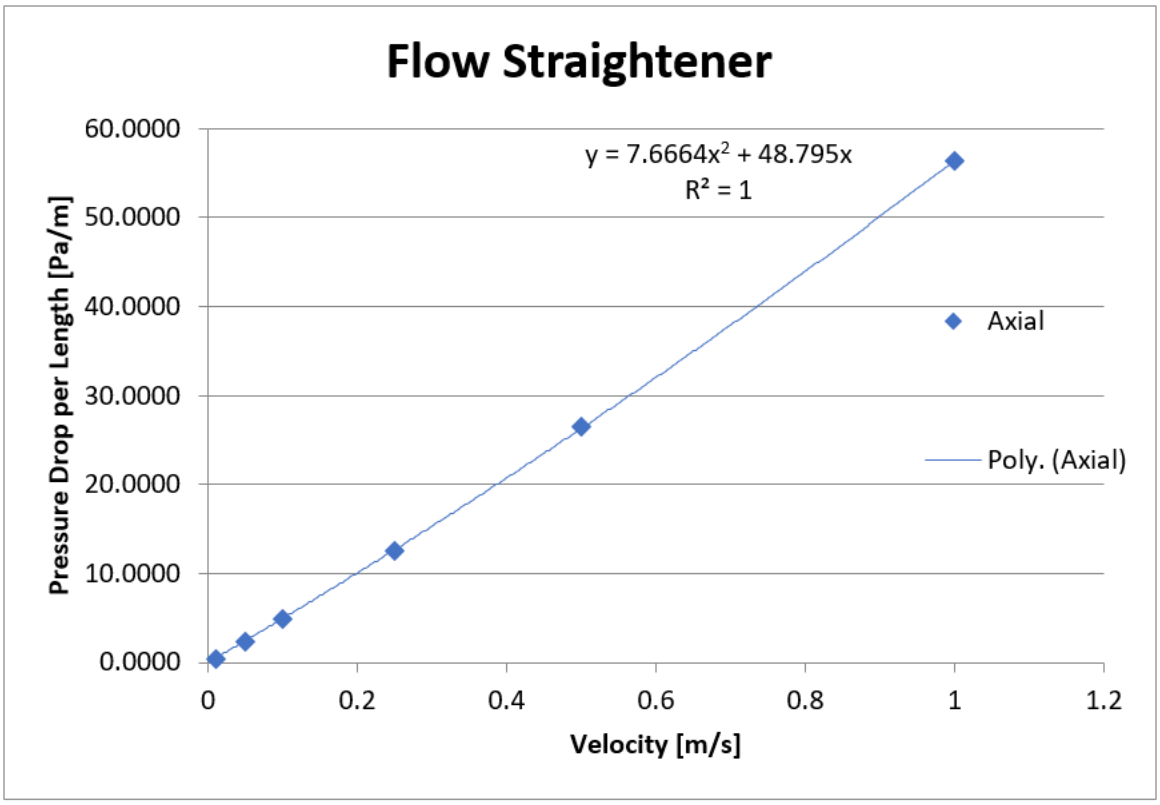

Figure D.12 Pressure drop versus superficial velocity for flow straightener model.

Table D.13 Calculated porous loss coefficients in air.

Component	Axial Inertial Coefficient α (kg/m^4)	Axial Viscous Coefficient β (kg/m^3-s)
Flow Straightener	7.67	48.80

D.2.9 Symmetry

The COBRA-SFS and detailed STAR-CCM+ models were both full models, so no symmetry boundary was used. A half symmetry model was used for the porous STAR-CCM+ model. Figure D.13 shows the geometry of the symmetry plane that was used.

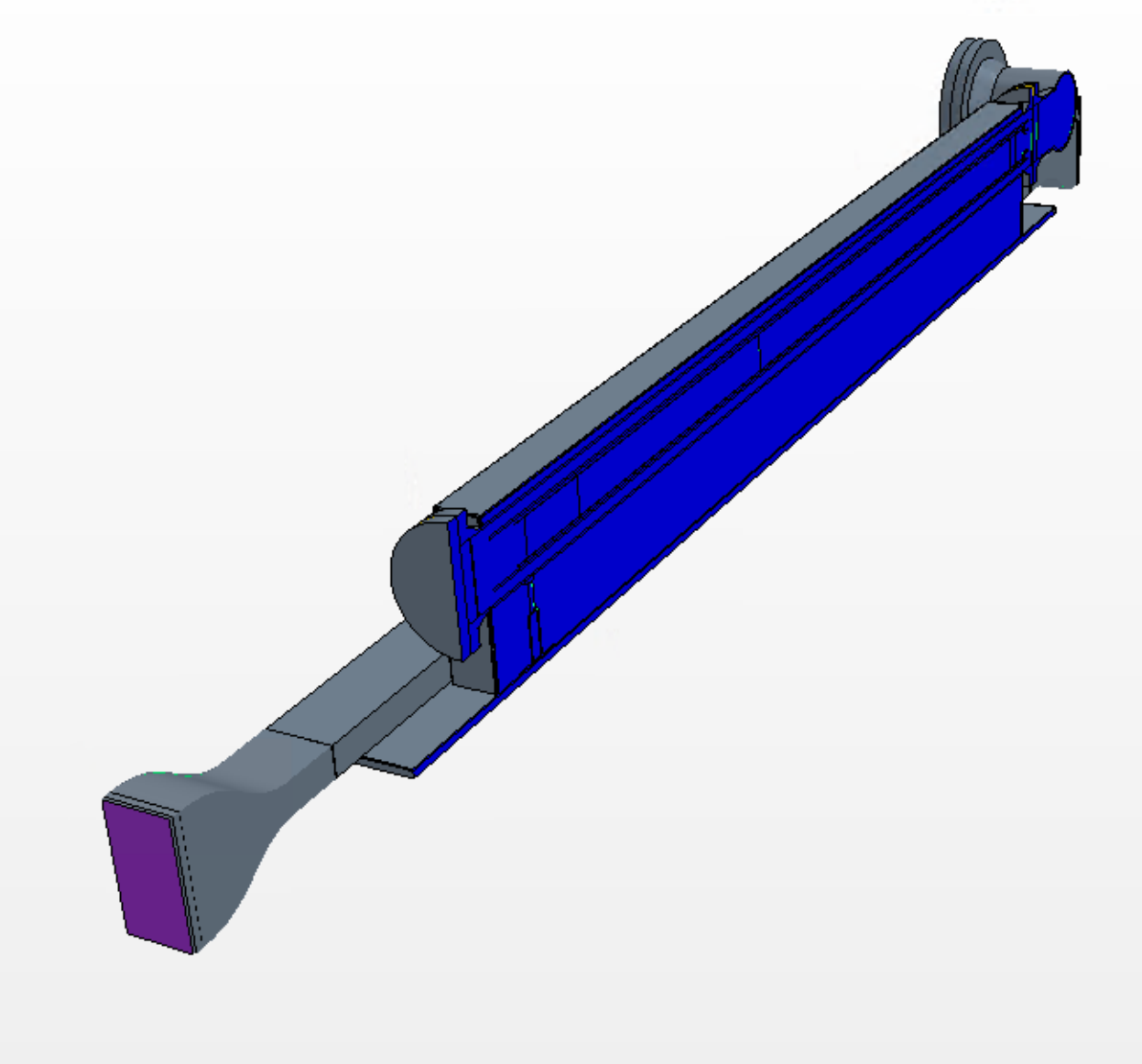

Figure D.13 Porous half symmetry model.

D.3 Model verification

D.3.1 STAR-CCM+ Grid Convergence Index (GCI) study

A mesh sensitivity study was performed on the porous half symmetry model to ensure that the mesh was sufficiently resolved. A mesh sensitivity study for the detailed model was not performed due to the very fine mesh required to adequately model the parts. The mesh sensitivity study was performed on the 2.5 Kw, 100 kPa air and helium filled canister cases for three different mesh sizes. The cell count was approximately doubled for each mesh refinement. In this modeling effort peak cladding temperature or maximum fuel region temperature was chosen as the parameter of interest for this grid convergence index study. Since peak cladding temperature occurs in the porous fuel region, the mesh refinements were focused on the porous fuel region and the canister fluid. The three successively finer meshes, shown in Figure D.14 through Figure D.16, were produced by refining the porous fuel and the canister fluid regions.

The mesh details are listed in Table D.15. All three meshes were run for the 2.5 kW, 100kPa helium and air cases. The resulting maximum fuel temperatures are presented in Table D.15 and Table D.16. All three meshes for both cases showed good agreement across the various mesh refinements. The maximum fuel temperatures were less than 1 K different between the different meshes. The airflow for both the helium and the air cases were within 1E-4 kg/s of each other.

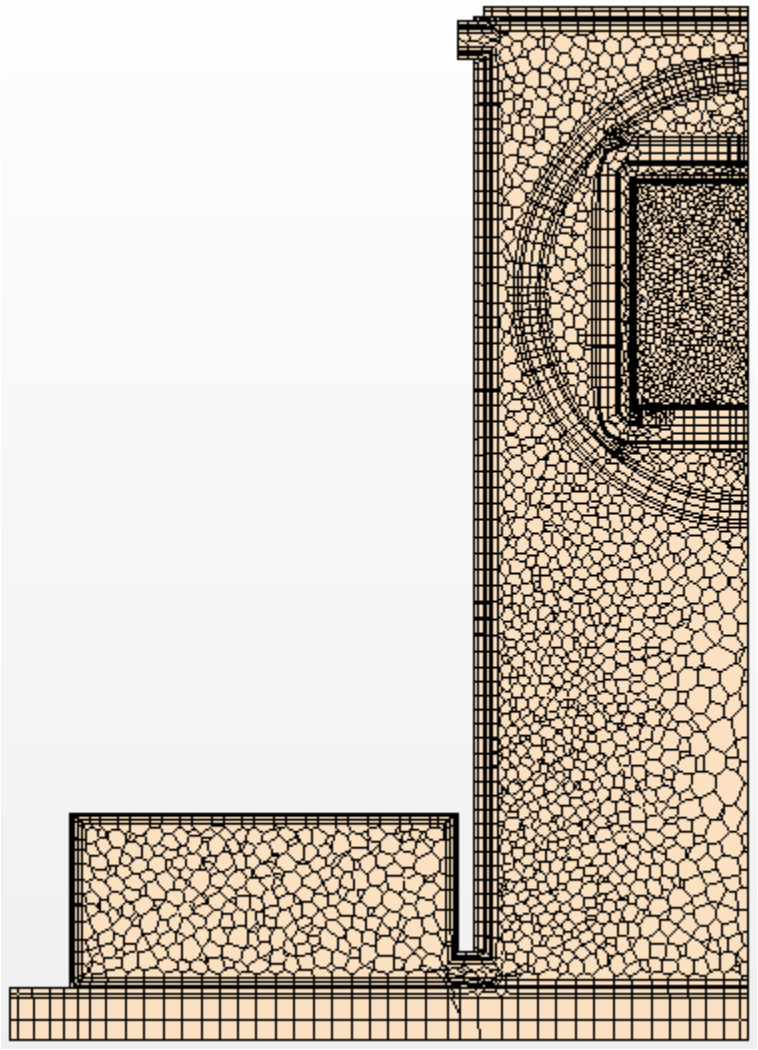

Figure D.14 Half porous coarse mesh refinement.

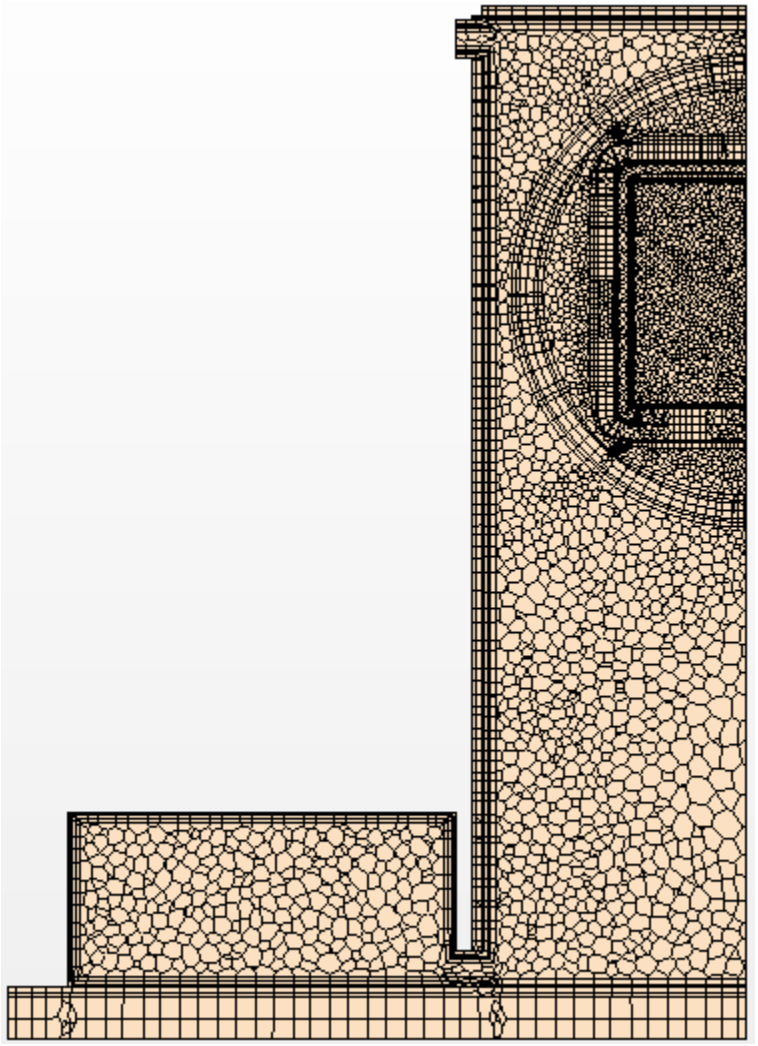

Figure D.15 Half porous medium mesh refinement.

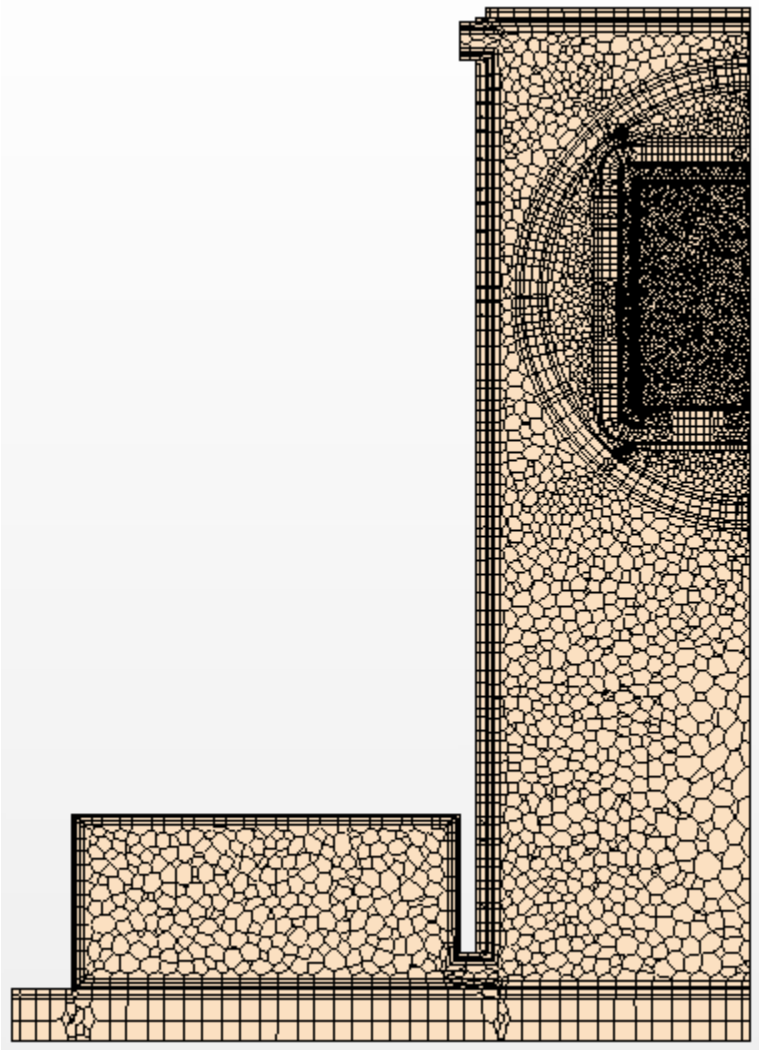

Figure D.16 Half porous fine mesh refinement.

Table D.14 Mesh details for mesh sensitivity study.

Mesh	Case #	# Cells	# Faces	# Vertices	*Solver Iteration Time (s)
Fine	1	11,241,472	70,933,181	60,346,470	8.99
Medium	2	6,015,310	35,137,842	29,501,497	5.22
Course	3	3,034,188	17,103,960	14,332,983	3.66

*Approximate time with 10 cores on an Intel Core i9-9940x processor

Table D.15 Mesh sensitivity results at 100 kPa air and 2.5 kW.

Mesh	Maximum Fuel Temperature (K)	Air Flow (kg/s)
Fine	662.16	0.02638
Medium	662.42	0.02646
Course	662.96	0.02649

Table D.16 Mesh sensitivity results at 100 kPa helium and 2.5 kW.

Mesh	Maximum Fuel Temperature (K)	Air Flow (kg/s)
Fine	553.84	0.02663
Medium	553.93	0.02668
Course	554.03	0.02667

Using the results from these meshing cases, an estimate of discretization error can be determined from calculating the grid convergence index. The grid convergence index is calculated following the procedures outlined in Roach (1999) and Stern *et al*. (2001). The method is based on generalized Richardson Extrapolation. For our application we will use the equation

$$\delta^*_{k_m} = \sum_{i=1}^{n} \left(\Delta x_{k_m}\right)^{p_k^{(i)}} g_k^{(i)} \qquad \text{D-3}$$

In Equation D-3, $\delta^*_{k_m}$ is the error, the Δx_{k_m} term is the grid sizing term, the $p_k^{(i)}$ term is the observed order of accuracy and the $g_k^{(i)}$ is the grid function of interest. For this case with three different grid sizes and solutions, this equation simplifies to [Stern *et al*., 2001]

$$\delta^*_{ij} = \frac{\epsilon_{ij}}{r_{ij}^{p_k} - 1} \qquad \text{D-4}$$

Where

$$\epsilon_{ij} = \frac{f_i - f_j}{f_i} \qquad \text{D-5}$$

And

$$r_{ij} = \left(\frac{N_j}{N_i}\right)^{(1/D)} \qquad \text{D-6}$$

The ϵ term in Equation D-4 and Equation D-5 is the relative solution difference between the different grids. The f term is some solution parameter of interest. For this study the maximum temperature of the porous fuel region was selected as the solution parameter of interest.

The term r_{ij} in Equation D-6 is the refinement ratio between the different grids in question. It follows that the number of cells in the grid are$N_1 > N_2 > \cdots > N_{n+1}$. D is the dimensionality of the grid. For this case

we are using a 3D grid so D=3. It is recommended that $r_{ij} > 1.3$ [ASME, 2009] although it may be difficult to achieve such a refinement ratio due to limits in computational resources. For the refinement ratios in the cases for this grid convergence index, the intermediate refinement ratios were approximately 1.23 and 1.25 for the coarse to medium and medium to fine refinements respectively. The overall refinement ratio between the coarse and fine grid was 1.55, which does satisfy the recommended minimum of 1.3. Since the solutions for this study showed quality asymptotic convergence, it is determined that the overall refinement ratio is sufficient.

The p_k term in Equation D-4 is the observed order of accuracy, which is easily implemented in structured mesh refinements (i.e., 2x refinement in all directions). However, in this case the mesh was refined primarily inside the canister. Instead the solver method accuracy is used, which is a 2nd order method. For a 2nd order method p_k is equal to 2.

The results of the GCI study are tabulated in Table D.17 and Table D.18. The grid convergence index (GCI column in the tables) was determined by multiplying δ^*_{ij} by a factor of safety of 3 [ASME, 2009]. Although for three grid GCI studies a factor of safety of 1.25 has been recommended, but for this study a factor of safety of 3 was used to be conservative despite having three different grids. For the final results, case 3 "coarse" containing approximately 3 million cells was selected as the final grid size due the computational efficiency. For the 2.5 kW, 100 kPa helium and air cases, the estimated error due to mesh grid size is ±1.72 K and ± 0.40 K respectively. The air case is significantly more sensitive to grid size which is consistent with the sensitivity studies in this report. After completion of the GCI study, this choice of grid size is sufficient for this model validation study.

Table D.17 GCI results for 100 kPa 2.5 kW helium case.

Case (i,j)	N_i	N_j	f_i (K)	f_j (K)	r_{ij}	ϵ_{ij}	Δ_{ij}	GCI	Error (K)
3,1	3034188	11241472	554.03	553.84	1.55	3.32E-04	2.38E-04	7.15E-04	0.40
3,2	3034188	6015310	554.03	553.93	1.26	1.71E-04	2.96E-04	8.88E-04	0.49
2,1	6015310	11241472	553.93	553.84	1.23	1.61E-04	3.11E-04	9.34E-04	0.52

Table D.18 GCI results for 100 kPa 2.5 kW air case.

Case (i,j)	N_i	N_j	f_i (K)	f_j (K)	r_{ij}	ϵ_{ij}	Δ_{ij}	GCI	Error (K)
3,1	3034188	11241472	662.96	662.16	1.55	1.20E-03	8.64E-04	2.59E-03	1.72
3,2	3034188	6015310	662.96	662.42	1.26	8.18E-04	1.41E-03	4.24E-03	2.81
2,1	6015310	11241472	662.42	662.16	1.23	3.88E-04	7.50E-04	2.25E-03	1.49

D.3.2 COBRA-SFS Mesh Sensitivity

A mesh sensitivity study was not performed for COBRA-SFS due to the nature of how the grid is constructed.

D.4 Areas for improvement

D.4.1 Lessons learned

The STAR-CCM+ detailed, STAR-CCM+ porous, and COBRA-SFS models compare reasonably well with each other. The predicted PCT values for the STAR-CCM+ detailed and porous model are within 5 K of each other. For the helium filled canister cases the detailed and porous model PCTs' are within 3 K, and for the air-filled canister cases the porous model was 4 to 5 K higher than the detailed model. The STAR-CCM+ porous model was much more computationally efficient with significantly shorter run times than the STAR-CCM+ detailed. The good agreement between the detailed and porous model indicates that a larger model with a full cask/fuel assembly (instead of the single fuel assembly represented in the HDCS) could be constructed at a computationally efficient element size with the porous media model.

Results from all three models showed that the air-filled canister models predicted significantly higher PCT values than the helium filled canister models. Air has a lower thermal conductivity than helium, making the contact resistance and gaps between parts more significant for the air cases. These parameters are hard to measure and can be difficult to quantify for best estimate models. Further study of contact resistance modeling especially in cases with high heat loads and low thermal conductivity gases is recommended for future work.

D.5 References

American Society of Mechanical Engineers, "ASME V&V 20-2009 – Standard for Verification and Validation in Computational Fluid Dynamics and Heat Transfer," New York, NY, November 2009.

Durbin, S.G. and E.R. Lindgren, "Thermal-Hydraulic Results for the Boiling Water Reactor Dry Cask Simulator," SAND2017-10551, Sandia National Laboratories, Albuquerque, New Mexico, 2017.

Lindgren, E.R. and S.G. Durbin, "Characterization of Thermal-Hydraulic and Ignition Phenomena in Prototypic, Full-Length Boiling Water Reactor Spent Fuel Pool Assemblies after a Complete Loss-of-Coolant Accident," SAND2007-2270, Sandia National Laboratories, Albuquerque, New Mexico, 2007.

Lindgren, E.R. and S.G. Durbin. Materials and Dimensional Reference Handbook for the Boiling Water Reactor Dry Cask Simulator. SAND2017-13058: Sandia National Laboratories, Albuquerque, New Mexico, 2017.

Lindgren, E.R., S.G. Durbin, R.J.M. Pulido, and A. Salazar, "Update of the Thermal Hydraulic Investigations of a Horizontal Dry Cask Simulator," SAND2019-11688 R, Sandia National Laboratories, Albuquerque, New Mexico, 2019.

National Institute of Standards and Technology, https://www.nist.gov.

Siemens PLM Software, STAR-CCM+ 14.02 (computer software), Plano, Texas, 2019.

Stern, F., W.V. Wilson, H.W. Coleman, E.G. Paterson, "Comprehensive Approach to Verification and Validation of CFD Simulations – Part 1: Methodology and Procedures," Journal of Fluids Engineering, American Society of Mechanical Engineers, New York, New York, 2001.

Suffield, S.R. J.M. Cuta, J.A. Fort and H.E. Adkins Jr., "CHARMER: A Python Based Program for Generating COBRA-SFS Boundary Conditions," PNNL-26574, Pacific Northwest National Laboratory, Richland, Washington, 2017.

TRW, "Spent Nuclear Fuel Effective Thermal Conductivity Report," BBAA000000-01717-5705-00010, Rev. 00, TRW Environmental Safety Systems, Inc., for the U.S. Department of Energy, Yucca Mountain Site Characterization Project Office, 1996.

White, F.M., “Viscous Fluid Flow,” Third Edition, McGraw-Hill, New York, 1974.

APPENDIX E ENUSA MODEL

The purpose of this appendix is to introduce the model construction, structure, approximations, and hypotheses used to create the Horizontal Dry Cask Simulator (HDCS) simulation model by ENUSA Industrias Avanzadas S.A., S.M.E. To this end, the first part of this appendix includes a brief description of the subchannel code, COBRA-SFS, used in the simulations, followed by the model description and conclusions.

E.1 Introduction to Code

COBRA-SFS is a subchannel code with the capability of including spent fuel storage systems with high levels of detail in the model, especially in fuel regions; for more details see [Pacific Northwest National Laboratory, 2018]. COBRA-SFS Cycle version 4a has been used to simulate the HDCS tests. The greatest strengths of the code are the flexibility of the subchannel modeling approach and the computational time used to solve the cases.

E.2 Model Description

COBRA-SFS models are divided in nodes according to the different regions and structures of the cask. The HDCS model has been modeled starting at the fuel rod cladding and extending to the outer vault, being divided into different regions. Figure E.1 represents the map node used in the HDCS, with a total of 40 solid nodes and 6 assemblies (assembly 1 represents the BWR fuel assembly; assemblies 2 to 6 represent different regions of the model). The air inlets have not been modeled due to the limited capability of COBRA-SFS to model these inlets.

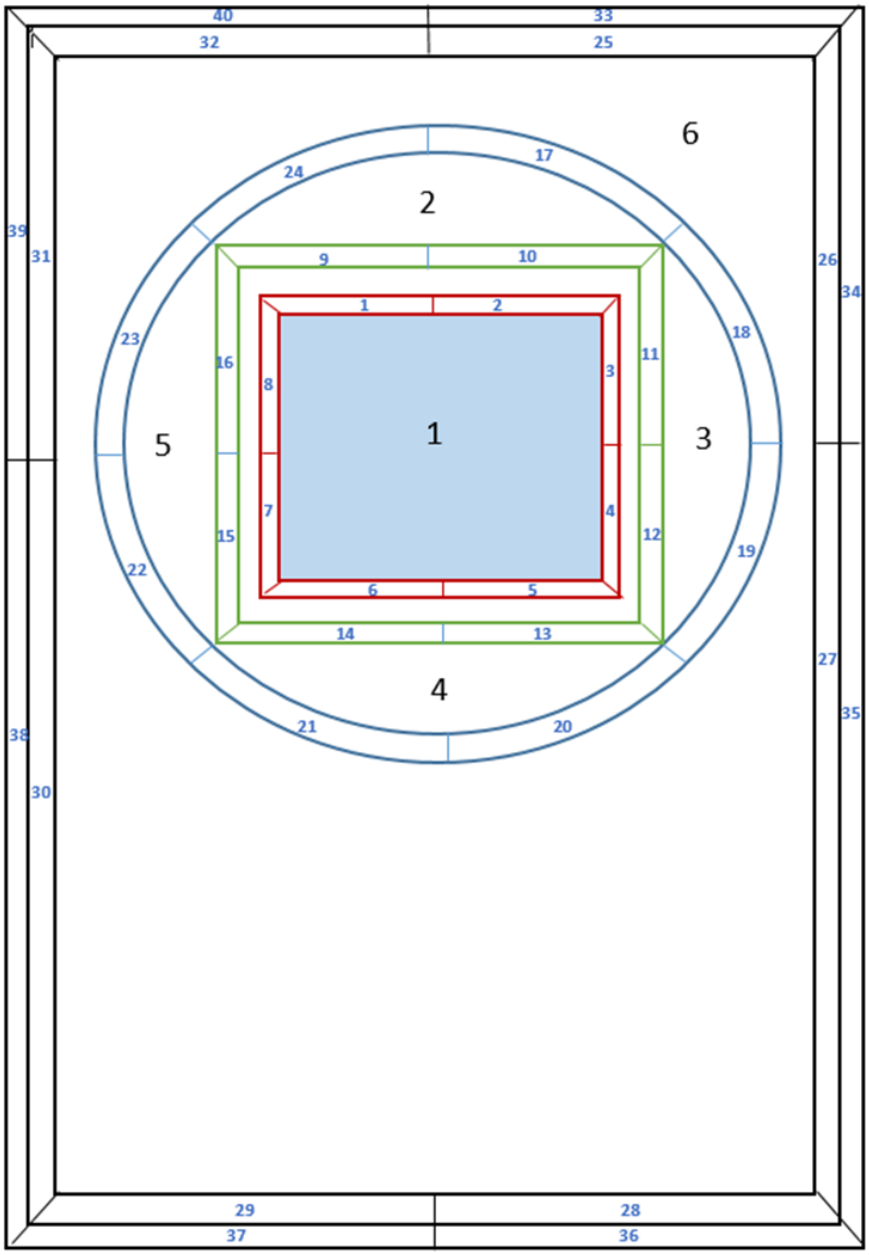

Figure E.1 COBRA-SFS HDCS map node representation.

E.2.1 Representation of Fuel Assembly

The 9×9 BWR fuel assembly has 74 heater rods (66 full-length rods and 8 partial-length rods) along with 2 water rods. In Figure E.2, the fuel assembly HDCS diagram is represented, where the red rods represent the water rods which were modeled by turning off the heat generation. The partial-length rods (in green) have been modeled as full-length rods, since COBRA-SFS has no specific module to model BWR partial-length rods.

In the rod profile results (Figure E.4 in Section E.3), the effect of considering the partial-length rods as full-length rods can be seen, as the model temperatures at the upper part of the rod are slightly higher than the experimentally measured temperatures.

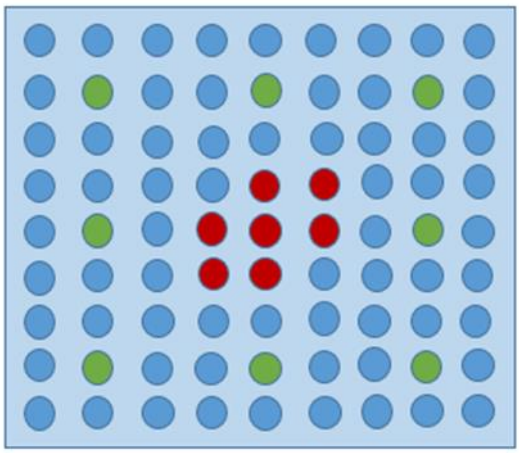

Figure E.2 Rods in fuel assembly.

E.2.2 Representation of HDCS Structures

Materials properties and dimensional data have been taken from the Handbook provided by Sandia National Laboratories [Lindgren and Durbin, 2017]. Helium and air properties have been taken from the National Institute of Standards and Technology [NIST, 2019] and are temperature dependent.

The approach of modeling radiation in fluid regions 2 to 6 has been taken (see Figure E.1).

E.2.3 Approximations and Treatments

E.2.3.1 Internal Fuel Assembly Treatment

Only the rod cladding has been modeled. This option considers all modes of surface heat transfer for the cladding, but does not include internal fuel conduction. This is the standard practice for steady state calculations in COBRA-SFS.

The flow regime inside the HDCS has been treated as laminar or turbulent depending on the Reynolds number.

E.2.3.2 External DCS Structure Treatment

Closure models do not apply to COBRA-SFS models.

E.2.3.3 Input Parameters

Solid material properties have been taken from the DCS Handbook [Lindgren and Durbin, 2017]. Fluid properties for air and helium, such as temperature, enthalpy, density, thermal conductivity, and specific heat capacity, have been taken from the NIST reference [NIST, 2019] and are temperature dependent. Average values for emissivity with axial variations have been used in the models.

E.2.3.4 Initial and Boundary Conditions

The experiments were conducted in Albuquerque, New Mexico, where the local ambient atmospheric pressure is 83.3 kPa – this is used as the reference pressure in the model. The ambient temperature was chosen to be 300 K.

The channel where the air flows (channel 6 in Figure E.1), is not connected to the plenum model. This is a standard practice for COBRA-SFS models which have two fluids in different regions of the model. With this geometrical configuration, COBRA-SFS is not able to carry out calculations in which the total inlet

mass flow is estimated. Therefore, the air mass flow was set as a boundary condition instead of being calculated.

E.2.3.5 Symmetry

Full symmetry applies to the model (see Figure E.1).

E.2.3.6 Model Sensitivity Analysis

Due to differences between our results and the experiment results, a sensitivity analysis of the inlet air mass flow boundary condition has been carried out. The calculations have been performed for three different cases with variations in the inlet air mass flow, in which case 1 has the lowest value of air mass flow rate and case 3 has the highest value. The results in Figure E.3 show how increasing the air mass flow decreases the cladding temperature, which is the expected result in the model. In summary, the model behaves as expected but the real value of the inlet air mass flow rate is needed to obtain accurate results.

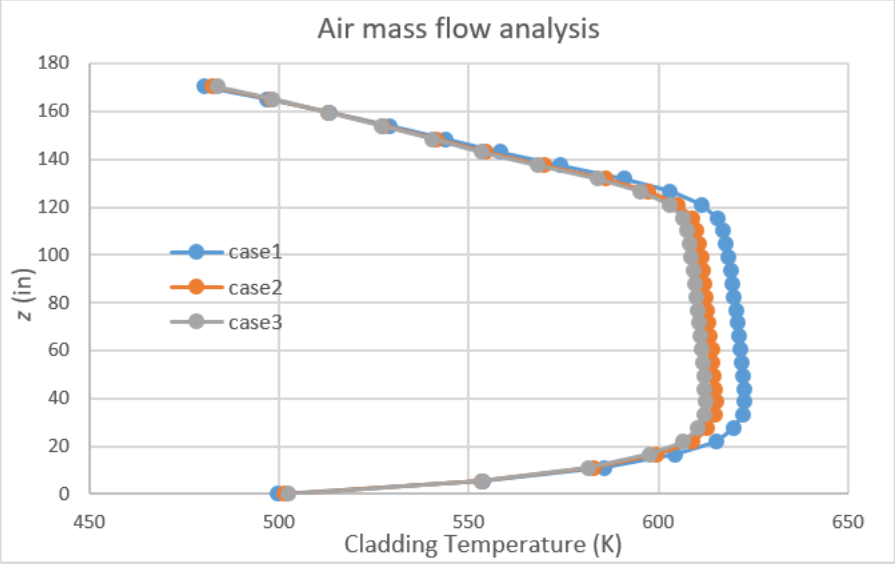

Figure E.3 Air mass flow analysis.

Another option to obtain this inlet air mass flow rate could be solving the simulation with a different code such as CFD and including the air mass flow rate results as an input in the COBRA-SFS model. This option has been used to obtain the air mass flow rate set as a boundary condition in the COBRA-SFS models using ENUSA's STAR-CCM+ CFD model for the vertical DCS [Pulido *et al*., 2020] but rotating the model to the horizontal position. This approach neglects structures that have been introduced in the HDCS model such as basket stabilizers, aluminium bridge plate and the vault.

Due to the short time available to create the new horizontal DCS model with the STAR-CCM+ code, results for the air mass flow rate were not generated. Therefore, the same inlet mass flow was used for the models.

E.3 Lessons Learned

This section provides a discussion of results obtained, which focused on peak cladding temperature (PCT) and air mass flow rate, and includes lessons learned and areas of improvement.

As mentioned in the previous section, due to the short time available to create the new models in STAR-CCM+, the air mass flow rate data was not obtained and an estimated value was used instead. COBRA-

SFS is not able to carry out calculations in which the total inlet mass flow is estimated. Therefore, the results show discrepancies compared to the experimental measurements. Future work will be carried out and with a realistic air mass flow rate, the error in the results should minimize.

Model axial temperature comparisons to the experimental results show a deviation in the modeling results at the top of the fuel axial level (Figure E.4) which is directly related to the effect of considering the partial-length rods as full-length rods, which a practice standard to model BWR partial-length rods in COBRA-SFS.

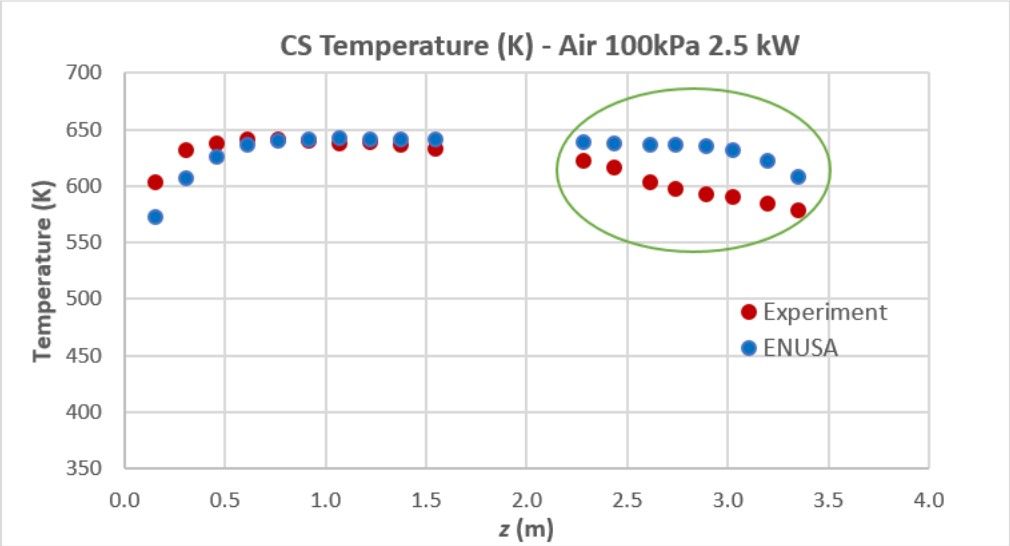

Figure E.4 CS Temperature (100kPa -2.5kW).

Future work needs to be done regarding the realistic air mass flow rate. Realistic values should be introduced in COBRA-SFS models and compared to the experimental results to verify that the error is related to this issue.

E.4 References

Lindgren, E.R. and S.G. Durbin, “Materials and Dimensional Reference Handbook for the Boiling Water Reactor Dry Cask Simulator,” SAND2017-13058R, Sandia National Laboratories, Albuquerque, New Mexico, November 2017.

Lindgren, E.R., S.G. Durbin, R.J.M. Pulido and A. Salazar, “Update on the Thermal Hydraulic Investigations of a Horizontal Dry Cask Simulator” SAND2019-11688 R, Sandia National Laboratories, Albuquerque, New Mexico, September 2019.

National Institute of Standards and Technology, https://www.nist.gov.

Pacific Northwest Laboratory, COBRA-SFS CYCLE 4A: Code System for Thermal Hydraulic Analysis of Spent Fuel Casks, Richland, Washington, 2018.

Pulido, R.J.M., E.R. Lindgren, S.G. Durbin, A. Zigh, J. Solis, S.R. Suffield, D.J. Richmond, J.A. Fort, L.E. Herranz, F. Feria, J. Penalva, M. LLoret, M. Galbán, J. Benavides, and G. Jiménez, "Modeling Validation Exercises Using the Dry Cask Simulator," SAND2019-6079R, Sandia National Laboratories, Albuquerque, New Mexico, January 2020.

This page is intentionally left blank.

APPENDIX F RESULTS TABLES

The tables in this Appendix correspond to the plots in the main body of the report and serve as a compilation of the experimental data collected and the model data generated. The following tables present test summary tables, which include measurement uncertainties. The tables also present the peak cladding temperatures, the PCT axial locations, the axial, vertical, and horizontal temperature profiles, and the air mass flow rates.

F.1 Test Summary Tables

Table F.1 Steady state peak temperature results for various components in the 0.5 kW, 100 kPa helium test.

0.5W 100 kPa Helium	Power (W)	Pressure (kPa)	PCT (K)	Channel (K)	Basket (K)	Vessel (K)	Vault (K)	Ambient (K)	Tot. Flow Rate (kg/s)
Average	**499**	**99.8**	**373.3**	**357.7**	**344.4**	**332.2**	**314.8**	**295.3**	**0.0165**
Max	503	100.0	373.5	357.9	344.6	332.6	316.2	298.3	0.0166
Min	493	99.6	372.8	357.4	344.1	331.8	314.4	294.1	0.0159
Observed Precision	2.1	0.19	0.26	0.2	0.3	0.4	0.6	0.9	0.0002
Instrument Uncertainty	13	0.37	3.7	3.6	3.4	3.3	3.1	3.0	0.0003
Combined Measurement Uncertainty	13	0.42	3.7	3.6	3.5	3.3	3.2	3.1	0.0004
Rod or Quadrant #			ES	2	4	2	2 (top)		
z-Location (m)			1.22	1.22	1.22	1.22	1.52		

Table F.2 Steady state peak temperature results for various components in the 1.0 kW, 100 kPa helium test.

1.0 W 100 kPa Helium	Power (W)	Pressure (kPa)	PCT (K)	Channel (K)	Basket (K)	Vessel (K)	Vault (K)	Ambient (K)	Tot. Flow Rate (kg/s)
Average	**1000**	**99.8**	**433.0**	**404.2**	**381.3**	**359.2**	**331.2**	**297.8**	**0.0195**
Max	1011	100.0	433.1	404.5	381.5	359.5	332.0	300.8	0.0208
Min	989	99.6	432.7	403.9	381.1	359.1	330.9	296.6	0.0185
Observed Precision	2.7	0.18	0.18	0.21	0.1	0.2	0.4	0.8	0.0005
Instrument Uncertainty	13	0.37	4.3	4.0	3.8	3.6	3.3	3.0	0.0003
Combined Measurement Uncertainty	13	0.41	4.3	4.0	3.8	3.6	3.3	3.1	0.0006
Rod or Quadrant #			ES	3	4	2	2 (top)		
z-Location (m)			1.22	1.52	1.22	1.22	1.22		

Table F.3 Steady state peak temperature results for various components in the 2.5 kW, 100 kPa helium test.

2.5 W 100 kPa Helium	Power (W)	Pressure (kPa)	PCT (K)	Channel (K)	Basket (K)	Vessel (K)	Vault (K)	Ambient (K)	Tot. Flow Rate (kg/s)
Average	**2503**	**99.8**	**558.6**	**505.8**	**463.5**	**420.6**	**367.7**	**296.7**	**0.0283**
Max	2518	100.1	559.4	506.7	464.7	422.3	370.1	302.3	0.0286
Min	2492	99.6	557.8	504.8	462.5	419.4	366.3	294.0	0.0273
Observed Precision	5.2	0.18	0.76	0.9	1.1	1.3	1.7	2.1	0.0003
Instrument Uncertainty	13	0.37	5.6	5.1	4.6	4.2	3.7	3.0	0.0003
Combined Measured Uncertainty	14	0.41	5.6	5.1	4.8	4.4	4.1	3.7	0.0004
Rod or Quadrant #			DT	2	4	2	2 (top)		
z-Location (m)			1.22	1.22	1.22	1.22	1.22		

Table F.4 Steady state peak temperature results for various components in the 5.0 kW, 100 kPa helium test.

5.0 W 100 kPa Helium	Power (W)	Pressure (kPa)	PCT (K)	Channel (K)	Basket (K)	Vessel (K)	Vault (K)	Ambient (K)	Tot. Flow Rate (kg/s)
Average	**5002**	**99.8**	**694.0**	**618.3**	**555.3**	**492.5**	**416.1**	**293.7**	**0.0354**
Max	5054	100.1	694.3	618.5	555.6	492.9	416.7	296.9	0.0358
Min	4976	99.6	693.7	617.8	554.9	491.9	415.6	292.3	0.0350
Observed Precision	8.6	0.18	0.23	0.28	0.27	0.34	0.38	0.44	0.0005
Instrument Uncertainty	13	0.37	6.9	6.2	5.6	4.9	4.2	2.9	0.0003
Combined Measured Uncertainty	16	0.41	6.9	6.2	5.6	4.9	4.2	3.0	0.0006
Rod or Quadrant #			DT	2	4	2	2 (top)		
z-Location (m)			1.22	1.22	1.22	0.91			

Table F.5 Steady state peak temperature results for various components in the 0.5 kW, 800 kPa helium test.

0.5 W 800 kPa Helium	Power (W)	Pressure (kPa)	PCT (K)	Channel (K)	Basket (K)	Vessel (K)	Vault (K)	Ambient (K)	Tot. Flow Rate (kg/s)
Average	**500**	**799.8**	**367.7**	**353.8**	**339.2**	**330.4**	**313.9**	**295.2**	**0.0157**
Max	505	800.1	367.9	353.9	339.4	330.7	314.7	297.6	0.0161
Min	494	798.6	367.4	353.6	338.9	330.1	313.4	293.7	0.0141
Observed Precision	2.4	0.19	0.21	0.2	0.2	0.3	0.5	0.8	0.0005
Instrument Uncertainty	13	0.37	3.7	3.5	3.4	3.3	3.1	3.0	0.0003
Combined Measured Uncertainty	13	0.42	3.7	3.5	3.4	3.3	3.2	3.1	0.0006
Rod or Quadrant #			ES	2	2	2	2 (top)		
z-Location (m)			1.22	1.22	1.22	1.22	1.52		

Table F.6 Steady state peak temperature results for various components in the 5.0 kW, 800 kPa helium test.

5.0 W 800 kPa Helium	Power (W)	Pressure (kPa)	PCT (K)	Channel (K)	Basket (K)	Vessel (K)	Vault (K)	Ambient (K)	Tot. Flow Rate (kg/s)
Average	**5000**	**799.8**	**677.1**	**604.1**	**536.7**	**486.0**	**411.8**	**293.2**	**0.0338**
Max	5020	800.1	677.4	604.4	537.2	486.4	412.2	295.5	0.0345
Min	4971	799.6	676.6	603.5	536.0	485.3	411.2	292.0	0.0333
Observed Precision	8.5	0.20	0.34	0.37	0.49	0.38	0.35	0.27	0.0008
Instrument Uncertainty	13	0.37	6.8	6.0	5.4	4.9	4.1	2.9	0.0003
Combined Measured Uncertainty	16	0.42	6.8	6.1	5.4	4.9	4.1	2.9	0.0008
Rod or Quadrant #			ES	2	2	2	2 (top)		
z-Location (m)			1.22	1.22	1.22	1.22	1.22		

Table F.7 Steady state peak temperature results for various components in the 0.5 kW, 100 kPa air test.

0.5 W 100 kPa Air	Power (W)	Pressure (kPa)	PCT (K)	Channel (K)	Basket (K)	Vessel (K)	Vault (K)	Ambient (K)	Tot. Flow Rate (kg/s)
Average	**500**	**99.8**	**426.6**	**385.7**	**354.0**	**331.5**	**315.2**	**296.6**	**0.0141**
Max	503	100.0	427.4	386.4	354.8	332.4	316.3	298.2	0.0149
Min	495	99.6	426.4	385.4	353.9	331.0	314.3	295.0	0.0131
Observed Precision	1.5	0.18	0.2	0.3	0.2	0.4	0.8	0.8	0.0006
Instrument Uncertainty	13	0.37	4.3	3.9	3.5	3.3	3.2	3.0	0.0003
Combined Measured Uncertainty	13	0.41	4.3	3.9	3.5	3.3	3.2	3.1	0.0006
Rod or Quadrant #			ES	2	4	2	2 (top)		
z-Location (m)			1.22	1.22	1.83	1.22	1.524		

Table F.8 Steady state peak temperature results for various components in the 1.0 kW, 100 kPa air test.

1.0 W 100 kPa Air	Power (W)	Pressure (kPa)	PCT (K)	Channel (K)	Basket (K)	Vessel (K)	Vault (K)	Ambient (K)	Tot. Flow Rate (kg/s)
Average	**1000**	**99.8**	**501.4**	**442.5**	**393.4**	**356.4**	**328.8**	**296.4**	**0.0194**
Max	1013	100.0	502.4	443.0	393.8	356.8	329.4	298.7	0.0202
Min	992	99.6	499.6	441.0	392.2	355.6	328.2	294.4	0.0188
Observed Precision	2.6	0.17	1.2	0.9	0.7	0.5	0.5	0.7	0.0007
Instrument Uncertainty	13	0.37	5.0	4.4	3.9	3.6	3.3	3.0	0.0003
Combined Measured Uncertainty	13	0.41	5.2	4.5	4.0	3.6	3.3	3.0	0.0007
Rod or Quadrant #			ES	2	4	2	2 (top)		
z-Location (m)			1.22	0.91	1.83	1.22	1.22		

Table F.9 Steady state peak temperature results for various components in the 2.5 kW, 100 kPa air test.

2.5 W 100 kPa Air	Power (W)	Pressure (kPa)	PCT (K)	Channel (K)	Basket (K)	Vessel (K)	Vault (K)	Ambient (K)	Tot. Flow Rate (kg/s)
Average	**2500**	**99.8**	**647.0**	**562.5**	**485.9**	**420.0**	**367.2**	**296.7**	**0.0277**
Max	2519	100.0	647.1	562.7	486.1	420.5	367.9	300.9	0.0280
Min	2484	99.6	646.9	562.4	485.6	419.6	366.6	294.7	0.0268
Observed Precision	5.8	0.18	0.09	0.13	0.23	0.39	0.54	0.92	0.0003
Instrument Uncertainty	13	0.37	6.5	5.6	4.9	4.2	3.7	3.0	0.0003
Combined Measured Uncertainty	14	0.41	6.5	5.6	4.9	4.2	3.7	3.1	0.0004
Rod or Quadrant #			DT	2	2	2	2 (top)		
z-Location (m)			0.61	0.91	1.22	1.22	1.22		

F.2 Peak Cladding Temperatures

Table F.10 Data comparison for the peak cladding temperatures from all tests.

			Temperature (K)				
Power (kW)	**Pressure (kPa)**	**Fill Gas**	**1**	**2**	**3**	**4**	**Experiment**
0.5	100	Helium	371.3	372.0	371.1	370.9	373.3
1.0	100	Helium	431.6	429.0	428.7	427.2	433.0
2.5	100	Helium	557.6	555.0	554.0	549.6	558.6
5.0	100	Helium	699.8	701.0	697.9	687.4	694.0
0.5	800	Helium	363.4	369.0	368.6	369.4	367.7
5.0	800	Helium	683.4	687.0	683.9	683.4	677.1
0.5	100	Air	414.9	419.0	422.9	428.7	426.6
1.0	100	Air	491.1	502.0	504.3	506.8	501.4
2.5	100	Air	639.4	657.0	661.7	645.5	647.0
5.0	100	Air	787.5	820.0	825.2	794.8	781.9

F.3 PCT Axial Locations

Table F.11 Data comparison for the PCT axial locations from all tests.

			PCT Axial Location (m)				
Power (kW)	**Pressure (kPa)**	**Fill Gas**	**1**	**2**	**3**	**4**	**Experiment**
0.5	100	Helium	1.67	1.22	1.52	1.89	1.67
1.0	100	Helium	1.67	1.22	1.22	1.89	1.67
2.5	100	Helium	1.68	1.22	1.22	1.89	1.68
5.0	100	Helium	1.68	0.91	0.91	1.89	1.68
0.5	800	Helium	1.55	1.83	1.52	1.89	1.55
5.0	800	Helium	1.56	1.22	1.22	1.89	1.56
0.5	100	Air	1.52	0.91	0.91	1.89	1.52
1.0	100	Air	1.52	0.91	0.61	1.89	1.52
2.5	100	Air	1.56	0.91	0.61	1.89	1.56
5.0	100	Air	1.59	0.91	0.61	1.89	1.59

F.4 Axial Internal Centerline Temperature Profiles

Table F.12 Data comparison for the internal centerline temperature profile coordinates as a function of the *z*-coordinate from the 100 kPa helium tests.

0.5 kW, 100 kPa Helium (Figure 3.2)					
	Temperature (K)				
z (m)	1	2	3	4	Experiment
0.61	368	363	367	365	371
1.219	371	370	371	371	371
1.829	371	366	371	369	370
2.438	367	370	366	367	366
3.658	343	339	341	349	343
1.0 kW, 100 kPa Helium (Figure 3.5)					
	Temperature (K)				
z (m)	1	2	3	4	Experiment
0.61	426	416	423	418	429
1.219	431	426	428	426	430
1.829	431	426	427	424	427
2.438	425	419	420	421	421
3.658	385	373	378	391	381
2.5 kW, 100 kPa Helium (Figure 3.8)					
	Temperature (K)				
z (m)	1	2	3	4	Experiment
0.61	550	536	548	535	555
1.219	556	549	553	549	553
1.829	557	547	549	544	548
2.438	545	534	534	539	537
3.658	475	452	461	487	466
5.0 kW, 100 kPa Helium (Figure 3.11)					
	Temperature (K)				
z (m)	1	2	3	4	Experiment
0.61	692	679	692	671	690
1.219	698	690	694	688	684
1.829	698	683	684	680	678
2.438	681	664	662	673	665
3.658	583	550	561	603	572

Table F.13 Data comparison for the internal centerline temperature profile coordinates as a function of the *z*-coordinate from the 800 kPa helium tests.

0.5 kW, 800 kPa Helium (Figure 3.14)					
	Temperature (K)				
z (m)	1	2	3	4	Experiment
0.61	355	356	363	363	365
1.219	359	363	368	370	364
1.829	359	364	368	367	363
2.438	355	360	364	366	360
3.658	333	333	339	348	335
5.0 kW, 800 kPa Helium (Figure 3.17)					
	Temperature (K)				
z (m)	1	2	3	4	Experiment
0.61	658	649	671	664	670
1.219	671	672	682	683	665
1.829	671	667	674	672	660
2.438	649	647	651	670	646
3.658	522	510	552	601	533

Table F.14 Data comparison for the internal centerline temperature profile coordinates as a function of the *z*-coordinate from the 100 kPa air tests.

0.5 kW, 100 kPa Air (Figure 3.20)					
	Temperature (K)				
z (m)	1	2	3	4	Experiment
0.61	402	404	421	421	421
1.219	406	410	421	427	421
1.829	406	407	415	426	418
2.438	399	398	403	423	412
3.658	360	355	365	399	373
1.0 kW, 100 kPa Air (Figure 3.23)					
	Temperature (K)				
z (m)	1	2	3	4	Experiment
0.61	476	478	503	497	496
1.219	482	486	499	505	494
1.829	482	479	488	503	489
2.438	469	465	471	499	481
3.658	405	396	414	464	427
2.5 kW, 100 kPa Air (Figure 3.26)					
	Temperature (K)				
z (m)	1	2	3	4	Experiment
0.61	628	634	659	639	645
1.219	634	637	646	650	637
1.829	634	620	624	646	630
2.438	614	596	597	641	615
3.658	514	487	512	591	527
5.0 kW, 100 kPa Air (Figure 3.29)					
	Temperature (K)				
z (m)	1	2	3	4	Experiment
0.61	779	799	822	780	778
1.219	785	791	796	793	769
1.829	784	762	762	788	762
2.438	758	730	726	782	744
3.658	641	593	619	720	651

F.5 Vertical Temperature Profiles

Table F.15 Data comparison for the vertical temperature profile coordinates at z = 1.219 m (48.0 in.) from the 0.5 kW 100 kPa and the 1.0 kW 100 kPa helium tests.

0.5 kW, 100 kPa Helium (Figure 3.3)						
		Temperature (K)				
Location	***x* (m)**	**1**	**2**	**3**	**4**	**Experiment**
Vault Top	-0.169	313	316	315	--	315
Pressure Vessel Top	-0.137	331	331	332	332	332
Basket Top	-0.090	343	342	341	341	344
Channel Top	-0.068	356	356	357	354	358
EQ	-0.057	361	365	362	363	366
ES	-0.029	370	372	370	370	373
WEU	0	371	370	371	368	371
Channel Bottom	0.068	343	344	342	344	348
Basket Bottom	0.090	341	342	342	341	344
Pressure Vessel Bottom	0.137	330	326	321	329	330
Vault Bottom	0.421	303	304	304	--	303
1.0 kW, 100 kPa Helium (Figure 3.6)						
		Temperature (K)				
Location	***x* (m)**	**1**	**2**	**3**	**4**	**Experiment**
Vault Top	-0.169	330	332	331	--	331
Pressure Vessel Top	-0.137	361	358	360	358	359
Basket Top	-0.090	382	376	377	374	381
Channel Top	-0.068	406	402	404	398	404
EQ	-0.057	414	418	413	414	420
ES	-0.029	429	429	427	425	433
WEU	0	431	426	428	422	430
Channel Bottom	0.068	383	377	378	381	387
Basket Bottom	0.090	379	377	378	375	381
Pressure Vessel Bottom	0.137	358	348	338	352	356
Vault Bottom	0.421	313	311	313	--	309

Table F.16 Data comparison for the vertical temperature profile coordinates at z = 1.219 m (48.0 in.) from the 2.5 kW 100 kPa and the 5.0 kW 100 kPa helium tests.

2.5 kW, 100 kPa Helium (Figure 3.9)						
		Temperature (K)				
Location	***x* (m)**	**1**	**2**	**3**	**4**	**Experiment**
Vault Top	-0.169	369	369	370	--	368
Pressure Vessel Top	-0.137	425	419	424	419	421
Basket Top	-0.090	467	454	457	451	462
Channel Top	-0.068	510	506	510	499	506
EQ	-0.057	526	537	527	528	536
ES	-0.029	552	555	550	547	558
WEU	0	556	549	553	543	553
Channel Bottom	0.068	469	457	459	467	477
Basket Bottom	0.090	460	456	458	454	464
Pressure Vessel Bottom	0.137	416	396	379	406	414
Vault Bottom	0.421	330	327	331	--	323
5.0 kW, 100 kPa Helium (Figure 3.12)						
		Temperature (K)				
Location	***x* (m)**	**1**	**2**	**3**	**4**	**Experiment**
Vault Top	-0.169	425	421	424	--	416
Pressure Vessel Top	-0.137	506	494	502	497	492
Basket Top	-0.090	569	549	552	545	555
Channel Top	-0.068	632	628	635	616	618
EQ	-0.057	654	675	658	660	663
ES	-0.029	692	698	690	684	693
WEU	0	698	690	694	679	684
Channel Bottom	0.068	573	553	556	572	577
Basket Bottom	0.090	558	552	555	548	555
Pressure Vessel Bottom	0.137	487	448	428	473	479
Vault Bottom	0.421	358	354	361	--	340

Table F.17 Data comparison for the vertical temperature profile coordinates at z = 1.219 m (48.0 in.) from the 0.5 kW 800 kPa and the 5.0 kW 800 kPa helium tests.

0.5 kW, 800 kPa Helium (Figure 3.15)						
		Temperature (K)				
Location	***x* (m)**	**1**	**2**	**3**	**4**	**Experiment**
Vault Top	-0.169	313	316	316	--	314
Pressure Vessel Top	-0.137	332	331	332	332	330
Basket Top	-0.090	340	339	339	340	339
Channel Top	-0.068	355	355	354	353	354
EQ	-0.057	359	364	359	362	362
ES	-0.029	363	368	367	369	368
WEU	0	359	363	368	367	364
Channel Bottom	0.068	339	338	339	343	341
Basket Bottom	0.090	337	338	339	340	338
Pressure Vessel Bottom	0.137	328	324	320	327	326
Vault Bottom	0.421	303	303	303	--	302
5.0 kW, 800 kPa Helium (Figure 3.18)						
		Temperature (K)				
Location	***x* (m)**	**1**	**2**	**3**	**4**	**Experiment**
Vault Top	-0.169	422	421	425	--	412
Pressure Vessel Top	-0.137	508	498	502	497	486
Basket Top	-0.090	559	540	541	543	537
Channel Top	-0.068	629	621	624	613	604
EQ	-0.057	653	668	647	657	650
ES	-0.029	682	687	679	681	677
WEU	0	671	672	682	675	665
Channel Bottom	0.068	550	533	538	566	551
Basket Bottom	0.090	538	532	537	542	530
Pressure Vessel Bottom	0.137	473	442	417	464	459
Vault Bottom	0.421	351	349	355	--	333

Table F.18 Data comparison for the vertical temperature profile coordinates at z = 1.219 m (48.0 in.) from the 0.5 kW 100 kPa and the 1.0 kW 100 kPa air tests.

0.5 kW, 100 kPa Air (Figure 3.21)						
		Temperature (K)				
Location	***x* (m)**	**1**	**2**	**3**	**4**	**Experiment**
Vault Top	-0.169	314	317	316	--	315
Pressure Vessel Top	-0.137	333	332	333	332	331
Basket Top	-0.090	352	346	346	353	354
Channel Top	-0.068	388	382	386	390	386
EQ	-0.057	401	411	400	416	415
ES	-0.029	415	418	419	428	427
WEU	0	406	410	421	425	421
Channel Bottom	0.068	353	353	348	369	367
Basket Bottom	0.090	348	347	348	356	354
Pressure Vessel Bottom	0.137	332	326	321	328	328
Vault Bottom	0.421	305	305	305	--	302
1.0 kW, 100 kPa Air (Figure 3.24)						
		Temperature (K)				
Location	***x* (m)**	**1**	**2**	**3**	**4**	**Experiment**
Vault Top	-0.169	327	332	336	--	329
Pressure Vessel Top	-0.137	358	358	362	358	356
Basket Top	-0.090	392	383	385	393	393
Channel Top	-0.068	448	441	449	451	442
EQ	-0.057	467	485	469	489	484
ES	-0.029	491	496	497	505	501
WEU	0	482	486	499	502	494
Channel Bottom	0.068	395	396	387	421	418
Basket Bottom	0.090	385	384	387	397	393
Pressure Vessel Bottom	0.137	357	345	341	351	351
Vault Bottom	0.421	311	309	314	--	307

Table F.19 Data comparison for the vertical temperature profile coordinates at z = 1.219 m (48.0 in.) from the 2.5 kW 100 kPa and the 5.0 kW 100 kPa air tests.

2.5 kW, 100 kPa Air (Figure 3.27)						
		Temperature (K)				
Location	***x* (m)**	**1**	**2**	**3**	**4**	**Experiment**
Vault Top	-0.169	368	368	372	--	367
Pressure Vessel Top	-0.137	424	419	424	420	420
Basket Top	-0.090	486	465	466	480	486
Channel Top	-0.068	568	567	577	571	562
EQ	-0.057	595	633	605	628	617
ES	-0.029	636	648	643	649	645
WEU	0	634	637	646	645	637
Channel Bottom	0.068	497	470	471	534	534
Basket Bottom	0.090	473	470	471	484	484
Pressure Vessel Bottom	0.137	416	393	378	404	408
Vault Bottom	0.421	330	327	330	--	321
5.0 kW, 100 kPa Air (Figure 3.30)						
		Temperature (K)				
Location	***x* (m)**	**1**	**2**	**3**	**4**	**Experiment**
Vault Top	-0.169	429	424	430	--	421
Pressure Vessel Top	-0.137	510	498	506	498	496
Basket Top	-0.090	597	563	565	576	585
Channel Top	-0.068	695	699	714	693	676
EQ	-0.057	727	784	748	765	741
ES	-0.029	780	803	792	791	777
WEU	0	785	791	796	787	769
Channel Bottom	0.068	621	617	573	659	655
Basket Bottom	0.090	579	571	572	578	582
Pressure Vessel Bottom	0.137	491	456	426	472	476
Vault Bottom	0.421	364	358	364	--	343

F.6 Horizontal Temperature Profiles

Table F.20 Data comparison for the horizontal temperature profile coordinates at z = 1.829 m (72.0 in.) from the 100 kPa helium tests.

0.5 kW, 100 kPa Helium (Figure 3.4)						
		Temperature (K)				
Location	***y* (m)**	**1**	**2**	**3**	**4**	**Experiment**
WEU	0	371	370	371	369	370
GU	0.029	368	371	368	369	370
IU	0.057	359	363	359	362	365
Channel	0.068	354	355	355	353	355
Basket	0.089	342	342	342	342	344
Pressure Vessel	0.137	331	329	331	331	331
Vault	0.165	304	307	305	--	306
1.0 kW, 100 kPa Helium (Figure 3.7)						
		Temperature (K)				
Location	***y* (m)**	**1**	**2**	**3**	**4**	**Experiment**
WEU	0	431	426	427	424	427
GU	0.029	426	427	423	424	429
IU	0.057	410	414	408	412	419
Channel	0.068	402	399	400	396	401
Basket	0.089	381	377	378	377	380
Pressure Vessel	0.137	360	353	357	356	358
Vault	0.165	314	316	314	--	315
2.5 kW, 100 kPa Helium (Figure 3.10)						
		Temperature (K)				
Location	***y* (m)**	**1**	**2**	**3**	**4**	**Experiment**
WEU	0	557	547	549	544	548
GU	0.029	548	548	541	544	550
IU	0.057	520	527	516	524	532
Channel	0.068	504	499	501	494	499
Basket	0.089	464	456	457	455	459
Pressure Vessel	0.137	419	405	416	413	416
Vault	0.165	333	335	332	--	334
5.0 kW, 100 kPa Helium (Figure 3.13)						
		Temperature (K)				
Location	***y* (m)**	**1**	**2**	**3**	**4**	**Experiment**
WEU	0	698	683	684	680	678
GU	0.029	686	685	674	680	677
IU	0.057	646	657	639	653	651
Channel	0.068	623	615	618	608	607
Basket	0.089	563	550	551	548	549
Pressure Vessel	0.137	493	471	488	485	482
Vault	0.165	362	365	359	--	361

Table F.21 Data comparison for the horizontal temperature profile coordinates at z = 1.829 m (72.0 in.) from the 800 kPa helium tests.

0.5 kW, 800 kPa Helium (Figure 3.16)						
		Temperature (K)				
Location	***y* (m)**	**1**	**2**	**3**	**4**	**Experiment**
WEU	0	359	364	368	367	363
GU	0.029	358	365	365	367	364
IU	0.057	355	359	357	359	358
Channel	0.068	351	351	352	350	350
Basket	0.089	339	339	339	339	338
Pressure Vessel	0.137	330	328	331	328	330
Vault	0.165	304	307	305	--	305
5.0 kW, 800 kPa Helium (Figure 3.19)						
		Temperature (K)				
Location	***y* (m)**	**1**	**2**	**3**	**4**	**Experiment**
WEU	0	671	667	674	672	660
GU	0.029	664	670	663	672	660
IU	0.057	632	644	627	644	635
Channel	0.068	610	602	605	598	589
Basket	0.089	546	535	534	536	529
Pressure Vessel	0.137	489	471	486	475	476
Vault	0.165	358	363	357	--	354

Table F.22 Data comparison for the horizontal temperature profile coordinates at z = 1.829 m (72.0 in.) from the 100 kPa air tests.

0.5 kW, 100 kPa Air (Figure 3.22)						
		Temperature (K)				
Location	***y* (m)**	**1**	**2**	**3**	**4**	**Experiment**
WEU	0	406	407	415	426	418
GU	0.029	404	409	408	426	419
IU	0.057	390	398	388	412	401
Channel	0.068	377	374	376	385	379
Basket	0.089	350	347	346	355	353
Pressure Vessel	0.137	332	329	332	331	331
Vault	0.165	306	308	307	--	306
1.0 kW, 100 kPa Air (Figure 3.25)						
		Temperature (K)				
Location	***y* (m)**	**1**	**2**	**3**	**4**	**Experiment**
WEU	0	482	479	488	503	489
GU	0.029	476	482	480	503	491
IU	0.057	452	466	451	484	467
Channel	0.068	433	429	433	444	433
Basket	0.089	389	384	384	396	392
Pressure Vessel	0.137	357	351	358	355	354
Vault	0.165	312	315	316	--	313
2.5 kW, 100 kPa Air (Figure 3.28)						
		Temperature (K)				
Location	***y* (m)**	**1**	**2**	**3**	**4**	**Experiment**
WEU	0	634	620	624	646	630
GU	0.029	622	623	613	645	634
IU	0.057	579	601	573	621	607
Channel	0.068	551	545	549	561	552
Basket	0.089	480	468	465	484	481
Pressure Vessel	0.137	419	405	415	413	414
Vault	0.165	333	335	332	--	333
5.0 kW, 100 kPa Air (Figure 3.31)						
		Temperature (K)				
Location	***y* (m)**	**1**	**2**	**3**	**4**	**Experiment**
WEU	0	784	762	762	788	762
GU	0.029	768	766	749	786	763
IU	0.057	712	739	702	757	729
Channel	0.068	678	669	673	682	665
Basket	0.089	587	566	562	580	577
Pressure Vessel	0.137	497	474	490	485	486
Vault	0.165	368	369	363	--	366

F.7 Air Mass Flow Rates

Table F.23 Data comparison for the air mass flow rates from all tests.

			Air Mass Flow Rate (kg/s)			
Power (kW)	**Pressure (kPa)**	**Fill Gas**	**1**	**2**	**3**	**Experiment**
0.5	100	Helium	0.0137	0.0135	0.0130	0.0165
1.0	100	Helium	0.0181	0.0200	0.0196	0.0195
2.5	100	Helium	0.0263	0.0275	0.0267	0.0283
5.0	100	Helium	0.0346	0.0340	0.0329	0.0354
0.5	800	Helium	0.0135	0.0132	0.0128	0.0157
5.0	800	Helium	0.0337	0.0328	0.0317	0.0338
0.5	100	Air	0.0136	0.0147	0.0145	0.0141
1.0	100	Air	0.0183	0.0188	0.0209	0.0194
2.5	100	Air	0.0263	0.0273	0.0265	0.0277
5.0	100	Air	0.0339	0.0354	0.0344	0.0359


Sandia National Laboratories